Hydrodynamics and Mass Transport in an Annular Flow Bioreactor

A Thesis submitted in accordance with the requirements of the University of Liverpool for the degree of Doctor of Philosophy

Stephen J. Curran BEng(Hons) M.Sc. AMIChemE

Department of Clinical Engineering
Faculty of Medicine
University of Liverpool

December 2002

Abstract

One of the most rapidly emerging fields in medicine is tissue engineering; the scientific discipline to regenerate functional tissues and organs in vitro. The long-term goals of tissue engineering are still some way off, but the areas where significant research is required have been identified. It has been established that the generation of functional tissue will only occur in a dynamic bioreactor environment and that this environment should, in the first instance, simulate the physiologic condition the tissue experiences in vivo.

The relationship between the hydrodynamics, mass transport of nutrients and oxygen and the shear stress field is a complex one within many types of bioreactor and these factors have a direct bearing on the viability, proliferation and normal morphogenesis of cells. In this study a specific type of bioreactor, the annular flow bioreactor, was developed to address this relationship.

The flow regimes within model bioreactors at two different geometric scales were characterised qualitatively by flow visualisation and quantitatively by Laser Doppler Anemometry (LDA) where subsequent quantitative calculations of the shear stress field for the varying flow condition were made. Qualitative studies on solute transport were addressed using dye tracer injection techniques in the larger model system. A modified concentric cylinder rheometer was used as a working bioreactor employing cell culture media and freely suspended L929 fibroblasts. The geometry matched the small-scale system for LDA and flow visualisation studies. Quantitative real time measurements of oxygen transport were established in this system using a fibre-optic oxygen probe. Under controlled conditions of flow and mass transport a series of experiments on the number and viability of cells within the bioreactor at defined time periods were established using flow cytometry for a maximum 24h experimental time.

In this study it has been found from LDA measurements that the shear stresses experienced by cells is lower in the larger scale system than it is in the smaller scale for the same flow regime. Dye tracer studies indicate that increased agitation promotes mass transport within the system and this has also been confirmed from oxygen transport measurements using cells. Increased agitation therefore promotes mass transport that is beneficial to cells but increases the shear stresses they experience which is to their detriment. A compromise therefore exists and the optimum condition found in the small-scale bioreactor appears to be operation at the hydrodynamic transition point between laminar Taylor-vortex flow and wavy-vortex flow. Here the shear stresses appear to be subcritical for most cell types, the cells remain well suspended in the media and the mass transport is sufficient. It is suggested that larger scale bioreactors can be operated in more agitated regimes of flow than this and will better promote mass transport but will maintain lower levels of shear stress. This has important implications for commercialising tissue engineering bioreactors.

Acknowledgements

I am grateful to my supervisor, Dr. Richard Black, for his guidance and insightful perspectives at various stages of this research project and for allowing me considerable freedom to take the work in a direction of my choosing.

Jim Blackhurst has made an invaluable contribution with the mechanical fabrication and modification of the experimental systems used in this study. I extend special thanks to him.

I would like to extend my thanks to the other members of the faculty of Clinical Engineering for their contributions, large and small whilst working toward this PhD and to the staff and students in the department with whom I have had the pleasure of working over the past four years. They have made my time here an enjoyable and rewarding one.

The support of my family, Michael, Patricia and Carmel has been a constant source of strength to me and for that I am eternally grateful.

The financial support of the University of Liverpool is gratefully acknowledged.

Table Of Contents

Chapter 1: Introduction

Chapter 2: Hydrodynamics of Concentric Cylinder Flows

Chapter 3: Flow Visualisation in Concentric Cylinder Flows

Chapter 4: Laser Doppler Anemometry: Principles of Measurement

Chapter 5: Laser Doppler Anemometry: Experimental Measurements and Modelling

Chapter 6: Relationships and Techniques for Mass Transport Studies

Chapter 7: Mass Transport in Concentric Cylinder Flows

Chapter 8: Experimental Studies of Oxygen Transport

Chapter9: Flow Cytometry

List of Figures

List of Plates

List of Tables

Nomenclature

a	acceleration	ms^{-1}
a'	interfacial area	m^2
c	velocity of light	ms^{-1}
c_A	mass concentration	kgm^{-3}
c_{Ao}	bulk concentration	kgm^{-3}
c_{Ai}	interfacial concentration	kgm^{-3}
d	gap width	m
e	voidage	
e_{ij}	rate of strain tensor	
d_{ed}	eddy velocity	ms^{-1}
d_p	particle diameter	m
f	focal length	m
k	Boltzmann constant	JK^{-1}
k_l	mass transfer coefficient	ms^{-1}
k_q	quenching coefficient	
ℓ_{bs}	beam separation	m
$\{\ell\}_i$	unit vector of incident light beam	
$\{\hat{u}\}_i$	unit velocity vector	
n	wavenumber	
r	radius	m
t	time	s
t_e	exposure time	s
u	velocity	ms^{-1}
u_{ed}	eddy velocity	ms^{-1}
u_{rms}	root mean square velocity	ms^{-1}
v	velocity	ms^{-1}
x_i	liquid phase fraction	
y_i	vapour phase fraction	
z	axial distance	m
C	constant (equation. 2.3)	
C_A	molar concentration	$mol\ m^{-3}$
C_D	drag coefficient	
D	diffusivity	m^2s^{-1}
E_K	kinetic energy	J
F_{st}	Stokes drag force	N
G_i	Gibbs free energy	J
H	Henrys constant	$Pa\ molfrac^{-1}$
I	identity matrix	
J_A	mass flux	kgs^{-1}
K_{SV}	Stern-Volmer constant	
M	torque	Nm
N	number of vortices	
N_A	molar flux	$mol\ s^{-1}$
P	pressure	Pa
Q_{O2}	Oxygen absorbtion rate	$kg\ s^{-1}$
R	Universal gas constant	$Jmol^{-1}K^{-1}$

α	wavenumber	
φ	beam separation (equation 4.16)	m
γ	shear rate	s^{-1}
μ	viscosity	Pas
μ_i	chemical potential	
ρ	density	kgm^{-3}
τ	shear stress	N
τ_o	wall shear stress	N
τ	torque	Nm
ν	frequency	Hz
ν	kinematic viscosity	m^2s^{-1}
ω	vorticity	
Δ	distance	m
Γ	aspect ratio	
Φ	phase angle	
Ω	angular velocity	rad s^{-1}

subscripts

av	average
c	suspension
crit	critical value
i	relates to inner cylinder
o	relates to outer cylinder
p	particle
pv	probe volume
r	radial component
RIF	refractive index fluid
s	solids
θ	azimuthal component
tr	traverse
z	axial component

dimensionless numbers

Bo	Bodenstein Number
Fr	Froude Number
Ga	Galileo Number
Gr	Grashof Number
Pe	Peclet Number
Re	Reynolds Number
Re_p	Particle Reynolds Number
Sc	Schmidt Number
Sh	Sherwood Number
St	Stanton Number
Ta	Taylor Number
Ta_{ch}	Chandrasekhar-Taylor Number

Chapter 1

Introduction

As we begin a new millennium we are experiencing a potentially revolutionary change in the way diseased or debilitated tissues in the body are treated. Traditionally in medicine, the problem has been addressed with a combined use of pharmaceutical, surgical and prosthetic means to allow the patient to live comfortably. At the present time this approach continues but the field of tissue engineering is now a thriving area of research encompassing engineering, biology, medicine and materials science, and in broad terms is the science of creating functional tissues and organs for transplantation as replacements to degenerative ones (Lewis, 1995). The term 'tissue engineering' appears to have first appeared at a series of National Science Foundation meetings in early 1987 in the USA. In October 1987, at a forum on emerging technologies, it was identified as an area for rapid industrial development. A formal definition was drafted at Lake Tahoe on February 26-29, 1988:

"Tissue engineering is the application of principles and methods of engineering and life sciences toward fundamental understanding of structure-function relationships in normal and pathological mammalian tissues and the development of biological substitutes to restore, maintain, or improve tissue functions".

Once defined, researchers in more traditional fields began experimenting with cells and synthetic materials, a practice that up to this point had been ongoing but on a much smaller and less coordinated scale. The motivation for researchers in the field was (and remains to be) the tremendous demand for replacement human tissues and the lack of available donors. Langer (1993) identified that treatment and lost work hours stemming from tissue and organ disease in the USA exceeded $400 billion.

Diseases of the heart and circulatory system are the biggest threat to life in the UK with over 235000 deaths in the year 2000, four out of ten of all deaths. In addition 1.5 million people suffer from angina and half a million have heart failure, predominantly due to occluded coronary arteries in the body. Whilst replacement of occluded vessels is traditionally achieved with the surgical implantation of Dacron grafts, the long-term patency is poor (How, 1996), a problem that may be overcome with a natural, tissue engineered graft (Greisler, 1996; Ratcliffe, 2000) as opposed to a synthetic one.

Cartilage regeneration via tissue engineering is a major research initiative (Temenoff, 2000). This tissue is relatively simple in structure being avascular and aneural and is composed of only one cell type, chondrocytes, and surrounding extracellular matrix (Vacanti, 1997). For these reasons it has been the focus for a very large number of investigations to understand the underlying factors for regeneration such as material properties (Vunjak-Novkovic, 1998) biological development (Freed, 1998) and mechanical stimuli (Vunjak-Novakovic, 1996; Vunjak-Novakovic, 1999; Obradovic, 1999). There is however a commercial incentive to provide replacement cartilage. Arthritis and related conditions are due to damage or inflammation of the cartilage tissue that separates bone tissues. In 2001 more than 7 million adults in the UK were prescribed with long-term health problems due to arthritis and related conditions. Approximately 4.4 million showed evidence of severe osteoarthritis in the hands, 550000 in the knees and 210000 in the hips. In 1999-2000, 206 million working days were lost due to arthritic

conditions in the UK and the total costs resulting from treatments amounted to £5.5 billion in 2000 in the UK alone.

Another active target for tissue engineering regeneration is skin tissue, again because of its relatively simple composition. Every year over 100000 people in the UK need to visit hospitals as a result of injuries from burns or scalds. Over 7000 of these are severe injuries 58% of which involve victims suffering extensive full thickness burns that require plastic surgery. Often for many years following the accident and aside from the physical pain, many victims suffer acute psychological distress as a consequence of their disfigurement. The tissue engineering of skin, predominantly from neonatal foreskin, is the most advanced area in tissue engineering and is now produced commercially (eg. Advanced Tissue Sciences, La Jolla, California). In the case of skin, the product moved from "invention" to "industry" with little input from the academic community. Wound healing is a major research area though, with emphasis on integrating tissue engineered skin that grows to leave no discernible evidence of scarring. For the generation of more complex organs such as liver, kidney, pancreas and heart, there will have to be a coordinated effort between industry and academia to make the ultimate goals of tissue engineering a reality.

The challenge of tissue engineering is considerable, but real, and the integration between life sciences and engineering has to be established quickly. New biomaterials are required to enhance cell seeding, influence phenotype and genotype retention and optimise tissue growth. Bioreactor development has been identified as an area of paramount importance (Naughton, 1998). Research in the area of bioreactor development for tissue engineering to this point has been limited and efforts are particularly required to address the influence of flow on cell aggregation, cell function and normal morphogenesis. Furthermore the convective and diffusive transport processes within the bioreactor have to be understood and controlled. Ultimately, for the goals of tissue engineering to be realised the bioreactors have to be scaled for commercialisation of the products and the optimum environment that is established in the lab to be recreated on a production scale is a major challenge.

1.1 Early Cell Culture and the Advent of Bioreactors

The cultivation of neuroblast cells of the frog in clotted lymph and the observed growth of fibrillae from the central body achieved by Harrison in 1907 is usually credited as the first tissue culture technique for the in vitro cultivation of animal cells. In 1912, Alex Carrel published work describing the in vitro cultivation of a strain of connective tissue cells from the chick heart grown in horse plasma. As the plasma clotted, a solid surface formed into which the heart cells explanted. The cells died after several days when unattended but regular feeding using aqueous extracts of whole chick embryos and subdividing them kept the cells in a state of active multiplication for many passages. The findings of Carrel led to the primary questions of in vitro animal cell culture that sought to better understand the differentiation of cells in the body and to explore the nature of humans by investigating the functioning of their cellular make-up using a controllable cell culture. In 1927, probably the first moves toward commercial exploitation of cell culture were made by Carrel who claimed to be producing all the smallpox vaccine that was currently being produced from a single sheep using one Carrel flask. This was not realised at that time and the last batches of the vaccine were produced in whole animals when the disease was eliminated in December 1979 (Spiers, 1997). For the next forty years since Carrel's first work, a large number of cultures were started from primary explants and kept alive as either initial cultures or passaged cells growing on glass or plastic tissue culture vessels. It remained until the 1950's before tissue masses were disaggregated and single cells were released for planting in culture. This was achieved using enzymes such as hyaluronidase, trypsin, collagenase and pronase. Enzymatic disaggregation is used to liberate monolayer cell cultures from the surfaces of culture vessels so that the cells can be transferred to additional culture vessels (subculturing) or used for experimental work. This procedure was adopted in the development of the first vaccine for poliomyelitis by Jonas Salk (1954, 1955) and signalled the first use of animal cell cultivation for humanitarian ends. The polio vaccine was based on the growth of the polio virus in anchorage dependent green monkey kidney cells. The live polio vaccine of Albert Sabin, produced by

similar methods, helped to eradicate polio from the Americas by September 1994. The 1960's produced vaccines against mumps, measles (Enders, 1960) and rubella (Elliot, 1984), and the baby hamster kidney (BHK21C13) cell culture system for the production of foot-and-mouth disease (FMD) vaccines (Mowat, 1962; Capstick, 1962) was the first commercially successful cell culture vaccine for animals. In all cases, the basic route to vaccine production was the same; primary cells are dispersed with enzyme (typically trypsin), planted in culture vessels, inoculated with virus, and the culture fluids are harvested after an appropriate inoculation period and held as bulk vaccine. Importantly around this time, attention was paid to the design of the culture vessel and efforts were made to address the scientific and engineering issues of scale-up from the laboratory spinner flasks to large scale stirred tank reactors, STR's (Elsworth, 1958; Smith, 1963; Molin, 1968; Radlett, 1971). In essence, these were the first commercial bioreactors. With the success of the FMD vaccine, the commercial value of anchorage dependent cell culture was assured and further research explored culture optimisation and scale-up (Levine, 1979; Spier, 1984; Montagnon, 1984). In 1969 Merck Sharp and Dohme received a license for the manufacture of the HPV-77 "Meruvax" strain of live attenuated rubella vaccine virus. In 1978 the RA27/3 strain replaced the HPV-77 strain and was licensed to the US. The RA27/3 strain was propagated in human diploid fibroblasts (WI-38) using roller bottles. The 1970's saw human interferon (IFN) production using human lymphoblastoid cells (Johnston, 1979). For more than two decades since the first discovery (Isaacs, 1962), supply shortage had meant that clinical evaluation of IFN could not progress. By the 1980's recombinant DNA technology emerged and large quantities of scarce and even completely novel proteins were produced. A number of expression systems have now been developed for mammalian cells allowing the production of several proteins of major therapeutic interest. Examples include tissue type-plasminogen activator (t-Pa), factors VIII and IX, erthropoeitin and human growth hormone.

1.2 General Types of Bioreactors

Commercial bioreactors broadly fall into three categories; stirred tank reactors (STR), plug-flow reactors (PFR) and airlift reactors (ALR). These commercial types have evolved from the laboratory scale vessels in which initial research data is obtained. Novel bioreactor designs are often based on modifications to one of these generic types and with the large number of 'new' bioreactors emerging in the field of tissue engineering it is important to address the capabilities of these systems.

The bioreactor is the unit in which the cells and supporting structures interact with the fluid media. The fundamental phenomena of the fluid mechanics and mass transport are established from the contacting patterns of the cell constructs with the fluid and these patterns are directly related to the internal geometric design of the reactor and the scale and mode of operation.

1.2.1 Stirred Tank Reactors (STR's)

The simplest version is the batch STR which is a closed cylindrical system containing the liquid medium, an inoculum of living cells and a fixed concentration of gas. Nothing is added or removed from the reactor. A rotating impeller stirs the contents. The impeller design is important for controlling the mixing and flow patterns within the reactor. Spinner flasks employ a magnetic stirrer bar to initiate mixing however beyond a volume of around 5l mixing is insufficient by this method (De Bruyne, 1988). Commonly employed types of impeller are the turbine impeller, marine propeller, flat blade impeller and helical ribbon impeller. A review of the types and flow patterns generated is provided by Joshi (1982) and McCabe (1985). It is convenient from a theoretical viewpoint to assume that batch STR's are *ideal* reactors, which means that they are perfectly mixed. In other words, freely suspended cells/constructs and oxygen and nutrients are homogeneously distributed throughout the liquid volume and no concentration gradients (Spier, 1995) exist so optimal mass transport ensues. In practical terms this is not normally the case. Whilst the tank design is such that dead zones are

limited (cylindrical walls and rounded bottom, typically), the mixing patterns generated by the rotating impeller cannot completely overcome this. In fact, a highly turbulent region exists around the impeller in a volume to the cubic power of the impeller diameter and laminar, or even dead zones, will exist in regions far from it (Cherry, 1986). This effect is prevalent in viscous or non-Newtonian media. In such circumstances the problem is alleviated by the use of helical ribbon impellers (Curran, 2000).

Commonly, filtered air is continuously perfused into the vessel to maintain an appropriate oxygen concentration level. Such a system, although not strictly a batch reactor, is often considered so. It is also often desirable to add a liquid stream of nutrient to the batch reactor as the reaction process occurs. If the stream is added intermittently, the reactor is considered as a *fed-batch* reactor. If a liquid stream is added continuously and withdrawn continuously to maintain a constant internal liquid volume the reactor is a *continuous* stirred tank reactor (CSTR). CSTR bioreactors normally incorporate a cell separator and a recycle stream of concentrated cells to increase the cell concentration per unit reactor volume per unit time.

1.2.2 Plug Flow Reactors (PFR's)

PFR's or tubular reactors are essentially fibres, tubes or pipes through which the liquid media passes. If the fluid passes through with a sufficiently large velocity, the flow profile approximates *plug flow* and there is then no variation of axial velocity over the cross section of the tube and there is perfect mixing. If the fluid velocity is lower and plug flow is not achieved (this is common to reduce shear stresses) then there will be imperfect mixing that influences the mass transport. The most commonly used type of PFR employed for cellular processing is the hollow-fibre bioreactor (Kumar, 1997). This type of reactor incorporates bundles of fibres through which cells and media flow (Davis, 1997). The fibres can have diameters as low as 100μm and may be treated to allow preferential adhesion of cells to the walls of the fibres.

1.2.3 Airlift Reactors

Airlift, as an alternative to standard stirred tank reactors, is considered to have a gentler mixing action and is proposed to be better suited to shear sensitive cells (Grima, 1997; Chisti, 1999). The airlift reactor is essentially a tall bubble column with a sparger at the base and an internal draft tube. It works on the principle that the gas mixture introduced by the sparger into the base of the draft tube establishes a circulation of medium owing to the density differential between the oxygenated air (in the draft tube) and the less oxygenated air in the outer zone (Chisti, 1989). Oxygen levels and pH can be controlled by varying the composition of the gas mixture. The critical factors are the reactor height, aspect ratio and gas flow velocity (Roussaeu, 1980). The optimum configuration for mixing is to have the draft tube diameter essentially the same as the total outside (downflow) zones and provide some gentle mechanical agitation at the sparger site with an impeller (Chisti, 1987, 2001). Whilst the most efficient gas velocity is in the range 0.5-1.5 ms^{-1}, velocities as high as 5 ms^{-1} are employed. Gentle mixing prevails in this type of reactor so that fluid shear forces are reduced, but problems associated with sparged bubbles (discussed shortly) can still present the problem of high stresses being imparted on the cells.

1.2.4 Annular Flow Reactors (AFR's)

Annular flow bioreactors, sometimes called rotating wall vessel (RWV) bioreactors are based on a system of concentric rotating cylinders. These are attractive bioreactors for understanding the fundamental fluid mechanics and mass transport effects of proliferating cells and nascent tissues due to the uniform and diverse range of hydrodynamic conditions that can be generated in the fluid. The systems can be designed such that independent rotation of the cylinders can be initiated and controlled thereby controlling the flow regime. In vertical orientation, there are gravitational effects in the fluid. In horizontal orientation the gravitational effect is almost eliminated which has led some researchers to call such systems 'microgravity' bioreactors (Unsworth, 1998). A number of studies are ongoing to investigate the

potential of these systems as tissue engineering bioreactors (Hammond, 2001).

Duke (1983) first explored the effects of gravity on the physiological behaviour of living cells and subsequently made computational studies of microgravity effects (Duke, 1989) and then experimental studies of the effects on chondrocytes in a space flight (Duke, 1992). The studies were made as part of a collaborative bioengineering research initiative of NASA in Houston, Texas where the microgravity effects on other tissues were investigated (Hymer, 1985; Kaplansky, 1991). Ground based experiments led to the development of the annular flow, RWV bioreactor (Goodwin, 1992). A number of studies on the behaviour of cells in such systems have been described in the last 10 years, particularly since the systems were introduced as a commercial product by spin-off companies of the NASA project (Synthecon Inc., Houston, TX; Celldyne, Houston, TX). A physical approach to understanding why a microgravity environment might enhance tissue generation has been given by Ingber (1999). At the present time, this type of bioreactor has the most promise for tissue engineering, but a clearer understanding of the optimum operation in terms of the hydrodynamic and mass transport environment is still required (Begley, 2000).

1.3 Engineering Aspects of Bioreactors

From the viewpoint of the biochemical engineer, bioreactors are designed to provide the optimal environmental conditions (biological, chemical and physical) for cell growth and specific productivity of cells. For the tissue engineer, cell productivity (in the sense of production of a marketable product) is not an issue; the ultimate objective is to facilitate the proliferation and differentiation of cells to form tissues that are as phenotypically and genotypically similar to the native tissue requiring replacement in the patient. A favourable biological condition requires that the desired cells can proliferate exclusively, without competitive/inhibitory cells in the system. Chemically, it is advantageous if the necessary organic and inorganic nutrients are delivered to the metabolic site at the optimal rate and concentration and with the correct pH, water activity, ionic strength etc.

Temperature, pressure, viscosity and agitation intensity are physical parameters that will influence both the biological and chemical environment within the bioreactor. It is often desired that the bioreactor environment simulates the in-vivo environment the native tissue experiences. Depending on the type of nascent tissue that is required to be generated, the physico-biochemical environment will accordingly vary so it is important that the tissue environment in-vivo is understood and then the bioreactor environment is well characterised to establish uniformity between the two. Moreover, sustaining this optimal environment is a major research endeavour in the scale-up and process control of the bioreactor (Hu, 1991).

1.3.1 Shear Stress Effects

Shear stress is a force per unit area acting on a surface in a tangential direction to flow that arises from a variation in velocity and is more rigorously discussed in Chapter 5. Animal cells are sensitive to shear forces (Brock, 1984; Thomas, 1990) due to their relatively large size of 10 to 30μm and the cell contents being protected only by the cell membrane (Hua, 1993). Whilst some cells cultures can be grown in free suspension of media, most require attachment to a biocompatible surface for controlled proliferation and differentiation. This is particularly so in tissue engineering. In such circumstances, if the attachment surface is fixed in place, the cells appear to be more susceptible to shear stress as they cannot freely rotate or translate to accommodate the imposed forces (Croughan, 1987). Although excessive shear forces will be detrimental to the cell some fluid shear may be desirable as it can lead to increased cell permeability (Fry 1968) and increased secretion of extracellular proteins (Abu-Reesh, 1989; Al-Rubeai, 1990). It can also influence the shape of the cell (Levesque, 1985). These effects all have a bearing on the cell physiology (Frangos, 1988) that is of paramount importance in tissue engineering. An alternative to a fixed scaffold support onto which cells can proliferate is the use of microcarrier beads (Butler, 1988). These are generally microporous spheres of an appropriate biomaterial onto and into which cells proliferate. They are typically 100-250μm in diameter and provide a very large surface area per unit culture

volume for cell attachment. The microcarriers should be neutrally buoyant in the media and will therefore behave like freely suspended cells in the bioreactor, hydrodynamically. Mechanisms of cell damage on microcarriers has been reviewed by Cherry (1988) and Lakhotia (1992).

In principle, it is prudent to firstly establish a critical shear stress level for a given culture of cells and a given bioreactor configuration. A number of experimental investigations have been made to establish a 'critical shear stress' and it is evident that this is dependent on the type of cell, the method of culture (free suspension/attached) and the time of exposure to the shear stress. A summary of some of the studies made to assess critical shear stress is presented in Table 1.1. In this table a range of cell types are given for varying degrees of shear stress exposure and exposure times. The various types of test apparatus that are used to stimulate cells has been reviewed by Brown (2000) and these include viscometers (concentric cylinder Couette and cone and plate types), laminar flow (LF) chambers and spinner flasks. Individual designs are common, as are modifications to the basic designs described by Brown (2000). These geometric changes will clearly have a bearing on the outcome of the shear experiments. It is evident from the wide range of data available that there is no unique critical shear stress that can be applied in the design of a cellular bioreactor. At best, guideline values can be used for a given set of experimental conditions. Furthermore, the culture time becomes critically important. At the present time, the majority of data available for the viability of cells (which is generally associated with critical shear stress) is for short-term experiments (< 24h). It seems probable that for longer-term culture operation at shear stress levels far below critical is advantageous. It is also apparent that cells in free suspension can withstand higher stress levels than adherent cells. The reason for this has been addressed from the theoretical viewpoint by Cherry (1986) and by Papoutsakis (1991) and also experimentally by McQueen (1987) and Croughan (1989). The size of eddies in the flow relative to the size of the cells/microcarriers appears to be important. Once the flow becomes turbulent it is possible to estimate the size of the smallest (Kolmogorov) eddies. If these are larger than the cells, the cells maybe

simply transported around inside the eddy, however, when the eddy is smaller than the size of the cell high shearing on the cell will occur. As the turbulence intensity increases, the smallest eddies become smaller and so the shearing damage will increase. Cells, which are fixed onto a stationary support, do not have this ability to move with the fluid and thereby experience significantly higher stresses.

An extensive review on the shearing effects on cells in bioreactors from a theoretical, experimental and commercial viewpoint has been compiled by Scheper (2000). As a rough guideline on the basis of the numerous data of Table 1.1, shear stresses in the range 0 to 10 dyn/cm^2 appear to be of most interest for the long term culture of freely suspended cells in bioreactors.

Cell Type	Test Apparatus	Exposure Level	Exposure Time	Reference
BHK-21, CHO-K1, Vero	Spinner Flask	70, 110, 200 rpm	0-250h	Wu (1999)
BHK	LF Chamber	0.26-5.4 N/m^2	2-24h	Stathopoulos (1985)
BHK	LF Chamber	0-2.5 N/m^2	0-24h	Ludwig (1992)
FS-4 Fibroblasts	Spinner Flask	0-30 dyn/cm^2	0-180h	Croughan (1989)
FS-4 Fibroblasts	Spinner Flask	1-12 s^{-1} (shear rate)	0-150h	Croughan (1987)
HDP-1 Mouse Hybridoma	Viscometer	50-1000 dyn/cm^2	0.5-3h	Abu-Reesh (1989)
CRL-8018 Hybridoma	Viscometer	0-50 dyn/cm^2	0-10 min	Petersen (1988)
TB/C3 Mouse Hybridoma	Viscometer	0.019-600 N/m^2	10 min to 24h	Born (1992)
6 Cell Types	Viscometer	1, 10, 100 N/m^2	5-20 min	Mardikhar (2000)
S hassjoo Cells	7l STR	200-300 rpm	0-14 days	Chen (2000)
VERO	Spinner Flask	70-200 rpm	0-140 h	Wu (2000)
hFOB Human Fetal Osteoblasts	LF Chamber	0-2 N/m^2	0-5 min	Jacobs (1998)
Leukocyte	LF Chamber	0.5-20 dyn/cm^2	0-2h	Dong (2000)
CHO	2l STR	0-250 rpm	0-100h	Michaels (1992)

Platelets	Viscometer	500-4000s^{-1} (shear rate)	100s	Rhodes (1998)
HUVEC	Cone Plate	4-400 N/m^2	0-250 min	Schnittler (1993)
HUVEC	LF Chamber	0-1 N/m^2	0-8h	Yoshikawa (1997)
SMC	LF Chamber	0.5-2.5 N/m^2	0-24h	Papadaki (1996)
Endothelial	Static Culture	0-2 N/m^2	0-24h	Sato (2000)
Endothelial	Cone-Plate	1-5 dyn/cm^2	up to 8 days	Dewey (1981)
Endothelial	LF Chamber	0.2-3 N/m^2	0-24h	Thoumine (1995)
Endothelial	LF Chamber	0.2-2.5 N/m^2	0-30h	Nollert (1991)
Endothelial	LF Chamber	1-8.5 N/m^2	0-24h	Levesque (1985)

Table 1.1 Experimental Studies on the Application of Shear Stress to Cells

1.3.2 Mass Transport Effects

From the outset it should be emphasised that mass transport and the hydrodynamic environment in the bioreactor are directly related. Internal fluid motion is initiated in a bounded fluid by introducing an externally imposed condition. This leads to a potentially unstable arrangement of the fluid resulting from the prevailing adverse gradient. The unstable fluid motions provide bulk convective mixing that promotes mass transfer. As the degree of the instability increases, the size of the mixing elements decreases. There are two extremes from a fluid mechanical viewpoint. A stationary, bounded fluid can be considered stable with no externally imposed condition. In this case there would be no mixing. The other theoretical extreme is a non-stationary bounded fluid that is in a state of maximal instability or chaos. In this case perfect and instantaneous mixing would occur as the mixing

elements would be infinitely small. This condition is approached in fluid mechanics when featureless turbulent flow ensues. By a similar analogy, the shear forces generated in the bounded fluid can be associated with the size of the externally imposed condition or the size of the mixing elements. In general terms, larger externally imposed conditions produce greater shear forces, and smaller mixing elements also produce greater shear forces (Cherry, 1986). Therefore it can generally be said that as a transition is made from stationary through laminar to featureless turbulent flows, the size of mixing elements passes from infinitely large to very[1] small and the state of mixing is described as macromixing through mesomixing to micromixing respectively. Spatial and temporal gradients are of paramount importance in assessing the mass transport capabilities of the bioreactor and with increased agitation the spatial gradient is reduced and the transport process occurs more quickly. This is an important issue in bioreactor scaling.

Since tissue engineering is concerned in the first instance with the controlled growth of cells it is prudent to understand and optimise the factors that promote growth. From a very elementary viewpoint one can look at the fundamental requirements of cellular growth from the aerobic respiration reaction:

$$C_6H_{12}O_6 + 6O_2 \rightarrow 6H_2O + 6CO_2 + \text{Chemical Energy}$$

The release of the chemical energy in the reaction is the driving factor for cellular growth. A large number of other factors must be taken into consideration with this elementary biochemical reaction, both biological and physico-chemical, but from the engineering perspective of bioreactor design it is evident that if the delivery of the two chemical components on the left side of the equation can be maximised, then all other things being equal, the cellular growth can be maximised. Whilst it is important to provide maximal delivery of the nutrients on the left side of the equation, it is equally important to remove the toxic component CO_2 from the cell reaction site. These two

[1]Theoretically one could say infinitely small mixing elements are produced at the extreme level of chaos, but in real systems one can only speak in degrees of scale, so as the turbulence becomes more intense so the size of the mixing elements decrease

simple conditions taken together form the fundamental problem of mass transfer to and from the metabolic reaction site, in this case the growing cell(s). The bioreactor is an engineering tool to promote mass transfer and cell growth. The fluid mechanical environment in the reactor must maintain homogeneous conditions throughout the vessel to prevent adverse physico-chemical gradients from developing. In other words, the reactor must provide adequate mixing. The degree of mixing in the reactor becomes a very critical issue and one that poses the greatest problem to the tissue engineer designing an appropriate bioreactor. Whilst very small scale mixing in the reactor would ensure optimal mass transfer even at the cellular level, the fluid shear forces associated with this so-called micromixing are often found to be very high, high enough to cause irreparable cell damage, even cell death. For this reason, the tissue engineer must design a reactor which operates in a range where the mixing provides sufficient mass transfer and the shear forces that are developed by the fluid motions are far lower than those that can cause cellular harm. In other words a compromise must be sought and this remains to be unidentified at this time.

From the elementary equation for aerobic respiration the two areas of mass transport that are important are identified, gaseous mass transport (for O_2 and CO_2) and solute mass transport. These require independent treatment since methods of delivery, viscosity, pressure and diffusivity are different for gases than solutes and along with other physical properties have a significant effect on the transport process. To a certain extent, the mass transport of solutes, which are generally supplied in liquid form, is governed entirely by the hydrodynamics in the reactor vessel. Oxygen transport on the other hand, whilst being significantly influenced by the hydrodynamics, is also influenced by the method to which it is delivered to the reactor, in particular with regard to the effect on cells.

Oxygen is sparingly soluble in cell culture media, 7.6mg/ml (Griffiths, 1988) and the demands from cells are high. Delivery systems for oxygen are designed to optimise the concentration of oxygen that reaches the metabolic site. The principal types of delivery are:

- Free surface aeration
- Oxygenation using bubbles
- Bubble-free aeration by membranes

Free surface aeration is really only used in small-scale cultures below a 5l liquid volume. Reliance is made on oxygen transfer through the air-medium interface. The baseline transfer rate is governed by the interface thermodynamics and is discussed in Chapter 6. This can be enhanced by the use of surface aerators described by Hu (1986) or by injecting air through multiple nozzles placed immediately above the interface (Van Wezel, 1982) or by generating surface waves on the liquid interface (Vazquez-Una, 2000).

Since free surface aeration is severely limited from the transport viewpoint the more common approach has been to aerate the media using oxygen or air bubbles. A range of different types of sparger to introduce gas bubbles are commonly encountered and these are reviewed by Joshi (1977). Typically, the sparger is located below the impeller is STR's but an alternative is to utilise the rotating impeller itself to deliver the bubbles. The impeller shaft is hollow, and orifices at the impeller drive gas bubbles out into the media as it rotates. The reason for this is that the rotation causes a pressure drop in the shaft and air is entrained into it and pulled downwards. A theoretical and experimental treatment of impeller induced aeration is given by Evans (1990).

As a general guideline, large bubbles (1-3mm) at low flowrates (5-10$cm^3l^{-1}min^{-1}$) are preferred but often not practical in tissue engineering reactors. The oxygen transfer properties of 'large' bubbles has been investigated by Zhang (1992) and microbubbles by Bredwell (1998). The major problem associated with using bubbles, particularly with freely suspended cells, is that when bubbles collapse or coalesce very high stresses are generated on the cells. This has been investigated extensively by a number of researchers (Handa-Corrigan, 1989; Kunas, 1990; Chalmers, 1991; Garcia-Briones, 1992). Simulations of the process of bubble collapse using computational fluid dynamics (CFD) by Garcia-Briones (1994) have shown that there is a very high localised energy dissipation that rapidly

increases as the bubble size decreases. This explains why larger bubbles have been found to be preferential and accounts for the lethal effects on cells caused by bubble collapse.

Bubble free aeration is seen to be the optimum route to provide adequate aeration in a tissue engineering bioreactor. This is generally achieved by allowing the air/oxygen to diffuse through a porous membrane or tube (Cote, 1987; Schneider, 1995). The membrane is fabricated from thin vinyl or polypropylene or more recently polytetrafluoroethylene (PTFE) that has hydrophobic properties and prevents cell adhesion. It is possible to fit these membranes over the orifices of a rotating gas-inducing impeller to provide enhanced bubble free aeration (Lehmann, 1987). The viability of cells in a bubble free system has been demonstrated to be enhanced when compared to a system using bubbles (Wagner, 1988).

1.3.3 Scaling Effects

The problem of reactor scale-up is one that remains to be a constant research endeavour in a host of chemical and biochemical applications both in research labs and in industry. The approach to scale-up is very much dependent on the process that is being scaled, in particular, the physical and chemical properties of the materials involved and the process operating parameters. There are three basic approaches that are used to provide scale-up in systems where a dynamic interaction between solid, liquid and gas phases are required:

- Geometric
- Dynamic
- Kinematic

In a geometric scale-up, ratios of relevant dimensions in the small-scale vessel are made and these are then maintained in the scaled-up version. This is perhaps the easiest approach to scale-up and is normally used as a starting point for any scale-up operation. In dynamic scaling an assessment

of the hydrodynamic forces is made in the small-scale vessel and these are replicated at the larger scale. Geometric scaling is used to establish the larger scale and then refinement of this is made to accommodate the correct forces. This can be an intricate and time consuming operation particularly if the hydrodynamics are complex and whilst the modern approach is to use CFD to model the small-scale environment and use this to provide scale-up, the computer codes are based entirely on physical theory and do not account for artefacts that manifest in practice. In other words CFD approaches provide an idealised case and the need for practical experiments are always required for validation. Kinematic scaling is much like the dynamic scaling where particle velocities are collated at the small-scale and replicated on scale-up. Particle tracking technologies and systems like Particle Image Velocimetry described in Chapter 4 allow for detailed kinematic information to be ascertained. This could be used as a validator for CFD codes in the future.

The problem of scale-up for tissue engineering bioreactors is a very complex one and significant research efforts will be needed to establish rigid procedures for scaling. The problem of scaling a unicellular bioreactor is not trivial. It is known that a compromise exists between the level of fluid shear resulting as a consequence of the hydrodynamics and the mass transport that can be delivered. Actual data for the compromise is difficult to provide; it is dependent on the cells and the system. Generally speaking though, the limiting factor in scale-up, particularly in maintaining cell density, is the efficient delivery of oxygen. Oxygen gradients within the bioreactor are of paramount importance and ideally should be eradicated (Tramper, 1995). If the delivery of oxygen can be optimised and cell viability can be maintained at the small-scale, spatial and temporal gradients for oxygen transfer can be established. On geometric scale-up, the question arises as to whether the cell concentration per unit reactor volume should be maintained as in the small scale, or whether this should also be accordingly scaled. In the former case, it is clear that the size of the cells is fixed so in a larger vessel using the same concentration of cells, there will be a proportional increase in the spatial gradient. In the latter case, the question arises as to whether the increased number of cells can be sustained from a media and oxygen

viewpoint. An initial starting point is to establish a mass transport correlation for the small scale system for a given cell population and then assess how successful this is on larger scale application. Mass transport correlations for oxygen transport are discussed in Chapters 6 through 8.

References

Abu-Reesh I, Kargi F, Biological Responses of Hybridoma Cells to Defined Hydrodynamic Shear Stress. *J. Biotechnol.* **9** 167-178 (1989)

Al-Rubeai M, Oh SKW, Musaheb R, Emery AN, Modified Cellular Metabolism in Hybridoma Subjected to Hydrodynamic and Other Stresses. *Biotechnol. Lett.* **12** 323-329 (1990)

Begley CM, Kleis SJ, The Fluid Dynamic and Shear Environment in the NASA/JSC Rotating-Wall-Perfused Vessel Bioreactor. *Biotech. Bioeng.* **70** (1) 32-40 (2000)

Born C, Zhang Z, Al-Rubeai M, Thomas CR, Estimation of Disruption of Animal Cells by Laminar Shear Stress. *Biotech. Bioeng.* **40** 1004-1010 (1992)

Bredwell MD, Worden RM, Mass Transfer Properties of Microbubbles. 1. Experimental Studies. *Biotechnol. Prog.* **14** (1) 31-38 (1998)

Brock TD, Smith DW, Madigan MT, *Biology of Microorganisms*. Prentice Hall. Englewood Cliffs. New Jersey. (1984)

Brown TD, Techniques for Mechanical Stimulation of Cells In Vitro: A Review. *J. Biomech.* **33** 3-14 (2000)

Butler M, A Comparative Review of Microcarriers Available for the Growth of Anchorage-Dependent Animal Cells. *in Animal Cell Biotechnology* **3** 283-303 (1988)

Capstick PB, Telling RC, Chapman WG, Stewart DL, Growth of a cloned strain of hamster kidney cells in suspended cultures and their susceptibility to the foot-and-mouth disease virus. *Nature* (London) **195** 1163-1166 (1962)

Carrel A, On the permanent life of tissues outside the organisms. *J. Exp. Med.* **15** 516-528 (1912)

Carrel A; Rivers TM, La fabrication du vaccin in vitro. *C. r. Seanc. Soc. Biol.* **96** 848-850 (1927)

Chalmers JJ, Bavarian F, Microscopic Visualisation of Insect Cell-Buuble Interactions-II: The Bubble Film and Bubble Rupture. *Biotechnol. Prog.* **7** 151-158 (1991)

Chen SY, Huang SY, Shear Stress Effects on Cell Growth and L-DOPA Production by Suspension Culture of *Stizolobium hassjoo* Cells in an Agitated Bioreactor. *Bioproc. Eng.* **22** 5-12 (2000)

Cherry RS, Papoutsakis ET, Hydrodynamic Effects on Cells in Agitated Tissue Culture Reactors. *Bioproc. Eng.* **1** 29-41 (1986)

Cherry RS, Papoutsakis ET, Physical Mechanisms of Cell Damage in Microcarrier Cell Culture Bioreactors. *Biotech. Bioeng.* **32** 1001-1014 (1988)

Chisti Y, Moo-Young M, Airlift Reactors: Characteristics, Applications and Design Considerations. *Chem. Eng. Commun.* **60** 1195-1242 (1987)

Chisti Y, Airlift Bioreactors. Elsevier. New York. (1989)

Chisti Y, Shear Sensitivity. *in Encyclopedia of Bioprocess Technology: Fermentation, Biocatalysis and Bioseparation* **5** 2379-2406 (1999)

Chisti Y, Jauregui-Haza UJ, Oxygen Transfer and Mixing in Mechanically Agitated Airlift Bioreactors. *Biochem. Eng. J.* **10** (2) 143-153 (2002)

Cote P, Bersillon JL, Huyard A, Bubble-Free Aeration Using Membranes. Mass Transfer Analysis. *J. Membrane Sci.* **47** (1-2) 91-106 (1989)

Croughan MS, Hamel JF, Wang DIC, Hydrodynamic Effects on Animal Cells Grown in Microcarrier Cultures. *Biotech. Bioeng.* **29** 130-141 (1987)

Croughan MS, Sayre ES, Wang DIC, Viscous Reduction of Turbulent Damage in Animal Cell Culture. *Biotech. Bioeng.* **33** 862-872 (1989)

Curran SJ, Heyes RE, Williams MC, Tanguy PA, Experimental Mixing Study of a Yield Stress Fluid in a Laminar Stirred Tank. *Ind. Eng. Chem. Res.* **39** (1) 195-202 (2000)

Davis JM, Hanak JAJ, Hollow-Fiber Cell Culture. *in Methods in Molecular Biology* **75: Basic Cell Culture Protocols** 77-89 (1997)

De Bruyne NA, The Design of Bench-Scale Reactors. *in Animal Cell Biotechnology* **3** 141-175 (1988)

Dewey CF, Bussolari SR, Gimbrone MA, Davies PF, The Dynamic Response of Vascular Endothelial Cells to Fluid Shear Stress. *J. Biomech. Eng.* **103** 177-185 (1981)

Dong C, Lei XX, Biomechanics of Cell Rolling: Shear Flow, Cell Surface Adhesion and Cell Deformability. *J. Biomech.* **33** 35-43 (2000)

Duke JC, Effects of Excess Gravity on In Vitro Chondrogenesis of the Embryonic Mouse Liomb. *Teratology* **27** 427-436 (1983)

Duke JC, Moore J, Montufar-Solis D, Continuing Studies of "CELLS" Flight Hardware. *Physiologist* [Suppl.] **32** (1) S57-S58 (1989)

Duke PJ, Daane E, Montufar-Solis D, Arizpe J, Chondrocyte Topology and Matrix Production in the CELLS Space Flight Experiment. *ASGSB Bull* **6** (1) 58 (1992)

Enders JF; Katz SL; Milovanovic MV; Holloway A, Studies on attenuated measles virus vaccine I: Development and preparation of the vaccine: techniques for assay of effects of vaccination. *N. Eng. J. Med.* **263** 153-154 (1960)

Elliot AY; Manufacture and testing of measles, mumps and rubella vaccine. *Proc. 19th Immunization Conf. On Immunization.* Boston MA May 21-24 pp. 79-83 (1984)

Elsworth R, Capel GH, Telling RC. Improvements in the Design of a Laboratory Culture Vessel. *J. Appl. Bacteriol.* **21** 80-85 (1958)

Evans GM, Reilly CD, Davidson JF, Carpenter KJ, A Fundamental Study of Gas-Inducing Impeller Design. *I.Chem.E Symposium Series No. 121* 137-152 (1990)

Frangos JA, McIntire LV, Eskin SG, Shear Stress Induced Stimulation of Mammalian Cell Metabolism. *Biotech. Bioeng.* **32** 1053-1061 (1988)

Freed LE, Hollader AP, Martin I, Barry JR, Langer R, Vunjak-Novakovic G, Chondrogenesis in a Cell-Polymer-Bioreactor System. *Exp. Cell Res.* **240** 58-65 (1998)

Fry DL, Acute Vascular Endothelial Changes Associated with Increased Blood Velocity. *Circ. Res.* **22** 165-197 (1968)

Garcia-Briones M, Chalmers JJ, Cell-Bubble Interactions, Mechanisms of Suspended Cell Damage. *Ann. NY Acad. Sci.* **665** 219-229 (1992)

Goodwin T, Jessup J, Wolf D, Morphologic Differentiation of Colon Carcinoma Cell Lines HT-29 and HT-29KM in Rotating Wall Vessels. *In Vitro Cell Dev Biol.* **28A** 47-60 (1992)

Greisler HP, Gosselin C, Ren D, Kang SS, Kim DU, Biointeractive Polymers and Tissue Engineered Blood Vessels. *Biomaterials* **17** 329-336 (1996)

Griffiths JB, Overview of Cell Culture Systems and their Scale-Up. *in Animal Cell Biotechnology* **3** 179-219 (1988)

Grima EM, Chisti Y, Moo-Young M, Characterization of Shear Rates in Airlift Bioreactors for Animal cell Culture. *J. Biotechnol.* **54** 195-210 (1997)

Hammond TG, Hammond JM, Optimised Suspension Culture: The Rotating Wall Vessel. *Am J Physiol. Renal Physiol.* **281** F12-F25 (2001)

Handa-Corrigan A, Emery AN, Spier RE, Effect of Gas-Liquid Interfaces on the Growth of Suspended Animal Cells. Mechanism of Cell Damage by Bubbles. *Enz. Microb. Technol.* **11** 230-235 (1989)

Harrison RG, Observations on the living developing nerve fibre. *Proc. Soc. Exp. Biol. Med.* **4** 140-143 (1907)

How TV, Black RA, Hughes PE, Haemodynamics of Vascular Prostheses. *Advances in Haemodynamics and Haemorheology* **1** 373-423 (1996)

Hu WS, Wang DIC, Mammalian Cell Technology: A Review from an Engineering Perspective. *in Mammalian Cell Technology* 167-197 (1986)

Hu WS, Peshwa MV, Animal Cell Bioreactors: Recent Advances and Challenges to Scale-Up. *Can. J. Chem. Eng.* **69** 409-420 (1991)

Hua J, Erickson LE, Yiin TY, Glasgow LA, A Review of the Effects of Shear and Interfacial Phenomena on Cell Viability. *Critical Rev. Biotech.* **13** (4) 305-328 (1993)

Hymer WC, Grindeland R, Farrington M, Fast T, Hayes C, Motter K, Patil L Microgravity Associated Changes in Pituitary Growth Hormaone (GH) Cells Prepared from Rats Flown on Spacelab 3. *Physiologist* [Suppl] **28** S197-S198 (1985)

Ingber D, How Cells (Might) Sense Microgravity. *FASEB J.* **13** [Suppl] S3-S15 (1999)

Isaacs A; Lindenmann J, Virus interference. *Proc. Roy. Soc. London B* **147** 258-267 (1967)

Joshi JB, Sharma MM, Mass Transfer and Hydrodynamic Characteristics of Gas Inducing Type of Agitated Contactors. *Can. J. Chem. Eng.* **55** 683-695 (1977)

Joshi JB, Pandit AB, Sharma MM, Mechanically Agitated Gas-Liquid Reactors. Review Article #7. *Chem. Eng. Sci.* **37** (6) 813-844 (1982)

Johnston MD; Christofinis G; Ball GD; Fautes KH; Finter NB, A culture system for producing large amounts of human lymphoblastoid interferon. *Dev. Biol. Standard* **42** 189-192 (1979)

Kaplansky AS, Durnova GN, Burkovskaya TE, Vorotnikova EV, The Effect of Microgravity on Bone Fracture Healing in Rats Flown on COSMOS-2044. *Physiologist* [Suppl] **34** (1) S196-S199 (1991)

Kumar RA, Modak JM, Transient Analysis of Mammalian Cell Growth in Hollow Fibre Bioreactor. *Chem. Eng. Sci.* **52** (12) 1845-1860 (1997)

Kunas KT, Papoutsakis ET, Damage Mechanisms of Suspended Animal Cells in Agitated Bioreactors with and without Bubble Entrainment. *Biotech. Bioeng.* **36** 476-483 (1990)

Lakhotia S, Papoutsakis ET, Agitation Induced Cell Injury in Microcarrier Cultures. Protective Effect of Viscosity Is Agitation Intensity Dependent: Experiments and Modelling. *Biotech. Bioeng.* **39** 95-107 (1992)

Langer R, Vacanti J, Tissue Engineering. *Science* **260** 920-926 (1993)

Levesque MJ, Nerem RM, The Elongation and Orientation of Cultured Endothelial Cells in Response to Shear Stress. *J. Biomech. Eng.* **107** (4) 341-347 (1985)

Lehmann J, Piehl GW, Schulz R, Bubble-Free Cell Culture Aeration with Porous Moving Membranes. *Dev. Biol. Std.* **66** 227-240 (1987)

Levine DW, Wang DIC, Thilly WG, Optimisation of Growth Surface Parameters in Microcarrier Cell Cultures. *Biotech. Bioeng.* **21** 821-846 (1979)

Lewis R, Tissue Engineering Now Coming Into Its Own as a Scientific Field. *The Scientist* **9** (15) 12-15 (1995)

Ludwig A, Kretzmer G, Schugerl K, Determination of a "Critical Shear Stress Level" Applied to Adherent Mammalian Cells. *Enz.Microb.Technol.* **14** 209-213 (1992)

McCabe WL, Smith JC, Harriot P, Unit Operations of Chemical Engineering. 4th Edition. McGraw-Hill Inc. New York. (1985)

McQueen A, Meilhoc E, Bailey J, Flow Effects on the Viability and Lysis of Suspended Animal Cells. *Biotechnol. Lett.* **9** 831-839 (1987)

Michaels JD, Kunas KT, Papoutsakis ET, Fluid Mechanical Damage of Freely Suspended Animal Cells in Agitated Bioreactors: Effects of Dextran, Derivatized Celluloses and Polyvinyl Alcohol. *Chem. Eng. Commun.* **118** 341-360 (1992)

Molin O, Heden CG, Large Scale Cultivation of Human Diploid Cells on Titanium Discs in a Special Apparatus. *Prog. Immunobiol. Standard* **3** 106-110 (1968)

Montagnon B, Vincent-Falquet JC, Fanget B, Thousand Litre Scale Microcarrier Culture of Vero Cells for Killed Polio Virus Vaccine. Promising Results. *Dev. Biol. Std.* **55** 37-42 (1984)

Mowat GN, Chapman WG, Use of BHK21 cell lines in the preparation of mouse attenuated line foot-and-mouth disease vaccines for the immunisation of cattle. *Nature* **196** 655-656 (1962)

Naughton G, Tissue Engineering-New Challenges. *ASAIO J.* Editorial 115-116 (1998)

Nollert MU, Diamond SL, McIntire LV, Hydrodynamic Shear Stress and Mass Transport Modulation of endothelial Cell Metabolism. *Biotech. Bioeng.* **38** (6) 588-602 (1991)

Papadaki M, McIntire LV, Eskin SG, Effects of Shear Stress on the Growth of Aortic Smooth Muscle Cells In Vitro. *Biotech. Bioeng.* **50** 555-561 (1996)

Papoutsakis ET, Fluid-Mechanical Damage of Animal Cells in Bioreactors. *Trends in Biotech.* **9** 427-437 (1991)

Petersen JF, McIntire LV, Papoutsakis ET, Shear Sensitivity of Cultured Hybridoma Cells (CRL-8018) Depends on Mode of Growth, Culture Age and Metabolite Concentration. *J. Biotechnol.* **7** 229-246 (1988)

Radlett PJ, Telling RC, Stone CJ, Whiteside JP, Improvements in the Growth of BHK21 Cells in Submerged Culture. *Appl. Microbiol.* **22** 534-537 (1971)

Ratcliffe A, Tissue Engineering of Vascular Grafts. *Matrix Biology* **19** 353-357 (2000)

Rhodes NP, Shortland AP, Rattray A, Williams DF, Platelet Reactions to Modified Surfaces Under Dynamic Conditions. *J. Mat Sci: Mats. in Med.* **9** 767-772 (1998)

Rousseau I, Bu'Lock JD, Mixing Characteristics of a Simple Airlift Reactor. *Biotechnol. Lett.* **2** 475-480 (1980)

Salk JE, Drech U, Younger JS, Bennett BL, Lewis LJ, Bazeley PL, Formaldehyde treatment and safety testing of of experimental poliomyelitis vaccines. *Am. J. Pub. Health* **44** 563-570 (1954)

Salk J, Considerations in the preparation and use of poliomyelitis virus vaccine. *J. Am. Med. Assoc.* **158** 1239 (1955)

Sato M, Nagayama K, Kataoka N, Sasaki M, Hane K, Local Mechanical Properties Measured by Atomic Force Microscopy for Cultured Bovine Endothelial Cells Exposed to Shear Stress. *J. Biomech.* **33** 127-135 (2000)

Scheper TH, Influence of Stress on Cell Growth and Product Formation. *Adv. in Biochem. Eng. Biotechnol.* **67** Springer Verlag. Heidelberg. (2000)

Schneider M, Raymond F, Marrison IW, Vonstockar U, Bubble-Free Oxygenation by means of Hydrophobic Porous Membranes. *Enz. Microb. Technol.* **17** (9) 839-847 (1995)

Schnittler HJ, Franke RP, Akbay U, Mrowietz C, Drenckhahn D, Improved In Vitro Rheological System for Studying the Effect of Fluid Shear Stress on Cultured Cells. *Am. J. Physiol.* **265** C289-C298 (1993)

Spier RE, Whiteside JP, The Description of a Device which Facilitates the Oxygenation of Microcarrier Cultures. *Dev. Biol. Std.* **55** 151-152 (1984)

Spier RE, Gradients in Animal and Plant Cell Technology Systems. *Enz. Microb. Technol.* **17** 91-92 (1995)

Spier RE, Kadouri A, The evolution of processes for the commercial exploitation of anchorage dependent animal cells. *Enz. Microb. Technol.* **21** 2-8 (1997)

Smith HM, Burrows TM, Laboratory Apparatus for the Suspended Culture of Tissue Cells. *Lab. Pract.* **12** 451-453 (1963)

Stathopoulos NA, Hellums JD, Shear Stress Effects on Human Embryonic Kidney Cells In Vitro. *Biotech. Bioeng.* **28** 1021-1026 (1985)

Temenoff JS, Mikos AG, Review: Tissue Engineering for Regeneration of Articular Cartilage. *Biomaterials* **21** 431-440 (2000)

Thomas CR, Problems of Shear in Biotechnology. in *Chemical Engineering Problems in Biotechnology.* Elsevier. London. (1990)

Thoumine O, Ziegler T, Girard PR, Nerem RM, Elongation of Confluent Endothelial Cells in Culture: The Importance of Fields of Force in the Associated Alterations of their Cytoskeletal Structures. *Exp. Cell Res.* **29** (2) 427-441 (1995)

Tramper J, Oxygen Gradients in Animal Cell Bioreactors. *Cytotechnology* **18** 27-34 (1995)

Unsworth BR, Lelkes PI, Growing Tissues in Microgravity. *Nature Medicine* **4** 901-907 (1998)

Vacanti CA, Vacanti JP, Bone and Cartilage Reconstruction *in Principles of Tissue Engineering.* RG Landes Company. (1997)

Van Wezel AL, Cultivation of Anchorage Dependent Cells and their Applications. *J. Chem. Tech. Biotechnol.* **32** 318-323 (1982)

Vazquez-Una G, Chenlo-Romero F, Sanchez-Barral M, Perez-Munuzuri V, Mass Transfer Enhancement Due to Surface Wave Formation at a Horizontal Gas-Liquid Interface. *Chem. Eng. Sci.* **55** 5851-5856 (2000)

Vunjak-Novakovic G, Freed LE, Biron RJ, Langer R, Effects of Mixing on the Composition and Morphology of Tissue Engineered Cartilage. *AIChE J.* **42** (3) 850-860 (1996)

Vunjak-Novakovic G, Obradovic B, Martin I, Bursac PM, Langer R, Freed LE, Dynamic Cell Seeding of Polymer Scaffolds for Cartilage Tissue Engineering. *Biotechnol. Prog.* **14** 193-202 (1998)

Vunjak-Novakovic G, Martin I, Obradovic B, Treppo S, Grodzinsky AJ, Langer R, Freed LE, Bioreactor Cultivation Conditions Modulate the Composition and Mechanical Properties of Tissue Engineered Cartilage. *J. Orthop. Res.* **17** 130-138 (1999)

Wagner R, Lehmann J, Growth and Productivity of Recombinant Animal Cells in Bubble-Free Aeration System. *Trends in Biotechnol.* **6** (5) 101-104 (1988)

Wu SC, Influence of Hydrodynamic Shear Stress on Microcarrier Attached Cell Growth: Cell Line Dependency and Surfactant Protection. *Bioproc. Eng.* **21** 201-206 (1999)

Wu SC, Huang GYL, Hydrodynamic Shear Forces Increase Japanese Encephalitis Virus Production from Microcarrier Grown VERO Cells. *Bioproc. Eng.* **23** 229-233 (2000)

Yoshikawa N, Ariyoshi H, Ikeda M, Sakon M, Kawasaki T, Monden M, Shear Stress Causes Polarized Change in Cytoplasmic Calcium Concentration in Human Umbilical Vein Endothelial Cells (HUVEC's). *Cell Calcium* **22** (3) 189-194 (1997)

Zhang S, Hand-Corrigan A, Spier RE, Oxygen Transfer Properties of Bubbles in Animal Cell Culture Media. *Biotech. Bioeng.* **40** 252-259 (1992)

Chapter 2

Hydrodynamics of Concentric Cylinder Flows

A very large number of experimental, theoretical and computational studies have been made over the last 120 years or so on the hydrodynamic behaviour of fluid contained between concentric rotating cylinders. Whilst a number of observations on transitions occurring between hydrodynamic states remain unanswered mathematically, some important criteria have already been established, both qualitatively and quantitatively, and which are invaluable in the hydrodynamic design of this type of system. In this chapter, a historical development of this knowledge is presented briefly alongside the useful mathematical theories that can be applied for the hydrodynamic design of a bioreactor based on the concentric cylinder arrangement.

2.1 Introduction: Early Studies of Concentric Cylinder Flows

The symmetry of the flow of fluid contained between two cylinders appears to have been first recorded by Isaac Newton in his famous 1687 work *Principia* where he hypothesised that the flow was composed of concentric streamlines. In 1848 Stokes suggested that the use of motes (dust particles) would provide a method to visualise the flow phenomena and confirm Newton's hypothesis. Stokes also suggested that the rotation of the

inner cylinder at a speed greater than that of the outer cylinder would produce circulating eddies in the flow. In 1881 Margules recognised that this type of flow could be used to measure viscosity and in 1888 Mallock constructed a viscometer based on the concentric cylinder arrangement. Mallock made two observations. The first was consistent with Stokes proposition that the flow was always unstable when the speed of the inner cylinder exceeded the speed of the outer cylinder. The second observation was that when only the outer cylinder rotated, the flow remained stable up to a critical outer cylinder rotational speed beyond which the flow became turbulent. In 1890 Couette developed a viscometer where only the outer cylinder could rotate. His findings agreed with Mallock in that a critical outer rotational speed existed beyond which the flow became unstable. It is attributable to this work that the solid body rotation a fluid experiences when only the outer cylinder rotates is now generally referred to as a Couette flow. The primary interest of Mallock and Couette was the measurement of viscosity and no experiments were made to investigate hydrodynamic instability in any detail. Orr (1907), Rayleigh (1916) and Harrison (1921) provided a link between the viscosity experiments of Mallock and Couette with a theoretical mathematical treatment of the system. They showed that Mallock's inner cylinder rotation experiments consistently operated above the critical rotational rate for hydrodynamic instability. Later researchers also showed that the early onset of turbulence with outer cylinder rotation was due to eccentricity of the coaxial cylinders.

2.2 Centrifugal Instability for Inviscid Fluids: Rayleigh's Criterion

Rayleigh first addressed hydrodynamic instability in Couette flow between 1916 and 1920. The work was initiated by a meteorological study of cyclones. The work of Mallock and Couette had suggested that for the same shear rate in the gap the flow would be laminar below a critical speed of outer cylinder rotation when the inner cylinder was stationary. However, for the same shear rate using inner cylinder rotation and a stationary outer cylinder, the flow could be unstable. Rayleigh developed a criterion to explain this

based on an energy analysis of the flow for an inviscid fluid. Before addressing this analysis, the instability can be reasoned on a purely physical basis.

Referral is made to Figure 2.1, where a fluid is contained between two cylindrical walls, either of which can rotate. The circular trajectory of a fluid element equidistant from either wall is indicated as Path 1. The element experiences a centripetal acceleration to maintain its circular path. The acceleration, a, is related to the radius of the path, r and the speed of the moving wall, Ω, according to

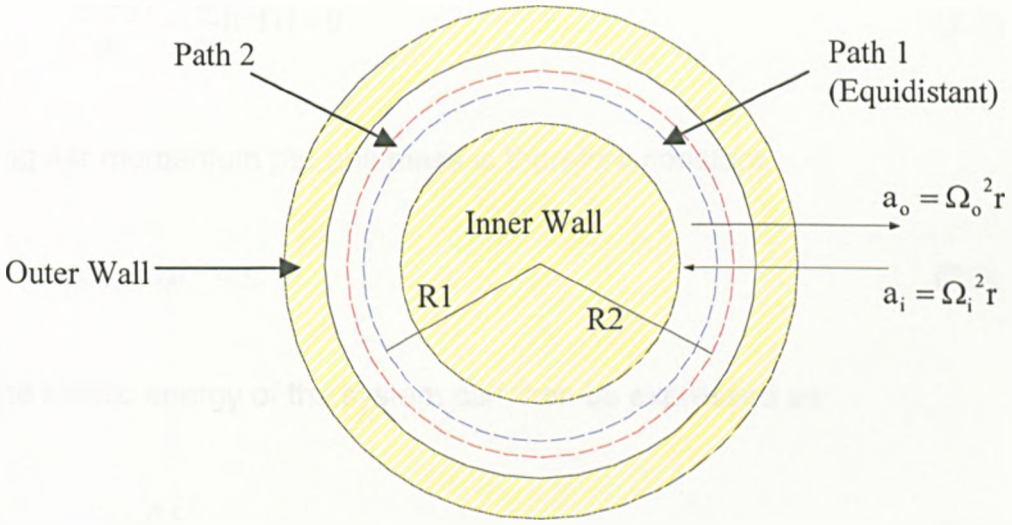

Figure 2.1 Flow paths of particles to illustrate Rayleigh's Criterion

$$a = \Omega^2 r \qquad (2.1)$$

For Path 1 the acceleration is the same irrespective of which wall is moving to maintain this radial path. Considering Path 2 however, if the outer wall rotates the element requires a lower acceleration to maintain this radial path whereas if the inner wall rotates a higher acceleration would be required to maintain the path. Due to the non-linear dependency on radius and rotational speed with respect to centripetal acceleration this cannot occur beyond a critical speed so a fluctuating disturbance is set-up in space as the

effects of radial position due to the inner and outer wall are realised. Beyond a critical speed, unstable periodic flows therefore develop. The periodicity will then be related not only to the magnitude and direction of the wall velocities, but also other influential forces such as shear stresses, pressure gradients and gravitational forces. To provide a mathematical criterion for this experimentally observed phenomenon, Rayleigh considered the energy transfer occurring in the system using a number of simplifying assumptions.

For purely azimuthal, axisymmetric, inviscid flow, neglecting gravitational forces, the angular momentum conservation equation reduces to

$$\frac{d(ru_\theta)}{dt} = \frac{d}{dt}\left(r^2\Omega\right) = 0 \qquad (2.2)$$

Angular momentum per unit mass is therefore constant:

$$ru_\theta = \Omega r^2 = C \qquad (2.3)$$

The kinetic energy of the system can then be expressed as:

$$E_K = \frac{\rho}{2}\frac{c^2}{r^2} \qquad (2.4)$$

Suppose the two elementary rings of Path 1 and Path 2 have equal heights and masses at r = R1 and r = R2 (R2 > R1). The kinetic energy of the two rings is therefore

$$E_{K_1} = \frac{\rho}{2}\frac{C_1^2}{(R1)^2} \qquad E_{K_2} = \frac{\rho}{2}\frac{C_2^2}{(R2)^2} \qquad (2.5)$$

If the two rings are now interchanged then due to angular momentum conservation, after interchange

$$E_{K_1} = \frac{\rho}{2}\frac{C_2^{\,2}}{(R1)^2} \qquad E_{K_2} = \frac{\rho}{2}\frac{C_1^{\,2}}{(R2)^2} \tag{2.6}$$

The exchange in kinetic energy (or centrifugal potential energy) is then

$$\begin{aligned}\Delta E_K &= \frac{\rho}{2}\left[\left(\frac{C_1^{\,2}}{(R1)^2} - \frac{C_2^{\,2}}{(R1)^2}\right) + \left(\frac{C_2^{\,2}}{(R2)^2} - \frac{C_1^{\,2}}{(R2)^2}\right)\right] \\ &= \frac{\rho}{2}\left(C_2^{\,2} - C_1^{\,2}\right)\left(\frac{1}{(R1)^2} - \frac{1}{(R2)^2}\right)\end{aligned} \tag{2.7}$$

For an interchange of rings to occur, a release of kinetic energy is required and the condition of $C_1 > C_2$ satisfies this given that R2 > R1. In this case instability is introduced to the system. Conversely, if $C_2 > C_1$ then the system is stable and Couette flow ensues. The Rayleigh criterion for system stability is simply expressed as

$$\frac{\Omega_2}{\Omega_1} > \left(\frac{R1}{R2}\right)^2 \tag{2.8}$$

Rayleigh's criterion can be simply stated thus: *for a rotating fluid in a cylindrical domain, stability is ensured if the angular momentum of elemental rings across the domain increases monotomically outward*

The Rayleigh criterion has been rigorously proved for an inviscid fluid and states that there is never a stable flow if the inner wall rotates and the outer is stationary, no matter how slow the inner wall rotates. For real fluids there are damping effects due to the fluid viscosity and the Rayleigh criterion is only observed as an outer limit, and hence stable laminar flows can be achieved with inner wall rotations at low angular velocities. For high rotation rates of the outer cylinder, the viscous forces are small relative to the dynamic forces and the Rayleigh criterion is approached as an asymptote. These effects have been observed experimentally.

2.3 Centrifugal Instability for Viscous Fluids: Taylor Number

Whilst the Rayleigh criterion is useful as a guideline for instability in concentric cylinder systems more detailed information on the onset and development of instability in viscous fluid systems is required. G. I. Taylor (1923) developed the fundamental theory for this as an extension to the work of Rayleigh. Taylor used a more sophisticated experimental apparatus than Couette or Mallock but based on their observations he maintained a narrow gap relative to the cylinder radii. The experimental assembly was 90 cm long and to avoid vibrational disturbance it was bolted to the walls and floor of the laboratory. The inner cylinder was of paraffin wax construction mounted on a 3/4 inch steel shaft and the radii investigated were in the range $2.93 < r_i < 3.80$ cm. The outer cylinder, $r_o = 4.035 \pm 0.01$cm included a 20cm glass section for flow visualisation. The cylinders could rotate independently in either direction and the ratio of angular velocities was continually controlled with a variable speed motor to ±0.5%. Water was used as the experimental fluid with temperature control to ±0.2°C. Ports on the inner cylinder allowed dye injection for flow visualisation. To theoretically address the centrifugal instability of a viscous fluid, Taylor solved the equations of motion and continuity for the stable Couette flow and then superimposed a small disturbance flow. His assumptions included axisymmetry, an axially imposed periodic disturbance flow and negligible gravitational effects. Whilst the mathematics for Taylor's theory are complex, the key steps in the analysis are presented for completeness where an eigenvalue given by $\sigma = i\alpha c$ can indicate a measure of stability.

The equations of motion and continuity are solved with no slip boundary conditions at the cylinder walls and no transverse pressure gradient, so the basic Couette flow equation only has an angular velocity component

$$V = Ar + \frac{B}{r} = \Omega r \qquad (2.9)$$

$$\text{where } \Omega = A + \frac{B}{r^2} \tag{2.10}$$

$$A = \frac{\Omega_i(\eta^2 - \mu)}{(\eta^2 - 1)} \quad \text{and} \quad B = \frac{\Omega_i r_i^2(\mu - 1)}{\eta^2 - 1} \tag{2.11}$$

$$\text{where } \eta = \frac{r_i}{r_o} \quad \text{and} \quad \mu = \frac{\Omega_o}{\Omega_i} \tag{2.12}$$

The disturbance velocity superimposed on this base flow is assumed to be periodic,

$$\mathbf{v} = \begin{pmatrix} v_r \\ v_\theta \\ v_z \end{pmatrix} e^{i\alpha(z - ct + n\theta)} \tag{2.13}$$

Characteristic time (t) and characteristic dimensions are required to mathematically assess the effect of the disturbance on the system. These are based on a gap width of $d = (r_o - r_i)$, where axial (z) and radial (r) dimensions are considered:

$$t = \frac{t^* \upsilon}{d^2}, \quad r = \frac{r^*}{d}, \quad z = \frac{z^*}{d} \tag{2.14}$$

For axisymmetric flows, there are no azimuthal waves and consequently the azimuthal wavenumber, n is zero. For a disturbed flow, the scaled axial wavenumber is α and the wave speed is *c*. The flow is linearly stable to external disturbances when the imaginary part of *c* is negative i.e. (Im (c) < 0). The superimposed disturbance will grow to create a hydrodynamic instability when the imaginary part of *c* is positive i.e. (Im (c) > 0). In situations where the imaginary part of *c* is zero (Im (c) = 0), the disturbance will neither grow nor decay and this is a transition point between linearly stable and unstable flow. The eigenvalue can be real or complex, where a complex number would indicate a periodic flow. An eigenvalue of zero indicates the critical condition between stable and unstable flow.

The flow equation for Couette flow with a superimposed disturbance, or the Taylor-Couette flow equation is then

$$\mathbf{V} = V\mathbf{e}_\theta + \mathbf{v} \tag{2.15}$$

This equation is substituted into the equations of motion and continuity and the resulting equations are linearized. Since the disturbance velocity is small compared to the basic Couette flow, products of the disturbance velocities become very small relative to the base flow. These products are therefore neglected in the linearized equations. The linearized system can be simplified to two equations

$$\left[DD_* - \alpha^2 + i\alpha c\right]\left(DD_* - \alpha^2\right)v_r = \frac{2\Omega\alpha^2 d^2}{\nu} v_\theta \tag{2.16}$$

$$\text{and} \quad \left[DD_* - \alpha^2 + i\alpha c\right]v_\theta = \frac{2Ad^2}{\nu} v_r$$

with no slip boundary conditions, $v_r = v_\theta = 0$ at $y = 0, 1$. For this case,

$$y = r - \frac{1-\varepsilon}{\varepsilon} \left(0 \le y \le 1\right), \quad \varepsilon = \frac{d}{r_o}, \quad D = \frac{\partial}{\partial y}, \quad D_* = D + \frac{1}{y + (1-\varepsilon)/\varepsilon} \tag{2.17}$$

The case for the narrow gap limit is also invoked

$$\varepsilon = d/r_o \to 0, \quad \Rightarrow D_* \to D, \quad \Rightarrow \Omega \to \left[1 - (1-\mu)y\right] \tag{2.18}$$

and this simplifies the two linearized equations to

$$\left[D^2 - \alpha^2 + i\alpha c\right]\left(D^2 - \alpha^2\right)v_r = \left[1 - (1-\mu)y\right]v_\theta \tag{2.19}$$

$$\text{and} \quad \left[D^2 - \alpha^2 + i\alpha c\right]v_\theta = -Ta\,\alpha^2 v_r$$

Here, v_r has been rescaled to

$$v_r = \frac{2\Omega_i d^2}{\nu} v_r \tag{2.20}$$

and

$$Ta = \frac{-4A\Omega_i d^4}{\nu^2} = \frac{4\Omega_i^2 r_i^4}{\nu^2} \frac{\eta^2 - \mu}{1-\eta^2} \left(\frac{1-\eta}{\eta}\right)^4 = \varepsilon Re_\theta^2 + O(\varepsilon^2) \tag{2.21}$$

where

$$Re = \frac{(\Omega_i - \Omega_o) d r_i}{\nu} \tag{2.22}$$

The Taylor number, Ta, is a measure of centrifugal to viscous forces whilst the Reynolds number is a measure of inertial to viscous forces. The relationship between these is illustrated in equation (2.21), namely that $Ta \propto Re^2$. The basis for the characteristic length scale in this analysis is d. The choice of an alternative for the characteristic length scale or indeed the characteristic time scale will lead to alternative definitions of the Taylor number and care must therefore be taken when comparing numerical data against varying forms of the Taylor number. For example, a number of authors including Chandrasekhar (1961) have used the outer cylinder radius, r_o as the characteristic length scale leading to the following definition of Taylor number, denoted as Ta_{Ch}

$$Ta_{Ch} = -\frac{4ABr_o^2}{\nu^2} = \frac{4\Omega_i^2 r_i^4}{\nu^2} \frac{(1-\mu)(1-\mu/\eta^2)}{(1-\eta^2)^2} \tag{2.23}$$

the two Taylor numbers of equations (2.21) and (2.23) are related as

$$\frac{Ta_{Ch}}{Ta} = \frac{(1-\mu)\eta^2}{(1-\eta^2)(1-\eta)^4} \tag{2.24}$$

Whilst these two are perhaps the most commonly used definitions of Taylor

number, some other authors have different characteristics for their particular application so other definitions do exist. Examples of these are summarised in the Table 2.1 below.

The Taylor-Couette system comprising two linearized parts has been given as equation (2.19) in the preceding section. To determine a critical value of the Taylor number, Ta_{crit}, at which this system becomes unstable and a transition is made from laminar Couette flow to Taylor-vortex flow, this system of equations must be solved simultaneously at the critical condition. Recalling equation (2.13), the critical condition exists when $c = 0$ where the imposed disturbance neither grows nor decays. Chandrasekhar used a Galerkin-type numerical method to solve this problem. The two parts of equation (2.19) are first combined to form a sixth order differential equation

Author	Characteristic	Taylor Number	
Lee (1995)	r_i length; Ω_i only	$Ta = \frac{r_i \Omega_i^{\,3} d^3}{\nu^2}$	(2.21a)
Takhar (1994)	a general length; Ω_o only	$Ta = \frac{\Omega_o a^2}{\nu}$	(2.21b)
Sugata (1991)	ζ fluid depth; Ω average annular rotation rate	$Ta = \frac{4\Omega^2 (r_o - r_i)^5}{\nu^2 \zeta}$	(2.21c)
White (1991)	D gap width; Ω_i only	$Ta = \frac{r_i D^3 (\Omega_i^{\,2} - \Omega_o^{\,2})}{\nu^2}$	(2.21d)
Mobbs & Ozogan (1984)	Eccentric cylinders; Ω_i; r_i	$Ta = \frac{2\Omega_i^{\,2} r_i d^3}{\nu^2 (r_i - r_o)}$	(2.21e)
Rudman (1994)	Ω_i only; r_i only;	$Ta = \frac{\Omega_i r_i d}{\nu} \left(\frac{d}{r_i}\right)^{0.5}$	(2.21f)
Sherman (1991)	r_i length; Ω_i only	$Ta = \frac{2\Omega_i^{\,2} r_i^{\,2} d^3}{\nu^2}$	(2.21g)
Schlichting (1987)	r_i length; Ω_i only	$Ta = \frac{\Omega_i d}{\nu} (r_i d)^{0.5}$	(2.21h)
Roberts (1965)	η ; Ω_i only	$Ta = \frac{2\eta^2}{1-\eta^2} \frac{\Omega^2 d^4}{\nu^2}$	(2.21i)

Table 2.1 Alternative Definitions of the Taylor number

$$\left[D^2-\alpha^2+i\alpha c\right]^2\left(D^2-\alpha^2\right)v_\theta=-Ta\,\alpha^2\left[1-(1-\mu)y\right]v_\theta \qquad (2.25)$$

the no slip boundary conditions are

$$\begin{aligned} &y=0,1 \quad v_\theta=0 \\ &y=0,1 \quad v_r=0 \quad =\left(D^2-\alpha^2\right)v_\theta \\ &y=0,1 \quad v_z=0 \quad =D\left(D^2-\alpha^2\right)v_\theta \quad =Dv_r \end{aligned} \qquad (2.26)$$

At the critical point of $c = 0$, and assuming a near solid body rotation for $\mu \rightarrow 1$, equation (2.25) can be simplified to a differential equation which can be solved analytically

$$\left[D^2-\alpha^2\right]^3 v_\theta=-Ta\,\alpha^2 v_\theta \qquad (2.27)$$

The solution of equation above has the form

$$v_\theta=C_1\cosh q_o x+C_2\sinh q_o x+C_3\cosh qx+C_4\sinh qx+C_5\cosh q^* x+C_6\sinh q^* x \qquad (2.28)$$

In equation (2.28) above, q_o, q, q^* are the roots to the equation $(q^2-\alpha^2)^3 = -Ta\,\alpha^2$ and $x = y-1/2$. The six no slip boundary conditions reduce the solution to a system of three equations of the form **AC** = 0. As first shown by Jeffreys (1928), this is identical to the Benard problem for the thermal instability of a fluid contained between two flat plates of differing temperatures. For a nontrivial solution to exist the determinant of **A** must be zero. This provides a characteristic equation in terms of the unknowns, α and Ta. α is known as the wavenumber and is related to the size of the resulting vortices that appear as the critical Taylor number is reached. Given a value of α, the critical Taylor number can be determined numerically.

A first approximation to equation (2.27) by Drazin and Reid is

$$\frac{1}{2}(1+\mu)\mathrm{Ta}_{\mathrm{Ch}} = \frac{\left(\pi^2+\alpha^2\right)^3}{\alpha^2\left[1-16\pi^2\alpha\cosh^2\frac{1}{2}\alpha\Big/\left\{\left(\pi^2+\alpha^2\right)^2\left(\sinh\alpha+\alpha\right)\right\}\right]} \qquad (2.29)$$

Using values of $2.5 < \alpha < 4$, a plot of Taylor number versus α is given for the case of μ=1 using equation (2.29) in Figure 2.2. Chandrasekhar numerically solved equation (2.27) at higher orders of approximation and determined values of α (for a given value of μ) at which Ta took a minimum value. The minimum value of Ta is of course the critical Taylor number at which instability occurs and is denoted as $\mathrm{Ta}_{\mathrm{crit}}$. The numerical results obtained by Chandrasekhar are given in Table 2.2

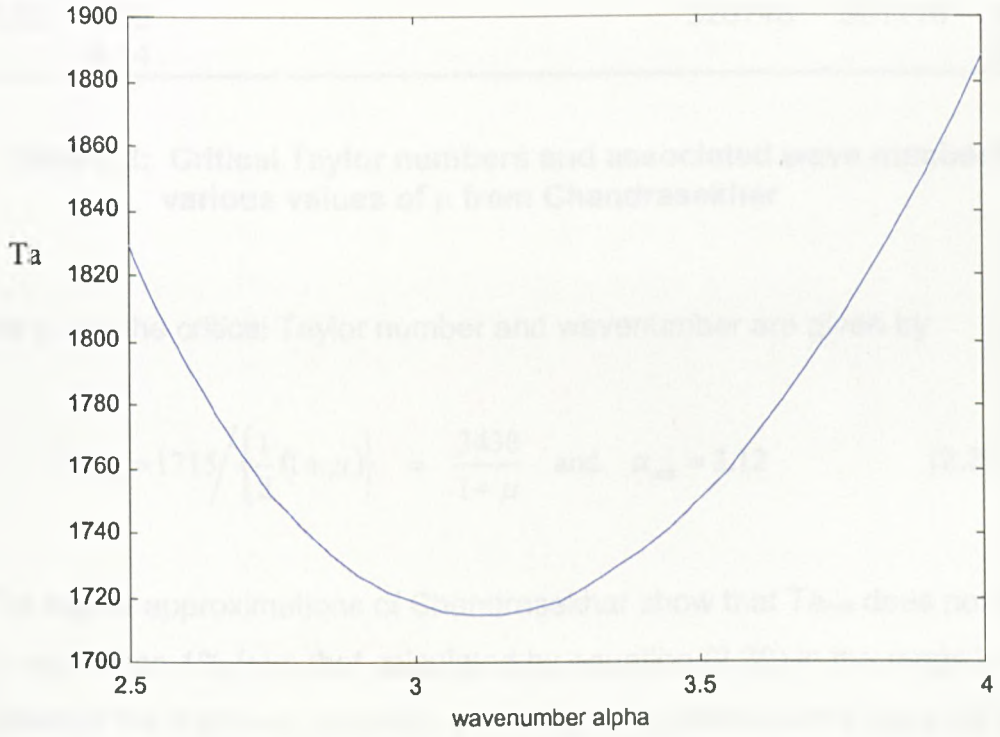

Figure 2.2 Plot of Taylor number versus wavenumber using equation (2.29) for μ = 1

μ	α	First Approx.	Second Approx.	Third Approx.	Fourth Approx.	Fifth Approx.	Sixth Approx.
1.00	3.12	1715.1	1715.1	1708.0			
0.50	3.12	2286.7	2284.8	2275.3			
0.25	3.12	2744.1	2736.4	2725.3			
0.00	3.12	3429.9	3403.6	3390.3			
-0.25	3.13	4573.4	4477.9	4462.5			
-0.50	3.20	6866.2	6430.6	6417.1	6414.8		
-0.60	3.25	8595.8	7694.5	7687.7			
-0.70	3.34	11514	9422.7	9432.6			
-0.80	3.50		11774	11820			
-0.90	3.70		14846	14943			
-0.95	3.86		16647	16764			
-1.00	4.00		18615	18735	18677		
-1.25	4.60			30497	30458		
-1.50	5.05			46000	46192		
-1.75	5.60			67189	67592		
-2.00	6.10			97090	95610		95585
-2.50	7.10				176810	177107	177108
-3.00	8.09				320748	301116	302496
	8.14						302482

Table 2.2: Critical Taylor numbers and associated wave numbers for various values of μ from Chandrasekhar

For $\mu \to 1$, the critical Taylor number and wavenumber are given by

$$Ta_{crit} = 1715 \Big/ \left\{ \frac{1}{2}(1+\mu) \right\} = \frac{3430}{1+\mu} \quad \text{and} \quad \alpha_{crit} = 3.12 \qquad (2.30)$$

The higher approximations of Chandrasekhar show that Ta_{crit} does not differ by more than 1% from that calculated by equation (2.30) in the range $0<\mu<1$, however the improved accuracy of the higher approximations have led to a more accurate equation for determining Ta_{crit}

$$Ta_{crit} \cong 1707.76 \left\{ 1 - 7.61 \times 10^{-3} \left(\frac{1-\mu}{1+\mu} \right)^2 + ... \right\} \quad \text{as } \mu \to 1 \qquad (2.31)$$

The values in Table 2.2 further suggest that for $\mu > -1.0$ the third approximation to Ta is sufficient but progressively higher approximations are required as $-3.0 < \mu < -1.0$. Thus it becomes progressively more difficult to

determine a critical Taylor number for counter rotation of the cylinders particularly when the magnitude of rotation is much higher on the outer cylinder relative to the inner cylinder. Thus in the limit $(1-\mu)\to\infty$ asymptotic relations can be made from the results of Table 2.2.

$$\mathrm{Ta}_{crit} \to \varsigma(1-\mu)^4 \quad \text{and} \quad \alpha(\mathrm{Ta}_{crit}) \to \varphi(1-\mu) \tag{2.32}$$

ς and φ are constants approximated from the results of Table 2.2, namely

$$\frac{\mathrm{Ta}_{crit}}{(1-\mu)^4}\begin{cases}=1180.2\\=1180.5\\=1181.6\end{cases} \quad \text{and} \quad \frac{\alpha(\mathrm{Ta}_{crit})}{1-\mu}\begin{cases}=2.03\\=2.03\\=2.035\end{cases} \quad \text{for} \quad 1-\mu\begin{cases}=3.0\\=3.5\\=4.0\end{cases} \tag{2.33}$$

For the case of counter rotation of the cylinders ($\mu<0$), the hydrodynamic instability arises due to a violation of Rayleigh's Criterion in the layers extending from the inner cylinder. In fact as $(1-\mu)\to\infty$, one might consider the critical Taylor number to be close for the case of $\mu=0$ with a gap width equal to the distance of transition off the inner cylinder, d_o where

$$d_o = \frac{d}{1-\mu} \tag{2.34}$$

The gap width appears as a fourth power in the general definition of Taylor number (given here as equation (2.21)) and this accounts for the definitions of equation (2.32) above. The constants ς and φ approximate to 1181.6 and 2.035 from Table 2.2 and are significantly different than the values of 3416 and 3.12 observed for $\mu=0$. The reason for this is the difference in the value of d_o obtained in the two cases when $\mu=0$ and when $(1-\mu)\to\infty$.

2.4 Wide Gap Concentric Cylinder Flows

The foregoing discussion on Taylor numbers for concentric cylinder flows has been restricted to the case where a narrow gap exists. A narrow gap is defined as being very much smaller than the mean gap radius,

$$d\left(=r_2-r_1\right)<<1/2\left(r_2-r_1\right) \tag{2.35}$$

For the case of a wide gap, which is the condition for $\eta \geq 0.5$, the Taylor number is redefined as

$$Ta=\frac{64}{9}\left(\frac{\Omega_1 r_1^{\,2}}{\nu}\right)^2 k \tag{2.36}$$

where

$$k=(1-\mu)(1-4\mu) \tag{2.37}$$

These definitions apply for $\eta=0.5$ and the Rayleigh criterion for this case is $\mu > 1/4$

From a numerical solution to the flow problem for the wide gap, Chandrasekhar has shown that

$$\begin{aligned} &Ta_{crit} \rightarrow 1.533x10^4 \text{ and } \alpha_{crit} \rightarrow 6.2 \\ &as \mu \rightarrow 1/4 \text{ and } k \rightarrow 0 \end{aligned} \tag{2.38}$$

In terms of angular velocity of the rotating walls, the Rayleigh criterion for the wide gap case may be expressed as

$$\varpi_2=\frac{1}{4}\varpi_1 \tag{2.39}$$

$$\varpi_1 = \frac{\Omega_1 r_1^2}{\nu} = \frac{0.375}{1-\mu}\sqrt{\frac{Ta}{k}} \tag{2.40}$$

$$\varpi_2 = \frac{\Omega_2 r_1^2}{\nu} = \mu\varpi_1 \tag{2.41}$$

For the critical case and as $\mu \rightarrow 1/4$,

$$\varpi_1 \rightarrow \frac{53.61}{\sqrt{(1-4\mu)}} \tag{2.42}$$

Roberts (1965) calculated Ta_{crit} and α_{crit} for progressively increasing gap width (η) and for the particular case of inner cylinder rotation only (μ=0). The Taylor number was defined as

$$Ta = \frac{2\eta^2}{1-\eta^2}\frac{\Omega^2 d^4}{\nu^2} \tag{2.43}$$

in the range $0.500 < \eta < 0.975$. A summary of the results found in this study is given in Table 2.3.

2.5 Torque measurements in concentric cylinder flows

The first measurements of torque in concentric cylinder flow were made by Couette in order to determine fluid viscosity. The torque that is generated by the rotation of one cylinder and transmitted to the other cylinder by the intervening fluid is given by

$$M = A\tau(r)dr \tag{2.44}$$

where A is the surface area of the cylinder and $\tau(r)$ is the shear stress.

η	Ta_{crit} (from equation (2.43))	α_{crit}
0.975	1723.89	3.1268
0.950	1754.76	3.1276
0.925	1787.93	3.1282
0.900	1823.37	3.1288
0.875	1861.48	3.1295
0.850	1902.40	3.1302
0.750	2102.17	3.1355
0.650	2383.96	3.1425
0.500	3099.57	3.1631

Table 2.3 Critical parameters for the onset of Taylor-vortex flow for inner cylinder rotation with varying gap width

The velocity distribution for Couette flow, with a stationary inner cylinder and moving outer cylinder, is given by equation (2.9) so the torque exerted on the inner cylinder is given by

$$M_{Cou} = -4\pi\mu\left\{\frac{r_i^2 r_o^2 h}{\left(r_o^2 - r_i^2\right)}\right\}\Omega_o \qquad (2.45)$$

From Couette's torque formula (equation (2.45)), the ratio of torque to rotation rate is constant. In practice this was found to be true for low rotation rates (< 1rev/s) but the torque increased at a faster rate for higher rotational speeds. Wendt (1933) made torque measurements in a concentric cylinder system for $0.68 < \eta < 0.935$, and measured torque exerted on the inner cylinder due to outer rotation and vice-versa. Couette demonstrated that equation (2.45) was only applicable for purely laminar flow, and transition from this would lead to a non-constant ratio of M/Ω. The instability is due to momentum transfer in the fluid between the cylinders as discussed in section 2.2. As the transfer of momentum between the cylinders changes, the moment exerted on the cylinders, M, also changes. The values of M in the

unstable region are compared to M_{Cou}, the laminar Couette condition of equation (2.45) over a range of Ω. Instability in the flow is evident when M/M_{Cou} increases from M/M_{Cou} =1. This first break is indicative of Ta_{crit} as transition is made from laminar to Taylor-vortex flow. The major change is the velocity distribution in terms of the radial component of the flow. Wendt provided a comprehensive data set of M/M_{Cou} for a wide range of independent rotational cylinder speeds from laminar into the far supercritical region. Experiments performed by Donnelly (1958) predicted the Ta_{crit} from torque measurements in this way to within 4%, and this error was attributable to uncertainties in the accuracy of the fluid viscosity, Ω and gap width. A second break in the torque curve was observed much later by Dehbler (1969) and by Cole (1976). This is attributable to the onset of wavy vortex flow. The magnitude of torque under supercritical flow conditions has also been explored by Stuart (1958) and Davey (1962). The prediction of the transition points for the flow from torque measurements amongst these authors generally does not vary from the theoretical predictions of Taylor to more than 5%, however for studies moving into the far more supercritical regions, the torque becomes non-linear following a relationship of the form

$$M = \Omega^n \qquad (2.46)$$

where n is typically in the range 1.3→1.8. The value of n, not unexpectedly is found to be extremely dependent on the geometry and viscosity of the fluid. The measurement of torque can serve as an accurate prediction of the more significant transitions in concentric cylinder flows namely, the first transition from laminar Couette to Taylor-vortex flow, and the second transition of Taylor-vortex to wavy-vortex flow, but it becomes progressively less useful for hydrodynamic prediction as higher supercritical flows are reached. An accurate knowledge of the fluid rheology and the geometry of the system is very important for torque measurements even for the primary transitions (Rattray, 1998).

2.6 Aspect Ratio Effects

The aspect ratio in a concentric cylinder system, Γ, is the ratio of the height of the fluid contained in the annular space between the walls of the inner and outer cylinders, h to the width of the annular gap, d:

$$\Gamma = \frac{h}{d} \tag{2.47}$$

The aspect ratio appears to only be significantly important once the second transition is reached, namely to wavy-vortex flow. In laminar Couette flow and the transition to Taylor vortex flow, it appears that the dependence on the radius ratio η is only significant from the geometric perspective. The aspect ratio appears to play no part in the outcome of the hydrodynamic structure or stability. This conclusion is on the basis of the experiments of Cole (1976) who examined the onset of wavy vortex flow for $1 < \Gamma$,107 and $0.894 < \eta < 0.954$ using torque measurements and flow visualisation techniques. In both sets of experiments it was established that Ta_{crit} for transition to wavy vortex flow increased rapidly for $\Gamma < 40$. This was in contrast to Ta_{crit} for the first transition to laminar Taylor-vortex flow which was the same for columns where $\Gamma > 8$. It was suggested that for $\Gamma < 8$ the discrepancy could be due to the formation of Eckman layers from end effects, which is discussed later. The number of azimuthal waves developed at the onset of wavy vortex flow was also found to be dependent on the aspect ratio, with fewer waves for large Γ and vice-versa. The radius ratio appeared to have little effect on the structure of the wave formation however, for columns where $\eta \leq 0.7$ the value of Ta at the onset of wavy flow was very much higher than the primary $Ta_{crit.}$ Similar general observations have been made by Lorenzen (1983) for columns where $\eta = 0.507$ and $10 \leq \Gamma \leq 17$ and from numerical studies by Edwards (1991) where $\eta = 0.87$ and $8 \leq \Gamma \leq 34$.

2.7 End Effects

Much of the theory pertaining to concentric cylinder flows stems from a superimposed disturbance on the initial laminar velocity profile for Couette flow in equation (2.9) and has been described in section 2.3. Equation (2.9) is true for an infinite fluid. For a concentric cylinder flow, this literally means that $\Gamma = \infty$. When the aspect ratio is large, the fluid contained in the annular space is approximated to an infinite fluid i.e. $\Gamma \rightarrow \infty$. In real systems of course, Γ has a finite value due to the horizontal boundaries at the top and bottom of the column and the question arises as to how large Γ can become before the assumption of an infinite fluid becomes valid. The horizontal boundary influence on the hydrodynamics is collectively referred to as the 'end effects' and they have an influence on the flow even at subcritical Taylor numbers. The fluid layers adjacent to these boundaries are called the Eckman layers and vortices form in these layers at $Ta << Ta_{crit}$. This effect has been demonstrated from the flow visualisation studies of Andereck (1986) but has been observed much earlier (eg. Coles (1965)). As Ta increases, further vortices develop on top of the Eckman layers until vortices developed from the top and bottom of the column meet in the middle of the column where upon Taylor-vortex flow ensues. The point at which the vortices meet in the middle is Ta_{crit}. When Γ is large the formation of vortices in the middle section of the annulus is observed to occur near instantaneously as Ta_{crit} is reached and this supports the linear stability theory proposed in section 2.3. When the length of the fluid column, h is not an even integer multiple of the gap width, d, there may be an initial mismatch of the converging vortices from the top and bottom of the column. This presents itself as a transient delay to laminar Taylor-vortex flow even when Ta_{crit} is reached. This has been experimentally observed by Park (1981) for large Γ columns and by Mullin (1982) for small Γ columns. In the latter case it was observed that in the region of mismatch a stagnant fluid region could be observed and vortices could be caused to appear or disappear depending on the rate of increment of Ta. For a well-proportioned column, if Ta is increased slowly, the number of vortices remains constant and the

wavelength is constant within experimental error since the average wavelength is given by

$$\alpha_{av} = \frac{2h}{Nd} \tag{2.48}$$

where N is the number of vortices. There is systematic uncertainty in the numbers of vortices that will form due to the quantization condition that an integer number of vortices will fill the annulus. This percentage systematic uncertainty in wavelength, $\partial\alpha$ is given by

$$\frac{\partial\alpha}{\alpha_{av}} = \pm 2\left(\frac{100}{N}\right) \tag{2.49}$$

Therefore, even for columns where h is not an even integer of d, eventually, and in all cases, a regular spacing of identical vortices is generated except in the Eckman layers that may differ slightly from the annular vortices, again due to the geometry. One would expect that the influence of the end effects would become more pronounced as Γ becomes smaller and this has been observed to be the case. Blennerhassett (1979) showed theoretically, that Ta_{crit} increases substantially as Γ decreases to the order of 1 up to the primary instability of laminar Taylor-vortex flow. Furthermore, Hall (1980) has demonstrated anomalous modes of flow when Γ becomes very small.

2.8 Effects due to the Rate of Acceleration

The hydrodynamic structure at steady state in concentric cylinder is influenced predominantly by system geometry, kinematic viscosity of the fluid and the relative rotational speed of the cylinder walls. With knowledge of these parameters, it has been suggested that the hydrodynamic state can be predicted, but a further question that arises is the uniqueness of the structure; can different structures be generated given the same initial and final parameters that influence the flow? A rigorous study by Donald Coles in

1965 graphically illustrated that the hydrodynamic structure was not dependent on just the three parameters mentioned above, but was also dependent on the path taken between the two states. The concentric cylinder apparatus of Coles had η = 0.874, Γ = 27.9 and silicone oil with a kinematic viscosity of 0.213 cm^2s^{-1}. All measurements were made at 21°C with a stationary outer cylinder and a fixed inner cylinder. Coles observed that up to 26 distinct stable flow states could be observed for the same final Taylor number when the rate of increase of the Taylor number from Ta = 0 was varied. The rate of increase of Ta is entirely due to the acceleration rate of the inner cylinder from rest in this case. Each of the states generated in these experiments was reproduced at least 3 times with replication of the Taylor number to 2-3%, and speed ranges of up to 14 times Ta_{crit}. The proof of nonuniqueness was provided by Snyder (1969) who produced 26, 24, 23 or 22 vortices at a fixed supercritical Taylor number in the same column depending on the initial conditions used and the path to the final condition. Koschmeider (1979) made similar experiments in a tall column (Γ = 123 and η = 0.896) using very slow acceleration rates of $7x10^{-4}$ rad/s^2 and sudden starts to $100Ta_{crit.}$ Similar observations were made that the final state differed depending on the acceleration. The acceleration rate appears to affect the wavelength established after time dependent starts, which is of course a function of Ta at which the start is made and the final Ta. It has been observed that the shortest wavelengths are generated for sudden start experiments. With progressively decreasing acceleration the wavelength can increase up to the critical wavelength α_{crit} (Burkhalter (1974)). The range of wavelengths generated for sudden starts and for slow increase in Ta is reproduced from Burkhalter (1974) in Figure 2.3.

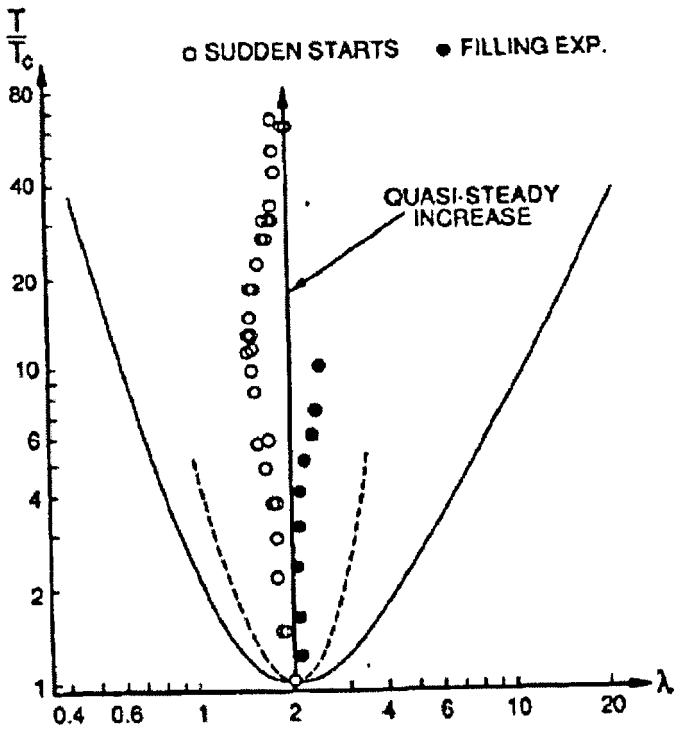

Figure 2.3 Wavelength of stable vortices after sudden starts (from Burkhalter (1974))

2.9 Concluding Remarks

The large number of studies on concentric cylinder flows have demonstrated that hydrodynamic state and stability is governed primarily by

- System geometry
- Cylinder speeds
- Fluid kinematic viscosity

With an accurate knowledge of these parameters, it is possible to a-priori estimate what the hydrodynamic state might be for a prescribed set of conditions and how transition to another state may be initiated or

alternatively, maintained under a different set of circumstances, using the theory presented above. There are a host of factors which can offset the theoretical predictions to a certain degree, so it is instructive in the first instance to verify the theoretical prediction qualitatively before embarking on quantitative measurements, and for this study this has been achieved using flow visualisation which is the subject of the next chapter.

References

Andereck CD, Liu SS, Swinney HL, Flow Regimes in a Circular Couette System with Independently Rotating Cylinders. *J. Fluid Mech.* **164** 155-183 (1986)

Blennerhassett PJ, Hall P, centrifugal Instabilities of Circumferential Flows in Finite Cylinders: Linear Theory. *Proc. Roy. Soc. London A* **365** 191-207 (1979)

Burkhalter JE, Koschmeider EL, Steady Supercritical taylor VorticesAfter Sudden Starts. *Phys. Fluids* **17** 1929-1935 (1974)

Chandrasekhar S, Hydrodynamic and Hydromagnetic Instability. Clarendon Press. Oxford. (1961)

Cole JA, Taylor-Vortex Instability and Annulus Length Effects. *J. Fluid Mech.* **75** 1-15 (1976)

Coles D, Transition in Circular Couette Flow. *J. Fluid Mech.* **21** 385-42 (1965)

Debler W, Fuhner E, Schaaf B, Torque and Flow Patterns in Supercritical Taylor-Vortex Flow. In *12th Int. Congr. Appl. Mech.* 158-178 (1969). Springer, Berlin.

Donnelly RJ, Experiments on the Stability of Viscous flow Between Concentric Rotating Cylinders. I. Torque Measurements. *Proc. Roy. Soc. London A* **246** 312-325 (1958)

Drazin PG, Reid WH, Hydrodynamic Stability. Cambridge University Press. (1981)

Edwards WS, Beane SR, Varma S, Onset of Wavy-Vortices in the Finite Length Taylor-Couette Problem. *Phys. Fluids A* **3** 1510-1518 (1991)

Hall P, Centrifugal Instabilities of Circumferential Flows in Finite Cylinders: Non-Linear Theory. *Proc. Roy. Soc. London A* **372** 317-356 (1980)

Jeffreys H, Some Cases of Instability in Fluid Motion. *Proc. Roy. Soc. London A* **118** 195-208 (1928)

Koschmeider EL, Turbulent Taylor-Vortex Flow. *J. Fluid Mech.* **93** 515-527 (1979)

Lee SHK, Sengupta S, Wei T, Effect of Polymer Additives on Gortler Vortices in Taylor-Couette Flow. *J. Fluid Mech.* **282** 115-129 (1995)

Lorenzen A, Pfister G, Mullin T, End-Effects on the Transition to Time-Dependent Motion in the Taylor Experiment. *Phys. Fluids* **26** 10-13 (1983)

Mobbs FR, Ozogan MS, Study of Sub-Critical Taylor-Vortex Flow Between Eccentric Rotating Cylinders by Torque Measurements and Visual Observations. *Int. J. Heat & Fluid Flow* **5** (4) 251-253 (1984)

Mullin T, Mutations of Steady Cellular Flows in the Taylor Experiment. *J. Fluid Mech.* **121** 207-218 (1982)

Park K, Donnelly RJ, Study of the Transition to Taylor-Vortex Flow. *Phys. Rev. A* **24** 2277-2279 (1981)

Roberts PH, The Solution of the Characteristic value Problems. *Proc. Roy. Soc. London A* **283** 550-556 (1965)

Rudman M, Thompson MC, Hourigan K, Particle Shear Rate History in a Taylor-Couette Column. *ASME Fluids Eng. Div. (FED)* **189** 23-30 (1994)

Schlichting H, Boundary Layer Theory. 7th Edition. McGraw-Hill Inc. New York. (1987)

Sherman HS, Viscous Flow. McGraw-Hill Inc. New York. (1991)

Snyder HA, Wave-Number Selection at Finite Amplitude in Rotating Couette Flow. *J. Fluid Mech.* **26** 545-562 (1969)

Stuart JT, On the Nonlinear Mechanics of Hydrodynamic Stability. *J. Fluid Mech.* **4** 1-21 (1958)

Sugata S, Yoden S, Effects of Centrifugal Force on Stability of Axisymmetric Viscous Flow in a Rotating Annulus. *J. Fluid Mech.* **229** 471-482 (1991)

Takhar HS, Ali MA, Soundalgekar VM, The Effect of Radial Temperature Gradient and Axial Magnetic Field on the Stability of Couette Flow: The Narrow Gap Problem. *Int. J. Energy Res.* **16** 597-621 (1992)

Taylor GI, Stability of a Viscous Liquid Contained Between Two Rotating Cylinders. *Phil. Trans. Roy. Soc. London A* **157**, 565-578 (1923)

Wendt F, Turbulente Stromungen Zwischen Zwei Rotierenden Konantalen Zylindern. *Ing. Arch.* **4** 577-595 (1933)

White, FM. Viscous Fluid Flow. McGraw Hill Inc. New York. (1991)

Chapter 3

Flow Visualisation of Concentric Cylinder Flows

In order to quantify the hydrodynamics in terms of Taylor number, critical Taylor numbers for transitions, wavenumbers and other parameters identified in Chapter 2, it is necessary to observe the conditions under which these changes take place. Flow visualisation studies have been carried out to achieve this in purpose built concentric cylinder systems. From these observations it is possible to make some preliminary estimations of modes of operation at which to operate the system to achieve a given flow condition and using this information detailed quantitative measurements of flow in the gap can be then made under these conditions.

3.1 Flow Visualisation of Metallic Particles

The technique of using metallic flakes seeded in an appropriate fluid was first realised by Benard (1900) and then for Taylor vortex flow by Lewis (1928). The technique of using metallic flakes was first described in detail by Schultz-Grunow (1956) who looked at Taylor-vortex flow over a wide range of Taylor numbers and this technique has been universally adopted by researchers since for Taylor-vortex and other flows. Before this time reliance was primarily made on the use of dye tracers which were appropriate for studying the primary transitions in concentric cylinder flows but were unsuitable for the assessment of the more complex transitions. In these circumstances, the technique of hot-wire anemometry was employed with varying success. Savas (1985) provides a review on the use of metallic particles in flow visualisation and a mathematical treatment on the orientation of the particles in the flow due to the fluid dynamics. The general conclusion that can be drawn from this work is that in images of flow obtained using this technique, dark areas correspond to flow along the observers line of sight whereas light areas correspond to flow perpendicular to the line of sight. Particles suitable for this type of flow visualisation technique include metallic coated polymeric flakes (e.g. Kalliroscope^{TM}), titanium coated particles (e.g. Timiron Supersilk^{TM}) aluminium powder and fish scales. The size of the particles can be important and filtering to a uniform size is normally employed. Additionally consideration of the particle density relative to the fluid density is required to ensure sedimentation effects are not excessive.

3.2 Experimental Facilities for Flow Visualisation Studies

Flow visualisation studies have been made in concentric cylinder systems at two scales, CC-25 and CC-75. The dimensions of the two systems are shown in Figures 3.1 and 3.2 and the manifold design and dimensions are shown in Figure 3.3. All dimensions are in millimetres.

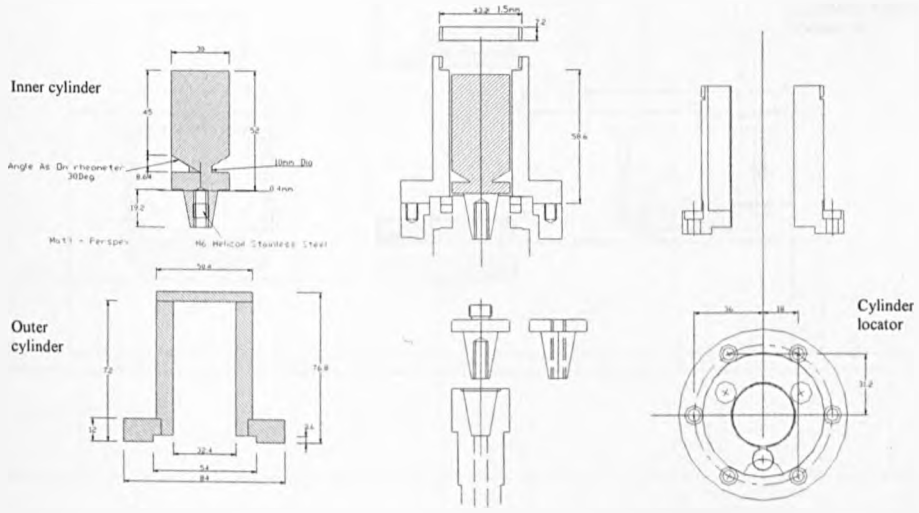

Figure 3.1 Dimensions of System CC-25

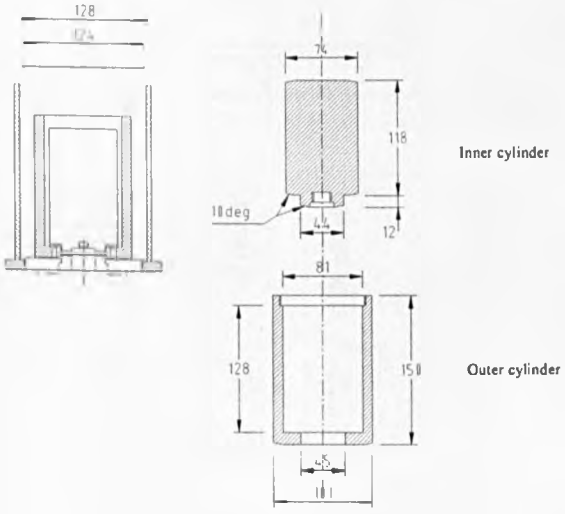

Figure 3.2 Dimensions of System CC-75

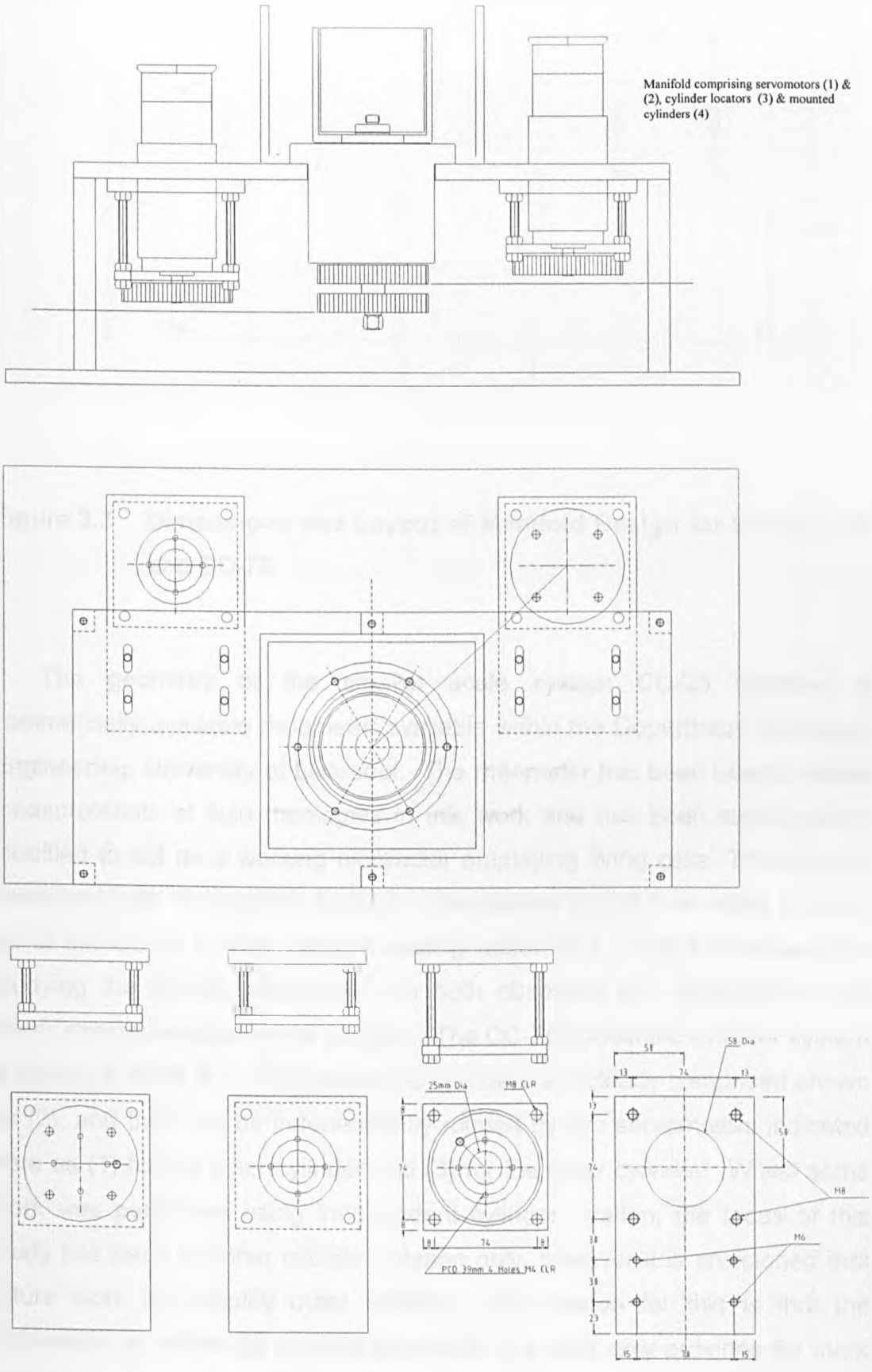

Figure 3.3 continues...

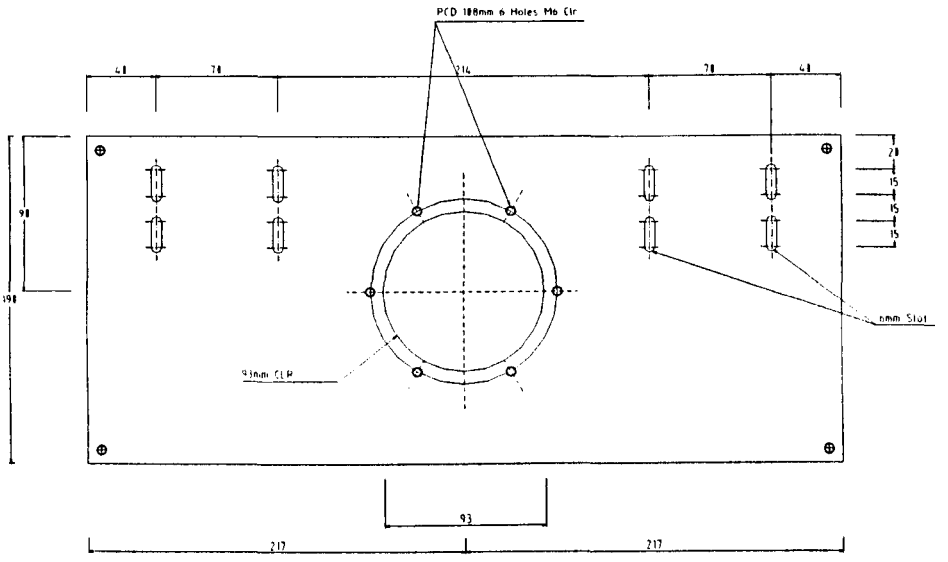

Figure 3.3 Dimensions and Layout of Manifold Design for both CC-25 and CC-75

The geometry of the smaller scale system CC-25 matches a commercially available rheometer available within the Department of Clinical Engineering, University of Liverpool. The rheometer has been used to make measurements of fluid rheologies in this work and has been subsequently modified to act as a working bioreactor employing living cells. This work is described later in Chapters 8 and 9. The system CC-75 is in effect a scale-up of the CC-25 system using a scaling factor of 3. This has allowed for studying the scaling relationship on both observed flow phenomena and shear stress development in the flow. The CC-75 concentric cylinder system is shown in Plate 3.1. The concentric cylinders are clearly comprised shown as (2), and they can be independently rotated by two servomotors indicated here as (1) for the inner cylinder and (3) for the outer cylinder. Whilst some work was performed using independent cylinder rotation, the focus of this study has been on inner cylinder rotation only, however it is envisioned that future work will employ outer rotation. The reason for this is that the rheometer on which the working bioreactor is based only provides for inner cylinder rotation; the outer cylinder is fixed stationary.

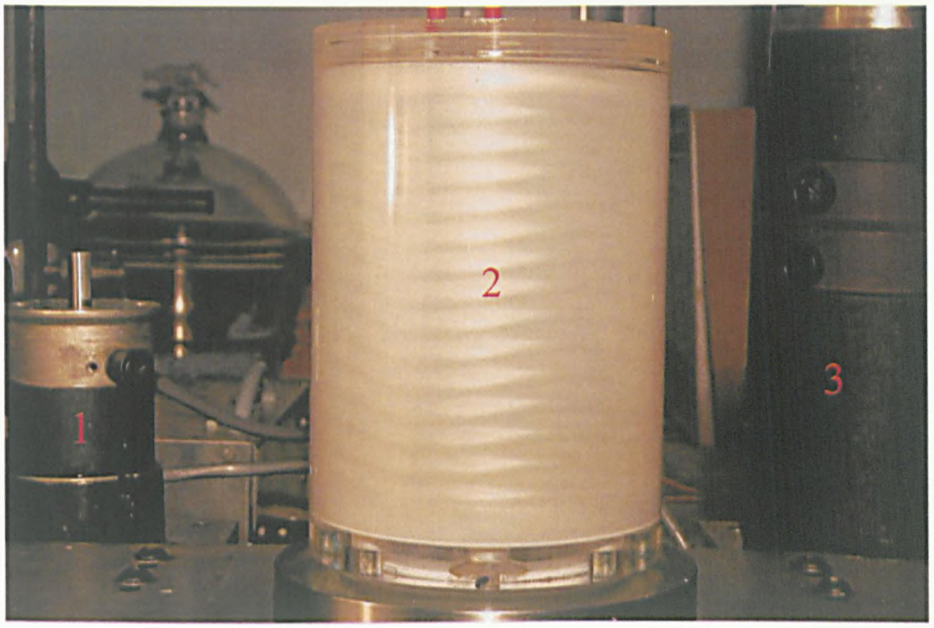

Plate 3.1 Concentric Cylinder System CC-75

The major difference in the design of CC-75 and CC-25, apart from scale, is to the inner cylinder of CC-25 where a conical section is cut into the base of the cylinder. This modification is to replicate the shape of the inner cylinder of the rheometer. It allows for near exact replication of the flow phenomena in CC-25 and in the working bioreactor. This conical section in fact has no substantial bearing on the flow in the annulus given the aspect ratio of the system, however replication has been made as an a-priori matter of caution given the possible anomalies from end effects described in Chapter 2. The conical section provides a uniform stress in the lower end of the system. The cylinders for the rheometer, here referred to as CC-25RS, and the cylinders of the experimental system CC-25 are shown together in Plate 3.2.

Plate 3.2 Concentric cylinders of CC-25 and CC-25RS

In Plate 3.2 the outer cylinder of CC-25 for the experimental flow visualisation system is (1) and the inner cylinder is (2). The components of the rheometer, CC-25RS, are the inner cylinder (3) and the outer cylinder (4). The internal fluid volume is maintained between the systems, as are the aspect ratio and other geometries pertinent to the hydrodynamics that develop for cylinder rotation. This means that flows characterised in the system CC-25 can be replicated in the system CC-25RS with good accuracy. The scale-up of the cylinders for CC-25 and CC-75 is shown in Plate 3.3 with the outer cylinder of CC-25 shown as (1) and the outer and inner cylinders of CC-75 as (2) and (3) respectively.

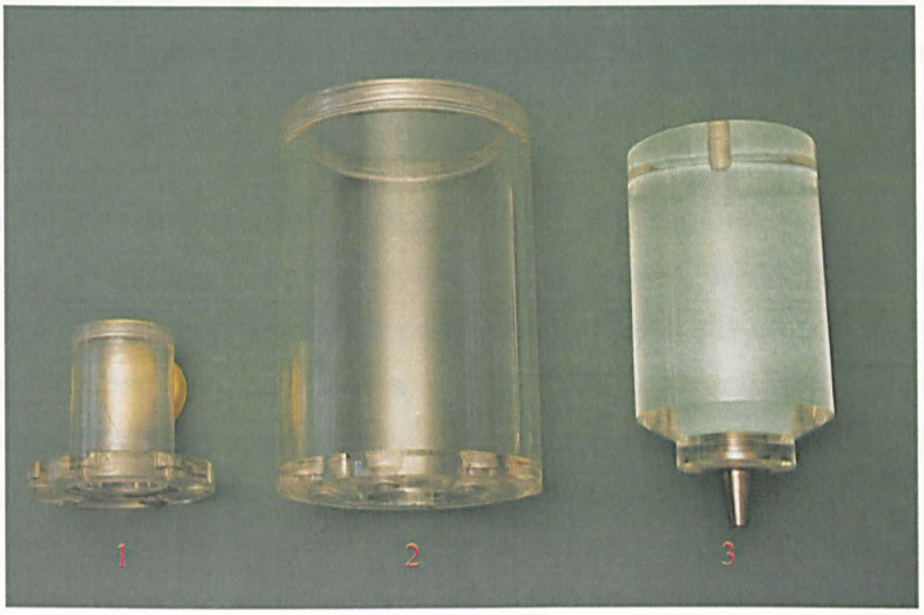

Plate 3.3 Scale-up for Cylinders of CC-25 and CC-75

The concentric cylinders for CC-25 and CC-75 have been machined in-house and are of heat treated cast polymethylmethacrylate (RS Components, UK). The system is so designed that either CC-25 or CC-75 can be mounted onto the same manifold which supports the motors and driving mechanism. This is illustrated in Plate 3.4 supporting CC-75. The cylinders can rotate independently from a rotating pulley system located from below the cylinders shown as (1) in Plate 3.4. The inner cylinder is fixed to a rotary steel shaft whist a second hollow steel shaft encloses this and is fixed to the outer cylinder. The rotary bearings and shafts for both cylinders are encased in a stainless steel housing (2). The pulleys for each cylinder are rotated independently using two servomotors. The outer cylinder is driven by an Electrocraft Max 650 DC driven servomotor and the inner cylinder is driven by an Electrocraft Max 250 DC driven servomotor (Electro-Craft Ltd, UK). The speed of the motors is controlled by varying the applied voltage to the servomotor using a personal computer OS/2 and a digital-analogue

conversion card (Brainboxes, UK). The software for speed control is written in Microsoft Quick Basic and is provided in Appendix A. The software allows for initial and final voltages to be specified along with a voltage ramping rate, independently for each cylinder. The speeds of the motors are accurately determined using a microprocessor tachometer No. 622-543 (RS Components Ltd., UK). Potentiometer circuits on the voltage supply box can be used to compensate for voltage drift of the motors, especially for establishing zero speed. The two motors, pulley system, cylinders and rotary housing are mounted on a steel supporting frame which sits on a steel board with a thick rubber foam layer. This is used to dampen any vibration of the system when operating at high speeds. Finally the whole system is bolted to an optical table to further remove any vibrational disturbances.

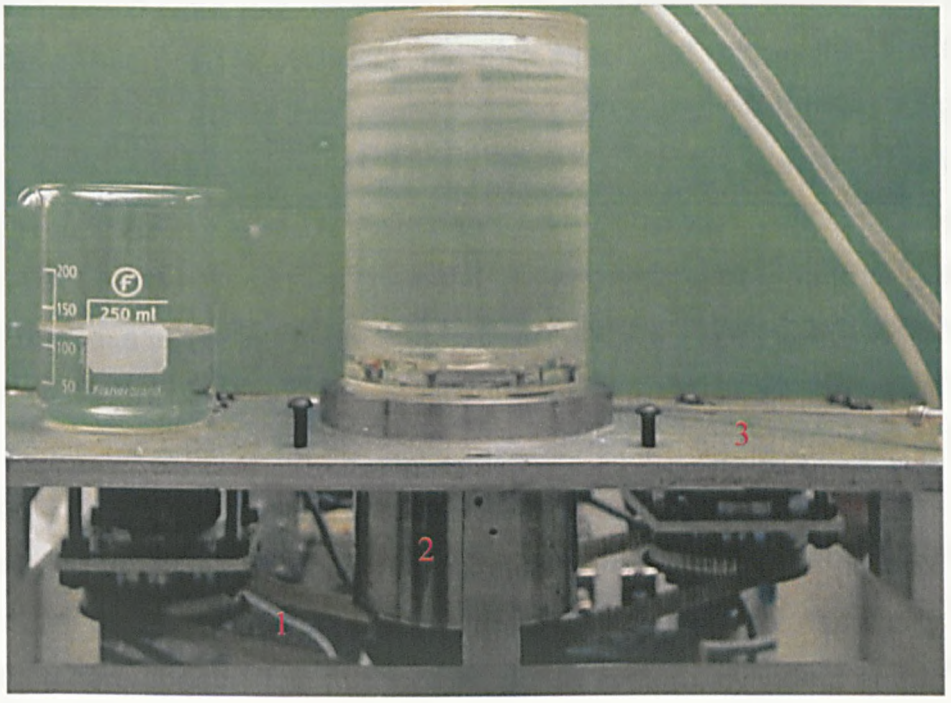

Plate 3.4 Manifold for Concentric Cylinder Rotation

3.3 Experimental Observations on Flow Transition

Experimental flow visualisation in the systems CC-25 and CC-75 has been achieved using a working fluid of water seeded with 0.2wt% Titanium dioxide particles (Timiron Supersilk, Merck, UK) filtered to a mean particle diameter of 8μm. A mercury lamp was used as an illumination source and a megapixel digital camera (Canon Power Shot Pro 70, Canon UK) was used to capture the images. Some of these images are presented in Section 3.3.2 to accompany a description of the flow whilst a complete series of images is presented in Appendix C for flows in the system CC-25.

3.3.1 Speed Calibration and Rotation Protocol

In Chapter 2 it was illustrated from the work of Coles (1965) that the final hydrodynamic state was dependent on the path taken to reach it and the rate of acceleration of the cylinders played a significant role in this. In the experiments carried out in this study, speed is controlled by the supply voltage to the servomotors driving the cylinders. In the first instance then, a calibration chart of voltage versus speed was generated. The cylinders rotate from the same mandrel at the base of the manifold in Plate 3.4(2) and frictional forces are imparted on one cylinder by the rotation of the other. Whilst every effort was made to make this as frictionless as possible this artefact could not entirely be removed and had to be accounted for in the calibration. In addition, it was observed that there was an inertial effect on the speed of the rotation of the cylinders when the motors ran freely and when the drive belts were fitted. This was also accounted for in calibration. Fortunately, the quantitative measurements made on annular flows were based on inner rotations only and this removed some of these problems. Calibration charts of speed-voltage are shown in Figures 3.4 and 3.5.

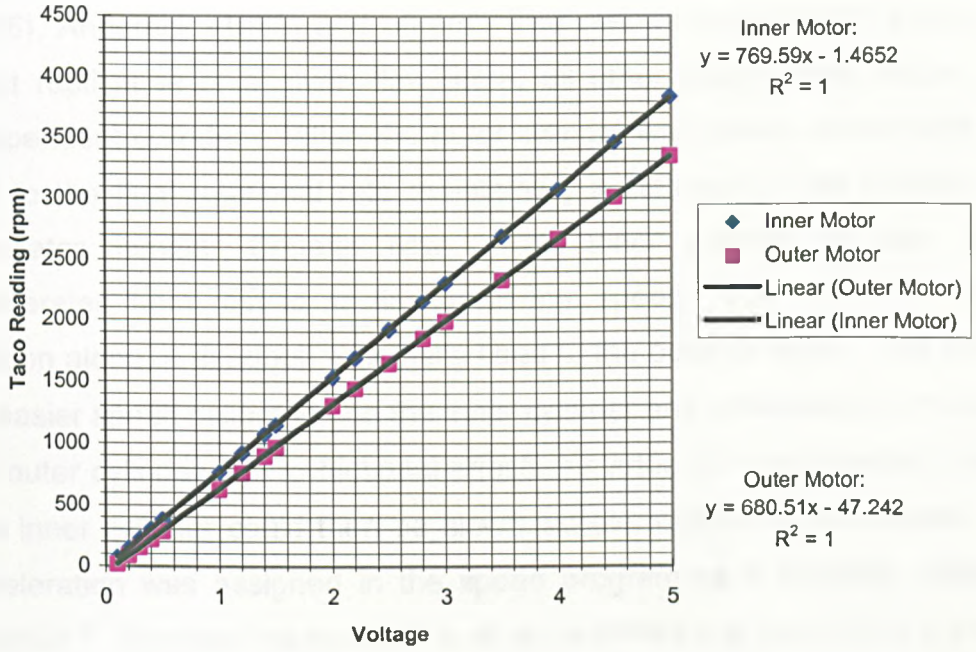

Figure 3.4 Speed Calibration of Servomotors with Detached Drive-belts

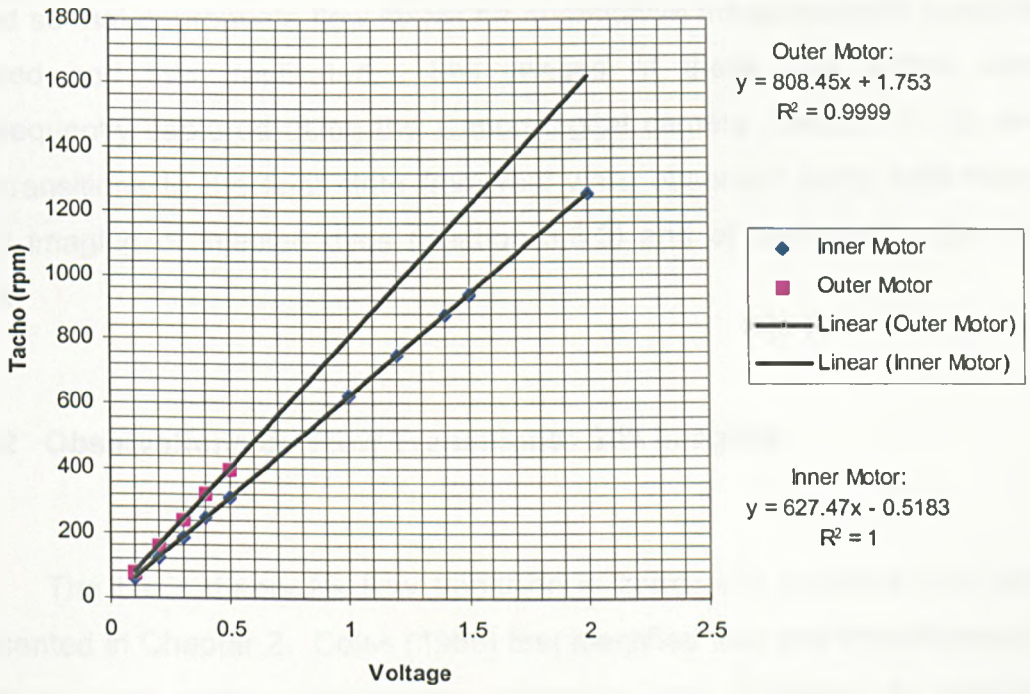

Figure 3.5 Speed Calibration of Servomotors with Drive-belts Attached

The protocol followed for cylinder rotation followed a thermodynamic pathway away from thermodynamic equilibrium ($\Omega_i=\Omega_o=0$) as used by Coles (1965), Andereck (1986) and others. The well-prescribed path allowed for exact replication of a given flow state, all other things being equal. For independent cylinder rotation the outer cylinder was slowly accelerated from rest to the final rotational rate maintaining a stationary inner cylinder; this generates laminar Couette flow. The inner cylinder is then slowly accelerated from rest to its final rotational speed. For the case of inner rotation alone, a deadbolt was firstly fitted to the outer cylinder. This allowed for easier speed calibration on the inner cylinder and prevented any motion of the outer cylinder due to frictional effects by virtue of inner cylinder rotation. The inner cylinder could then be slowly accelerated to its final speed. The acceleration was assigned in the speed program as a ramping voltage of $0.001Vs^{-2}$. This was maintained for all experiments and was found to provide a sufficiently slow acceleration that all of the flow transitions reported (e.g. Andreck (1986)) could be realised and reproduced. In the first instance, video imaging of the flow was made with a video camera and transferred to VHS tape for a range of rotational speeds for both inner and outer rotation. The speeds of rotation associated with a given flow state on the tape was noted so that appropriate flow states for quantitative measurements could be studied and then replicated. Still images of these flow states were subsequently captured using the Canon digital camera (Section 3.3.2) and the transitions to the final state from rest were observed using high-speed CCD imaging of injected dyes (Section 3.3.3) and of particulates (Section 3.3.4)

3.3.2 Observations on Flow Transitions: Still Imaging

The basic theory for flow transition in concentric cylinders has been presented in Chapter 2. Coles (1965) first identified that two distinct types of transition can occur; catastrophic transition and transition by spectral evolution.

3.3.2.1 Transition by Spectral Evolution

Transition by spectral evolution takes place when the inner cylinder rotation rate exceeds the outer cylinder rotation rate and the most general case of this, which has been widely investigated, is the condition of the outer cylinder at rest and only the inner cylinder rotating. The flow is laminar and circumferentially stable up to a certain speed of inner cylinder rotation for a given geometry. This is Couette flow and is shown for CC-25 in Plate 3.5(a). As the speed increases, the primary hydrodynamic transition occurs to Taylor-vortex flow in Plate 3.5(b). This occurs at the critical Taylor number where secondary flow phenomena are superimposed on the primary Couette flow and counter rotating toroidal vortices that are periodic in the axial direction are observed. According to Savas (1985), the dark areas are the sinks and indicate radial inward motion of the particles. The thin dark lines are the sources indicating radial outward motion of particles and the light areas indicate particle motion in the azimuthal direction. The Taylor-vortex flow is represented schematically in Figure 3.6 where U_i is the rotational speed of the inner cylinder (Schlichting, 1987). With further increased speed, travelling waves which are periodic in the circumferential direction develop and become superimposed on the Taylor-vortex flow thereby producing a doubly periodic or wavy vortex flow phenomena, first described by Coles (1965). This is shown in Plate 3.5(c). With still further increases in speed, a modulated wavy vortex flow ensues (Plate 3.5(d)) as a result of higher modes being generated by harmonics of the two fundamental frequencies in the doubly periodic wavy vortex flow. A discrete spectrum to higher frequencies is achieved with continued speed increments and more complex stable flow structures form (Plate 3.5(f)), however on reaching this point several non-stable wavy vortex flows appear (Plate 3.5(e)). At sufficiently high speeds the sharp spectral lines become broadened and a continuous spectrum gradually reforms. This second continuous spectrum indicates featureless turbulent flow. In the larger scale system, CC-75, the structure of the vortices in the supercritical region is better observed. A series of images taken into the highly supercritical regime are shown in Plate 3.6.

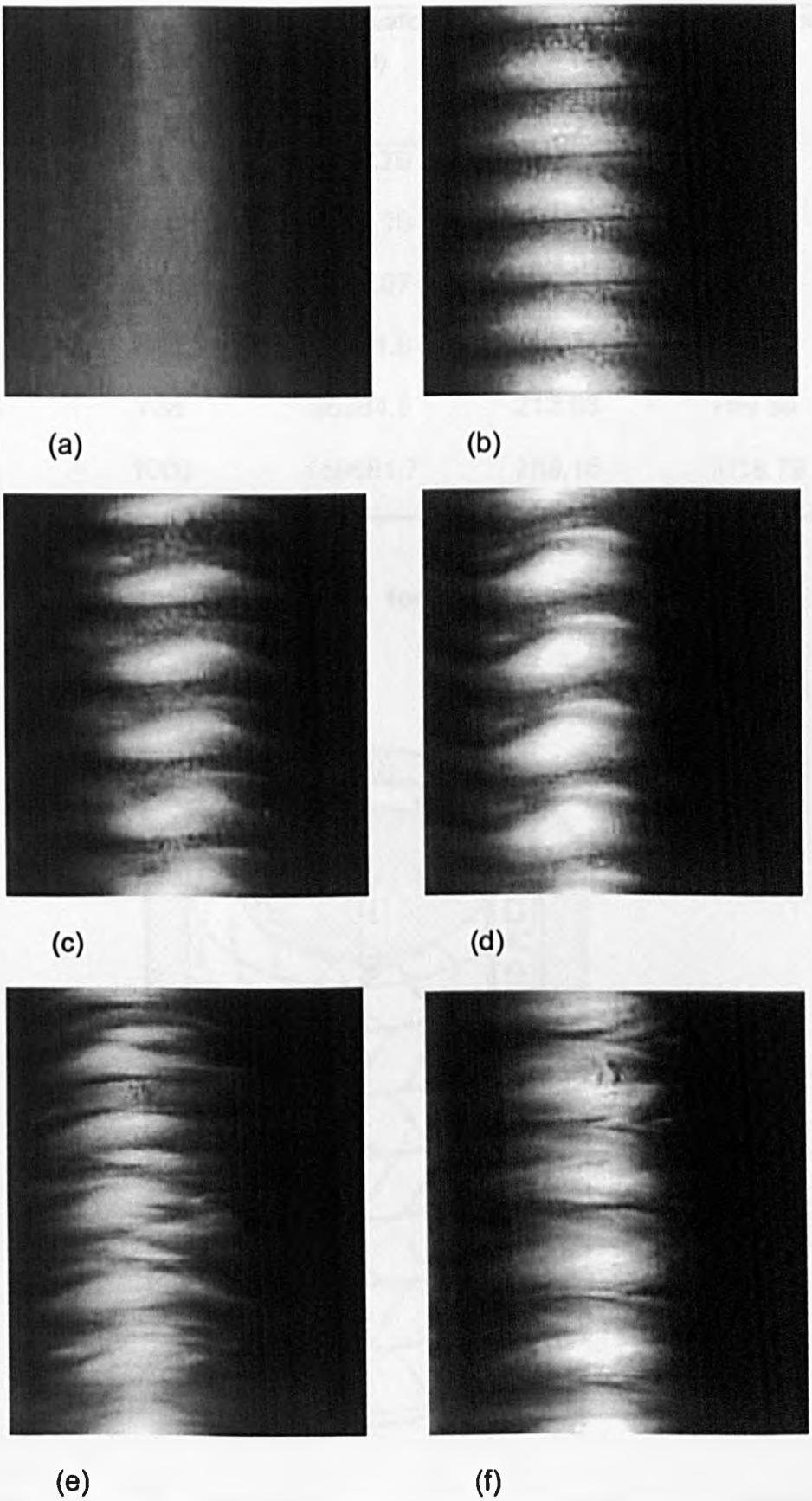

Plate 3.5 Selected Flow Visualisation Images for CC-25 and Inner Cylinder Rotation

Image from Plate 3.5	Estimated mean shear in rheometer (s^{-1})	Ta_{Ch} (equation 2.23)	Ta_i (equation 2.21f in Table 2.1)	Re_i (equation 2.22)
(a)	100	1597.76	28.82	101.91
(b)	130	2686.10	37.37	132.14
(c)	216	7453.07	62.25	220.10
(d)	400	25551.6	115.27	407.54
(e)	738	86984.5	212.68	759.30
(f)	1000	159681.7	288.16	1018.79

Table 3.1 Dimensionless Numbers for Flow Visualisation Images of Plate 3.5

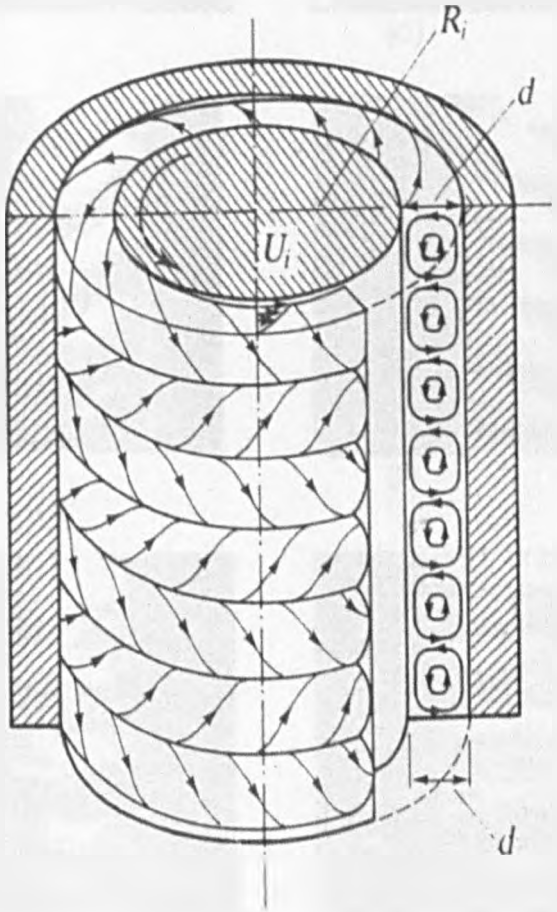

Figure 3.6 Schematic of Taylor-Vortex Flow (from Schlichting (1987))

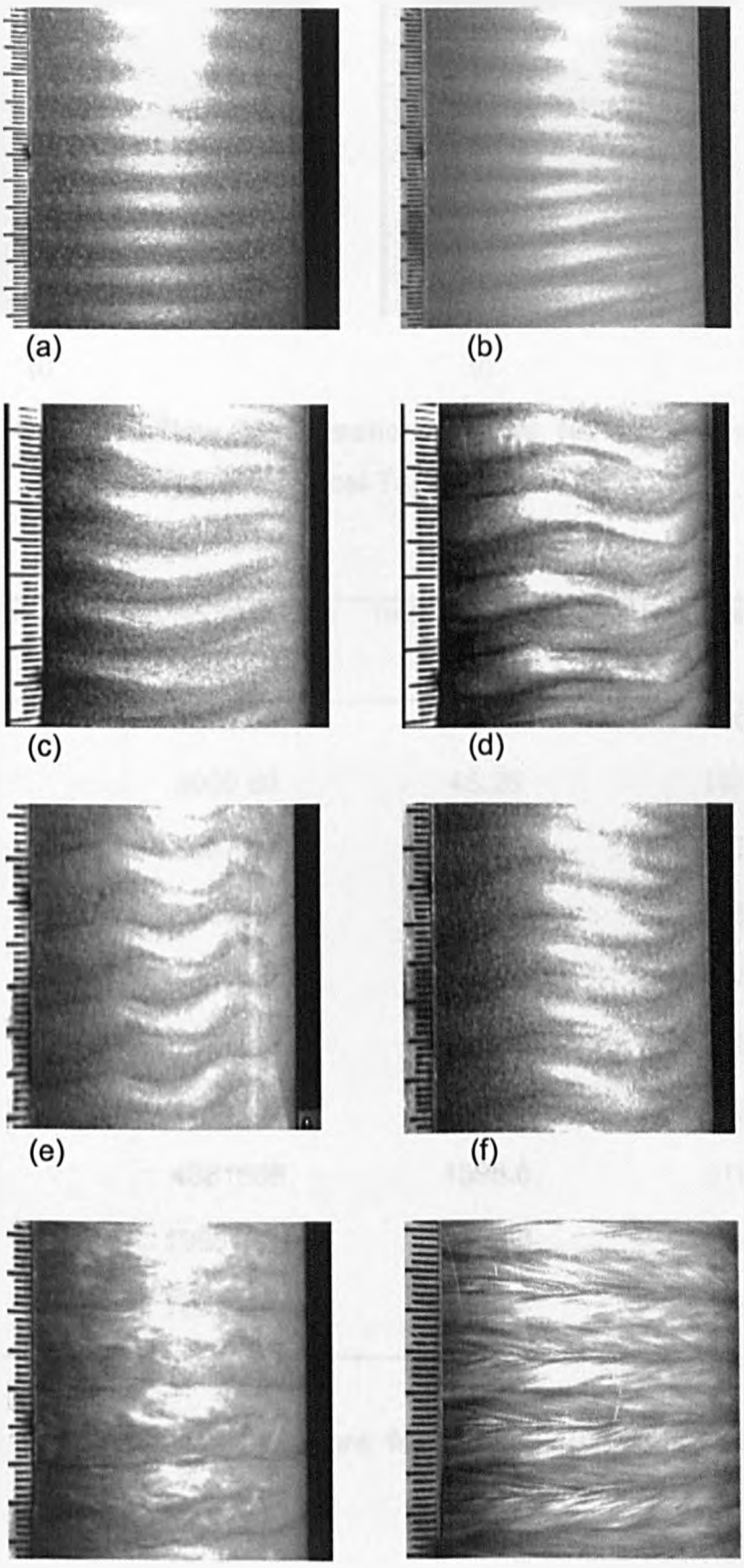
(a)
(b)
(c)
(d)
(e)
(f)
(g)
(h)

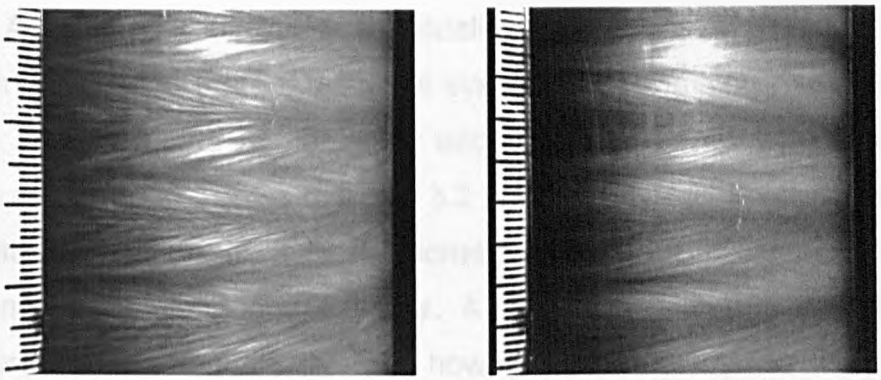

(i) (j)

Plate 3.6 Selected Flow Visualisation Images for CC-75 and Inner Rotation in Supercritical Taylor-Vortex Flow

Image from Plate 3.6	Ta_{Ch} (equation 2.23)	Ta_i (equation 2.21f in Table 2.1)	Re_i (equation 2.22)
(a)	3374.64	42.04	136.67
(b)	3909.68	45.25	147.12
(c)	5097.82	51.67	167.99
(d)	6443.37	58.09	188.86
(e)	55471.2	170.43	554.14
(f)	91240.3	218.58	710.69
(g)	1211105	796.36	2589.3
(h)	4881668	1598.8	5198.4
(i)	19601381	3203.8	10416.7
(j)	78555166	6413.7	20853.3

Table 3.2 Dimensionless Numbers for Flow Visualisation Images of Plate 3.6

Associated with the flow visualisation images of Plate 3.5 for the system CC-25 and Plate 3.6 for the system CC-75 are calculated values of Taylor and Reynolds numbers for each of the flow conditions illustrated. These are given in Tables 3.1 and 3.2 respectively. The values have been calculated based on the system geometry, the mean fluid rheology and the rotational speed of the inner cylinder. A number of definitions exist for Taylor number, as illustrated in Table 2.1, however in this study the Taylor number has been defined either as Ta_{Ch} from equation (2.23) or by using the form of the Taylor number used by Rudman (1994) given as equation (2.21f). The reason for this is that this is a definition for inner cylinder rotation only, and since the quantitative measurements of this study apply solely to inner rotation it is an appropriate choice. The geometry of the system relevant to the flow is indicated in Figures 3.1 and 3.2 and the key parameters assisting in calculations are summarised in Table 3.3.

	CC-25	CC-75
r_i (m)	0.0125	0.037
r_o (m)	0.0135	0.0405
d (m)	0.001	0.0035
d/r_i	0.08	0.0946
Γ	35	32.86
η	0.926	0.914

Table 3.3 Geometric Parameters for Systems CC-25 and CC-75

The rheology of the fluid has been found to be weakly non-Newtonian[+] for a 0.2 wt% suspension of Timiron particles in water. The viscosity increases slightly over the shear rate range measured under laminar Couette flow conditions using CC-25RS cylinders. A mean fluid kinematic viscosity of

[+] observed under laminar flow conditions. Secondary flows provide additional stresses.

$9.89x10^{-7}m^2s^{-1}$ has been used over the range of rotational speeds measured. The fluid rheology is shown in Figure 3.4. A comparison to media at 37°C used in the functioning bioreactor (Chapter 8) is shown.

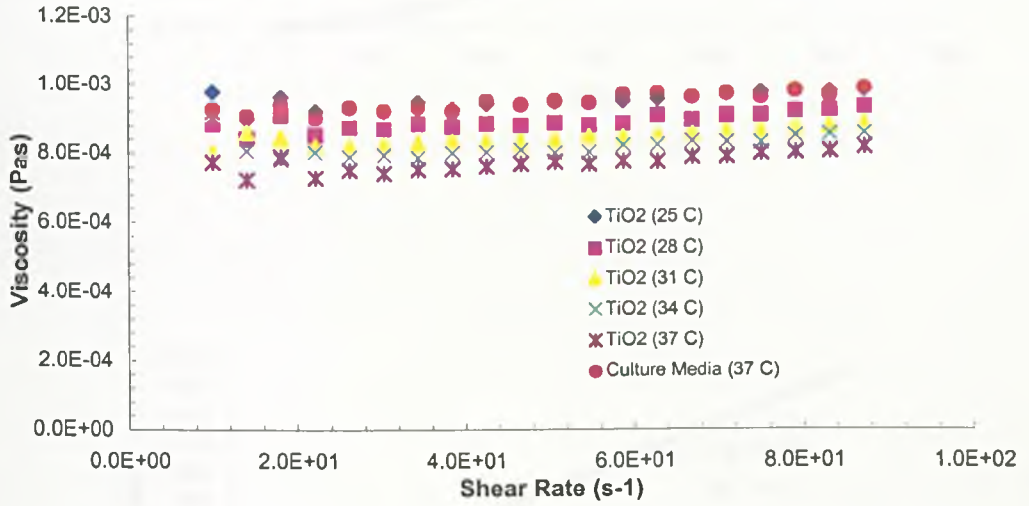

Figure 3.7 Rheology of 0.2 wt% Timiron-Water Solution

The relationship between the dimensionless numbers of Tables 3.1 and 3.2 is important. It was proposed in Section 2.3 that $Ta_{Ch} \propto Re^2$. When the definition of Taylor number changes it is likely that this relationship will change. The relationships between the three dimensionless numbers for the system CC-75 are shown in Figure 3.8. The same relationships are correct for the system CC-25.

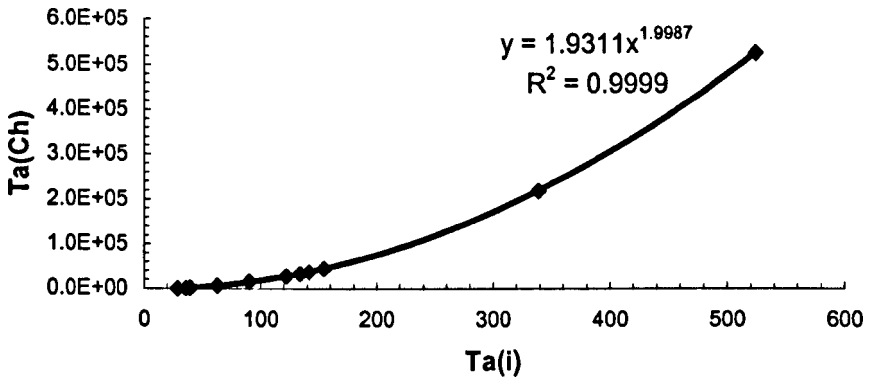

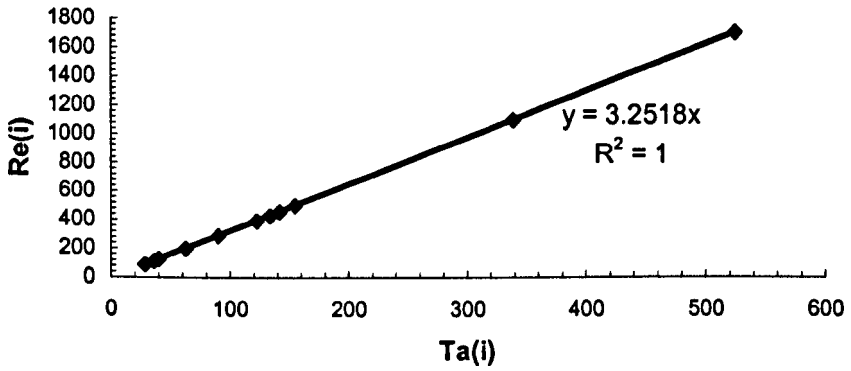

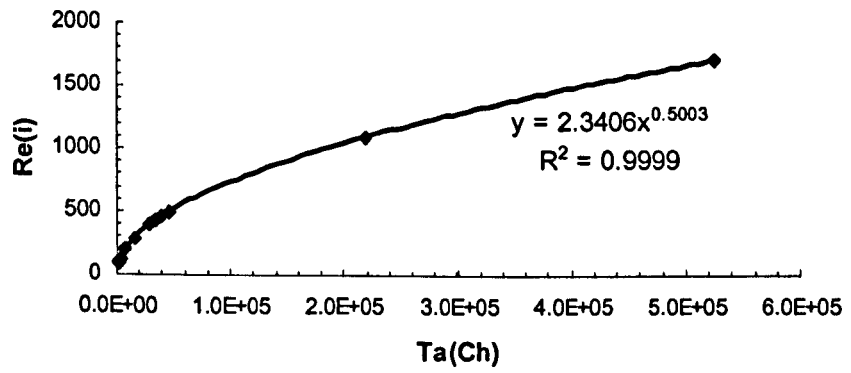

Figure 3.8 Relationship of Ta_{Ch}, Ta_i and Re_i for CC-75

3.3.2.2 Catastrophic Transition

Catastrophic transition from laminar flow to turbulent flow, as defined by Coles (1965), takes place when the outer cylinder rotation rate exceeds the inner cylinder rotation rate. A state of intermittency will be observed between the limiting laminar and turbulent regimes of flow where finite regions of laminar and turbulent flow coexist and distinct, well-defined interfaces between the two flow conditions are clearly visible. The interfaces themselves may be at points of transition from laminar to turbulent flow or vice-versa. The most clear cut case of intermittency is spiral turbulence. Here, a spiralling turbulent ribbon rotates through the predominantly laminar flow at approximately the mean velocity of the two cylinders. At certain speeds of rotation, intermittency is observed as turbulent spots or bursts in the predominantly laminar flow which randomly appear and disappear. The range of flow regimes that can be generated has been explored by Andereck (1986), mostly from flow visualisation studies. In this work, a map of flow states for combinations of inner and outer Reynolds numbers has been reproduced as Figure 3.9.

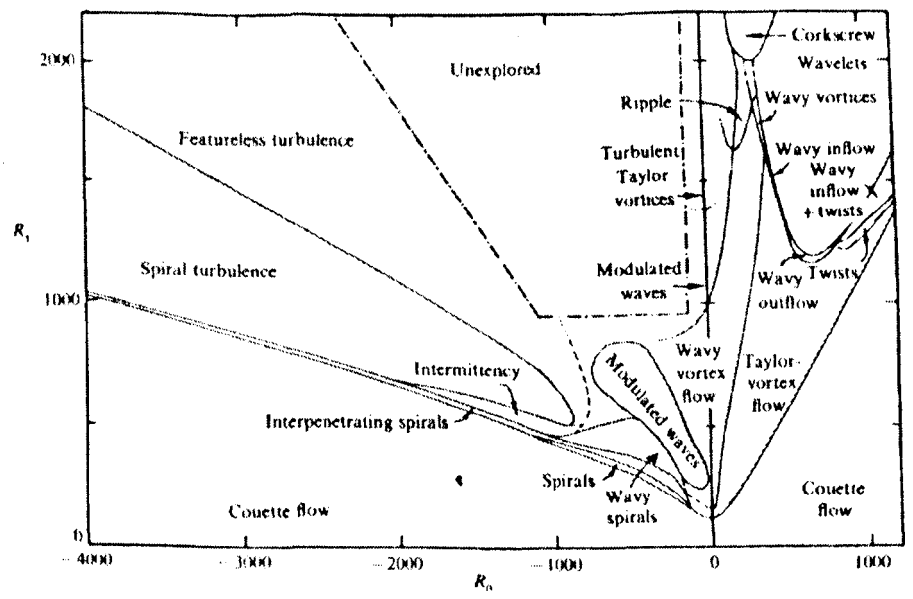

Figure 3.9 Attainable Regimes in Concentric Cylinder Flow (from Andereck (1986))

3.3.3 Observations on Flow Transitions: Dye Tracer Injection

Still Images of the steady hydrodynamic states in the concentric cylinder system are very useful for qualitative characterisation of flow structure and mixing efficiency and are presented in section 7.3. Since dispersion in wavy-vortex flow is much faster than laminar Couette or Taylor-vortex flow, little qualitative information can be gained on the behaviour of newly introduced fluid into the system at a prescribed hydrodynamic equilibrium. This is important when qualitatively assessing the mixing and mass transport potential of a given flow regime which is an important criteria in bioreactor design. To assess this, a series of sequential timed images have been captured using a high-speed CCD camera (HCC-1000, high resolution CMOS camera, VDS Vosskuhlner GmbH). The injected fluid was a black printing ink (Quink, Parker UK) and the fluid in the annulus was water. The ink density was measured as 1.294gcm^{-3} and to provide neutral buoyancy, the water density was increased by the addition of sodium chloride. Density data for sodium chloride solution at 25°C taken from Perry (1984) is shown in Figure 3.10.

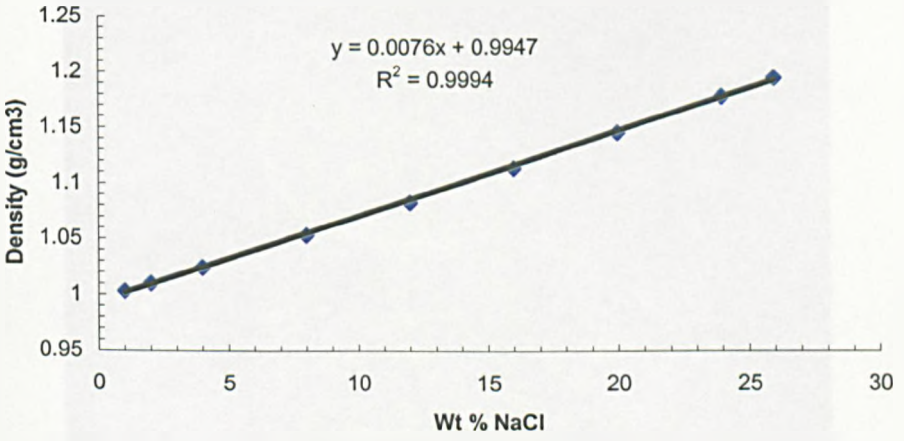

Figure 3.10 Density of Aqueous Sodium Chloride at 25°C

On this basis, a 39.38 wt% solution of sodium chloride was required to provide near neutral buoyancy of the ink.

CC-75 was modified to allow for dye injection into the annular space at a range of axial positions to investigate the effect of this on mass transport for a given flow regime. This is the subject of Chapter 7. The modifications to CC-75 are shown in Plate 3.7. The outer cylinder is stationary and a viewbox is fitted around two sides. The flat walls of the viewbox facilitated imaging with the high-speed camera. The camera was directed at one of the flat walls of the viewbox. The viewbox was slowly filled with distilled water to prevent air bubbles forming. In Plate 3.7 ports for filling/draining the viewbox are indicated as (1). A port for injection into the top of the annular gap is indicated as (2). Injection into the centre of the headspace is shown as (3) and a series of injection ports along the vertical axis of the annulus are shown as (4). For all dye tracer injection work, a 1 ml. syringe was filled with ink and was inserted into a selected port on the vessel. All other ports were blanked. For a range of different combinations of flow regime and injection location referral is made to Chapter 7.

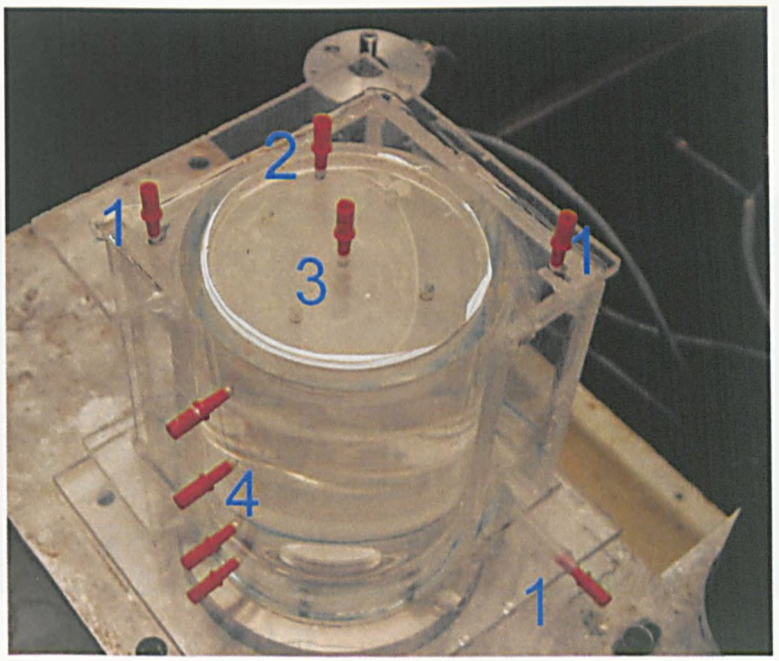

Plate 3.7 Modified CC-75 for Flow Transition Studies Using Dye Tracers

In this chapter, the effect of injection into two supercritical wavy vortex flows is presented.

3.3.3.1 Injection Into Wavy-Vortex Flow (Ta_i = 122.28)

The inner cylinder was rotated at the fixed slow acceleration of $0.001Vs^{-2}$ to a final output of 0.04V on the servomotor. This provided an inner cylinder rotational speed of 29.318 rpm. At this condition, Ta_i was 122.28 and Re_i was 397.59. This established a steady wavy-vortex flow regime. The flow was left for 20s to guarantee the equilibrium flow condition was established. The high-speed camera was set to collect images at 9 per second for 1024x1024 pixel resolution. This was initiated prior to injection. 0.5 ml. of dye was then injected quickly in one smooth movement into the flow. The elapsed time was recorded by the camera and allowed for a time stamp to be applied to selected images. Injection was made in the third port down from the top of the vessel into the annulus ((4) in Plate 3.7). A sequence of images for this flow condition is shown in Plate 3.9.

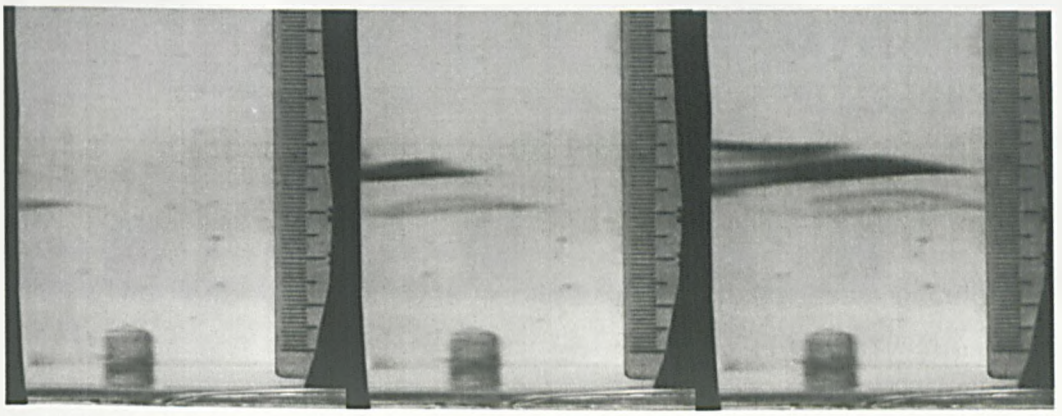

t = 1s t = 1.5s t = 2s

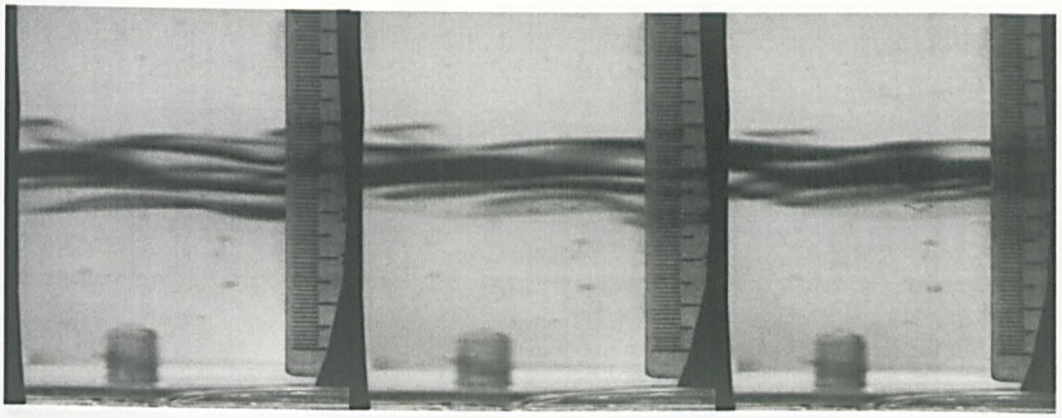

t = 2.5s t = 3s t =3.5s

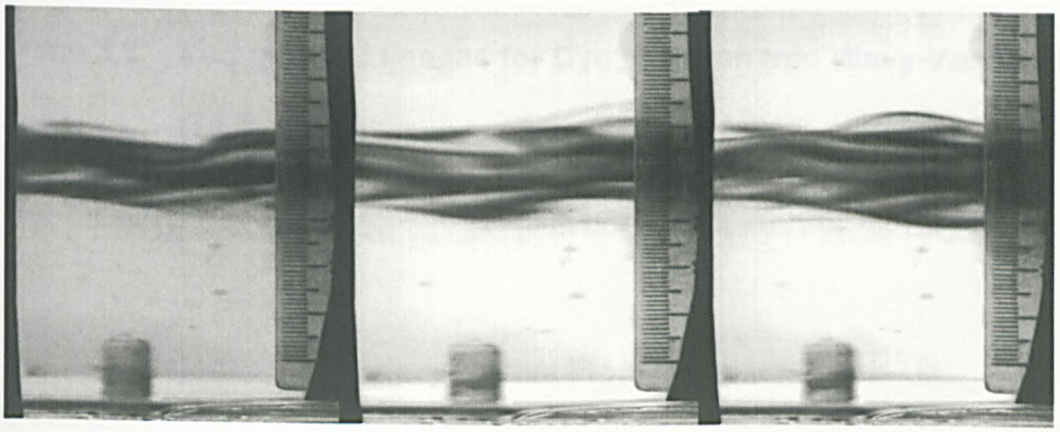

t = 4s t = 5s t = 9s

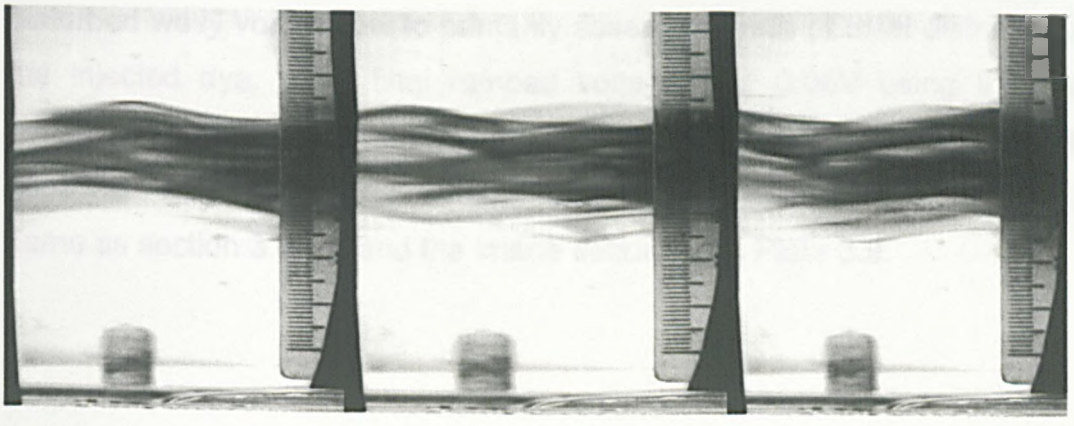

t = 11s t = 13s t = 15s

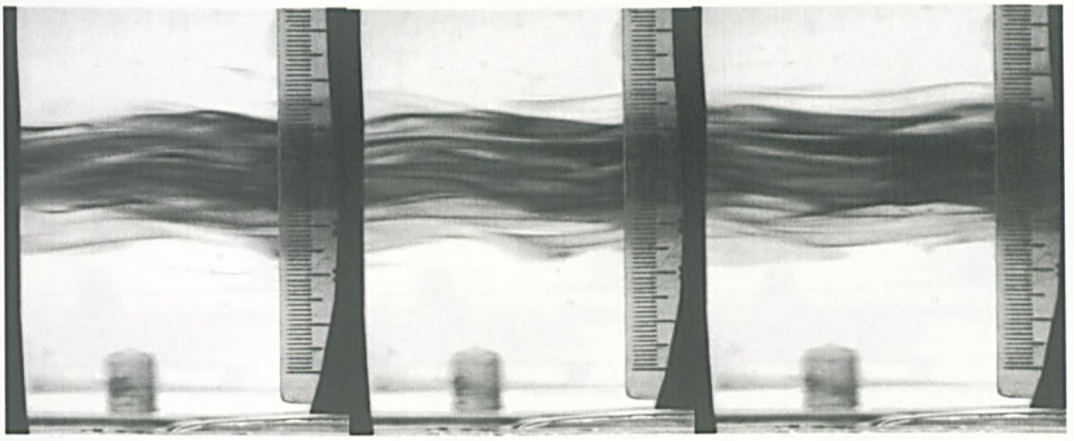

t = 18s t = 20s t = 22s

Plate 3.8 Sequence of Images for Dye Injection Into Wavy-Vortex Flow (Ta_i = 122.28)

3.3.3.2 Injection Into Wavy-Vortex Flow (Ta_i = 186.48)

The same experiment as in Section 3.3.3.1 was repeated for a more disturbed wavy vortex flow to primarily assess the rate of axial distribution of the injected dye. The final ramped voltage was 0.06V using the same acceleration and this generated an inner cylinder speed of 44.71 rpm. In this case Ta_i = 186.48 and Re_i = 606.32. The injection volume and location is the same as section 3.3.3.1 and the image sequence is Plate 3.9.

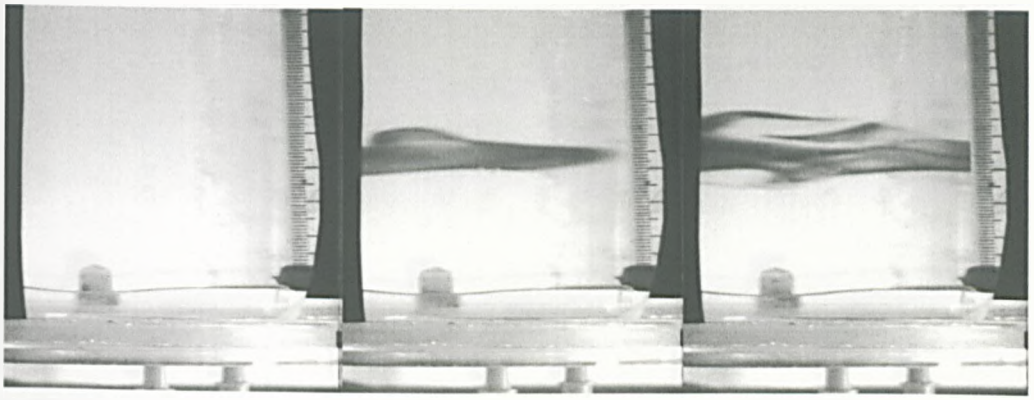

t = 0 t = 0.5s t = 1s

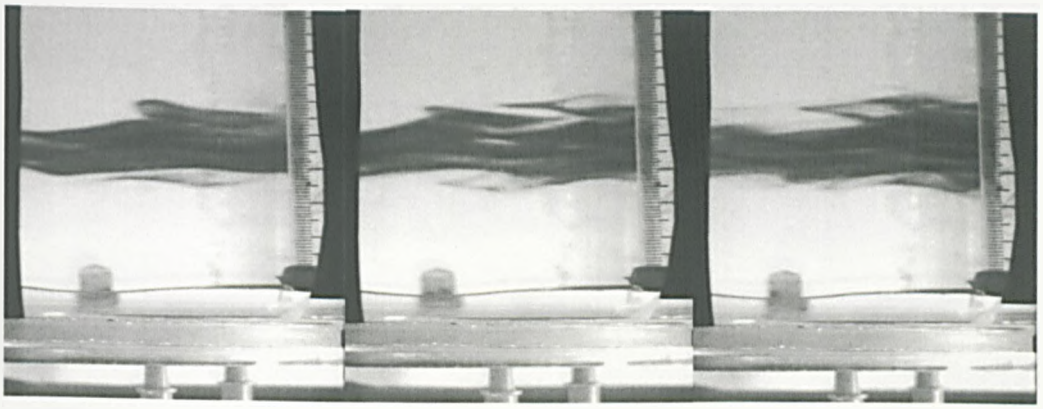

t = 1.5s t = 2s t = 2.5s

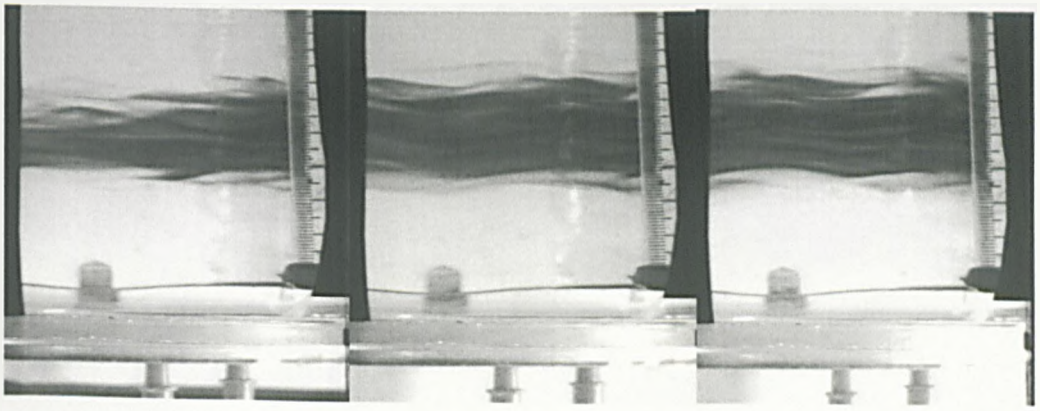

t = 3s t = 4s t = 5s

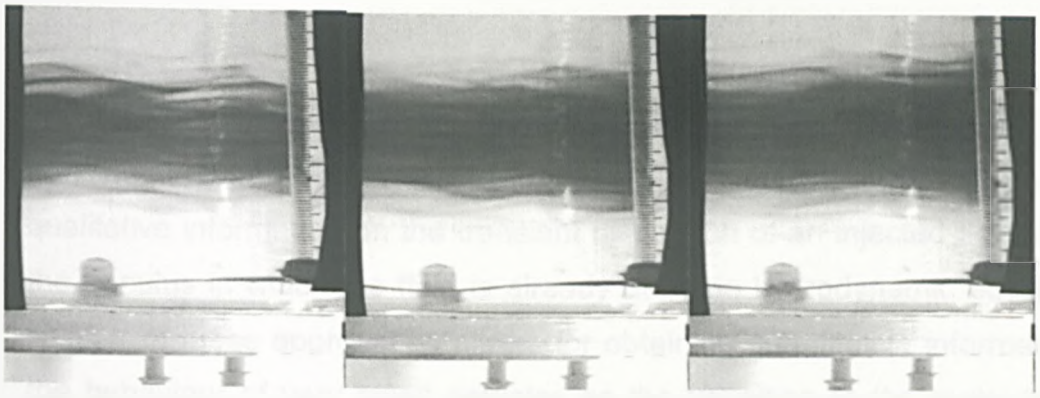

t = 7s t = 9s t = 12s

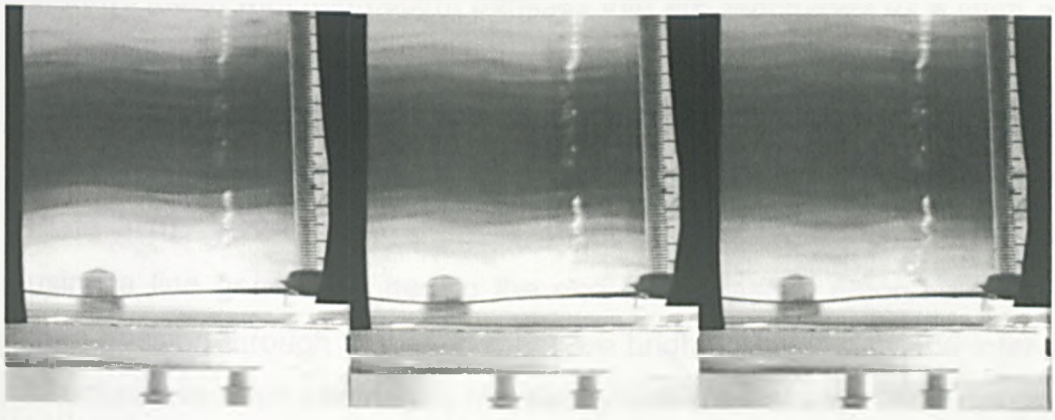

t = 18s t = 22s t = 35s

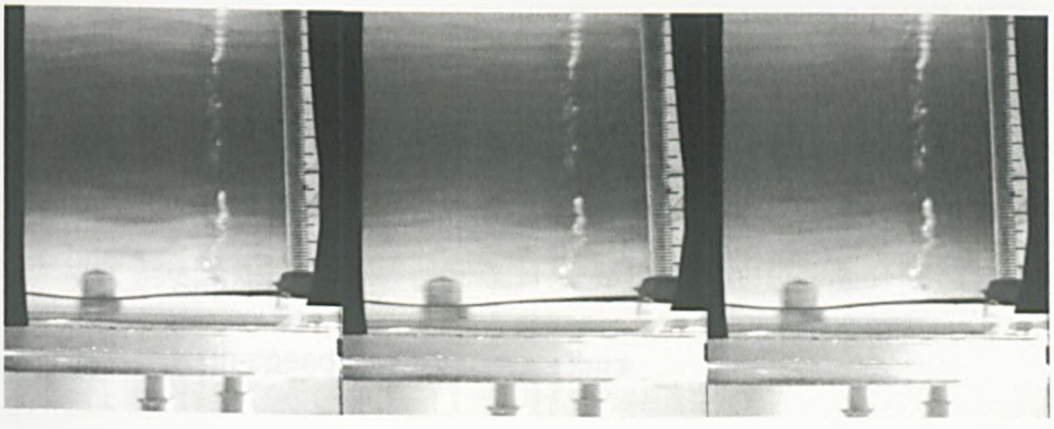

t = 40s t = 50s t = 60s

Plate 3.9 **Sequence of Images for Dye Injection Into Wavy-Vortex Flow (Ta_i = 186.48)**

3.3.4 Observations on Flow Transitions: Particulate Flows

Still imaging of flows as in Section 3.3.2 allows for good imaging of the flow at a hydrodynamic equilibrium and dye tracer injection gives good qualitative information on the transient dispersion of an injected solution into the annulus in which the fluid is already at some hydrodynamic equilibrium. Neither of these approaches allows for obtaining quantitative information on the behaviour of very small particles as the transition to the hydrodynamic equilibrium is made. This has been achieved using high-speed CCD imaging of flows laden with fluorescent particles that are illuminated by a laser source in the system shown in Plate 3.7. The particles used were Rilsan Blue and filtered to a mean diameter of 125μm. The laser source used is a 16mW He-Ne laser (Melles Griot 05-LHR-981). The experimental set-up is shown in Plate 3.10. A 2-D laser sheet is projected into the annulus of the vessel using a line generator fitted to the end of the laser. Fluorescent particles then passing through the laser sheet are brightly illuminated and inter-vortex structure can then be imaged transiently with the camera. The components of Plate 3.10 are:

1. Laser (with line generator)
2. CC-75 system. (The laser sheet is illuminated red)
3. Microprocessor tachometer components
4. Servomotor
5. High-speed CMOS camera lens

Images were collected again at the rate of 9 fps and 1024x1024 resolution and initiation was made prior to rotation of the inner cylinder. The inner cylinder was accelerated from rest to a prescribed speed and a sequence of images were captured to show particle behaviour in the flow as transition is reached. In addition it has been possible to generate file movies of the flow

for further qualitative analysis. Selected images captured for the flow condition 0.06V (Ta_i = 186.48) are shown in Plate 3.11.

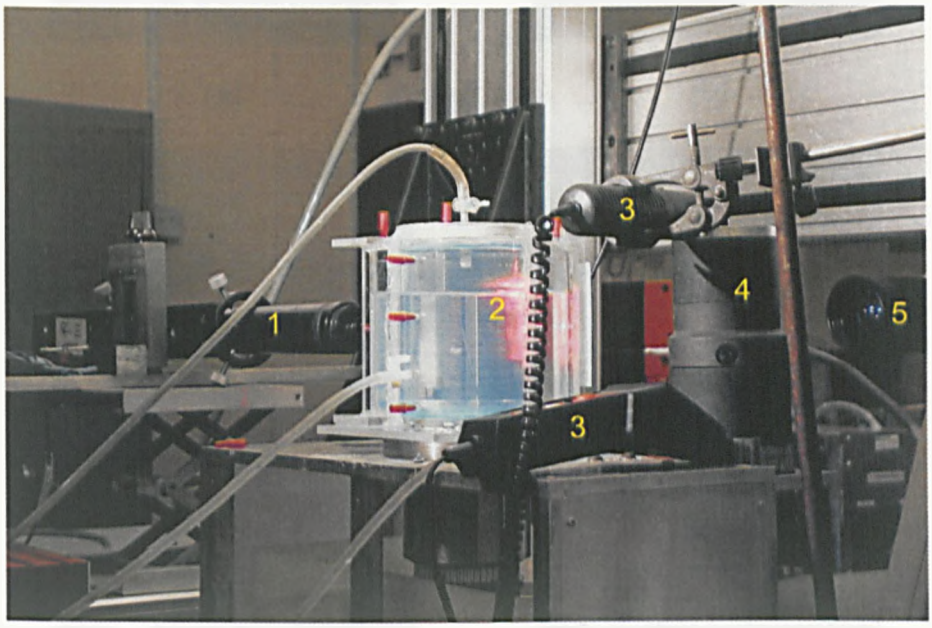

Plate 3.10 Particulate Imaging of Flows Using High-Speed CCD Camera and Laser Illumination

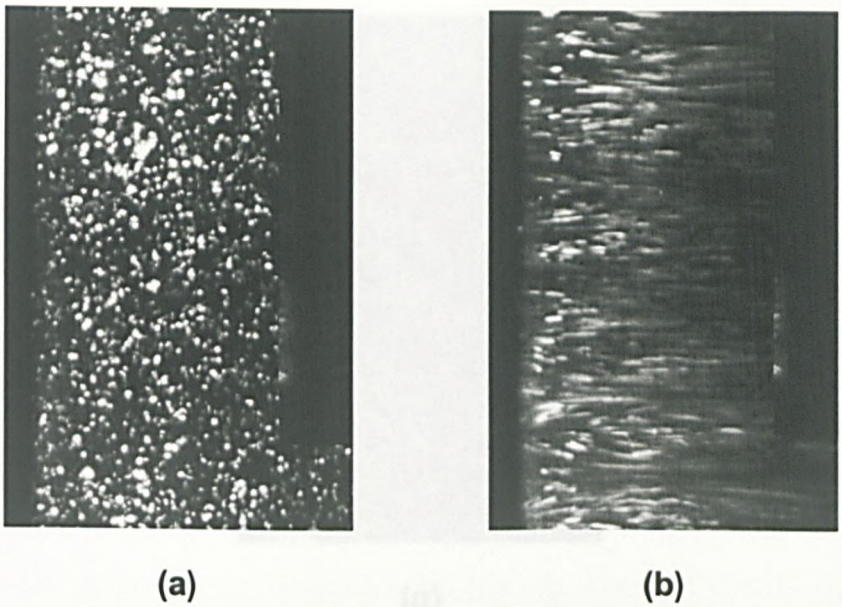

(a) (b)

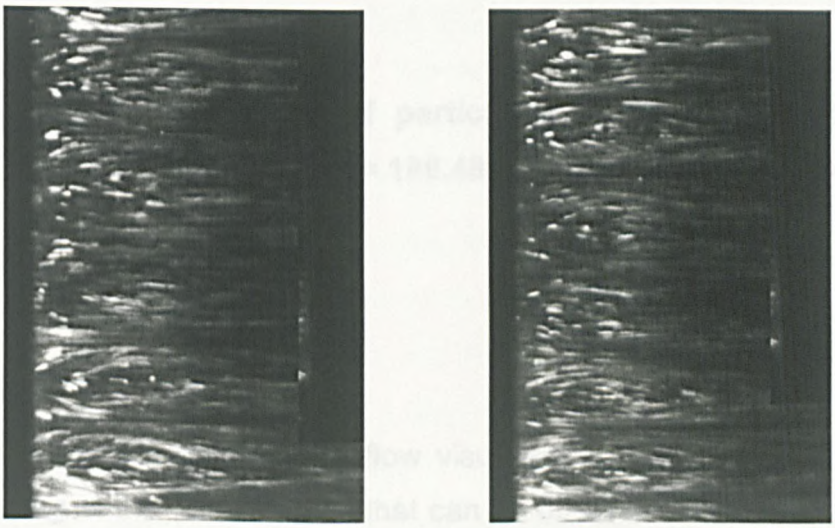

(c) (d)

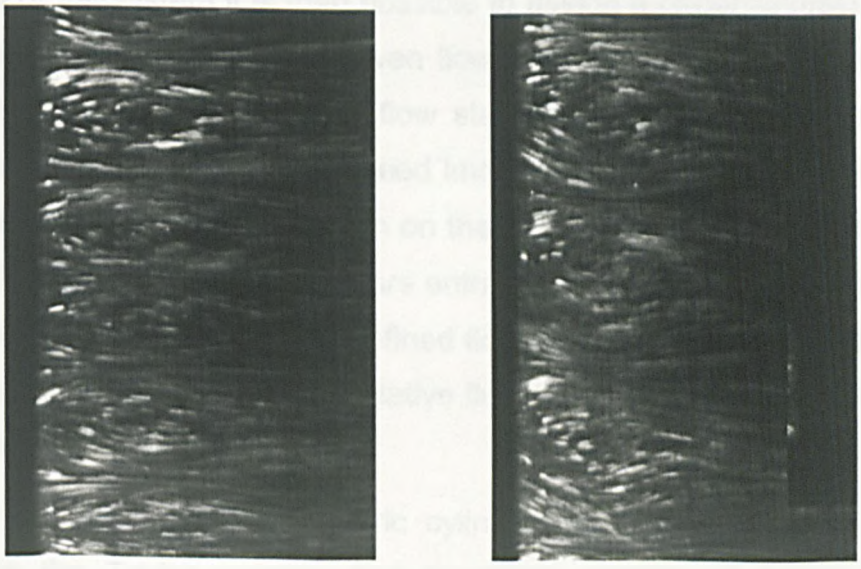

(e) (f)

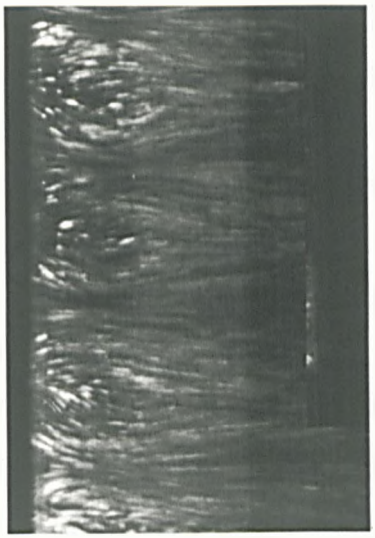

(g)

Plate 3.11 Selected images of particulate flows using High-Speed CCD Imaging at Ta_I = 186.48, from rest (a) to stable flow (g)

3.4 Concluding Remarks

The various techniques of flow visualisation used here allow for an understanding of the flow regimes that can be obtained in annular flow when only the inner cylinder rotates. With a knowledge of the rheology and geometry of the system it is then possible to assign a dimensionless number (Reynolds, Taylor) to indicate a given flow regime. Influencing factors such as acceleration rate on the final flow state can be qualitatively assessed using this approach. With high speed image capture it is possible to obtain some basic quantitative information on the transient dispersion of solute into a given flow and how particulates are entrained into the vortices that form. It is possible to then establish well-defined flow regimes in the flow at any scale of vessel and make detailed quantitative fluid mechanical and mass transport measurements.

In this study, two concentric cylinder systems have been used to determine the Taylor number and Reynolds number at which the flow transitions occur based on the system geometry, fluid rheology and rotational

speed of the inner cylinder. Theoretically, the Taylor number (Ta_i) for the primary transition from laminar Couette flow to laminar Taylor-vortex flow occurs at 42 using equation (2.21f) to define Taylor number. In CC-25, Ta_i = 37.37 and in CC-75 Ta = 42.04 for this primary transition. There is a small discrepancy between the two systems and neither one exactly matches the theoretical case. It is noted though, that the theoretical case is for a pure homogeneous fluid. In the studies performed here, the fluid is non-homogeneous with fine solid particles (TiO_2) suspended in water and this will serve to slightly deviate from theory. More importantly though is the need to maintain exact concentricity between the cylinders. Whilst every effort has been made to achieve this it is noted that the gap size in CC-25 is only 1mm. Concentricity of the rotating inner cylinder to maintain this 1mm gap has been checked using a dial test indicator. During the time of experiments for this study, the non-concentric rotation in CC-25 was found to vary between 25 and 75μm. This is approximately a maximum 8% of the gap size. Over time, the PMMA cylinders are subject to slight deformation. This non-concentricity is most likely to be the major contributor to the reduced Ta_i value at transition (Roesner, 1978; Mullin, 1982). In CC-75, the maximum measured non-concentricity by dial test indicator measurements was 90μm which is less than 3% of the gap size. In this case, it observed that the experimental Ta_i for the primary transition is a near exact match to the theoretically predicted value. It is concluded that non-concentric displacements of ≤ 3% of the gap size are advisable and this is more easily achieved as the gap width is increased whilst maintaining an aspect ratio greater than 20.

The flow visualisation studies performed here verify the findings of Andereck (1986),[+] in that there is very narrow window in which purely laminar Taylor-vortex flow can be achieved when only the inner cylinder rotates. This requires very careful and accurate control of the rotational speed of the inner cylinder to maintain the desired Ta_i particularly as the scale of the vessel increases when much slower speeds are required to simulate the same flow regime. In addition, the fluid rheology will contribute significantly to controlling Ta_i. Experimental flow visualisation studies performed at 25°C

[+] Refer to Figure 3.9

with 0.2wt% TiO_2 particles suspended in water have a near exact rheology to cell culture medium used to culture cells in a working bioreactor CC-25R at 37°C (Chapter 8), allowing for the flow condition to be reproduced at the same Ta_i in CC-25R as in CC-25 used for visualisation studies.

These studies allow for a-priori selection of defined flow regimes in concentric cylinders at any scale if the geometry and fluid rheology are known by applying a suitable inner cylinder rotational speed. This is particularly advantageous when it is not possible to visualise the flow pattern in, for example, bioreactors constructed of PTFE or stainless steel. In addition to providing a defined flow regime, the high-speed image capture information obtained here can allow for estimation on the time required to reach steady state and the size, structure and behaviour of the individual vortices in systems of other sizes.

References

Andereck CD, Liu SS, Swinney HL, Flow Regimes in a Circular Couette System with Independently Rotating Cylinders. *J. Fluid Mech.* **164** 155-183 (1986)

Benard H, Les Tourbillons Cellulaire dans une Nappe Liquide. *Rev. Gen. Sci. Pure Appl.* **11** 1261-1271, 1309-1328 (1900)

Coles D, Transition in Circular Couette Flow. *J. Fluid Mech.* **21** (3) 385-425 (1965)

Lewis JW, Observed Structures in Rotating Cylinder Flows. *Proc. Roy. Soc. A London* **117** 388-406 (1928)

Perry RH, Green D, Perry's Chemical Engineers Handbook. 6th Edition. McGraw-Hill Inc. New York.

Mullin T, Mutations of Steady Cellular Flows in the Taylor Experiment. *J. Fluid Mech.* **121** 207-218 (1982)

Roesner PH, Hydrodynamic Stability of Cylindrical Couette Flow. *Arch. Mech.* **30** 619-627 (1978)

Rudman M, Thompson MC, Hourigan K, Particle Shear-Rate History in a Taylor-Couette Column. *ASME Fluid Eng. Div. (FED)* **189** 23-30 (1994)

Savas O, On Flow Visualization Using Reflective Flakes. *J. Fluid Mech.* **152** 235-248 (1985)

Schultz-Grunow F, Hein H, Beitrag zur Couettestromung. *Z. Flugwiss.* **4** 28-30 (1956)

Chapter 4

Laser Doppler Anemometry: Principles of Measurement

4.1 Introduction

A prerequisite in quantifying the numerous aspects of experimental fluid mechanics is a knowledge of the fluid velocity, ideally at all points in the fluid domain. In practical terms, the number of points at which velocity data can be determined is finite and this number is not only related to the resolution of the measuring instrument but also to the degree of accuracy required for the investigation. In many cases of engineering the fluid domain is large leading to large-scale flow structures, and so the spatial resolution requirement of the instrument may not be a problem. In biofluid mechanics however, knowledge of data at the cellular level is often desired meaning that a high spatial resolution is required. If the fluid domain is also large then a large number of data points may also be required. The selection of the probe type to measure the fluid velocity can be based on this criterium initially.

Fluid mechanical measuring probes fall into two basic categories, invasive (mechanical) probes or non-invasive probes. Non-invasive probes are normally a preferred choice since invasive probes may disturb the nature of the fluid motion being measured and thereby provide erroneous data to the true nature of the flow phenomenon that presides when the probe is

removed. Non-invasive probes tend to be more expensive than invasive probes however they are superior in systems where space is confined or where a flow environment exists which could be damaging to a mechanical probe such as a high temperature or corrosive flow. In bioengineering applications, sterility of the environment is normally a high priority so the use of a mechanical probe would require sterilisation of the probe and then appropriate installation whilst maintaining the sterile environment, and this can often be difficult and expensive.

Commonly used invasive and non-invasive probes for velocity measurement are described briefly.

4.1.1 Invasive (Mechanical) Probes

Pitot Tubes

These measure local velocities in the flow by measuring the difference between impact pressure and static pressure. The Pitot tube consists of an impact tube facing directly into the stream to measure impact pressure plus one or more sidewall taps to measure local static pressure. Both this and the Combined Pitot-static tube are limited in their range of usefulness and are sensitive to the angle of attack of the fluid. Disturbances upstream of the probe can cause large errors in measurement due to the turbulence generated and its effect on the static pressure measurement. Modifications to basic Pitot tube to overcome this include the impact tube for boundary layer measurements, shielded total pressure tubes which are less sensitive to the angle of attack and the reverse Pitot tube or pitometer which provides up to 40% more of a range of measurement than the standard type. All of these tubes still have the basic limitation of flow disturbance and slow response time.

Turbine Flowmeter

This consists of a rotating tube containing a turbine that is free to rotate on a shaft supported by one or more bearings and located on the centreline of the tube. Magnetic detection of the rotational speed of the turbine provides an indication of the flow velocity. This has limited use due to its size and interference with the flow and is typically limited to non-corrosive low temperature flows.

Vane Anemometer

An anemometer strictly refers to an instrument that measures gas velocities but is now generalised to encompass all fluids. The vane anemometer is specifically designed for gas measurements and operates, much like the turbine meter, using a windmill type arrangement whose rotational speed corresponds to the gas flow speed. The same limitations of this instrument apply as to those of the turbine flowmeter.

Current Meter

This instrument measures velocities in open channels (like rivers) and comes in two types, the cup meter and the propeller meter, both of which operate like the turbine flowmeter.

Hot Wire Anemometer

This generally comprises a fine platinum wire that is heated and exposed to the fluid stream being measured. Increased fluid velocity increases the heat transfer from the wire to the fluid cooling the wire and altering its electrical resistance. In the constant current anemometer changes in resistance relate to velocity change in the fluid whereas in the constant resistance anemometer changes in the current that are needed to maintain a constant wire resistance are indicative of the fluid velocity changes. The difference is only in electrical circuitry. This system works reasonably well for gas flows

and the use of very fine wires can minimise the effect of flow disturbance due to invasion. Although the response time is fast and might be well suited as an economical measuring technique the modifications to the probe for use in liquid flows are still unsatisfactory due to difficulties arising from bubbles in the flow or particles/debris adhering to the wire and then generating spurious results. In addition this technique is not well suited to very temperature sensitive systems.

4.1.2 Non-Invasive Probes

Magnetic Resonance Imaging

The MRI machine is essentially a large magnet with a large cylindrical bore through it. In medicine, the patient is positioned inside the bore where the MRI scan takes place. Whilst a profile of tissue types can be established with MRI (its common use), blood flow measurements can also be established. The MRI machine applies a radio frequency pulse specific only to the hydrogen atom through a coil. Protons in the region of the incident pulse are caused to spin, or resonate, and this is proportional to the strength of the magnetic field. The resonant frequency or Larmor frequency is measured and can be used to map a tissue or velocity flow field after application of Fourier transforms. The mapping region and magnetic strength is carefully controlled by three gradient magnets in the machine.

Doppler Ultrasound

Doppler ultrasound is used in medicine to detect and measure blood flows. Measurement is based on the Doppler effect and this is described later in this chapter. Briefly, a sound wave at a prescribed frequency is directed at the blood flow with a prescribed incident angle, and the reflector of the sound is the red blood cells in the flow. The change in frequency of the reflected sound is measured by the Doppler Ultrasound equipment and along with the other parameters mentioned, calculation of the blood velocity is made and recorded.

Particle Image Velocimetry (PIV)

PIV is a non-invasive optical technique to measure particle velocities in both gas and liquid flows. Tracer particles are added to the flow and simultaneous velocity measurement of a number of particles are made in the flow domain. The PIV measurement process involves the following steps:

- **Tracer particle seeding**
  Tracer particles are added to the fluid in the flow domain to track the fluid motion and provide a signal for software processing. The seeding particles are normally fluorescent, excited by the laser illumination of the flow domain.

- **Flow domain illumination**
  A flat sheet of laser light illuminates a slice of the flow domain. The seeding particles fluoresce or scatter the light depnding on the choice of particle. This light is detected by a camera placed in an orthogonal plane to the light sheet. The light sheet is pulsed twice over a known time interval (t).

- **Image acquisition**
  The first pulse of the laser freezes images of the initial positions of the seeding particles and this is captured as the first frame on the camera. The camera frame advances and the camera captures light scattered by the particles from the second light pulse. There are thus two recorded frames in the camera of particles in their initial position and in their position after time (t) due to the fluid motion in the flow domain.

- **Vector processing**
  Each of the camera images are divided into interrogation regions. Using a Lagrangian computation, the vector field is determined based on particle motion between two identical regions between the two camera frames.

The advantages of this system are that flow phenomena within the whole of the flow domain can be established quickly. Disadvantages are that the number of data points within each interrogation region may be small or insufficient depending on the particle seeding and it might also be difficult generating a flat light sheet in the flow domain of interest depending on the geometry of the system and the material of construction of the system.

Flow Visualisation

Particles can be introduced to the flow to provide a visual record of the flow phenomena in the domain as time progresses. The record can be made using still camera images or by the use of cinematography or high speed image capture. In any case, illumination of the flow domain is an important issue. The choice of seeding particle is also important. The particles should be of a density that matches the fluid such that sedimentation does not occur within the time frame of the experiment and the particles should be able to scatter sufficient light. Flow visualisation experiments have been described in detail in Chapter 3.

Laser Doppler Anemometry

Laser Doppler Anemometry (LDA) measures local fluid velocity from the change in frequency of radiation between a stationary source and receiver due to scattering by particles along the wave path. A laser is commonly used as the incident illumination source. Near instantaneous measurement of particle velocities through a fixed point in space is provided as a real time Eulerian velocity data set. The technique is essentially independent of temperature and pressure and can be used in a range of different flow systems with transparent fluids containing particles whose velocity is measured. The LDA system has no limitations in terms of the flow phenomena or the fluid environment unlike the hot-wire and hot film anemometers. Other advantages of the system are that the spatial resolution is very good and there is very good directional and positional reference with no variation of calibration factor. The major disadvantages of the system are

that good optical access is required to the measuring volume and that the velocity record is discontinuous. Since LDA has been the chosen method to quantify the experimental fluid mechanics of this study, the system will be described in detail.

4.2 The LDA System

The LDA system used in this work is a two component system supplied by Dantec Elektronik and represented schematically in Figure 4.1. The system is composed of three basic sections; laser light source, optical system and photodetector with other ancillaries.

The light source is a 100mW Argon-ion gas laser emitting a single beam. The special properties of a gas laser are its spatial and temporal coherence. The spatial coherence describes the ability of the light field to form interference fringes in space. It is related to the apparent source size or the number of transverse modes active in the light source. Gas lasers operate in the fundamental optical mode of the cylindrical laser cavity, called the TEM_{oo} mode. This means that the laser light may be focussed to the smallest possible spot and thus all the energy of the laser can be concentrated in a small measuring volume. The Argon-ion laser has the special capability of emitting only a single laser line (most emit a number of lines with interference) due to the insertion of a second resonant cavity (a Fabry-Perot etalon) in the laser tube.

The optical system contains beam splitters, various prisms for directing the beams internally in the optical system and front-end optics. The photodetector or backscatter receiver consists of a section containing a 45° mirror and photomultiplier tube optics with a pinhole spatial filter and an interference filter matched to the laser line.

The single laser beam from the argon-ion source enters the optical system and the beamsplitters separate it into six beams of three colours corresponding to the spectral peaks of the laser source. One pair of same

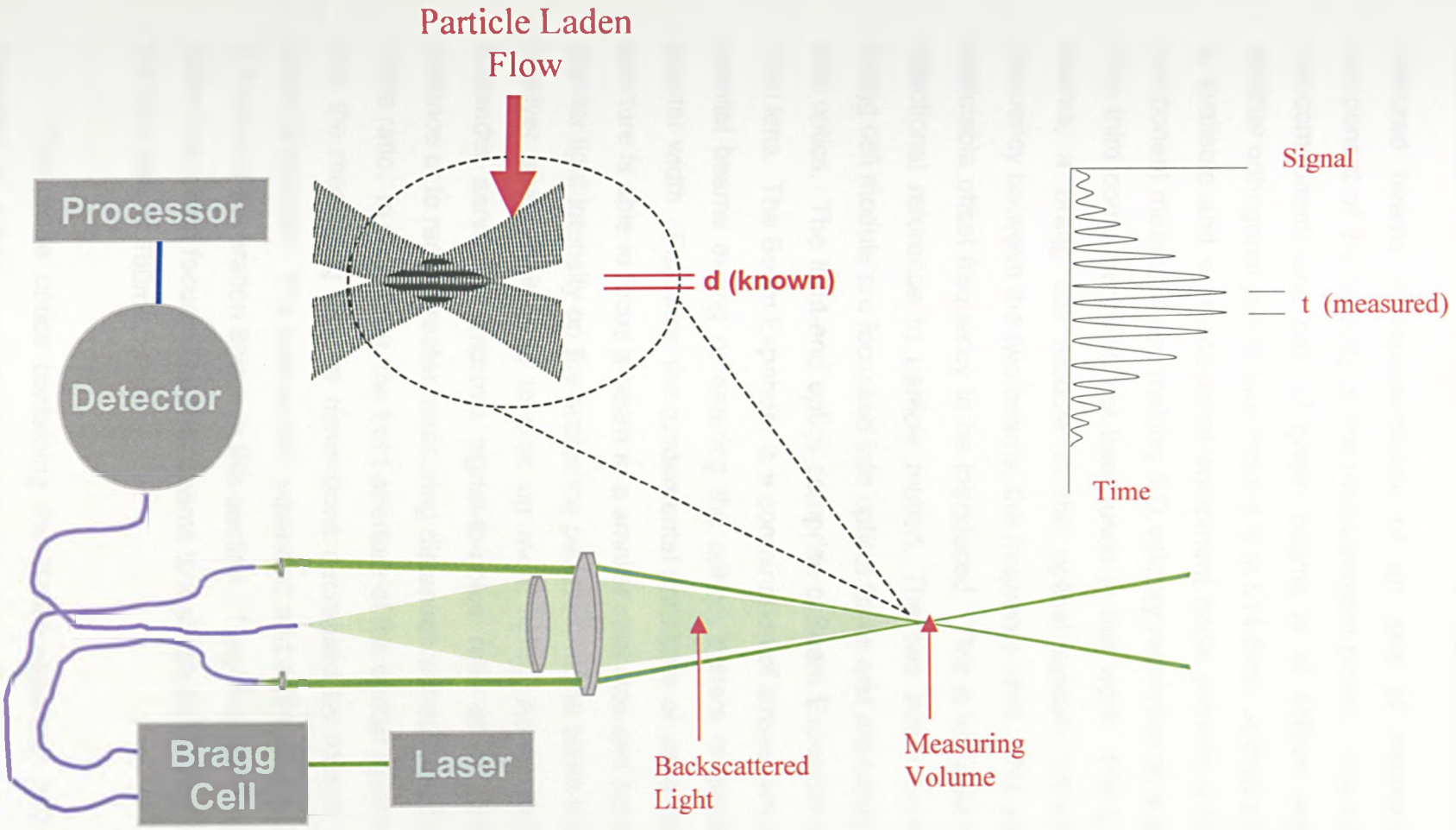

Figure 4.1 Schematic of Dantec Laser Doppler Anemometer

coloured beams is representative of an axis of measurement (or a component of the velocity at the measurement point). The system used is two-component; one pair of green beams is at 488nm wavelength and another orthogonal pair of blue beams is at 514.5nm. A third pair at 476.5nm is available and with additional equipment could provide a further velocity component measurement making 3-D velocity resolution at a point possible. This third component has not been used in this work. For a given pair of beams, a Bragg cell module in the optical system introduces a fixed frequency between the two beams, the *frequency shift*. This allows a stable, selectable offset frequency to be introduced. This is important for providing directional reference to particle motion. The two beam pairs leaving the Bragg cell module are focussed into optical fibres and are carried to the front-end optics. The front-end optics comprise a Beam Expander section and a front lens. The Beam Expander is a combination of lenses, which convert the parallel beams exiting or entering the optical system to parallel beams of greater width. Following the fundamental principles of wave theory, a larger aperture is able to focus a beam to a smaller spot size and hence to create a greater light intensity on the scattering particles, at the same time the greater receiver aperture is able to pick up more light. As a result, the Beam Expander serves to improve signal-to-noise ratio at a given measuring distance or to reach greater measuring distances without sacrificing signal-to-noise ratio. In short then, the front aperture of the optical system is increased and the measuring volume dimensions decreased by means of the optical Beam Expander. The beams are expanded and collimated at a diameter of 2.2mm and separation 85mm in this section. They then pass out through the main lens which focuses the four beams to a single point. The focal length of the front lens is 160mm.

The probe optics containing the Beam expander and front lens is mounted on a three way traverse system with a 12.5μm step size resolution in each direction. The light exiting the front lens of the optic probe takes the form of four beams, a pair of green beams and a pair of blue beams. The four beams are delivered to the front lens via four optical fibres. A given pair of beams lie in an orthogonal plane to the other pair. The intersection of two

beams of same colour forms an elliptical measuring volume. This measuring volume can be manoeuvered into the flow domain by means of the traverse. Particles in the flow scatter the incident light. Some of the backscattered light is collected back into the large front lens. This light is directed back into a fifth optical fibre via a further lens and enters a pinhole section that acts as a spatial filter. The scattered light passes through a colour separator to divide the combined scattered light into the two representative incident beams. The separate light sources are directed onto two photomultiplier tubes which act as detectors for each of the scattered light components. The photomultplier tubes are each energised by a high level voltage and this generates an electrical output current which is proportional to the square of the energy of the incident electro-magnetic radiation absorbed on the detector surface. The power of the signal is further enhanced with an adjustable gain amplifier.

The signal generated by the photomultiplier tubes is the Doppler frequency. This is proportional to the mean velocity of a particle as it passes through the measuring volume. Any noise in the signal is filtered out before signal processing occurs. Separate hardware units called Burstware Spectrum Analysers (BSA1 and BSA2) perform signal processing on the two light components separately using Fast Fourier Transform (FFT) algorithms. The output signal from each of the BSA's was interfaced with a personal computer via an IEEE interface. Software in the PC (Burstware) allowed for configuration/editing of the signal processing parameters and the traverse settings to control the probe optics. A large number of signals are generated for each traverse position in the flow domain. The number and quality of signals depends on the flow system, particle seeding, signal processing parameters etc. however for each traverse position the number of signals to be collected and the sampling time for collection can be set via the PC. A file is saved in the PC containing all the signals sampled for each traverse position. Subsequent processing of these files to generate velocity flow maps is performed separately using these files.

4.2.1 The Doppler Effect

The laser beam source for the probe optics described above provides an incident electromagnetic wave onto the seeded particles in the flow domain. The particles backscatter light to the probe optics but by virtue of their motion in the fluid flow. This backscattered light is considered as a moving wave source with a velocity vector $\{\hat{u}\}_i$.

The photodetector that receives this wave source can be considered as a stationary observer. The photodetector will then record a different wavelength from that emitted by the source as illustrated in Figure 4.2. This is due to the emitted waves occupying a space given by the distance

$$[c - \{\hat{u}\}_i \{\ell\}_i] \cdot t \tag{4.1}$$

whereas the equivalent distance for a stationary source is $c \cdot t$. The wavelength recorded from a moving source by a stationary observer is therefore

$$\lambda' = \frac{c - \{\hat{u}\}_i - \{\ell\}_i}{\nu} \tag{4.2}$$

Since $c = \lambda \nu$, the corresponding frequency is

$$\nu' = \frac{\nu}{1 - \frac{1}{c}\{\hat{u}\}_i \{\ell\}_i} \tag{4.3}$$

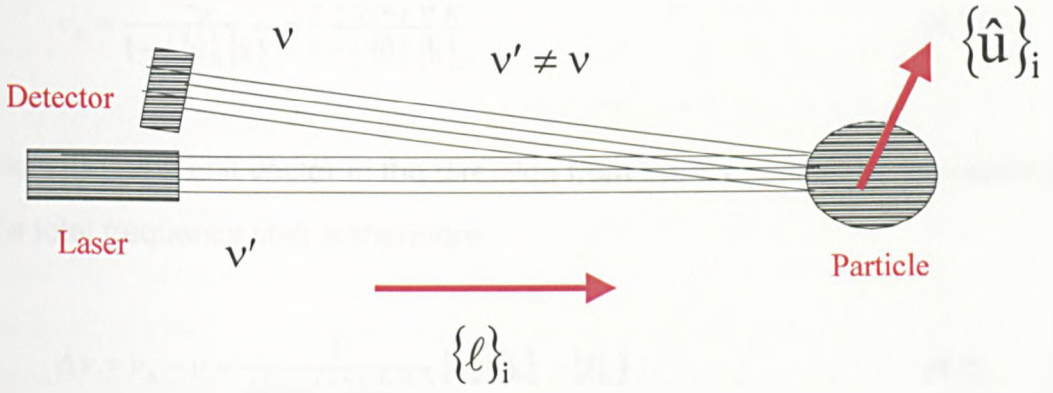

Figure 4.2 Principle of Doppler frequency shift for a moving particle and stationary light source and detector

The frequency difference then between an emitting stationary (laser) source and an emitting moving (scattering particle) source is given by:

$$\nu' - \nu = \Delta\nu = \frac{\nu}{c}\frac{\{\hat{u}\}_i\{\ell\}_i}{1-\frac{1}{c}\{\hat{u}\}_i\{\ell\}_i} \qquad (4.4)$$

Since the velocity of the emitting particle is far smaller than the velocity of the propagating wave, this reduces to

$$\Delta\nu = \frac{1}{\lambda}\{\hat{u}\}_i\{\ell\}_i \qquad (4.5)$$

The moving particle is in fact a moving transmitter and as noted receives light from the stationary laser source and retransmits the light to the stationary observer (phtotdetector). The frequency of the transmitted waves is equivalent to that of the received waves:

$$\nu_p = \nu\left[1-\frac{1}{c}\{\hat{u}\}_i\{\ell\}_i\right] \qquad (4.6)$$

where $\{\ell\}_i$ is a unit vector in the direction from the stationary laser source to the moving transmitter. The frequency is Doppler shifted due to the transmitter movement relative to the receiver, so the final frequency is

$$\nu_A = \frac{\nu_p}{1-\frac{1}{c}\{\hat{u}\}_i\{k\}_i} = \frac{1-\frac{1}{c}\{\hat{u}\}_i\{\ell\}_i}{1-\frac{1}{c}\{\hat{u}\}_i\{k\}_i} \tag{4.7}$$

where $\{k\}_i$ is a unit vector in the direction from the transmitter to the receiver. The total frequency shift is therefore

$$\Delta\nu = \nu_A - \nu = \frac{1}{\lambda\left(1-\frac{1}{c}\{\hat{u}\}_i\{k\}_i\right)}\{\hat{u}\}_i(\{k\}_i - \{\ell\}_i) \tag{4.8}$$

As before, the particle velocity is much less than the propagating wave speed, $c >> |\hat{u}|$, so

$$\nu_D = \frac{1}{\lambda}\{\hat{u}\}_i(\{k\}_i - \{\ell\}_i) \tag{4.9}$$

4.2.2 Heterodyne Detection

The theory outlined above can be applied to the LDA system for measuring particle velocity if the basic assumption is that the laser is a stationary wave source and the scattering particles act as moving receivers and transmitters of this source. Initially consideration is made of a stationary incident wave source with unit vector $\{\ell\}_i$ and two stationary detectors at two locations A and B having unit vectors $\{k\}_i$ and $\{m\}_i$ say. The frequencies at points A and B due to the particle motion are given as

$$\nu_A = \nu\left[\frac{c-\{\hat{u}\}_i\{\ell\}_i}{c-\{\hat{u}\}_i\{k\}_i}\right] \quad \text{and} \quad \nu_B = \nu\left[\frac{c-\{\hat{u}\}_i\{\ell\}_i}{c-\{\hat{u}\}_i\{m\}_i}\right] \tag{4.10}$$

$$\Delta\nu = \nu_A - \nu_B = \frac{\nu\left[1-\frac{1}{c}\{\hat{u}\}_i\{\ell\}_i\right]}{\left[1-\frac{1}{c}\{\hat{u}\}_i\{k\}_i\right]\left[1-\frac{1}{c}\{\hat{u}\}_i\{m\}_i\right]} \cdot \frac{\{\hat{u}\}_i}{c}(\{k\}_i - \{m\}_i) \tag{4.11}$$

$$\nu_D = \Delta\nu = \frac{1}{\lambda}\{\hat{u}\}_i(\{k\}_i - \{m\}_i) \tag{4.12}$$

In practice, this approach of using a single wave source and two photodetectors to determine the particle velocity cannot be achieved due to the slow response time of the photodetectors that are currently available. This problem can be overcome by using the heterodyne technique whereby light waves scattered in different directions are superimposed to obtain a signal with a frequency corresponding to the frequency difference of the two scattered waves. As described, the Dantec system produces two pairs of incident light beams, one pair for each component of the velocity. The two incident light beams in a given pair cross in space. A particle passing through the intersection of the beams will scatter light from each of the two beams. Each one of the beam paths have a unit vector $\{\ell_1\}_i$ and $\{\ell_2\}_i$. The unit vector from the transmitter (particle) to the detector is $\{k\}_i$ as before. The intersection of the two beams is described as the probe or measuring volume. The scattered light from each beam has Doppler shifted frequencies given by

$$\nu_1 = \left[\frac{c - \{\hat{u}\}_i \{\ell_1\}_i}{c - \{\hat{u}\}_i \{k\}_i}\right] \tag{4.13}$$

$$\nu_2 = \left[\frac{c - \{\hat{u}\}_i \{\ell_2\}_i}{c - \{\hat{u}\}_i \{k\}_i}\right] \tag{4.14}$$

The two scattered waves interfere on the surface of the photodetector producing a *beat* signal which has a frequency given by the frequency difference $\Delta\nu = \nu_2 - \nu_1$. For particle velocities much smaller than that of light this difference is

$$\nu_D = \frac{1}{\lambda}\{\hat{u}\}_i(\{\ell_2\}_i - \{\ell_1\}_i) \tag{4.15}$$

The signal generated is transient consisting of a spherical region of sinusoidal intensity variations. As the particle crosses the probe volume an output is generated called the Doppler burst. It is noted that the frequency of the resulting signal is independent of the direction of light collection, i.e. the

unit vector $\{k\}_i$ is not present. Large apertures used for signal collection can be used to create high signal-to-noise ratios. When the two incident beams are separated by an angle 2φ, the frequency detected can be otherwise written as

$$\nu_D = \frac{1}{\lambda}\{\hat{u}\}_i[\{\ell_2\}_i - \{\ell_1\}_i] = \frac{2\hat{u}_\perp \sin\varphi}{\lambda} \qquad (4.16)$$

$\hat{u}_\perp$ is the instantaneous velocity taken as being perpendicular to the bisector of the incident beams and in the same plane as the incident beams. This is in effect the velocity of the particle and is determined from the signal frequency using

$$\hat{u}_\perp = \frac{\nu_D \lambda}{2\sin\varphi} \qquad (4.17)$$

The term $\frac{\lambda}{2\sin\varphi}$ is taken as the calibration factor of the instrument and this is a constant.

4.2.3 Calibration Factors

The wavelengths of the two light components are slightly different and this resulted in slightly different calibration factors for each component. Only the angle of intersection of the beams 2φ is required to determine the calibration factor for each component. The intersection of the beams is set by the manufacturer. Confirmation that all four beams passed through a single point was achieved by directing the four beams through a microscope lens and checking they passed through a single point at the focal lens of the microscope lens. The probe optics were then directed at a distant target approximately 2m away without the microscope lens. The position of the four spots generated by the beams was recorded. Based on their separation and the distance from the front lens, the angle of intersection of the beams 2φ

could be determined. The calibration factors for the instrument were evaluated as

$$C_U = 1.263\ ms^{-1}MHz^{-1}$$

$$C_V = 1.205\ ms^{-1}MHz^{-1}$$

These values were incorporated into the Burstware software program.

4.2.4 Directional Reference

The velocity component of a particle is determined based on the frequency shift which occurs in each beam for a pair of beams generating a measuring volume in the LDA system, as described above. There will be a difference between these frequency shifts only if the particle moves in the plane of the two beams. This difference is the basis of the velocity measurement, however if a particle path is not in the plane of the beams, the frequency shift for both beams will be the same i.e. the frequency difference will be zero and no interference will be generated on the photodetector so no signal is registered.

The Bragg Cell module provides a fixed frequency shift between the beams of 40MHz. This means that a stationary particle in the plane of the two beams will generate a frequency shift of 40MHz to the photodetector. The frequency shift due to any particle motion in the plane of the beams, the *Doppler shift*, will add or subtract to this fixed shift of 40MHz. Based on whether the resulting shift is less than or exceeds 40MHz the signal processor can distinguish negative or positive flow direction.

4.2.5 Probe Volume dimensions

The transmitted laser light is polarised using polarising filters, orienting the light waves and removing randomly oriented background light. The diameter of a focused spot from the laser can be determined from the laser beam intensity and is proportional to the wavelength of the laser λ and the

focal length of the lens, *f* (Chu, 1974). For the beam geometry used, the elliptical volume in air was found to be 180μm in the major diameter and 36μm in the minor diameter for the green and blue channels. Calibration of this system for Couette flow in a PMMA concentric cylinder showed that the mean value of the transit time multiplied by the velocity was 21 ± 5μm which is the mean effective probe minor diameter (Rattray, 1998).

4.3 LDA Burstware Settings

There are a number of system and sampling settings that are required to be assigned for the LDA system to obtain velocity data from a given flow experiment. These settings are entirely dependent on the experimental set-up, the flow regime, the fluid used, particle seeding etc. The majority of these settings can be configured in the Burstware software for a given experimental set-up and can be saved for that particular experiment. For a different experiment, these settings may require modification, and may be saved as a different parameter file.

In order to optimise the system and sampling settings for a particular experiment it is necessary to run a number of preliminary experiments operating under the flow conditions desired and manually adjust the Burstware parameters to optimise collection of velocity data. Altering one parameter in the settings often has a bearing on the setting for another parameter, so a guideline protocol was developed to modify parameters in a prescribed way to reach the optimal case of collecting velocity data. Some settings were fixed by the hardware and could not be altered such as photomultiplier current and traverse step size. The major parameters for modification in the software are the centre frequency and bandwidth, the photomultiplier voltage and the signal gain.

4.3.1 Frequency Shift

A frequency shift of 40MHz is applied to one side of each LDA beam pair so that directional reference can be made for scattering particles passing through the probe volume. From preliminary experiments, the mean velocity of particles in the flow can be determined. The centre frequency is set to correspond approximately to the mean velocity. The bandwidth is then set which limits the velocities that can be measured either side of the centre frequency. In preliminary experiments this is set to be quite wide such that all possible velocities in the flow might be recorded. Based on analysis of this data it is likely that the bandwidth can be reduced to record a more narrow range of data. In fact, the bandwidth should be set to its minimum value whilst still capturing all possible particle velocities in the given flow since this reduces aliasing and sampling noise and also improves the frequency resolution.

4.3.2 Photomultiplier Voltage

Doppler bursts are fed to two BSA hardware modules, one for each channel. On one of the BSA modules a series of LED's are triggered as a Doppler burst is received. This is indicative of the photomultiplier voltage that should be set to an optimal range for the size and frequency of triggering. On the other BSA module, a cathode ray oscilloscope could be connected up to monitor the Doppler burst and again, an optimal photomultiplier voltage could be assigned for this channel. The LED spectrum (or CRO) could be used as an indicator of the frequency of Doppler bursts. Within this pre-assigned photomultiplier voltage range, a second voltage assignment could be used to increase or reduce the signal for the detector thresholds for each channel. The detector threshold is high enough such that any background noise will not cause a Doppler burst but increased frequency of Doppler bursts would rise above them. In effect, the assignment of the voltages in the Burstware program provided some control over the data rate that was achievable for a given experimental set-up.

4.3.3 Signal Gain

Signal gain could be used to increase the signal power for each channel, maintaining signal-to-noise ratio, but only to a certain limit. Beyond this limit, noise was amplified to a level that would trigger the burst detectors, and introduce some invalidity to the measured burst. As the frequency of noise associated triggering of the detectors increased, the validation rate of the data decreased as noisy signals triggered the photodetectors for greater time periods. In effect, signal gain assignment in the Burstware program provided some control over the data validation rate for the given experimental set-up.

4.3.4 Oversize Rejection

If a poor velocity record is still obtained having tried to optimise the factors above, this may be due to contamination in the flow where air bubbles or large flocculated particles do not follow the true flow pattern and generate a spurious velocity record. In such circumstances, oversize rejection can be used to reject bursts having a greater intensity than a predetermined limit. Alternatively if very noisy signals are generated producing very poor validation for the velocity record, the quality factor can be set above the default zero setting and then bursts are only accepted above a set percentage of the pedestal mean value, so only the strongest signals would be accepted.

4.4 The Flow System for LDA Measurement

The concentric cylinder system for quantifying the fluid flow has been previously described. LDA measurements have been made in the system at two scales. The small scale vessel, CC-25, corresponds to a commercially available rheometer (Stresstech, Rheologica Instruments). This rheometer has been modified such that it can operate as working bioreactor incorporating living cells. The modifications to the rheometer and its operation, along with the results of the cell work are presented later. It is

sufficient to note at this stage that the design of the system for LDA measurements does not differ significantly from the working bioreactor such that it has any bearing on the fluid flow phenomena. The larger scale system, CC-75 is scaled up by a factor of three on the rheometer geometry. The difference in scale only relates to the concentric cylinder manufacture as both systems operate from the same manifold onto which the other peripherals such as motors and pulleys are fixed.

Accurate spatial resolution is required for LDA measurements, CC-25 having a 1mm annular space where measurements are made and CC-75 having a 3mm annular gap. Because the LDA is an optical measuring system, the geometry of the system is important with particular regard to optical access. The surface through which the laser beams pass must be transparent and the normal choice of material for designing flow system sections is polymethylmethacrylate (PMMA, Plexiglass, Perspex), optical glass or Pyrex glass for high temperature systems. Ideally, the light beams should pass across a stationary, flat, clean and smooth surface. This prevents distortion of the incident laser light beams that will generate erroneous backscattered data. Clearly, it is not always possible to ensure that the manufacture of the system has such a surface; the concentric cylinder configuration here being a common practical case. In such circumstances, a viewbox arrangement is employed (Budwig, 1994). The basic principle is that the fluid flow section under investigation is immersed in a flat walled tank. The walls of the tank should be of the same material of construction as the flow section. The tank is filled with a fluid that has the same refractive index as the material of construction of the tank walls and flow section. Before addressing the problem of refractive indexing matching, the problems associated with curved surfaces will be briefly addressed.

4.4.1 Non-Flat surfaces

The problem of laser beam refraction, as applied to LDA measurements through curved surfaces, has been addressed by Boadway (1981). The orientation of the optical system for measurement of a particular velocity component is summarised as:

- For *axial* velocity measurements, the optical system should be oriented such that both beams are in a plane that passes through the axis of the cylinder and the bisector between the two beams at a right angle to the axis.
- For *radial* velocity measurements, as for *tangential* measurements, the laser beams should be in a plane that is perpendicular to the axis of the cylinder, the bisector of the beams being on that plane and also perpendicular to the axis. Due to refraction of light through the material of the curved surface there is a virtual crossover point which is different from the real crossover point as shown in Figure 4.3. Measurement of radial velocity at different radial positions is achieved by moving the optical set-up sideways in the given plane of orientation.

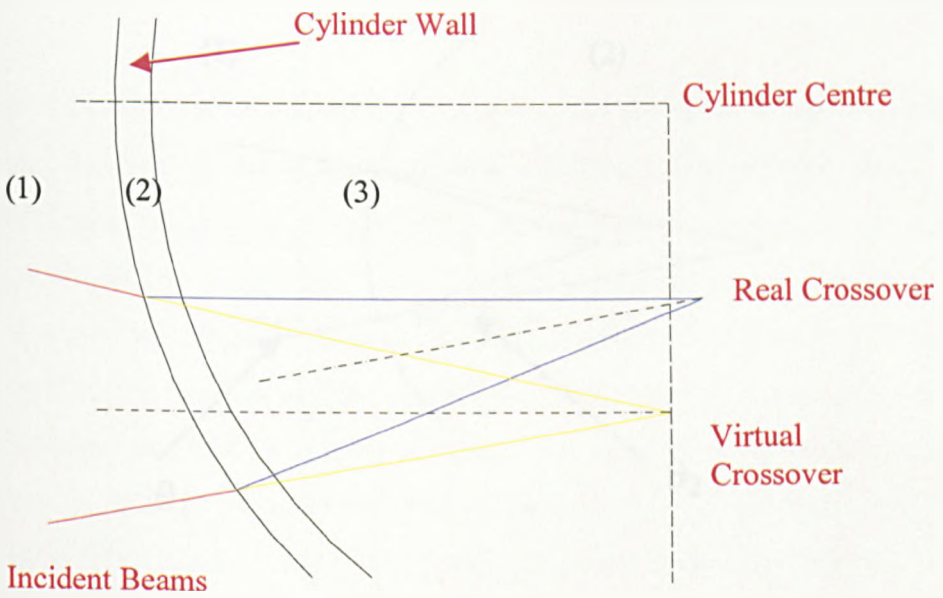

Figure 4.3 Refraction of incident laser beams during radial velocity measurement

It is evident in Figure 4.3 that there is a two dimensional shift in the crossover point of the laser beams, from the virtual crossover to the real crossover point. The crossover point is in fact the probe volume for LDA measurement, and knowledge of the location of this point is extremely important for LDA measurements.

4.4.2 Refractive Index Tuning

The real crossover point occurs if there is refractive index mismatch between media (1), (2) and (3) in Figure 4.3. In practice, medium (3) will be the working fluid in which measurements are to be made and so in all likelihood it will not be possible to make a refractive index match between media (2) and (3). A viewbox arrangement, filled with an appropriately selected fluid, can be used to make a refractive index match between media (1) and (2) and this has the effect of reducing the shift of crossover point from two dimensions to one dimension (Edwards, 1984), as shown in Figure 4.4. The one-dimensional offset between the virtual and real crossover point will be reduced as the refractive indices between media (1) and (2) approach each other.

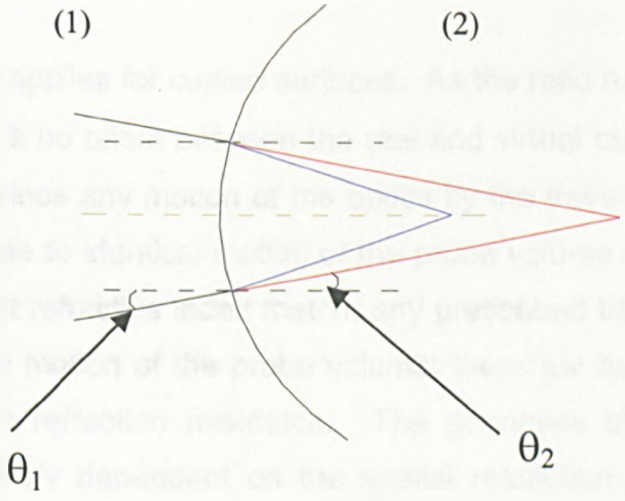

Figure 4.4 1-D translation of intersection point after refractive index matching of the cylinder wall with a viewbox fluid

The effect of a mismatch in the index of refraction can be determined rigorously using the Fresnel propagation principle, this is computationally demanding and provides no more useful information than using the more simplified approach of Snells law. This law states that for a ray traversing a surface where there is a step change in the index of refraction (Figure 4.5) then:

$$n_1 \sin\theta_1 = n_2 \sin\theta_2 \qquad (4.18)$$

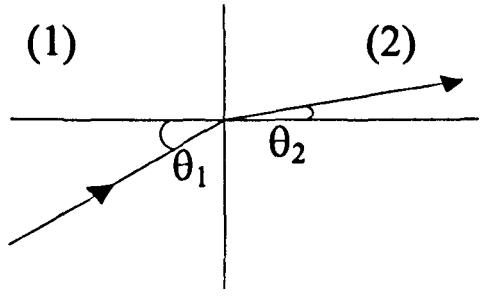

Figure 4.5 Snell's Law for refraction through a plane surface

This law equally applies for curved surfaces. As the ratio $n_1/n_2 \rightarrow 1.0$ then $\theta_1 \rightarrow \theta_2$ and there is no offset between the real and virtual crossovers. This is the ideal case, since any motion of the optics by the traverse mechanism of the LDA will relate to identical motion of the probe volume for measurement. Without a perfect refractive index match, any prescribed traverse motion will not be the same motion of the probe volume; there will be a proportionality factor related to refraction mismatch. The goodness of refractive index matching is entirely dependent on the spatial resolution required for LDA measurements. This is particularly the case in the near wall region.

The refractive index of liquids can be measured using commercially available refractometers. The refractive index of solids cannot be measured accurately at the present time but methods to estimate their refractive index

have been reviewed by Budwig (1994). A list of approximate indices for a variety of commonly used transparent solids is given in this review. PMMA is quoted as being in the range 1.48 to 1.49. As a large number of LDA experiments were carried out, and contamination of the index matching fluid was unavoidable over time, the cost of the matching fluid was an important issue along with availability and also issues of handling and toxicity.

Many of the approaches used to solve refractive index matching problems provided in the literature are very often unique in terms of the application and selection of the solid and liquid materials. In the most ideal case, the viewbox fluid and the annular fluid are the same, both of which having an exact match to the solid material of construction. However, it is often difficult to achieve this, particularly with regard to the annular fluid, since the physical properties of this fluid (density, viscosity etc.) become very important in influencing the flow phenomena. Thompson (1990) used a combination of steam-distilled turpentine and Tetralin as a fluid match for PMMA. Whilst a very good match was reported, the fluid viscosity was low and caused crazing and softening of the PMMA. For any experiments where the outer cylinder is required to rotate, it is more desirable to have a viewbox fluid with a high viscosity. In this case, the motion of this fluid is generally more easily contained in the laminar regime and spurious data due to flow phenomena in this fluid are eliminated. Northrup et al. (1990) used a combination of Dow Corning mineral oil 550 and Union Carbide organosilicone L42 at 27°C, and Braun et al. (1990) used Dow Corning mineral silicone oil 556 and Dow Corning mineral oil 550 at 25°C to match PMMA. Both combinations provided a high viscosity fluid, however the temperature sensitivity on the refractive index was not provided nor was the degradation behaviour of the fluid with time. Chen (1990) carried out refractive index matching experiments for a solid slurry pipe flow in a silica gel test section. Using a range of concentrations of sodium iodide in water a refractive index variation between 1.333 and 1.487 was reported. The concentration of sodium iodide was varied up to 60 wt% and temperature varied between 40 and 60°C to achieve these refractive indices. The viscosity of the solution is low, and use of such a fluid would require extremely close monitoring of concentration and temperature. Parker (1996)

used sodium iodide solution to provide refractive index matching in a PMMA concentric cylinder apparatus to study turbulent Taylor vortex flow. A 64.8wt% solution gave a refractive index of 1.5025. To maintain a refractive index of 1.4905 ± 0.0005 under turbulent Taylor vortex flow, the lower end of the annulus required temperature maintenance of 26.7 ± 0.1°C and 28.7 ± 0.1°C at the upper end with constant monitoring with an Abbe-type refractometer. Other problems associated with this fluid are that it slowly crystallises when exposed to air and these crystals can extrude in to small crevices, and it deteriorates readily, turning a brownish colour, when exposed to light. This latter problem can be somewhat overcome by the addition of small amounts of sodium thiosulphate (Parker, 1990) or ascorbic acid (Jacobs, 1988). A number of other potential fluids to use as a refractive index match are provided by Budwig (1994) along with density and viscosity data for these fluids. Alongside sodium iodide, other aqueous solutions that potentially match the refractive index of PMMA are zinc iodide, potassium thiocyanate, ammonium thiocyanate, and sodium thiocyanate. These all have essentially the same problems and limitations that the sodium iodide solutions have. Glycerin is identified as a promising fluid having a maximum refractive index of 1.47, and whilst the viscosity becomes high as the refractive index increases, so too does the fluid density. A number of organic liquids are identified as promising viewbox fluids for PMMA. Some of these such as dibutylphthalate (n=1.49) would provide an excellent match to PMMA, however this fluid is carcinogenic and was deemed unfit for frequent use. Sunflower oil (n=1.4734) was used as a suitable match to the grade of PMMA (n=1.4874) used for the manufacture of the concentric cylinder modelling system in this study. It is low cost, can be readily replaced, is well suited for frequent use and has stable physical properties over prolonged time periods under the environmental conditions for the experimental runs. The refractive index of sunflower oil was determined at 27°C using a 60 E/D A89134 High Accuracy Refractometer (Bellingham & Stanley Ltd., UK).

4.4.3 Calculating Refractive Index Mismatch in the Modelling System

The laser beams from the LDA optics pass through a flat PMMA wall of the viewbox, through the refractive index matching (RIM) fluid, sunflower oil, and through the outer cylinder of the annular flow vessel. The probe volume is then in the annular space where velocity measurement is made. The crossover point of the beams is offset spatially twice; the first time as it passes through the RIM fluid and then again as it passes through the outer cylinder. The actual spatial offset which results between traverse step motion and the actual probe volume location has been calculated on this basis.

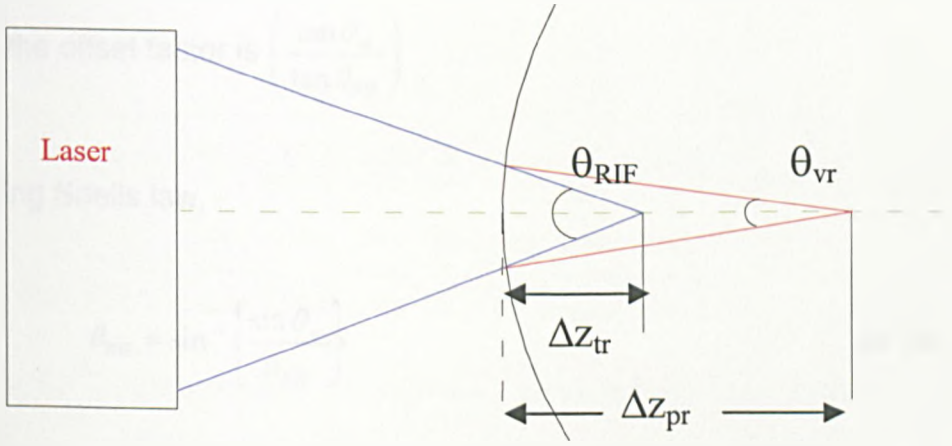

Figure 4.6 Calculation of probe volume translation due to refractive index mismatch in LDA measurements

It is clear that the motion of the traverse in a radial direction towards the annular space will move the probe volume radially in the annular space:

$$\Delta z_{tr} = \Delta z_{pv} \qquad (4.19)$$

With referral to Figure 4.6 the actual motion of the probe volume relative to the motion of the traverse can be expressed as:

$$z_{pv} \tan\theta_{RIF} = z_{tr} \tan\theta_{vr} \tag{4.20}$$

$$\frac{z_{pv}}{z_{tr}} = \frac{\tan\theta_{vr}}{\tan\theta_{RIF}} \tag{4.21}$$

Actual probe volume motion is then related to traverse motion as

$$\Delta z_{pv} = \left(\frac{\tan\theta_{vr}}{\tan\theta_{RIF}}\right)\Delta z_{tr} \tag{4.23}$$

so the offset factor is $\left(\frac{\tan\theta_{vr}}{\tan\theta_{RIF}}\right)$

Using Snells law,

$$\theta_{RIF} = \sin^{-1}\left\{\frac{\sin\theta_{vr}}{n_{RIF}}\right\} \tag{4.24}$$

When the index of refraction for the viewbox fluid is known only the angle of the virtual crossover between the beams, θ_{vr} is required. This angle can be calculated if the beam separation at the probe optics and the focal length of the optic lens is known. From Figure 4.6:

$$\frac{\theta_{vr}}{2} = \tan^{-1}\left(\frac{\ell_{bs}/2}{f}\right) \tag{4.25}$$

The beam separation for the green and blue channels is fixed by the LDA hardware. The key parameters and results of calculations to estimate the probe volume offset due to refractive index mismatch in the experimental rig used for LDA measurements are given in Table 4.1

4.4.4 Traverse Datum Settings: Finding the Wall

The offset factors for the green and blue channels can be used to determine how close to the wall the LDA optics can be moved so that the probe volume will measure particle velocities in the flow domain. These offset factors meant that it was not possible to make measurements right on the wall; this could only be achieved with a perfect refractive index match between the viewbox fluid and PMMA.

	Channel	
	Green	Blue
Beam Separation	66.2821mm	70.0493mm
θ_{vr1}	23.405°	24.695°
θ_{vr2}	16.04°	16.89°
θ_{RIF}	15.46°	16.28°
Offset factor	1.5055	1.5145
Refractive Index Air	1.0	
Refractive Index PMMA	1.4874	
Refractive Index Sunflower Oil	1.4734	

Table 4.1 Parameters used in calculating the probe volume translation for refractive index mismatch in LDA measurements

Before each experiment could be performed, a zero position or datum for the traverse had to be established. No fixed datum exists for the LDA optics. The traverse and optics are fixed on an optical table as is the concentric cylinder vessel. The coordinate and measuring system of the LDA are shown in Figure 4.7. This is achieved by rotating the optic head and fixing it into position with the supporting collar that is fixed to y-component of the traverse. In a darkened room, the laser beams and their intersection points can be visualised. The probe volume can be moved to the desired position for a datum level. Initially, the y-coordinate of the traverse is

adjusted until the probe volume lies approximately in the z-y plane and perpendicular to the axis of the concentric cylinders.

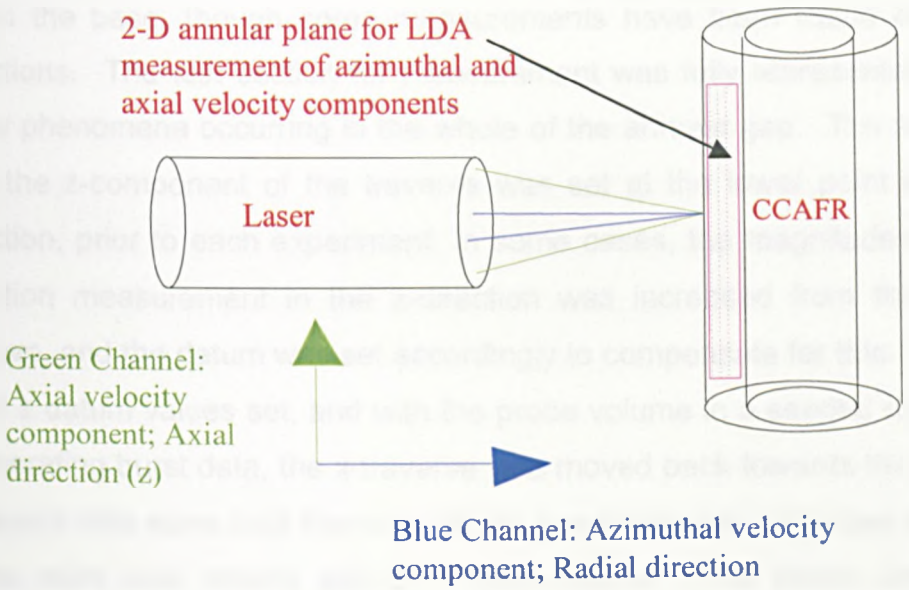

Figure 4.7 Coordinate system for LDA velocity measurements in concentric cylinder system

At this point the fluid in the test section is seeded with particles, and the inner cylinder is set to rotate at the prescribed speed that is required for the experimental measurement. The traverse is now moved in the x-direction in prescribed step sizes. Initially these step sizes in the x-direction can be large, but as the probe volume nears the measurement test section, the step size can be reduced to a value that corresponds to approximately 0.2 of the annular gap size. When the probe volume is observed to be in the annular gap, the Burstware parameters discussed above are modified to provide a reasonably high data rate with good validation (>60%). The y-direction of the traverse can now be moved in small step sizes to ensure correct probe volume location perpendicular to the co-axis of the rotating cylinders. Once the y-plane was adequately located, this position was set as a zero datum for

the y-traverse. The datum for the z-axis is chosen arbitrarily for a vertically oriented concentric cylinder system. The annular gap has a height of 130mm for the system CC-75 and 44.7mm for CC-25. In general, a 15mm vertical section of the flow has been quantified using LDA for CC-75 from a height of 65mm from the base of the flow, and for a 10mm section for CC-25, 23mm from the base, though some measurements have been made over larger sections. The test section for measurement was fully representative of the flow phenomena occurring in the whole of the annular gap. The zero datum for the z-component of the traverse was set at the lower point of the test section, prior to each experiment. In some cases, the magnitude of the test section measurement in the z-direction was increased from those stated above, and the datum was set accordingly to compensate for this. With the y and z datum values set, and with the probe volume in a seeded rotating flow generating burst data, the x-traverse was moved back towards the outer wall in small step sizes until the point where burst data was no longer registered. This point was initially set as a zero datum. The probe volume was considered to be 21μm. The x-traverse step size was then set at 20μm, and moved radially towards the inner wall into the rotating flow. At the first point when burst data was registered, this x-position of the traverse was reset as the zero datum. This effectively set a position that was as close to the wall as was possible to make measurements for the whole of the 2-D annular flow field without making any Burstware parameter adjustments. With the probe volume fixed at these prescribed datum points, the z-traverse was moved vertically along the test section, to ensure that burst data would recorded at a suitable data rate and validity. This procedure also provided confirmation on the exactness of the vertical orientation of the wall and any possible distortion of the PMMA over time. After this check was performed prior to each experiment, the probe volume was then returned to the datum position in the x, y and z planes. With the datum points set, and the location of the outer wall determined, the next step was to determine the location of the inner wall. This was facilitated by the fact that the size of the annular gap was known. The offset from the outer wall due to refractive index mismatch in effect reduced the annular gap size to the inner wall. Making this deduction, the traverse was moved in the radial x-direction by this amount. The burst data

rate was checked at this new position. If the data rate was very poor, or the validation was poor, the traverse step size was set to 20μm, and then moved back towards the outer wall again until a high data rate was achieved. In the more laminar flows, this latter adjustment was not normally necessary since the flow phenomena in the near wall region was very similar to the flow in the annular core, so the Burstware parameters provided sufficient data rate and validation even at the wall. For more disturbed flows, there was sufficient difference in the flow structure at the inner wall from the annular core that noisy and spurious data resulted at the wall for the Burstware parameters that had been set. It was found that the distance required to move the probe volume off the wall and then obtain good data was small enough that an interpolation of the core data could be made to resolve the flow on the wall with adequate accuracy. The alternative to this situation would be to collect data in the core region with a given set of Burstware parameters, then to modify the parameters and collect data only in the near wall region. This approach would require additionally programming the traverse motion for core measurements and near wall measurements independently.

4.4.5 Near Wall Measurements: Interpolation

The offset factors for the blue and green channels, which relate the traverse motion to the actual probe volume location, are sufficient to provide very good resolution of the flow regime even in the small-scale system CC-25. The only problem that this causes is in obtaining very near wall measurements, in particular at the outer wall of the annulus and this is only encountered for the more disturbed flows. However, because the wall speeds are known and there is excellent resolution of the flow in the major domain of the annular region, the flow in the near wall region can be estimated with a 2-D interpolation with reasonable accuracy. The 2-D interpolation is performed on both the outer and inner walls, where necessary, for the very thin layer that cannot be measured due to either the effect of refractive index mismatch or due to noisy data collection by virtue of the nature of the flow. The interpolation uses processed velocity data for the annular core and the known speed of the wall. The interpolation uses a

spatial resolution that is much smaller than the either the radial or axial step size motion of the traverse. Interpolated velocities in the near wall region are used in the calculation on near wall shear stresses using the same calculation procedure that is used for the annular core and is described later.

4.4.6 Traverse Motion

The probe volume can be manoevered to any desired position within the limits of the traverse rails. The motion can be performed manually using the Burstware software, or a sequence of movements of the traverse can be programmed. Manual motion is achieved by assigning a step size and a maximum distance of movement for each of the traverse directions in the Burstware and then using the keyboard; one step movement is performed with each key press, one key for each of the traverse directions. This would mean for example, that if the maximum distance is set at 50mm and the step size is set at 1mm, for a given traverse direction the key could be depressed 50 times before the software overrides any further motion on a subsequent key depression. Location of the walls is determined using this manual approach of individual controlled step motion.

A 2-D region for LDA measurement is prescribed in the radial (x-direction) and axial (z-direction) for the test section. The y-position is fixed. The step size for radial and axial movements is set as 0.05mm and 0.5mm respectively for CC-25, and 0.1mm and 1mm respectively for CC-75. The traverse was programmed for sequential motion for a given experimental run. The probe volume was initially located at the datum point for the outer wall and the upper axial limit for the test section. After adequate data collection at a point, the traverse moved radially at the constant prescribed radial step increment to the next position, and continued until the point of adequate data collection at the outer wall. The motion then brought the probe volume back to the datum point at the outer wall and the lowered by the axial prescribed step size. Radial measurements are then made for the new axial position until the probe volume is returned back to the outer wall and again lowered axially. This process is repeated making point measurements in radial lines,

moving progressively lower, with prescribed step increments, until all velocities at points in the 2-D field have been measured and recorded. Post processing of the velocity data that is collected and computation of the shear field is described in detail later.

4.4.7 Particle Seeding

The principle of operation of the LDA has previously been described; velocity measurement is based on backscattering of incident light from particles suspended in the fluid and not from the fluid itself. A number of criteria therefore have to be met when addressing the selection of appropriate particles to seed the fluid with. The selection of particles is often specific to the application. In general, and in the case of this study, the interest is in the velocity of the continuous phase into which the scattering particles are dispersed and so it is necessary to select particles whose motion will almost identically reflect the fluid motion.

4.4.7.1 Ideal properties of seeding particles

Like many other factors in the experimental set-up for LDA measurements, the choice for seeding particles is dependent on the configuration and operation of the experiment and the fluids used in the system. Since the particle motion is representative of the fluid flow in the system, then the particles should have the following general properties:

- Be able to follow the flow accurately
- Scatter light efficiently
- Be non-toxic, non-corrosive, non-abrasive, non-volatile
- Be chemically inactive

Additional considerations are that the particles are clean, cheap and easily produced if required in large amounts or a large number of experiments are performed frequently. The first two properties are perhaps the most important, and once the first of these, namely that the particles follow the fluid

streamlines accurately, then the second one is optimised if possible. In the current study, two particle types were used; Timiron Supersilk MP-1005 (Merck GmbH) and hollow glass spheres (65997-17-3, Potters Industries UK). The Timrion particles are titanium dioxide flakes with a mean size of 15μm and density 2.9 g/cm^3. The glass spheres were filtered to a mean particle diameter of 8μm with a mean density of 0.951 g/cm^3. When used, the Timiron flakes were added at a concentration of 0.095 wt% whereas the glass spheres were used to a maximum concentration of 0.1 wt%. In order to simulate the potential behaviour of freely suspended cells in the bioreactor environment, the glass spheres were representative of single cells and the small proportion of Timiron flakes were representative of flocculated cells and in combination, provided an indication of real cell behaviour for a prescribed flow regime. In some instances, a small amount of sodium azide (0.015 wt%) was added to the solution to improve the obtained signal.

4.4.7.2 Particle motion

Since the particle motion in the fluid is used as the basis of measurement for LDA, it is appropriate to briefly provide some theory on the particle motion in moving fluids. All particles immersed in a fluid are subject to a buoyancy force that is related to the density difference between the particle and the surrounding fluid. Ideally, particles used in LDA measurements to represent the fluid flow should be neutrally buoyant, i.e. the density difference between the particle and surrounding fluid is zero. In a flowing fluid, there is an additional force to buoyancy made up of two components: the skin friction (or viscous drag force) and the form drag (due to the pressure distribution in the fluid). For creeping flow, when the fluid velocity is low relative to the particle and the Reynolds number is low, the drag force is given by the Stokes drag, after the Navier-Stokes equations for the particle motion were solved under these flow conditions by Stokes in 1851,

$$F_{St} = 3\pi d_p u \qquad (4.26)$$

where d_p is the particle diameter. As the Reynolds number increases, deviations from Stokes law progressively increase. Skin friction constitutes one third of the drag force and form drag constitutes two thirds, but as Re increases the skin friction becomes proportionally less and the form drag proportionally more. The relationship between drag force and velocity is best represented by two dimensionless groups. The first is the particle Reynolds number, given by:

$$Re_p = \frac{ud_p\rho}{\mu} \tag{4.27}$$

the second dimensionless group is $R'/\rho u^2$, where R' is the force per unit projected area of particle in a plane perpendicular to the direction of motion. For a spherical particle the projected area is that of a circle of the same diameter as the sphere:

$$R' = \frac{4F}{\pi d_p^{\,2}} \tag{4.28}$$

$R'/\rho u^2$ is a form of drag coefficient and is often denoted by C'_D in the literature. A drag coefficient, C_D is frequently defined as the ratio of R' to $1/2\rho u^2$ and so

$$C_D = 2C'_D = \frac{2R'}{\rho u^2} \tag{4.29}$$

For Stokes law,

$$C_D = 24\frac{\mu}{ud_p\rho} = 24\,Re_p^{-1} \tag{4.30}$$

For $Re_p \leq 2$, the following expression is given by Oseen (1913)

$$C_D = 24 Re_p^{-1}\left(1+\frac{3}{16}Re_p\right) \qquad (4.31)$$

Dallevelle(1948) proposed that $C_D/2$ in the range $0.2 \leq Re_p \leq 1000$ could be regarded as composed of a portion related to Stokes law, and a constant portion accounting for non-viscous effects

$$\frac{C_D}{2} = 12 Re_p^{-1} + 0.22 \qquad (4.32)$$

Schiller and Naumann (1933) proposed the following relationship for the same range of Re_p:

$$\frac{C_D}{2} = 12 Re_p^{-1}\left(1+0.15 Re_p^{0.687}\right) \qquad (4.33)$$

A generalised equation applicable for a wide range of Re_p is proposed by Wadell (1934):

$$\frac{C_D}{2} = \left(0.445+\frac{3.39}{\sqrt{Re_p}}\right)^2 \qquad (4.34)$$

Finally, Khan and Richardson (1987), using a large data experimental data set for C_D and Re_p suggested that a good correlation up to $Re_p = 10^5$ is

$$\frac{C_D}{2} = \left[1.84 Re_p^{-0.31} + 0.293 Re_p^{0.06}\right]^{3.45} \qquad (4.35)$$

Using equation (4.35), the total force on a particle in a fluid flow up to $Re_p = 10^5$ is given by

$$F = \frac{\pi}{4} d_p^2 \rho u^2 \left[1.84 Re_p^{-0.31} + 0.293 Re_p^{0.06}\right]^{3.45} \qquad (4.36)$$

4.4.7.3 Light scattering by particles

The efficiency of particles as light scatterers can be based on the particle scattering cross section, C_{scat} which is defined as the ratio of the power P_{scat} in Watts scattered in all directions to the incident light intensity (W/m^2) incident on the particle and has dimensions of area (m^2). For a scattered light distribution $I(\theta, \varphi)$ at a distance r from the particle the power through an elemental surface of area $r^2 \sin\theta d\theta d\varphi = r^2 d\omega$ and therefore

$$C_{scat} = \frac{P_{scat}}{I_o} = r^2 \int \frac{I(\theta,\phi)}{I_o} d\omega \qquad (4.37)$$

For increasing particle size, the magnitude of C_{scat} increases, and representative values of C_{scat} based on equation (4.37) are given in Table 4.2

Scattering Mode	C_{scat} (m^2)
Rayleigh scattering (atoms, molecules)	10^{-33}
Thompson scattering (free electrons)	10^{-30}
Mie Scattering (micron-scale particles)	10^{-12}
Spheres 100μm diameter	10^{-8}

Table 4.2 Scattering Cross Sections, C_{scat} for Various Particles

The idealised case of light scattering for LDA measurements is when the scattering cross section is roughly proportional to the geometrical cross section. This condition is met for moderately sized Mie particles. In general, 100μm sized particles are too large for practical LDA measurements. Calculations performed by Meyers (1971) have shown that Rayleigh and Thompson scattering is insufficient to provide an adequate signal-to-noise ratio.

4.4.7.4 Sedimentation and Flocculation

In a quiescent fluid, particles that are not neutrally buoyant rapidly reach their terminal falling velocity as the frictional drag forces become equal to the gravitational forces. This is the free settling condition and the rate of sedimentation is dependent on the size of the fluid column and the magnitude of the terminal falling velocity of the particles. As the concentration of particles increases and the void fraction in the fluid reduces, the sedimentation rate becomes less than the terminal falling velocity and hindered settling occurs. The sedimentation rate for a solution of fine particles is difficult to predict as a large number of parameters are involved. Particles in a polar medium acquire an electric charge and the magnitude of this along with their spatial distribution is largely attributable to the rate at which they will flocculate. The spatial distribution is of course related to their concentration in the liquid medium. For a volumetric constant, C, the suspension viscosity is determined from the Einstein equation:

$$\mu_c = \mu(1 + K'C) \tag{4.38}$$

The voidage in the solution is given by

$$e = (1 - C) \tag{4.39}$$

and the effective buoyancy force is calculated from

$$\rho_s - \rho_c = e(\rho_s - \rho) \tag{4.40}$$

The suggested settling velocity of particles in the fluid can be estimated from

$$u_c = \frac{K'd^2(\rho_s - \rho)g}{\mu_c} \tag{4.41}$$

This holds for C up to 0.02 and the particle shape factor, K' is 2.5 for spheres. For higher concentrated suspensions the solution viscosity is approximated from

$$\mu_c = \mu e^{K'C/(1-a'C)} \qquad (4.42)$$

where a second shape factor, a' is 39/64 for spheres. The complexity of flocculated suspensions and the factors influencing sedimentation make it difficult to predict the sedimentation rate with any accuracy. Most particles are not in a quiescent fluid but in an agitated one and in the case of annular flows, the particles are exposed to a centrifugal field acting orthogonally to the gravitational field and which is potentially several orders of magnitude greater. In such cases it is useful to relate potential sedimentaion to the relative magnitudes of these two fields. Using dimensional analysis the flow field is represented by the particle Reynolds number (or Taylor number) and the gravitational field is represented by the Galileo number. This latter is the ratio of buoyancy forces to viscous forces and is given by

$$Ga = \frac{d_p^{\,3}\rho(\rho_s - \rho)g}{\mu^2} \qquad (4.43)$$

The falling velocity of particles is determined from

$$u_c = \frac{\mu}{\rho d_p}\left[2.33Ga^{0.018} - 1.53Ga^{-0.016}\right]^{13.3}\left[1 + 2.4\frac{d_p}{d}\right]^{-1} e^{-n} \qquad (4.44)$$

The basis of the correlation is a relationship between particle sedimentation in a two phase fluid and one at infinite dilution and is based on a large body of data for quiescent and fluidised systems studied by Khan and Richardson (1989). The sedimentation index, n, in equation (4.44) is evaluated on the basis of a combination of values for Re and Ga and whilst a number of such correlations exist, Garside and Al-Dibouni (1977) use a correlation again

based on a large body of data for both quiescent and fluidised systems which has general application:

$$\frac{5.1-n}{n-2.7} = 0.1 Re_p^{0.9} \qquad (4.45)$$

References

Boadway JD, Karahan E, Correction of Laser Doppler Anemometer Readings for Refraction at Cylindrical Interfaces. *DISA Information* **26** 4-6 (1981)

Bourke PJ, Brown CG, Drain LE, Measurement of Reynolds Stress in Water by Laser Anemometry. *DISA Information* **12** 12-24 (1971)

Braun MJ, Canacci VA, Hendricks RC, Flow Visualisation and Quantitative Velocity and Pressure Measurements in Simulated Angle and Double Brush Seals. *Paper at 45th Annual Metting STLE, Dever, Colorado.* (1990)

Brodkey RS, The Phenomena of Fluid Motions. Dover Publications Inc. New York. (1967)

Budwig R, Refractive Index Matching Methods for Liquid Flow Investigations. *Expt Fluids* **17** 350-355 (1994)

Chen RC, Kadambi JR, LDV Measurements of Solid Slurry Flow Using Refractive Index Matching Technique. *Particulate Sci Technol.* **8** 97-109 (1990)

Chu B, Laser Light Scattering. Academic Press. London. (1974)

Dallavelle JM, Micromeritics. 2nd Edition. Pitman Publishers. London. (1948)

Durst F, Muller R, Jovanic J, Determination of the Measuring Position in Laser-Doppler Anemometry. *Expt. Fluids* **6** 105-110 (1988)

Durst F, Melling A, Whitelaw JH, Principles and Practice of Laser Doppler Anemometry. Academic Press. London. (1976)

Edwards RV, Dybbs A, Refractive Index Matching for Velocity Measurements in Complex Geometries. *ISI Quarterly* **10** (4) 3-11 (1984)

Elias CB, Desai RB, Patole MS, Joshi JB, Mashelkar RA, Turbulent Shear Stress: Effect on Mammalian Cell Culture and Measurement Using Laser Doppler Anemometer. *Chem.Eng.Sci.* **50** (15) 2431-2440 (1995)

Garside J, Al-Dibouni MR, Velocity-Voidage Relationships for Fluidization and Sedimentation in Solid-Liquid Systems. *Ind. Eng. Chem. Proc. Des. Dev.* **16** 206-213 (1977)

Jacobs DA, Jacobs CW, Andereck CD, Biological Scattering Particles for Laser Doppler Anemometry. *Phys. Fluids* **31** (12) 3457-3461 (1988)

Khan AR, Richardson JF, The Resistance to Motion of a Solid Sphere in a Fluid. *Chem. Eng. Commun.* **62** 135-141 (1987)

Khan AR, Richardson JF, Fluid-Particle Interactions and Flow Characteristics of Fluidized Beds and Settling Suspensions of Spherical Particles. *Chem. Eng. Commun.* **78** 111-118 (1989)

Meyers JF, Investigation of Basic Parameters for the Application of a Laser Doppler Anemometer. *AAIA Paper No. 71-288* (1971)

Morrison GL, Johnson MC, Tatterson GB, Three-Dimensional Laser Anemometer Measurements in an Annular Seal. *J.Tribology* **113** 421-427 (1991)

Northrup MA, Kulp TJ, Angel SM, Fluorescent Particle Image Velocimetry: Application to Flow Measurement in Refractive Index Matched Porous Media. *Appl. Optics* **30** 3034-3040 (1991)

Orr C, Particulate Technology. MacMillan Publishers. New York (1966)

Oseen CW, Uber den Gultigkietsbereich der Stokesschen Widerstandsformel. *Ark. Mat. Astr. Fys.* **9** (16) 1-15 (1913)

Parker J, Merati P. An Investigation of Turbulent Taylor-Couette Flow Using Laser Doppler Anemometry in a Refractive Index Matched Facility. *Trans ASME* **118** 810-818 (1991)

Rattray A, Platelet Response to Haemodynamic Shear Forces. Ph.D. thesis. University of Liverpool. (1998)

Schiller L, Naumann A, Uber die Grundlegenden Berechnungen der Schwerkrafttaufbereitung. *Z. Ver. deut. Ing.* **77** 318-320 (1933)

Thompson BE, Refractive Index Matching Techniques in Complex Rocket Engine Flow Configurations. *Paper presented as SRA Contractor Final Report R89-900072-F* (May, 1990)

Wadell H, The Coefficient of Resistance as a Function of Reynolds Number for Solids of Various Shapes. *J. Franklin Inst.* **217** 459-462 (1934)

Chapter 5

Laser Doppler Anemometry: Experimental Measurements and Modelling

Laser Doppler Anemometry measurements have been made in a 2-D plane in the annulus of the systems CC-25 and CC-75 described in Chapter 2 using the Dantec LDA system described in Chaper 4. The measurements have been made over a wide flow range and for each given flow a large velocity data set has been generated for each system. Given this data set, it has been possible to compute in detail the shear stress field that particles in these flows will experience. Before the data is considered, attention is first given to the theory used to make the computation of the shear stress field based on the LDA velocity data.

5.1 Shear Stress Determination from Velocity Data

It is clear that a fluid in static equilibrium experiences no shearing forces, however, a fluid in motion will experience such forces and due to the physical property of viscosity which the fluid possesses, these forces are manifested as shear stresses within the fluid. The shear stresses are related to transverse velocity gradients, or rate of strain components within the fluid

by virtue of its motion. This is analogous to the theory of elasticity applied to an elastic solid where the stress is related to strain, the most simple case of which is Hookes law.

Real fluids do not slip at a solid boundary, irrespective of whether they are in static equilibrium or not. This is an experimental fact and implies that for a fluid flowing parallel to a solid boundary, elements of fluid immediately adjacent to the boundary are stationary. As one moves in a normal direction away from the wall, the velocity will increase until it reaches the free stream velocity. This distance is the boundary layer thickness, and the fluid contained therein is the boundary layer. Typically the boundary layer is thin relative to the complete domain of the fluid motions. Following this, the simplest case of shearing flow is between two parallel plane boundaries, separated by a distance, Δ, one of which is stationary and one which moves with a velocity u_o, say. Under laminar flow conditions a straight-line velocity profile is generated increasing from zero at the stationary boundary to u_o at the moving boundary. The shear stress generated in such circumstances is given by Newton's law of friction.

$$\tau = \mu \frac{u_o}{\Delta} \tag{5.1}$$

The coefficient of viscosity, μ, which is often assumed to be constant can be dependent on the system physical properties, the most significant of which is temperature. An approximate relationship for variation of the coefficient of viscosity with temperature is

$$\mu = \alpha \exp\left(\frac{\beta}{kT}\right) \tag{5.2}$$

where k is the thermal conductivity of the material. The viscosity is dependent on the material and is left to experimental measurement to evaluate the constants α and β in equation (5.2), but it is apparent that the viscosity generally decreases with increasing temperature. Experimental

data for water viscosity and kinematic viscosity is shown in Table 5.1 from Kay (1990).

Temperature, T (°C)	0	20	40	60	80	100
Viscosity, μ (Pas) E-03	1.79	1.01	0.656	0.469	0.357	0.284
Kinematic Viscosity, ν (m^2s^{-1}) E-06	1.79	1.01	0.661	0.477	0.367	0.296

Table 5.1 Viscosity-Temperature Variation for Water

5.2 Local and Global Shear Determination

In the case of equation (5.1) above for uniform shear flow, the shear stress is constant. More generally, for a two-dimensional fluid stream having undisturbed free stream velocity u_1 flowing past a solid wall, the boundary layer that is developed is indicated in Figure 5.1

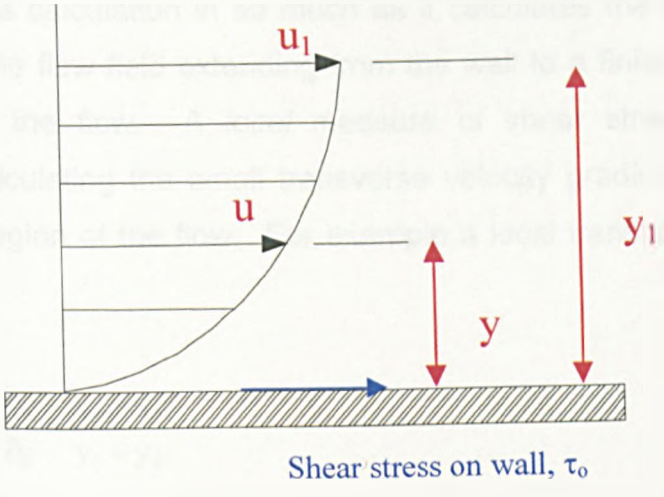

Figure 5.1 Uniform Shear Flow and Wall Shear Stress

The fluid velocity u is only a function of y which is the distance measured normal to the wall. The magnitude of u will increase from zero at the wall to the free stream value, u_1 at $y=y_1$. At any level *y*, the shear stress is given by

$$\tau = \mu \frac{du}{dy} \tag{5.3}$$

For $y > y_1$ the shear stress is zero due to there being no change in the transverse velocity gradient (du/dy). In reality, it is often the case that another solid boundary will exist and be met as y_1 continues to increase, as would be the case for a two-dimensional pipe flow, for example. In such a case, another boundary layer would be observed as the other boundary is approached. Normal practice therefore, is to take the maximum value of y_1 to be at the midpoint of two given boundaries or what would the point of maximum free stream velocity. It is this latter case that is assumed when referring to Figure 5.1. As y decreases, the magnitude of the shear stress will increase until a maximum value of shear stress, τ_o is reached at the wall

$$\tau_o = \mu \left(\frac{du}{dy} \right)_{y=0} \tag{5.4}$$

The shear stress calculated by equation (5.3) might be considered as a *global* shear stress calculation in so much as it calculates the shear stress over a region of the flow field extending from the wall to a finite distance, in this case y, into the flow. A *local* measure of shear stress might be determined by calculating the small transverse velocity gradients occurring within a smaller region of the flow. For example a local transverse gradient could be given by

$$\tau = \mu \frac{\partial u}{\partial y} = \frac{u_3 - u_2}{y_3 - y_2} \tag{5.5}$$

5.3 Non-Newtonian Flow Phenomena

In equation (5.3) a linear relationship is assumed to exist between the shear rate and the shear stress; a constant viscosity is found for any shear rate applied to the fluid. This is often found not to be the case for real fluids, and some form of non-linear relationship is found to relate the shear stress and shear rate where the viscosity is shear dependent. This behaviour is almost entirely dependent on the material property and is estimated from carefully controlled shear stress-shear rate measurements in a rheometer. A good biological example of this non-Newtonian flow behaviour is blood. The viscosity of blood for varying shear rate is shown in Figure 5.2 for a number of different experiments taken from the literature. It is evident from this data that no unique rheology curve exists for blood and that the behaviour can vary among different samples. This is instructive from two viewpoints. The first is that rheological behaviour is strongly dependent on the fluid structure and that biologically this can widely vary and this leads to the second point that in experimental measurements it is vitally important to maintain physico-chemical uniformity between the samples of subsequent experiments if comparisons are to be made. A number of non-linear models exist for non-Newtonian flows and these are often based on rheological measurements made on polymeric fluids. These types have fluids have been used as analogues for blood and other biological fluids to experimentally model flows in the vasculature and other parts of the body. Whilst a number of these can provide a good rheological model to the real bio-fluid in a fixed range of shear rate they are normally not sufficient for the whole range of shear rates that would be encountered in nature and reaching this goal remains to be an active research area. A summary of the non-Newtonian mathematical models used for bio-fluids are listed in Table 5.2. Some of these have been used to fit* the experimental rheology data of Figure 5.2 and the results are shown in Figures 5.3, 5.4 and 5.5. It is evident that some of the more complex models that incorporate the viscoelastic components of the blood better approximate the rheological behaviour over a wider range of shear rate

* Experimental data of Figure 5.2 fitted by multiple non-linear least squares regression using the rheology models of Table 5.2

but deviations occur at the lower and higher end of the shear rate range. A summary of the model parameters obtained is shown in Table 5.3. If a generalised correlation is available to relate the rheology of a more complex fluid to that of a simple fluid for similar shears on the macroscale (and this can be achieved using rheometry), then it might be possible to make an apriori estimation of what might happen at the micro (cellular) scale in a complex fluid on the basis of microscale flow measurements made by LDA in the simple fluid.

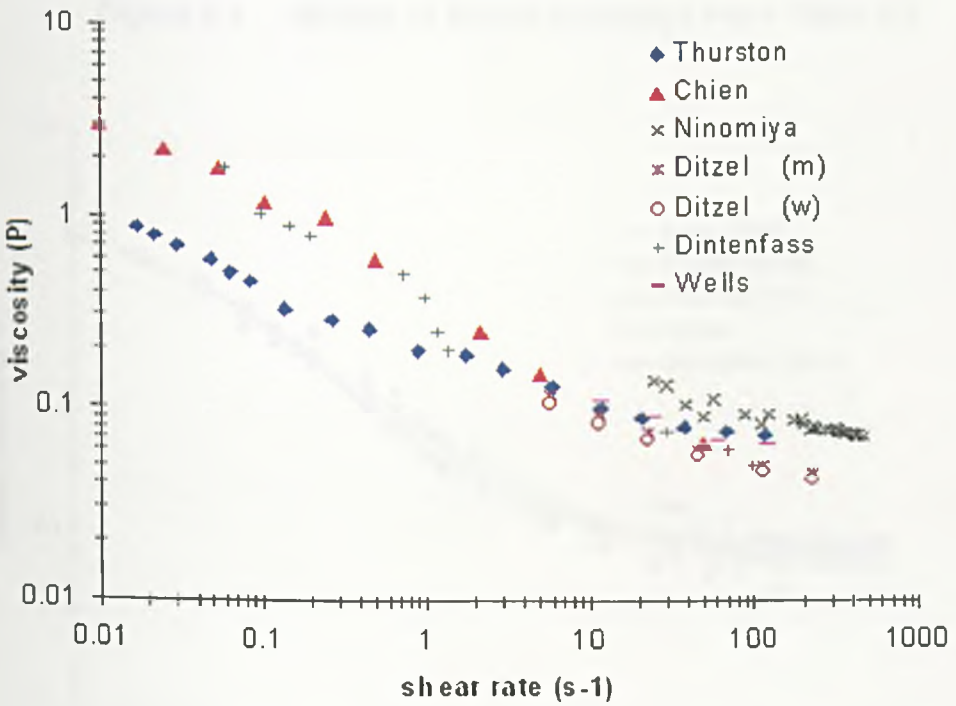

Figure 5.2 Human Blood Viscosity Data taken from literature

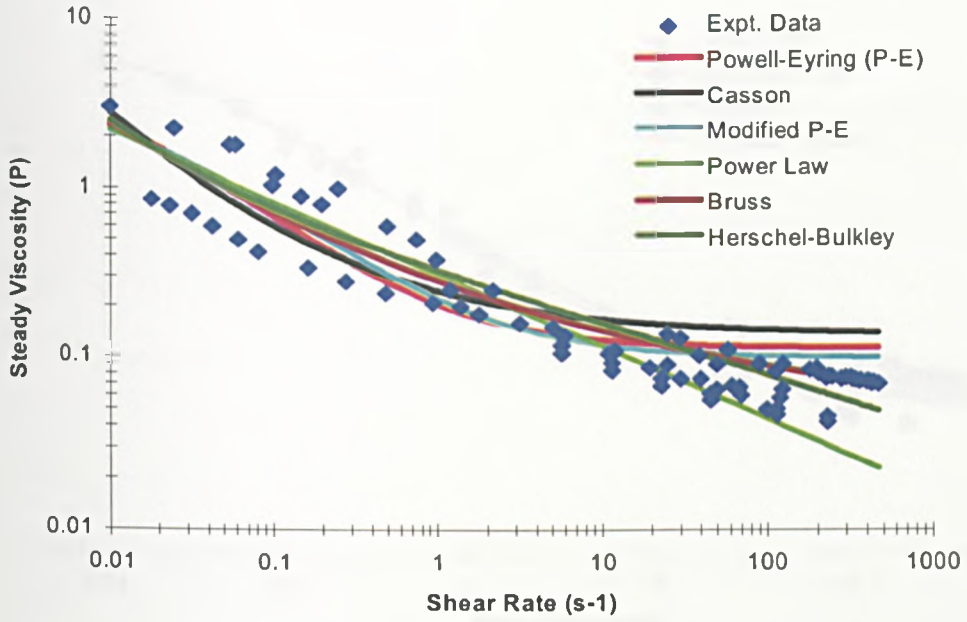

Figure 5.3 Models of Blood Rheology from Table 5.2

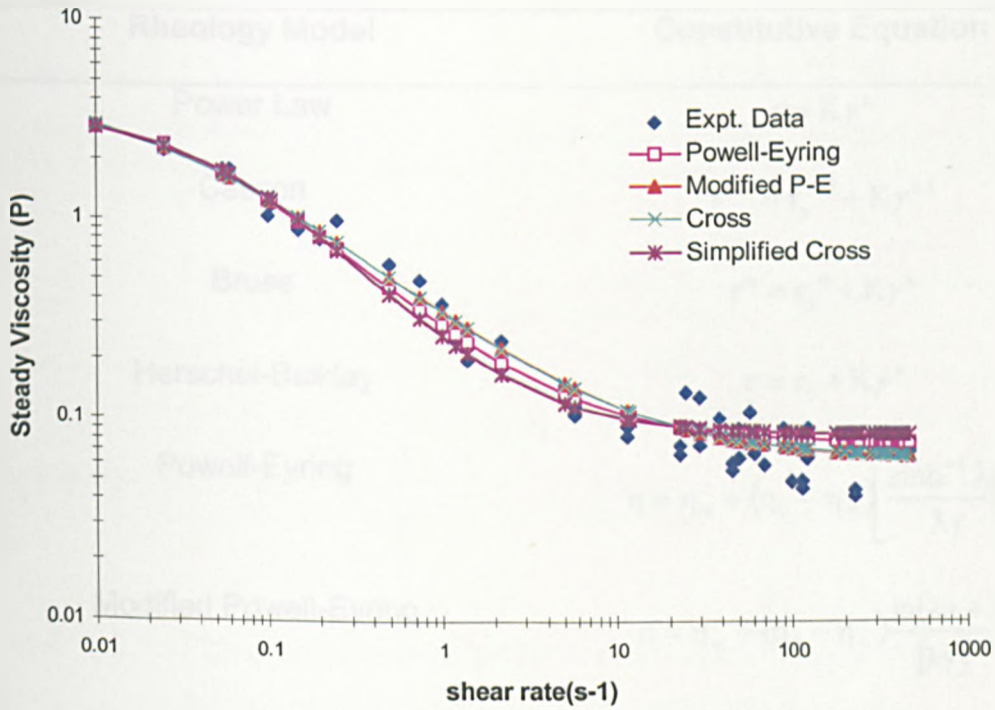

Figure 5.4 Models of Blood Rheoloy from Table 5.2[+]

[+] The data of Thurston shown in Figure 5.2 is omitted in the modelling data for Figures 5.4 and 5.5

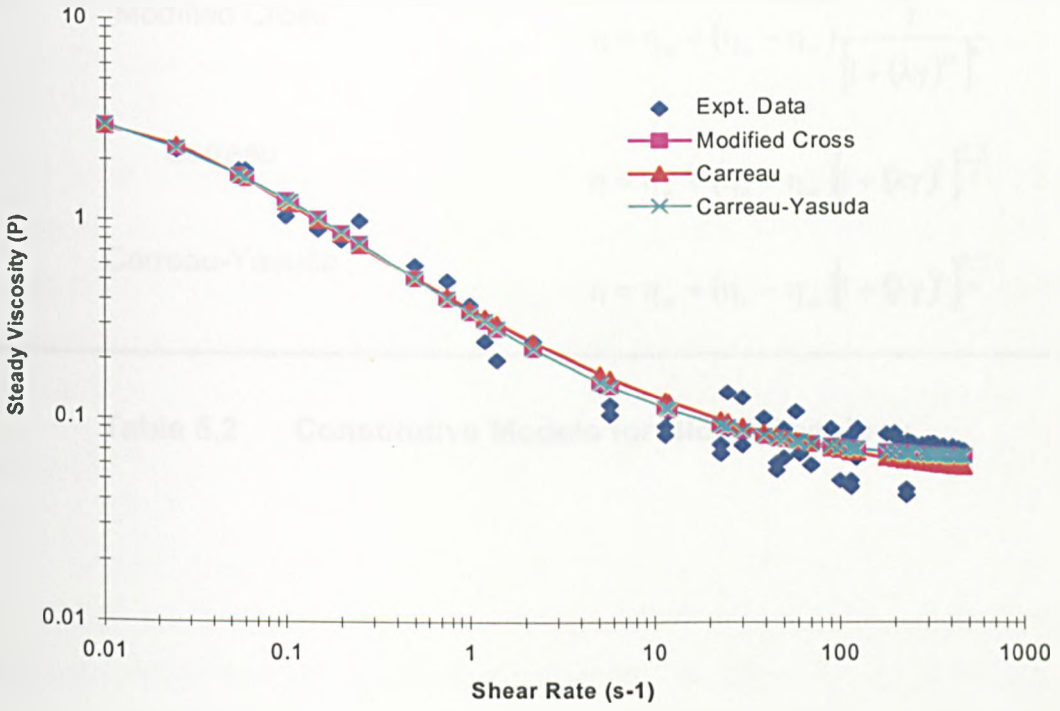

Figure 5.5 Models of Blood Rheology from Table 5.2

Rheology Model	Constitutive Equation
Power Law	$\tau = K\dot{\gamma}^{n}$
Casson	$\tau^{0.5} = \tau_y^{0.5} + K\dot{\gamma}^{0.5}$
Bruss	$\tau^{n} = \tau_y^{n} + K\dot{\gamma}^{n}$
Herschel-Bulkley	$\tau = \tau_y + K\dot{\gamma}^{n}$
Powell-Eyring	$\eta = \eta_\infty + (\eta_o - \eta_\infty)\left[\frac{\sinh^{-1}\lambda\dot{\gamma}}{\lambda\dot{\gamma}}\right]$
Modified Powell-Eyring	$\eta = \eta_\infty + (\eta_o - \eta_\infty)\frac{\ln(\lambda\dot{\gamma}+1)}{[\lambda\dot{\gamma}]^{n}}$
Cross	$\eta = \eta_\infty + (\eta_o - \eta_\infty)\frac{1}{1+(\lambda\dot{\gamma})^{m}}$
Simplified Cross	$\eta = \eta_\infty + (\eta_o - \eta_\infty)\frac{1}{1+\lambda\dot{\gamma}}$

Modified Cross	$\eta = \eta_\infty + (\eta_o - \eta_\infty)\frac{1}{\left[1+(\lambda\gamma)^m\right]^a}$
Carreau	$\eta = \eta_\infty + (\eta_o - \eta_\infty)\left[1+(\lambda\gamma)^2\right]^{\frac{n-1}{2}}$
Carreau-Yasuda	$\eta = \eta_\infty + (\eta_o - \eta_\infty)\left[1+(\lambda\gamma)^a\right]^{\frac{n-1}{a}}$

Table 5.2 Constitutive Models for Blood Rheology

Model	Equation	τ_y (Pa)	K	n	sd
Casson	(1.1)	1.303E-02	0.368	0.5	0.275
Power Law	(1.12)	0	0.311	0.575	0.263
Bruss	(1.4)	1.693E-04	0.504	0.205	0.261
Herschel-Bulkley	(1.2)	1.185E-03	0.320	0.695	0.258

Model	Equation	η_o (Pas)	η_∞ (Pas)	λ (s)	m	sd
Powell-Eyring	(1.5)	3.128E-01	1.138E-02	189	-----	0.277
Modified Powell-Eyring	(1.6)	3.272E-01	9.900E-03	123	1	0.274

Table 5.3 Fitted parameters for blood rheology models listed in Table 5.2 by multiple least squares regression

5.4 Rate of Strain: Considerations on Spatial Resolution in the Calculation

In a simple two-dimensional system indicated in Figure 5.1, the tranverse velocity gradient is one-dimensional and there is just this one component for the rate of strain in the fluid. This is taken to be the shear rate, γ and for a Newtonian fluid the relationship holds that

$$\gamma = \frac{\partial u}{\partial y} \tag{5.6}$$

In a real three-dimensional fluid flow system, there are three components for the fluid velocity and three space dimensions. Additionally, for non-steady flows there will be the time domain that, in effect, can be considered as another dimension. For complete resolution of the rate of strain at a point in the fluid the rate of strain tensor requires calculation at that point in the fluid and so considerations on the relative motion in the neighbourhood of the point must be made. As indicated in equation (5.5) there is some choice to be made on the resolution of the calculation that is required for local rate of strain determinations. There are certain criteria that can be used to assist in these choices:

- Knowledge of the velocity vectors in the flow field is required to compute rate of strain calculations. The accuracy and resolution of these data is important for deciding on a resolution basis to make the rate of strain computation. This is often determined by the instrument used to make the measurements of velocity in the flow field. Clearly if an instrument is used which does not measure all three velocity components at a given point in the flow field then the calculation of the rate of strain at that point will be equally restricted.
- If the accuracy of the data that is measured is very good and is very reliable, it might then be possible to interpolate the observed data to achieve a higher spatial resolution which may improve the local rate of strain data.

- The spatial resolution of the rate of strain computations should be comparable to the spatial resolution of a typical fluid element on which the effect of shear is required to be known. For example, if there is interest in the shearing effects on large particles in the flow field, a spatial resolution comparable to the particle size is recommended. Equally, if one is interested in the shear stresses required to disrupt a large floc into its component elements then a larger resolution would suffice. However if the interest is on the shearing effects on the elemental pieces of the floc then a much smaller spatial resolution would then be required. In short, it is necessary to tailor the spatial requirements of the calculation to the needs of the problem, and in some instances perform sequential calculations with refined spatial resolution.

5.5 Rate of Strain: Mathematical Formulation of the Problem

With the considerations of Section 5.4 in mind the mathematics of the problem can be developed. Consideration of a position vector $\boldsymbol{r}$ is first required. The coordinates of $\boldsymbol{r}$ are based on a chosen orthogonal coordinate system. The most common orthogonal system is the Cartesian (x, y, z as a cubic grid) system and the following discussion uses this system as a basis in the main. The particular problem of concentric cylinder flow is best approached using a cylindrical coordinate system; r, ϕ, z. The fluid velocity at any given position $\mathbf{r}$ in the system is $\boldsymbol{u}$ (associated as u, v, w in Cartesian coordinates and u_r, u_ϕ, u_z in cylindrical coordinates). At a neighbouring location $(\boldsymbol{r} + d\boldsymbol{r})$ the velocity is given by $(\boldsymbol{u} + d\boldsymbol{u})$. The differential velocity is then given by

$$d\mathbf{u} = (d\mathbf{r} \cdot \nabla)\mathbf{u} \qquad (5.7)$$

The fluid vorticity requires introduction at this stage, and although it is not of importance in the calculation of the rate of strain for a Newtonian fluid, it can be significant for non-Newtonian fluids and is thus included for

completeness of the generalised flow problem. The vorticity ω of a fluid can be thought of as a form of angular velocity and is therefore a vector quantity. It is defined mathematically as the curl of the vector velocity **u** so

$$\omega = \text{curl}\,\mathbf{u} = \nabla \times \mathbf{u} \tag{5.8}$$

The components of vorticity for a Cartesian coordinate system are

$$\omega_x = \left(\frac{\partial w}{\partial y} - \frac{\partial y}{\partial z}\right), \omega_y = \left(\frac{\partial u}{\partial z} - \frac{\partial w}{\partial x}\right), \omega_z = \left(\frac{\partial v}{\partial x} - \frac{\partial u}{\partial y}\right) \tag{5.9}$$

For practical problems in rotational flow, which relates to the particular study of concentric cylinder flows, the cylindrical coordinate system for vorticity components is more appropriate

$$\text{r direction} \quad \omega_r = \left(\frac{1}{r}\frac{\partial u_z}{\partial \phi} - \frac{\partial u_\phi}{\partial z}\right)$$

$$\phi \text{ direction} \quad \omega_\phi = \left(\frac{\partial u_r}{\partial z} - \frac{\partial u_z}{\partial r}\right)$$

$$\text{z direction} \quad \omega_z = \left(\frac{u_\phi}{r} - \frac{\partial u_\phi}{\partial r} - \frac{1}{r}\frac{\partial u_r}{\partial \phi}\right) \tag{5.10}$$

The differential velocity of equation (5.7) is expressed in its full form as

$$du = \frac{\partial u}{\partial x}dx + \frac{\partial u}{\partial y}dy + \frac{\partial u}{\partial z}dz \tag{5.11}$$

where similar expressions can be written for dv and for dw by substitution of v and w for u. These can be further written in an alternative form that also incorporates components of the vorticity vector ω

$$
\begin{aligned}
du &= e_{xx}dx + e_{yx}dy + e_{zx}dz + \tfrac{1}{2}(0 - \omega_z dy + \omega_y dz) \\
dv &= e_{xy}dx + e_{yy}dy + e_{zy}dz + \tfrac{1}{2}(\omega_z dx + 0 - \omega_x dz) \\
dw &= e_{xz}dx + e_{yz}dy + e_{zz}dz + \tfrac{1}{2}(-\omega_y dx + \omega_x dy + 0)
\end{aligned}
\qquad (5.12)
$$

The form of the differential velocity in equation (5.12) accounts for all the forces the fluid element may experience in three dimensions namely, expansion (or contraction), shearing and rotation. The shearing and expansion (or contaction) terms can be decoupled from the rotational effects by expressing the velocity gradient tensor ($\partial u_i/\partial x_j$) as the sum of a *symmetric tensor* and an *antisymmetric tensor.* The symmetric tensor represents the rate of strain on the fluid element including both the effects of extension (or contraction) and shearing and takes the general form

$$
e_{ij} = \frac{1}{2}\left(\frac{\partial u_i}{\partial x_j} + \frac{\partial u_j}{\partial x_i}\right) \qquad (5.13)
$$

The components of the rate of strain tensor can now be written out in full as

$$
\begin{aligned}
&e_{xx} = \frac{\partial u}{\partial x}, \; e_{yy} = \frac{\partial v}{\partial y}, \; e_{zz} = \frac{\partial w}{\partial z} \\
&e_{xy} = e_{yx} = \frac{1}{2}\left(\frac{\partial u}{\partial y} + \frac{\partial v}{\partial x}\right) \\
&e_{yz} = e_{zy} = \frac{1}{2}\left(\frac{\partial v}{\partial z} + \frac{\partial w}{\partial y}\right) \\
&e_{zx} = e_{xz} = \frac{1}{2}\left(\frac{\partial w}{\partial x} + \frac{\partial u}{\partial z}\right)
\end{aligned}
\qquad (5.14)
$$

The antisymmetric tensor accounts for the rotation of the fluid element and is given by

$$\xi_{ij} = \frac{1}{2}\left(\frac{\partial u_i}{\partial x_j} - \frac{\partial u_j}{\partial x_i}\right) \tag{5.15}$$

The rate of rotation, or angular velocity, of a fluid element is equal to half the magnitude of the vorticity vector which is clearly evident from comparisons of equations (5.9) and (5.14). However, for the case of a Newtonian fluid, a simple linear relationship exists between the stress tensor, τ_{ij} and the velocity gradient tensor ($\partial u_i/\partial x_j$) and coupled with the conditions of symmetry, the antisymmetric tensor becomes uninvolved in the relationship. The rate of strain tensor can now be expressed completely in three dimensions and in Cartesian coordinates in the following general format

$$e_{ij} = \begin{bmatrix} e_{xx} & e_{yx} & e_{zx} \\ e_{xy} & e_{yy} & e_{zy} \\ e_{xz} & e_{yz} & e_{zz} \end{bmatrix} \tag{5.16}$$

Substitution for the components of the rate of strain tensor is made using equation (5.14)

$$e_{ij} = \begin{bmatrix} \frac{\partial u}{\partial x} & \frac{1}{2}\left(\frac{\partial u}{\partial y} + \frac{\partial v}{\partial x}\right) & \frac{1}{2}\left(\frac{\partial w}{\partial x} + \frac{\partial u}{\partial z}\right) \\ \frac{1}{2}\left(\frac{\partial u}{\partial y} + \frac{\partial v}{\partial x}\right) & \frac{\partial v}{\partial y} & \frac{1}{2}\left(\frac{\partial v}{\partial z} + \frac{\partial w}{\partial y}\right) \\ \frac{1}{2}\left(\frac{\partial w}{\partial x} + \frac{\partial u}{\partial z}\right) & \frac{1}{2}\left(\frac{\partial v}{\partial z} + \frac{\partial w}{\partial y}\right) & \frac{\partial w}{\partial z} \end{bmatrix} \tag{5.17}$$

Given the particular problem of concentric cylinder flow, it is appropriate at this stage to modify equation (5.17) such that the coordinate system is cylindrical rather than Cartesian and an expression for the rate of strain tensor can be used directly in the concentric cylinder study. Doing this,

$$e_{ij} = \begin{bmatrix} \frac{\partial u_r}{\partial r} & \frac{1}{2}\left(\frac{\partial u_r}{\partial \phi} + \frac{\partial u_\phi}{\partial r}\right) & \frac{1}{2}\left(\frac{\partial u_z}{\partial r} + \frac{\partial u_r}{\partial z}\right) \\ \frac{1}{2}\left(\frac{\partial u_r}{\partial \phi} + \frac{\partial u_\phi}{\partial r}\right) & \frac{\partial u_\phi}{\partial \phi} & \frac{1}{2}\left(\frac{\partial u_\phi}{\partial z} + \frac{\partial u_z}{\partial \phi}\right) \\ \frac{1}{2}\left(\frac{\partial u_z}{\partial r} + \frac{\partial u_r}{\partial z}\right) & \frac{1}{2}\left(\frac{\partial u_\phi}{\partial z} + \frac{\partial u_z}{\partial \phi}\right) & \frac{\partial u_z}{\partial z} \end{bmatrix} \quad (5.18)$$

In equation (5.18) the rate of strain tensor contains both the strains due to shearing effects where the flow is tangential to the fluid element and the normal strain effects that may be either extensional or compressive and exist due to fluid motions normal to the fluid element. These latter effects are mathematically given by the diagonal elements of the matrix in equation (5.18). The other components of the matrix are the shearing strains.

5.6 Application of the Rate of Strain Tensor to LDA Data

LDA data has been obtained in a 2-D meridional plane of the annulus between the two cylinders. The configuration is illustrated in Figure 5.6. The velocity components of the real 3-D flow are included in this figure. Of these, only the azimuthal component of velocity (u_ϕ) and the axial component of velocity (u_z) are measured at each nodal point in the domain using Laser Doppler Anemometry. No measurement of the radial velocity component (u_r) is made.

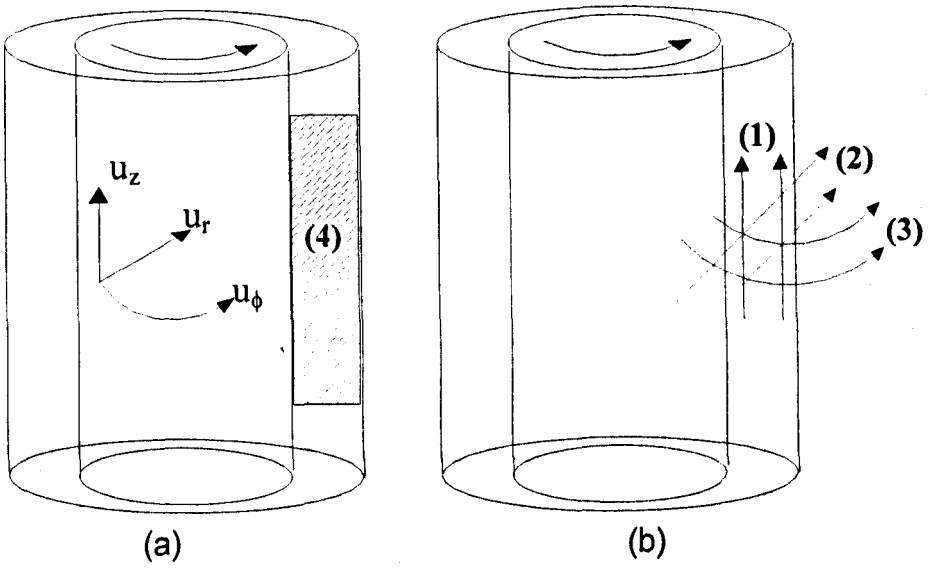

Figure 5.6 Schematic representation of annular flow with a rotating inner cylinder (a) and the shearing forces resulting from 2-D LDA velocity measurements (b)

The meridional plane in which velocity measurements are taken is illustrated as **(4)** in Figure 5.6(a) and is composed of a 2-D grid of nodal points at each of which a burst sample of LDA data is collected of a prescribed size of $2x10^5$ bursts. The known wall velocities for the inner and outer cylinders were used to generate an acceptable bandwidth for the data. Data outside two standard deviations of the mean value obtained from the Gaussian distribution of the burst sample was removed. The number and spatial resolution of nodal points in this meridional domain are predetermined for a given flow state to ensure that sufficient velocity data is collected in a continuous collection mode. This means that data is collected for every point in the domain with no interruptions either to the flow state or to the Burstware program. The resolution, size and location of the domain has been varied for a large number of experimental LDA measurements depending on the given flow state to ensure a given velocity data set is reproducible at different locations in the annular space if the flow is well structured, uniform and equilibrated. Samples of these data are presented in detail later. These are representative of the larger group of data that has been collected to form

more general conclusions on the flow transitions, shear stress determinations and effect on scaling.

The LDA data is collected for nodal points moving from the outer cylinder to the inner cylinder in a radial direction. The velocity data recorded at these points taken together can provide a mean velocity profile in 1-D across the gap. The nodal points which form radial lines of velocity data are successively collected moving vertically downwards through the annular gap thereby allowing a 2-D mean velocity flowmap to be generated. The reason for measurement firstly in a radial direction and then progressing vertically downwards each time lies in defficiencies of the experimental facility used to make the LDA measurements. It has been described in Chapter 3 that a refractive index matched facility is required to obtain accurate velocity from LDA measurements. To achieve this, the present reactor is of PMMA construction and sunflower oil has been used to make a refractive index match between the rotating walls. There has been some problems with the rotary seals particularly on the larger outer wall which has meant that over the time period required for complete data collection in a meridional domain there has been sufficient leakage of oil such that the PMMA-oil-PMMA continuous path required to ensure refractive index matching was broken and the laser encountered a PMMA-air-PMMA path. Such a circumstance results in a zero data rate for LDA collection and causes the software to crash in post-processing of the data. For this reason, LDA measurements that allowed the probe beam to collect all radial points and then move axially downwards was employed. This ensured that the probe beam always passed through an oil medium. In an exaggerated sense, the laser beam was continually "chased" by the dropping oil level; the beam was always below the level of the oil. At a later time, a header tank was used to maintain a relatively constant oil level, but the method of data collection moving radially from outer to inner cylinder and then axially downwards was continued since it placed stringent demands on the subsequent software programs for matrix computations.

The data collected at each nodal point in the domain requires averaging numerically to obtain a representative mean velocity at that point. Given a good estimate of the mean velocity, it is then possible to determine

fluctuating velocities away from the mean using the whole of the burst sample at that nodal point in the domain. The raw data sampled at each point is numerically processed in Matlab using procedures described in foregoing theory as the basis of calculation. Software has been purposely written to sequentially read in the LDA burst data file obtained at a single nodal point in the domain and average it. Given the size of the domain and the number of nodal points, the program will generate a matrix equivalent to the domain size where the matrix elements correspond to the nodal points of the domain. The ensemble averaged velocity at each nodal point is then read in to the corresponding element of the matrix. Using this procedure, separate matrices are generated for the two components of the velocity that are measured by LDA, namely, u_ϕ and u_z. On the basis of the two matrices that now exist for mean flow velocity components and a knowledge of the corrsponding dimensions of neighbouring elements of the matrix to the real 2-D flow domain, the rate of strain tensor can now be implemented to calculate relative changes in velocity with space in the real domain.

Equation (5.18) contains all the components required for complete calculation of the rate of strain on a fluid element in three dimensions, however the spatial domain for measurement and the components of velocity that are measured, mean that not all of the components of equation (5.18) can be used in the calculation. It is important to determine which components can be calculated and what they relate to in terms of fluid motion on a given element in the spatial domain. Spatial changes exist radially (r-dimension) and axially (z-dimension) in the 2-D meridional domain. Clearly, no spatial changes can exist in the azimuthal (ϕ-direction) else this would constitute a 3-D domain and therefore changes in $\partial\phi$ cannot be included in calculations. Only the radial component of velocity is not measured in the domain. Three possible shearing strains can therefore be measured on a fluid element given this measurement configuration and these are illustrated in Figure 5.6(b) as **(1)**, **(2)**, and **(3)**.

(1) represents azimuthal velocity changes, u_ϕ with changes in the radial direction and is represented by $(\partial u_\phi/\partial r)$. This can be calculated as part of any component of equation (5.18).

(2) represents azimuthal velocity changes, u_ϕ in the axial direction and is represented by $(\partial u_\phi/\partial z)$. This can be calculated as part of any component of equation (5.18).

(3) represents axial velocity changes, u_z in the radial direction and is represented by $(\partial u_z/\partial r)$. This can be calculated as part of any component of equation (5.18).

No other part of any shear strain component can be determined either because that part of the velocity component is not measured or because the 2-D domain restriction means no spatial change can be made.

Of the normal strains that the fluid can experience, calculated using the diagonal elements of the matrix of equation (5.18), only one can be calculated, $(\partial u_z/\partial z)$. Again, the other two normal strains cannot be evaluated since the radial component is not measured and no changes in the azimuthal direction can be determined. This means only axial compression (or extension) will be accounted for in the overall rate of strain calculation.

Given the restrictions outlined above, it now remains to simplify equation (5.18). This is

$$e_{ij} = \begin{bmatrix} 0 & \frac{1}{2}\left(\frac{\partial u_\phi}{\partial r}\right) & \frac{1}{2}\left(\frac{\partial u_z}{\partial r}\right) \\ \frac{1}{2}\left(\frac{\partial u_\phi}{\partial r}\right) & 0 & \frac{1}{2}\left(\frac{\partial u_\phi}{\partial z}\right) \\ \frac{1}{2}\left(\frac{\partial u_z}{\partial r}\right) & \frac{1}{2}\left(\frac{\partial u_\phi}{\partial z}\right) & \frac{\partial u_z}{\partial z} \end{bmatrix} \qquad (5.19)$$

5.7 Limitations of the Two-Dimensional Rate of Strain Calculation

It should be noted at this stage that calculation of the rate of strain on a fluid element using the two dimensional approach is clearly restricted and that the final calculated value for the rate of strain will be smaller than the actual case for a three dimensional analysis. For the flow states investigated however, the contribution of the radial velocity component to the overall strain rate is small relative to the contributions of the other two components of velocity. For laminar Couette flows, an azimuthal solid body rotation of the fluid should exist where the radial and axial components of velocity are zero so the flow field is two-dimensional in the axial and radial field with azimuthal symmetry. As the Taylor number is increased to the point investigated in this study, wavy Taylor vortex flow is reached. Even under these circumstances the azimuthal wavelength of wavy vortex flow is far greater than the axial wavelength and this implies much greater shear disturbance in the axial direction than in the radial direction. Many of the reported data in this area are typically based on CFD simulations of the flow, normally assuming a 2-D flow in the r-z plane with azimuthal symmetry, following the line of calculation here (Ashwin 1997; Howes 1998; King 2001; Majumdar 1977; Moser 1983; Wereley 1994, 1998). CFD codes clearly work with an idealized system where calculations follow a simplified equation system and where calculations of such values such as rate of strain and shear stress use idealised velocity data within the field based on fixed boundary conditions. The LDA data used here are measured values for a real system and the subsequent calculations have a strong experimental basis from the outset. Thus the stress calculations here are more realistic than CFD models and can be used to validate CFD for a real system in a 2-D meridional measurement plane.

5.8 Pseudo-Shear Rate from Rate of Strain Data

The rate of strain calculation that can now be made consists of a number of shearing strains and one normal strain after imposing the restrictions of the measurement configuration. In an incompressible fluid,

however, the strain rate at a *point* can be decomposed into the sum of pure compressions and pure extensions. With an appropriate set of orthogonal axes, no shear strains exist and point deformation of the fluid element is due only to extensive and compressive strains. A detailed discussion on this concept has been given by Chong (1990). Generally, the flow at a point can be one of three types, with

- compression along one axis and extension along the other two,
- compression along one axis, extension along the second and no strain along the third,
- compression along two axes and extension along the third.

Equation (5.7) above can otherwise be expressed using the rate of strain tensor as

$$\mathbf{du} = \mathbf{e}_{ij}\mathbf{r} \tag{5.20}$$

or written in its generalised form in cylindrical coordinates as

$$\begin{pmatrix} du_r \\ du_\phi \\ du_z \end{pmatrix} = \begin{pmatrix} e_{11} & e_{12} & e_{13} \\ e_{21} & e_{22} & e_{23} \\ e_{31} & e_{32} & e_{33} \end{pmatrix} \begin{pmatrix} r \\ \phi \\ \theta \end{pmatrix} \tag{5.21}$$

This can be solved as an eigenvalue problem whose eigenvectors are ε and whose eigenvalues are λ

$$[\mathbf{e} - \lambda\mathbf{I}]\varepsilon = 0 \tag{5.22}$$

The eigenvectors clearly define the orthogonal coordinate system along which the fluid motions occur and these motions are now considered to have a purely extensive or purely compressive effect. The eigenvalues can be determined by solving the characteristic equation

$$\det[\mathbf{e}-\lambda\mathbf{I}]=0 \tag{5.23}$$

Negative eigenvalues indicate a compressive strain whereas positive eigenvalues will indicate an extensional strain. The magnitude of the extension or compression is simply the magnitude of the eigenvalue. The eigenvectors clearly vary from point to point in the flow and so too does the sign and magnitude of the eigenvalues. This reiterates the point that this analysis is a *local* analysis and is valid only in the vicinity of the point of the flow at which the rate of strain is calculated. The spatial resolution between the neighbouring points will again influence the magnitude of the resulting eigenvalues. At a different point in the flow, the rate of strain tensor will of course be different, as will the magnitudes and directions of the local compressive and extensive fluid motions.

A pseudo-shear rate is used to quantify deformations on a fluid element assuming only compressive and extensional strains. The assumption of the fluid being incompressible has to be valid for this interpretation of element deformation to be true. The pseudo-shear rate, γ, has been used for shear rate computations for Taylor-vortex flow using CFD by Rudman (1998) and is given by

$$\gamma=\left(2\sum_{i=1}^{3}\sum_{j=1}^{3}e_{ij}e_{ij}\right)^{\frac{1}{2}} \tag{5.24}$$

γ is the square root of twice the contraction of e_{ij} with itself and although this may not be best correlated to the deformation of a fluid element in every circumstance it must be remembered that in an incompressible fluid there cannot be extension without compression, therefore, a large extension necessarily implies a large compression which both imply a large deformation, or γ value.

5.9 Application of Rate of Strain Data for Non-Newtonian Fluids

Baaijens (1993) has addressed the use of a 2-D rate of strain model in the calculation of shear stresses exerted in non-Newtonian fluids. In this case blood flow is modelled numerically and the rheological equations used are the Power Law and Casson models. The form of equation (5.24) is verified by Baaijens from first principles assuming isothermal, incompressible and simple shear flow in 2-D domain using the continuity and momentum equations for a Newtonian fluid. The pseudo-shear rate that results from equation (5.24) is then be substituted into an appropriate rheological model to investigate the non-Newtonian effect on shear stress for the same shearing conditions. This suggests that on the basis of shear rate data determined for a Newtonian fluid it can be translated to a non-Newtonian model by substitution of the shear rate data into the model and thereby make a comparison of the Newtonian and non-Newtonian shear stress effect for a prescribed flow condition. This approach might be useful in a-priori estimations of the shear stresses on cells in non-Newtonian media on the basis of measurements in Newtonian media.

5.10 Spatial Resolution and Velocity Profiles from LDA Data

5.10.1 CC-25

The spatial resolution for the nodal points of LDA measurement in the system CC-25 was 0.05mm radially and 0.5mm axially. The number of nodal points in the 2-D domain given this resolution was variable depending on the flow condition identified by the Taylor number. Fewer points were used for more disturbed flows since disturbances in the near wall boundary layers provided spurious data in this region, so data for the near wall regions was left to interpolation described in Section 5.12. 1-D velocity profiles radially across the gap were initially generated at fixed axial positions to provide an indication of the flow disturbance. A series of these, for different axial positions in the gap, were superimposed to assess axial disturbance of the flow. The velocity profiles were generated for both the azimuthal and the

axial velocity components. Some of these profiles are shown in the following sections where the radial distance is taken from the outer stationary wall and increases as progression is made to the moving inner wall. The axial distance increases for progression vertically up the annulus. The U-component velocity is the azimuthal velocity (u_φ) and the V-component velocity is the axial velocity (u_z).

5.10.1.1 Laminar Couette Flow

In Figure 5.7.1 the profiles are for Ta_i = 35.07 that corresponds to a laminar Couette flow just below transition to laminar Taylor-vortex flow from flow visualisation studies. The wall speed of the rotating inner cylinder to generate this Ta_i is $0.12ms^{-1}$. This allows for reasonably accurate interpolation for the near wall velocities. For a purely laminar Couette flow the ideal theoretical velocity profile for the azimuthal velocity component would be a straight line with velocity zero at the stationary wall increasing to the inner wall rotating velocity. In practice, artefacts of the system including imperfect refractive index matching, particle dispersion and most notably imperfections in system geometry will cause deviations away from this. The probe volume of the LDA beam intersection will serve to give variation in the observed velocity within it. The major diameter of the probe was 180μm so it would not be possible to obtain accurate data for velocities closer to the wall than this. The axial component of velocity ideally would be a straight line with all points having zero velocity. Deviations from this may be observed due sedimentation effects of particles or small imposed axial motions. In Figure 5.7.1(a) the velocity profile deviates off from a straight line approximately 0.6mm in from the outer wall and a small disturbance is observed as the outer wall is approached. This is expected as Ta_i for the flow is very close to the critical point for transition to Taylor-vortex flow. The effect of disturbance throughout the annular gap can be observed in Figure 5.7.1(c) for 41 different axial positions superimposed onto each other. In general, axial disturbance both radially across the gap and axially up the gap is small and this expected for a laminar flow. The disturbance in the axial velocity component initially appears large and erratic in Figure 5.7.1(b)

however the magnitude of the disturbance is very small. The velocity component is small and negative and in the system configuration this is indicative of particles moving very slowly downwards in the annulus, in other words very slow sedimentation. For the superimposed condition of 41 axial positions in Figure 5.7.1(d) it is evident that sedimentation is not uniform at any axial position in the system and this would indicate that there is no fixed axial disturbance in the flow pattern which is expected for a laminar Couette flow.

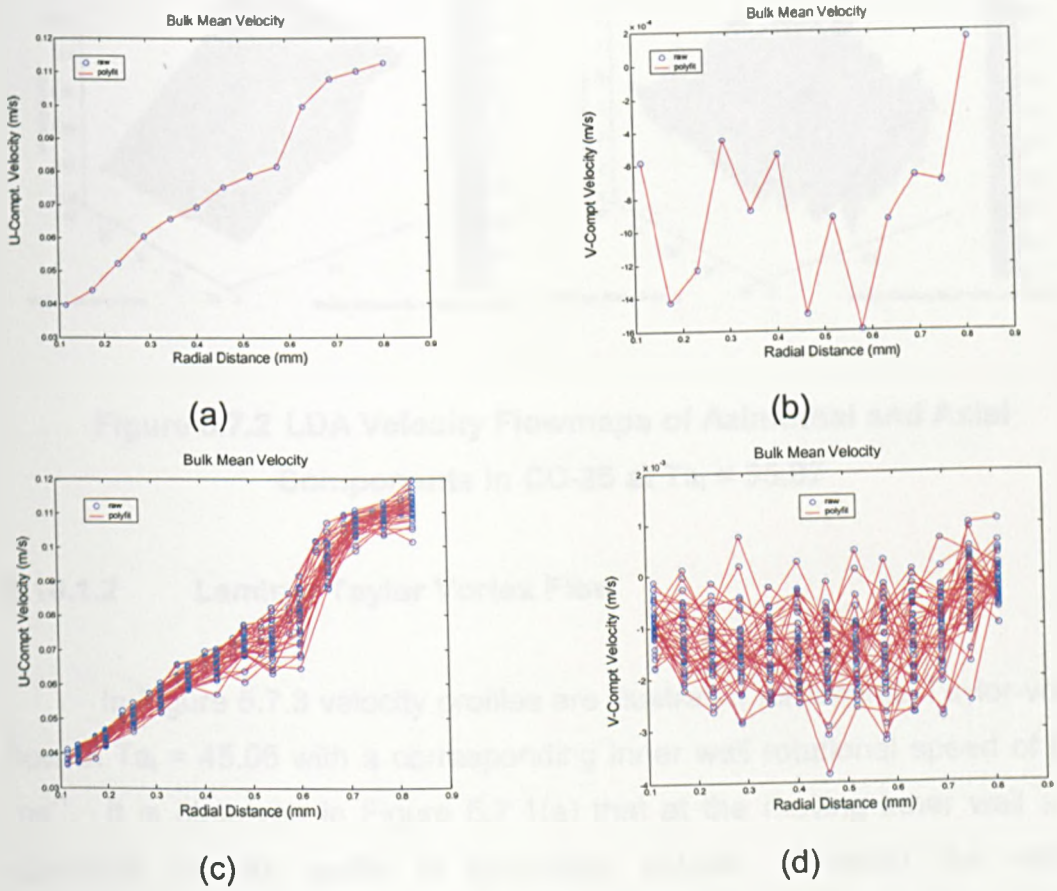

Figure 5.7.1 LDA Velocity Profiles for Ta_i = 35.07 (CC-25)

Velocity flowmaps of averaged LDA velocity data for all measured points in the annulus are presented in Figure 5.7.2 for Ta_i = 35.07. The surface plots illustrate an approximate structure to the flow that is not readily obtained from the colour maps.

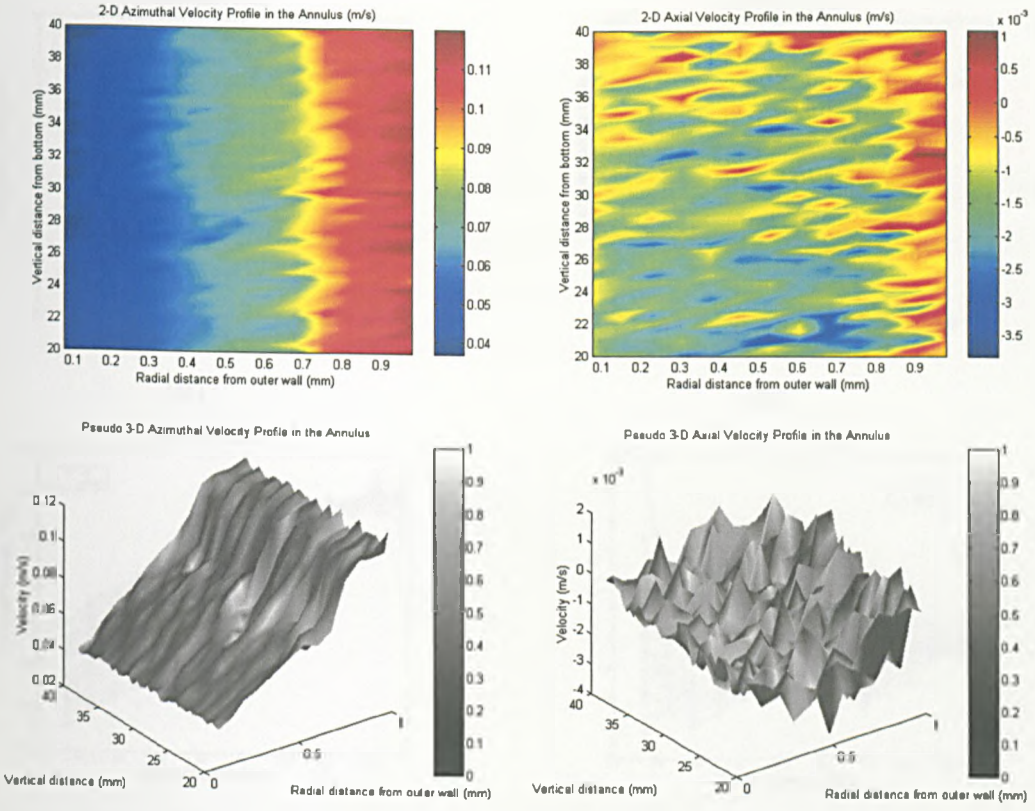

Figure 5.7.2 LDA Velocity Flowmaps of Azimuthal and Axial Components in CC-25 at Ta_i = 35.07

5.10.1.2 Laminar Taylor Vortex Flow

In Figure 5.7.3 velocity profiles are illustrated for laminar Taylor-vortex flow at Ta_i = 45.06 with a corresponding inner wall rotational speed of 0.16 ms^{-1}. It is observed in Figure 5.7.1(a) that at the moving inner wall a flat azimuthal velocity profile is generated outside of which the velocity decreases. This is indicative of a thicker laminar boundary layer forming in Taylor-vortex flow than in laminar Couette flow, consistent with the findings of (Jones 1981; Marcus 1984; Meyer 1967; Rudman 1998; Rudolph 1998; Ryrie 1992; Wereley 1994, 1998, 1999a, 1999b). This is also observed in Figure 5.7.3(c) for 34 superimposed axial positions with a few exceptions. In the core radial region of the flow, between approximately 0.2mm and 0.7mm, there is a broader variation of the velocities depending on axial position in the annulus. This is due to the counter-rotating Taylor-vortices that form in this region.

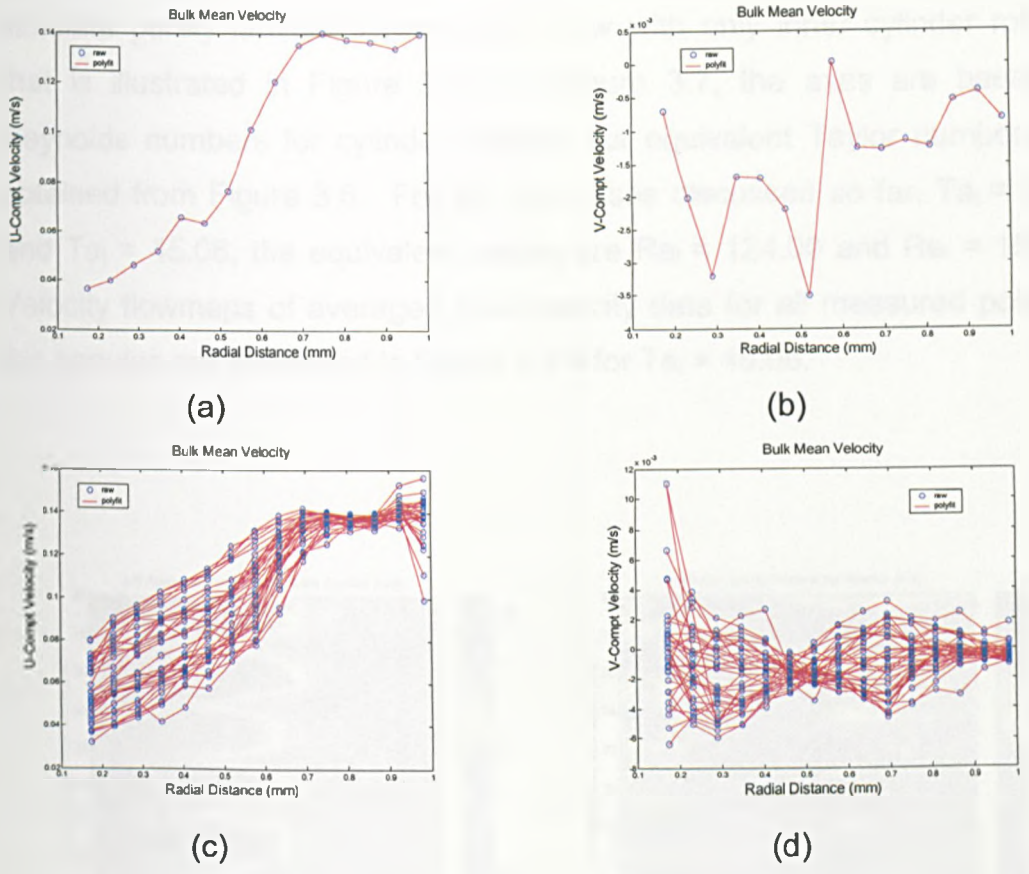

Figure 5.7.3 LDA Velocity Profiles for Ta_i = 45.058 (CC-25)

The higher velocities are encountered at the leading edges of the vortices and progressively decrease to a minimum velocity at the vortex centroids. It is observed that in general, for any axial position, the shape of the velocity profile is maintained indicating that there is no fixed imposed axial disturbance in the flow and this is expected in laminar Taylor vortex flow. The axial velocity profile of Figure 5.7.3(b) is not significantly different from 5.7.1(b) indicating again a slow negative axial velocity with no apparent pattern, however for a superimposed profile of 34 axial positions in 5.7.3(d), it is evident that the average velocity of sedimentation is reduced a little compared with 5.7.1(d) and a pattern resembling a figure '8' is emerging. The crossover centre of this is approximately at 0.5mm. This pattern is indicative of the onset of wavy-vortex flow where an organised axial disturbance prevails in the flow. For Ta_i = 45.06 the magnitude of this disturbance is very small and is not noticed in flow visualisation studies. However, it demonstrates the very small window of opportunity that exists to

simulate purely laminar Taylor-vortex flow with only inner cylinder rotation that is illustrated in Figure 3.7. In Figure 3.7, the axes are based on Reynolds numbers for cylinder rotation but equivalent Taylor numbers are obtained from Figure 3.6. For the two cases discussed so far, Ta_i = 35.07 and Ta_i = 45.06, the equivalent values are Re_i = 124.00 and Re_i = 159.30. Velocity flowmaps of averaged LDA velocity data for all measured points in the annulus are presented in Figure 5.7.4 for Ta_i = 45.06.

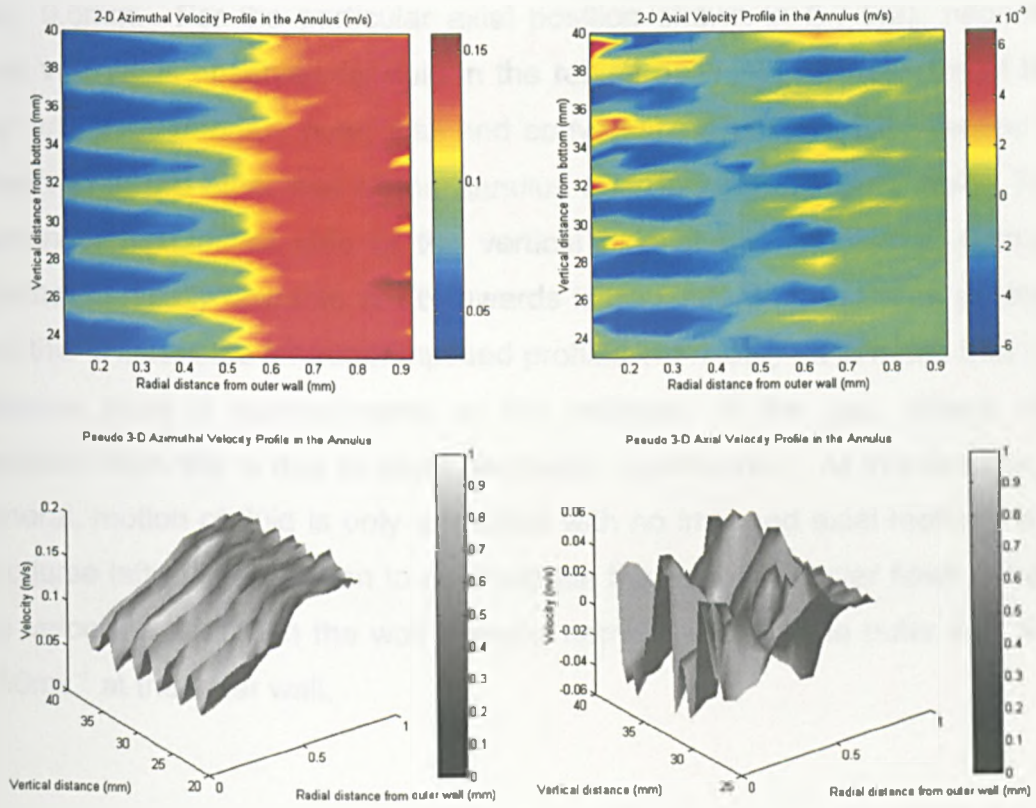

Figure 5.7.4 LDA Velocity Flowmaps of Azimuthal and Axial Components in CC-25 at Ta_i = 45.06

5.10.1.3 Wavy-Vortex Flow

In Figure 5.7.5 velocity profiles are illustrated for wavy Taylor-vortex flow at Ta_i = 141.92 with a corresponding inner wall rotational speed of 0.50 ms^{-1}. The azimuthal velocity profile is flat at either wall indicative of the wall boundary layers and has a steep linear profile in between in 5.7.5(a). This region indicates the vortex region. The shape of the profile is uniform throughout the annulus as indicated in 5.7.5(c). The wavy nature of the flow is clearly identified from the axial velocity profile in 5.7.5(b) where the inflexion point of the wave is observed at approximately the mid-point of the gap, 0.5mm. For the particular axial position shown in 5.7.5(a), negative axial velocity is observed for fluid in the region between the midpoint of the gap and the stationary outer wall and conversely, a positive axial motion is observed in the other half of the annulus approaching the inner wall. The motion of fluid either side of the vertical axis of the annulus at 0.5mm, whether vertically upwards or downwards is dependent on the axial position and this is illustrated for superimposed profiles in 5.7.5(d). It is noted that the inflexion point is approximately at the midpoint of the gap, where any deviation from this is due to slight geometric imperfection. At this location in general, motion of fluid is only azimuthal with no imposed axial motion. It is of course left to interpolation to approximate the boundary layer flows, where the velocities approach the wall speeds, namely zero for the outer wall and 0.50ms^{-1} at the inner wall.

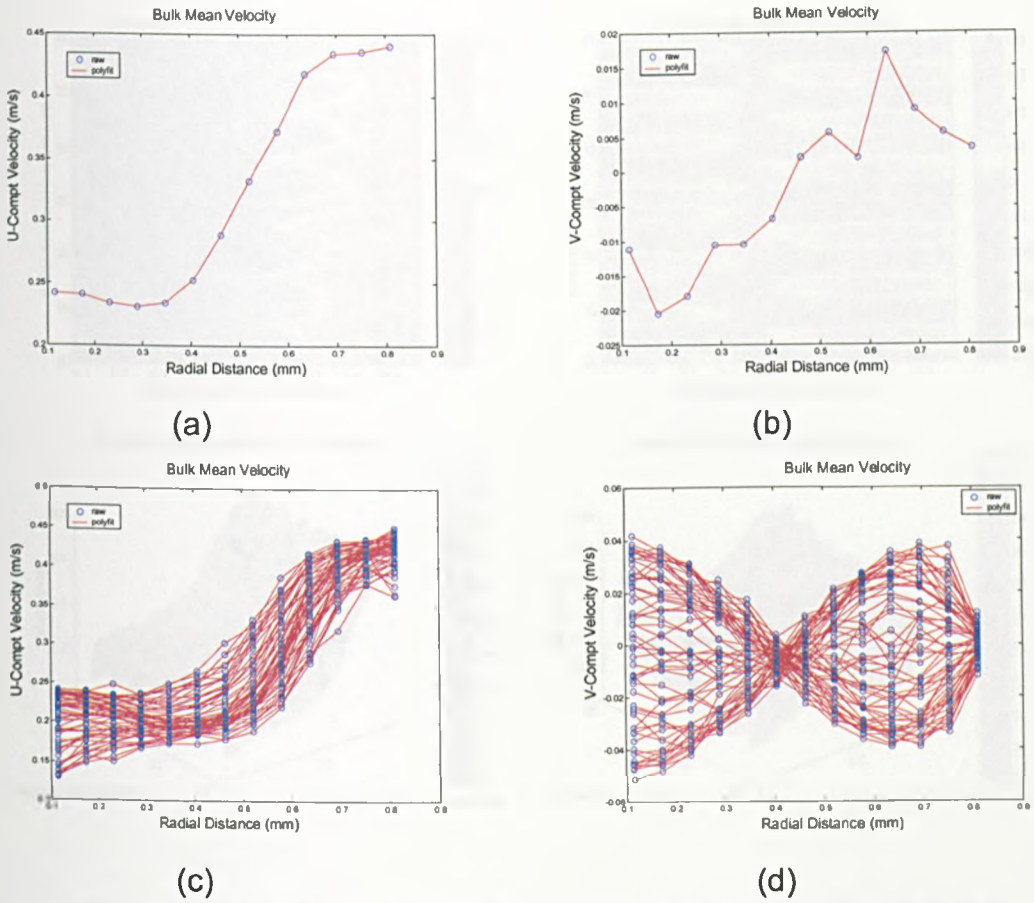

Figure 5.7.5 LDA Velocity Profiles for Ta_i = 141.924 (CC-25)

Velocity flowmaps of averaged LDA velocity data for all measured points in the annulus are presented in Figure 5.7.6 for Ta_i = 141.92.

5.10.2 CC-75

The spatial resolution for the nodal points of LDA measurement in the system CC-25 was 0.1mm radially and 1mm axially. The scaled concentric cylinder system allowed for much better resolution of flow in the gap and provided for better measurement of velocities in the near wall regions, since geometrical imperfections associated with wall rotation did not have as significant an impact in the prevailing annular flows as it did for the much smaller gap of CC-25. The procedure for generating the velocity profiles

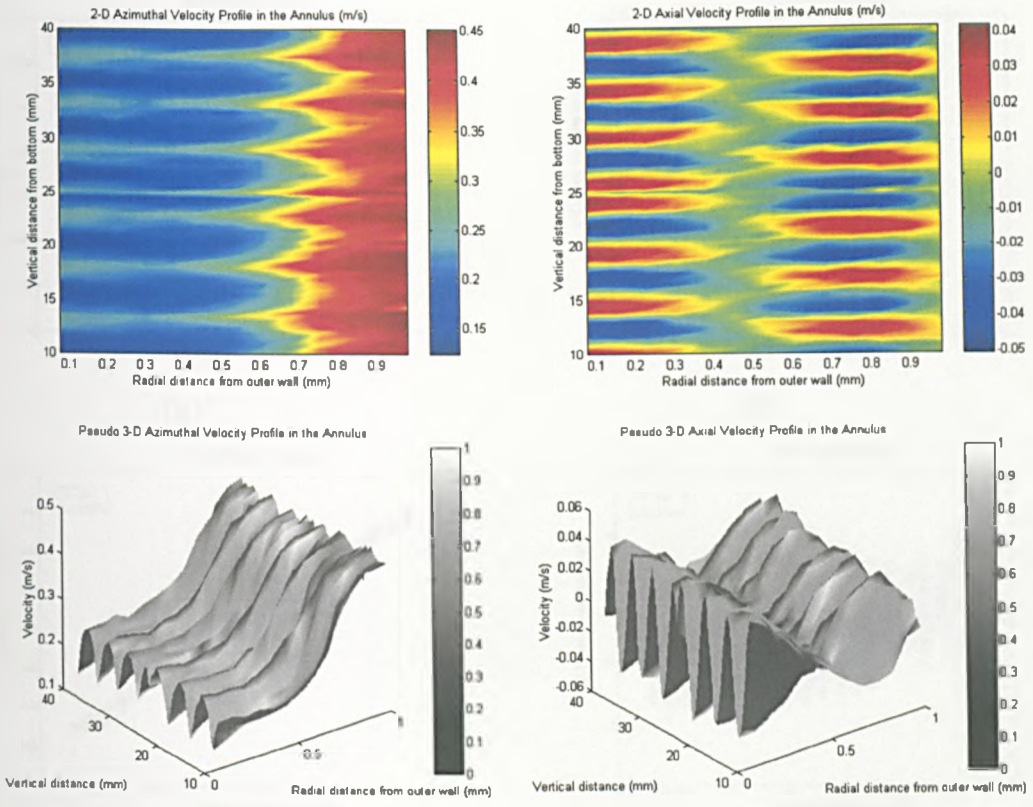

Figure 5.7.6 LDA Velocity Flowmaps of Azimuthal and Axial Components in CC-25 at Ta_i = 141.92

essentially follows that described in Section 5.10.1 and comparative velocity profiles are therefore shown in the next three sections here.

5.10.2.1 Laminar Couette Flow

In Figure 5.7.7 the velocity profiles are for Ta_i = 38.83 corresponding to a laminar Couette flow just below transition to laminar Taylor-vortex flow from flow visualisation studies. The wall speed of the rotating inner cylinder is 0.036ms^{-1}. The azimuthal velocity profile is observed to be near linear for a laminar profile in 5.7.7(a) and this is the general case for all axial position measured shown in 5.7.7(c). The axial velocity profile of 5.7.7(b) again takes a fairly random structure but in all cases the velocities are negative indicating slow particle sedimentation. Whilst in general, the curves of Figure 5.7.1 are

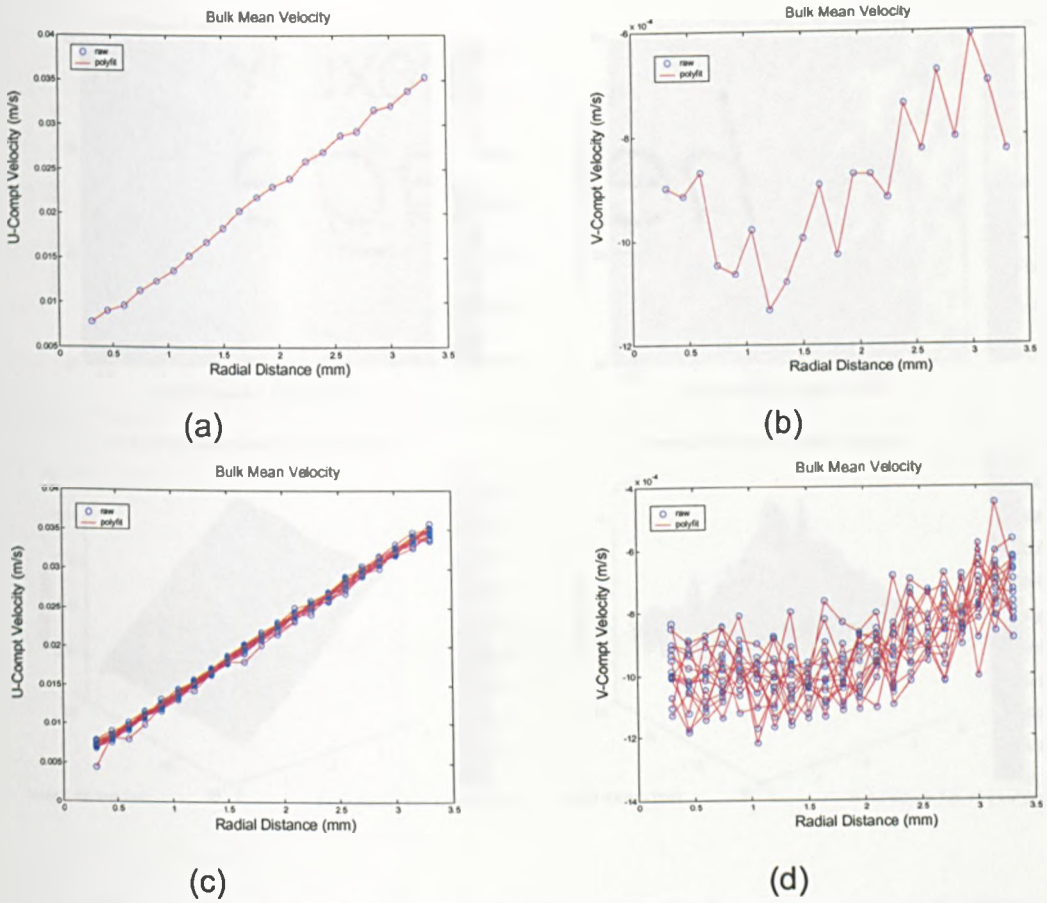

Figure 5.7.7 LDA Velocity Profiles for Ta_i = 38.83 (CC-75)

comparable to those of 5.7.7, it is observed in 5.7.7(b) and (d) that the magnitude of the settling velocity decreases for measurements made closer to the moving wall, an effect not noticed as much in 5.7.1(b) and (d). In addition, the magnitude of the sedimentation velocity appears to be reduced for the system CC-25. This suggests that in purely laminar Couette flows, smaller scale systems better maintain particle suspension when only inner wall motion takes place and that the sedimentation velocity increases both in magnitude and position for particles in larger systems that are closer to the stationary wall.

Velocity flowmaps of averaged LDA velocity data for all measured points in the annulus are presented in Figure 5.7.8 for Ta_i = 38.83.

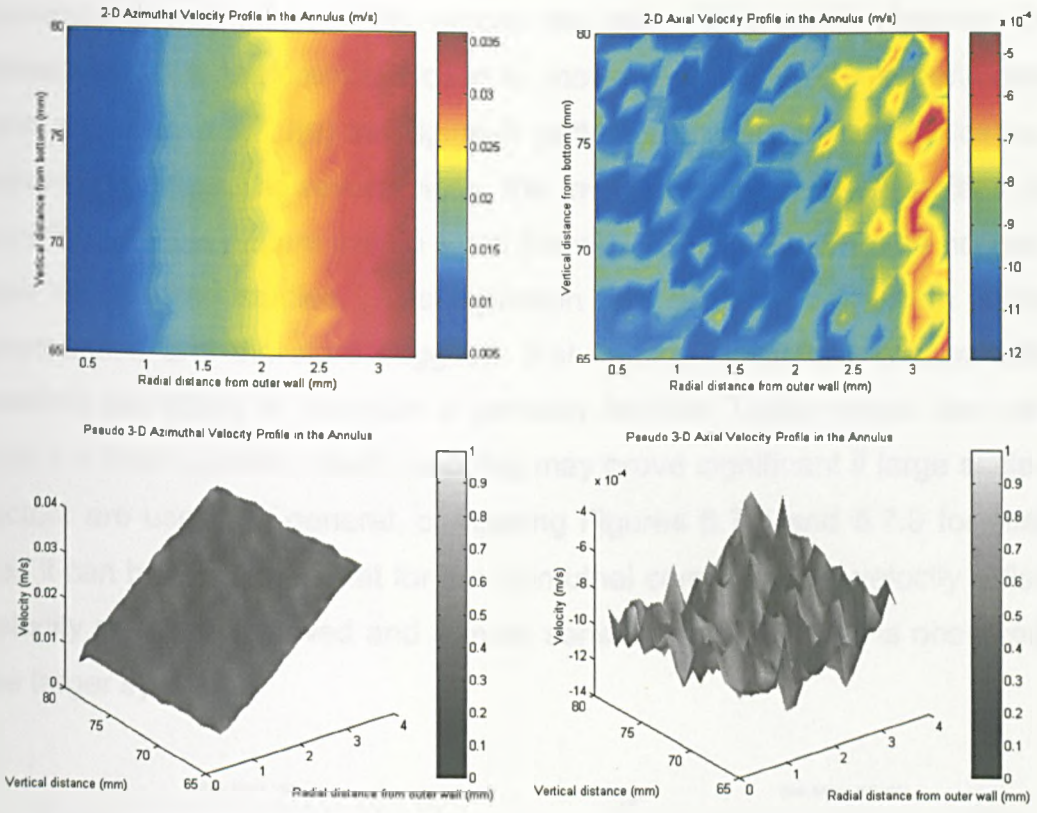

Figure 5.7.8 LDA Velocity Flowmaps of Azimuthal and Axial Components in CC-75 at Ta_i = 38.83

5.10.2.2 Laminar Taylor-Vortex Flow

In Figure 5.7.9 the velocity profiles are for Ta_i = 45.25 corresponding to a laminar Taylor-vortex flow from flow visualisation studies. The speed of rotation of the inner wall is 0.042ms^{-1} for this Ta_i. The azimuthal component of velocity in 5.7.9(a) does not differ significantly from 5.7.7(a). It is observed that there is some curvature generated and slight disturbances near the walls indicating the formation of boundary layers at the edge of Taylor vortices that are forming. For 15 superimposed axial positions in 5.7.9(c) there is evidence of profile broadening in the region outside of the boundary layers of the walls indicating again vortex formation with the lower velocities at the vortex centres and higher velocities at the vortex edges. The axial velocity profile in 5.7.9(c) has small negative magnitudes of velocity indicating slow particle sedimentation but the pattern appears saw-tooth, indicating a

tendency to maintain stability across the gap. It is again observed that resuspension is preferential closer to moving wall. For 15 superimposed axial positions in 5.7.9(d) the 'figure-8' pattern emerges which is indicative of wavy-vortex flow, however, since the magnitudes of the velocities that contribute to this pattern are so small the wavy effect would not be noticed in flow visualisation studies. In comparison with 5.7.3(d) the pattern is more pronounced and therefore suggests that scaling up of the system further restricts the ability to maintain a perfectly laminar Taylor-vortex flow when only the inner cylinder rotates and this may prove significant if large scale-up factors are used. In general, comparing Figures 5.7.3 and 5.7.9 for similar Ta_i, it can be concluded that for the azimuthal component of velocity a flatter velocity profile is achieved and a more sensitive axial velocity is observed in the larger system.

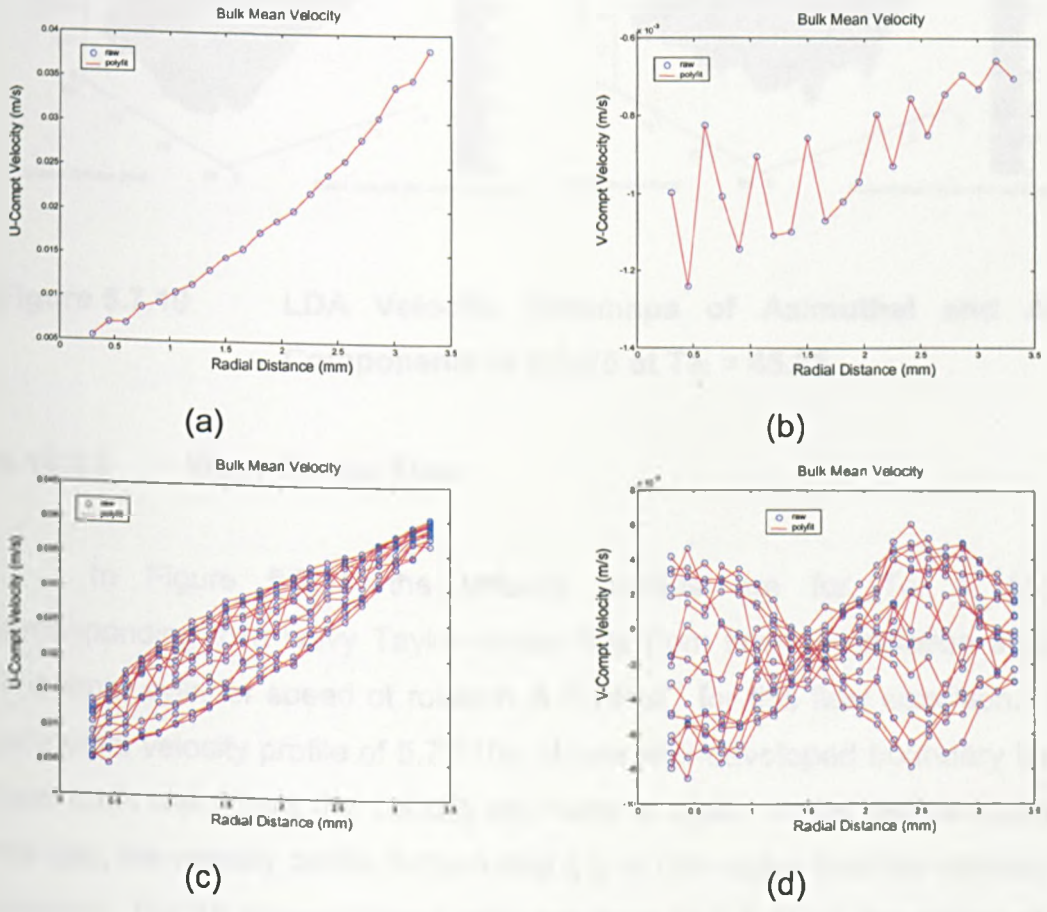

Figure 5.7.9 LDA Velocity Profiles for Ta_i = 45.25 (CC-75)

Velocity flowmaps of averaged LDA velocity data for all measured points in the annulus are presented in Figure 5.7.10 for Ta_i = 45.25.

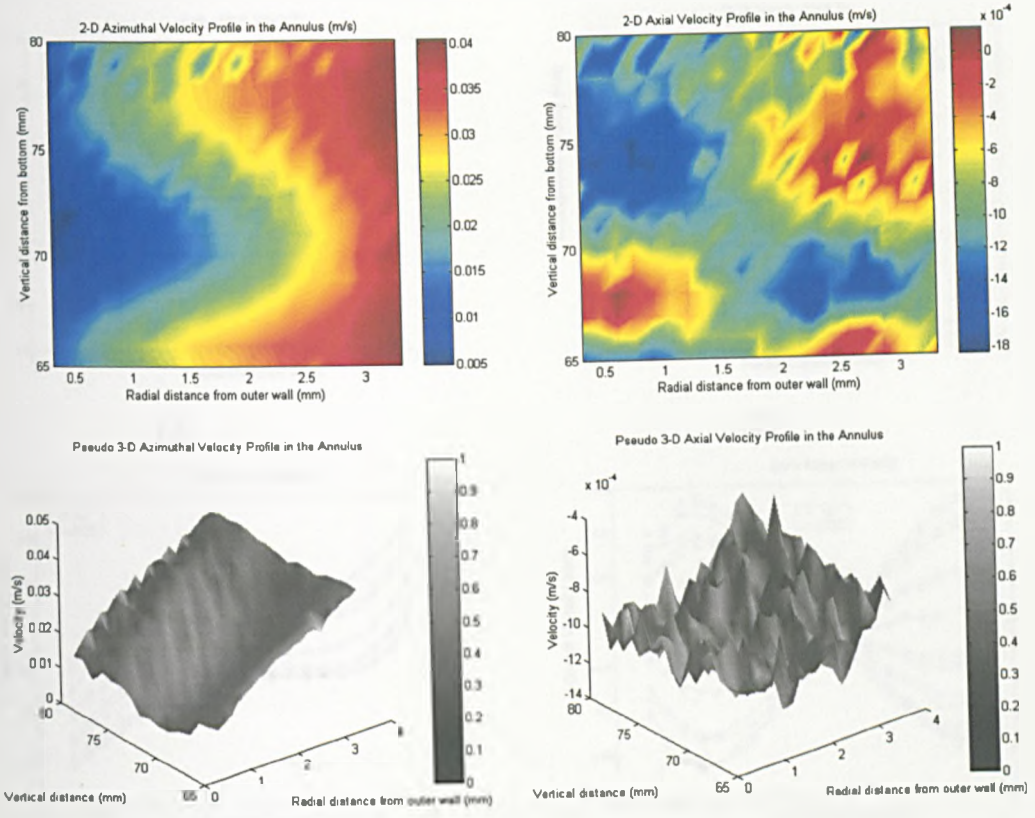

Figure 5.7.10 LDA Velocity Flowmaps of Azimuthal and Axial Components in CC-75 at Ta_i = 45.25

5.10.2.3 Wavy-Vortex Flow

In Figure 5.7.11 the velocity profiles are for Ta_i = 147.96 corresponding to a wavy Taylor-vortex flow from flow visualisation studies. The inner cylinder speed of rotation is 0.14ms^{-1} for this flow condition. The azimuthal velocity profile of 5.7.11(a) shows well-developed boundary layers from each wall where the velocity decrease is rapid. In the central region of the gap, the velocity profile flattens and it is in this region that the vortices are present. For 15 superimposed axial positions in 5.7.11(c), the shape of the profile is reasonably consistent indicating a stable flow and the upper velocity indicates the edge of the vortex with the minimum velocity being at the vortex centre. The axial profiles of 5.7.11(b) and (d) show that there is stabilisation

of the wave formation and that the inflexion point is again observed as the midpoint of the gap, in this case at 1.75mm.

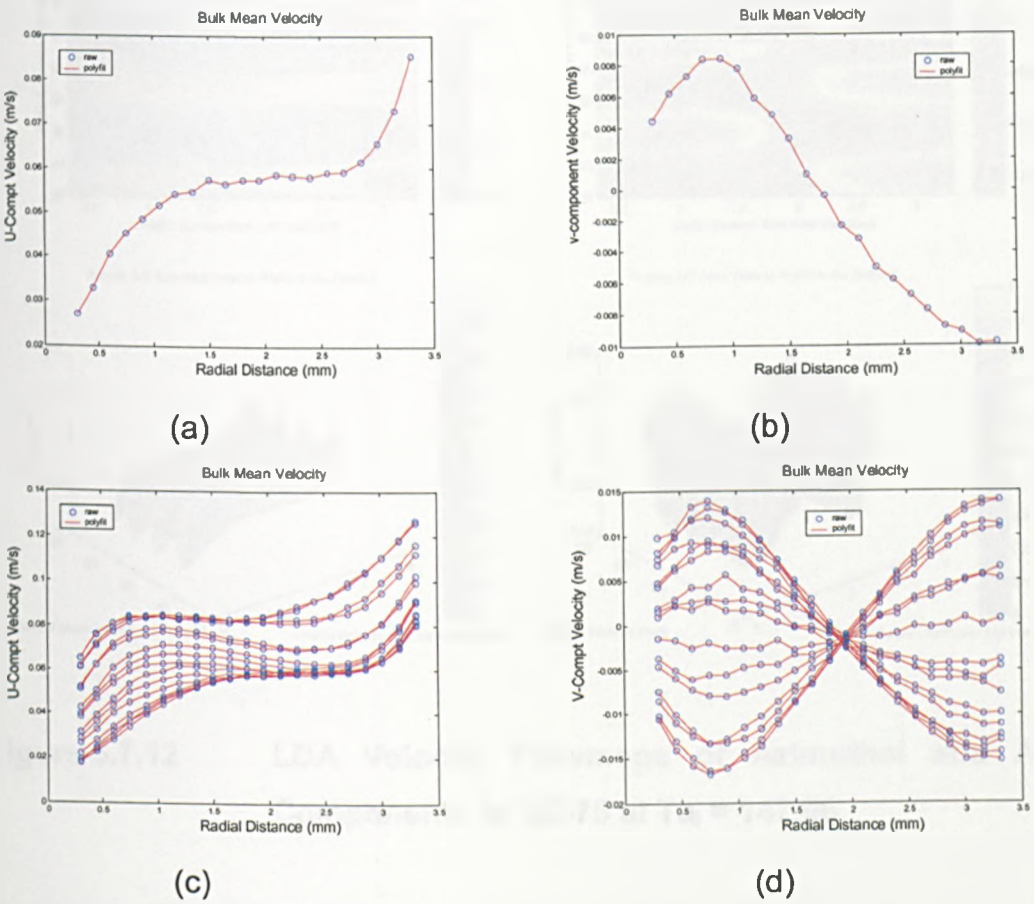

Figure 5.7.11 LDA Velocity Profiles for Ta_i = 147.96 (CC-75)

Symmetry of the axial wave is evident from 5.7.11(d) not only in terms of the fact that inflexion is at the centre of the gap but also in terms of the amplitude of the wave which takes a value of approximately 0.015ms^{-1} at the this Taylor number. Velocity flowmaps of averaged LDA velocity data for all measured points in the annulus are presented in Figure 5.7.12 for Ta_i = 147.96.

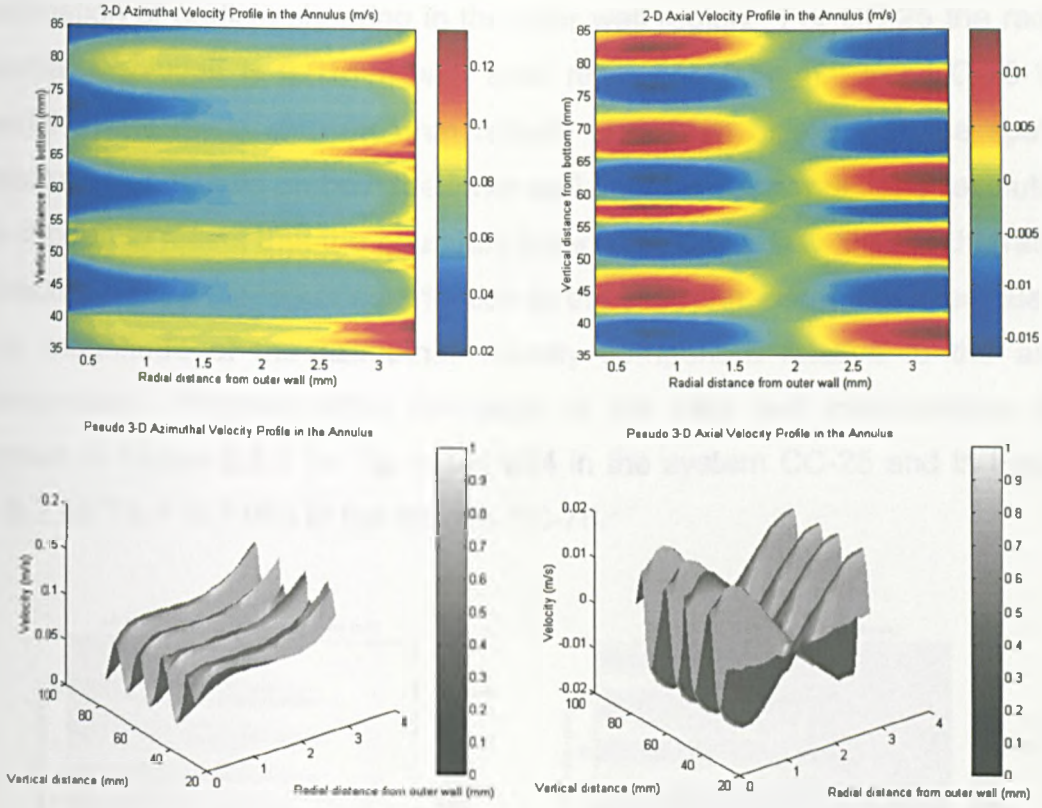

Figure 5.7.12 **LDA Velocity Flowmaps of Azimuthal and Axial Components in CC-75 at Ta_i = 147.96**

5.11 Near Wall Interpolations

LDA measurements have been made in systems CC-25 and CC-75 in what is referred to here as the 'core' region of the annulus in a 2-D plane illustrated in Figure 5.6. In the near wall boundary layers, it was not possible to obtain good data from the Doppler bursts for a long enough time period to obtain a meaningful representation of the mean velocity in this region. At the moving wall this was due to a noisy signal where despite a reasonable data rate being obtained, the validation of the data was low. Conversely, at the stationary outer wall the validation was good but the rate of data collection was low. In these regions, the velocity profiles have been estimated using a 2-D linear numerical interpolation based on the core region velocities and the known velocities of the walls (Hanselman, 1996). The numerical interpolations were performed using the Matlab software package. Near wall estimation of velocities uses a refined spatial resolution for more precise

estimation of particle shearing in the near wall region. For CC-25 the radial spatial resolution is 0.01mm with axial resolution 0.5mm. For CC-75 the radial resolution is also 0.01mm radially and 1mm axially. These spatial resolutions are used on both the inner wall and the outer wall. The resolution is chosen to reflect that the boundary layers are essentially 'thin' in the radial direction where the major contribution to the shearing force originates due to the magnitude of the azimuthal velocity component relative to the axial component. Representative flowmaps of the near wall interpolations are shown in Figure 5.8.1 for Ta_i = 141.924 in the system CC-25 and in Figure 5.8.2 for Ta_i = 147.963 in the system CC-75.

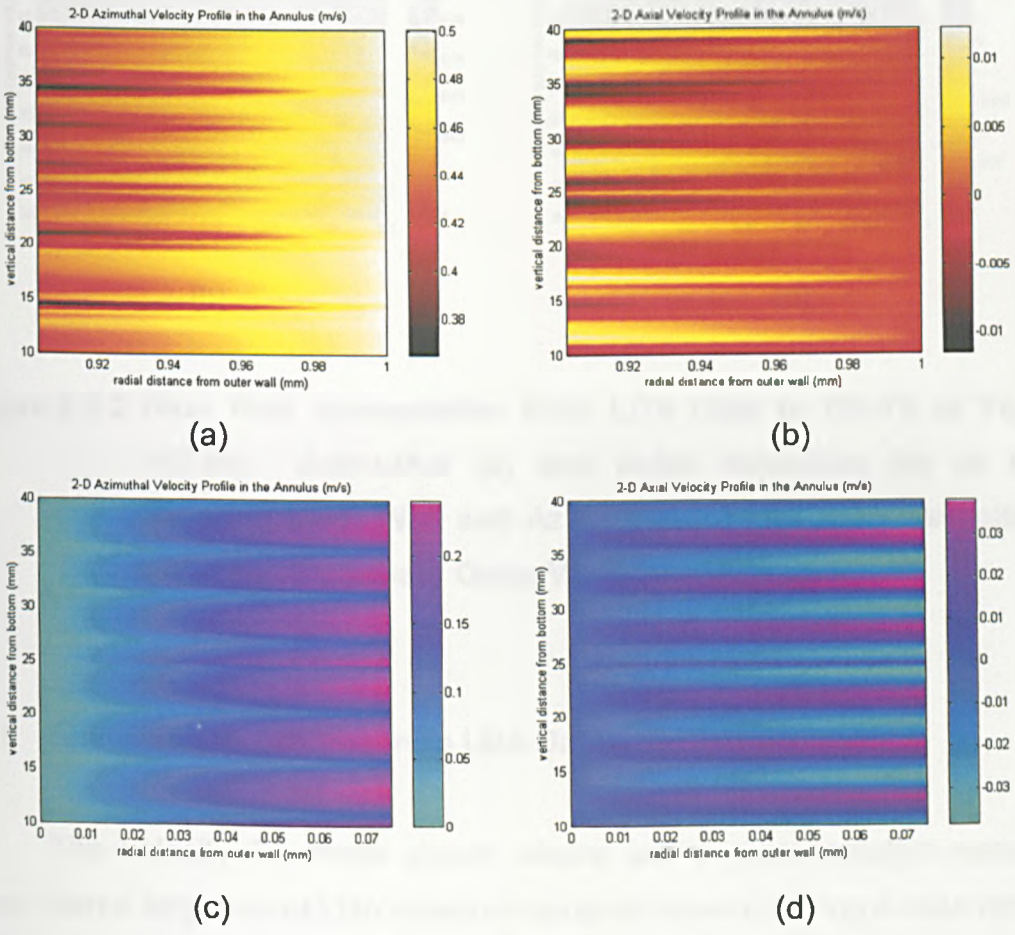

Figure 5.8.1 Near Wall Interpolation from LDA Data in CC-25 at Ta_i = 141.92: Azimuthal (a) and Axial Velocities (b) at the Rotating Inner Wall and Azimuthal (c) and Axial Velocities (d) at the Stationary Outer Wall

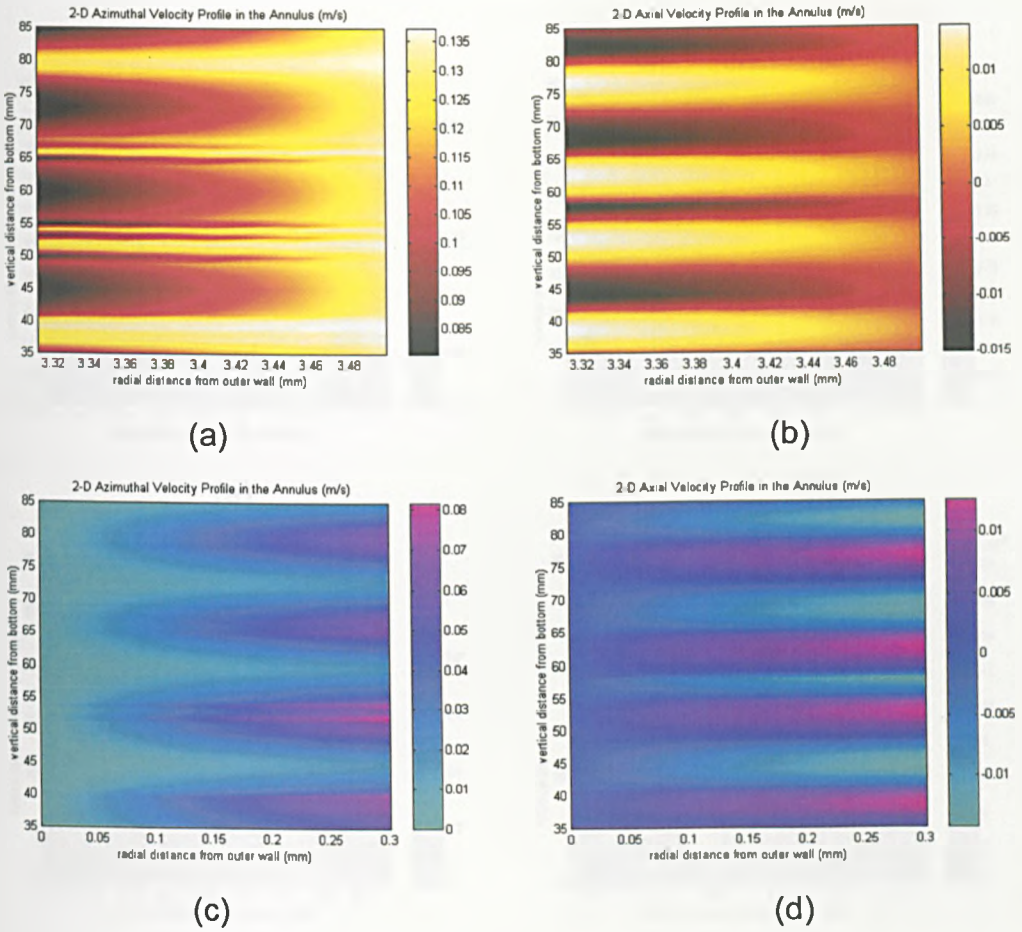

Figure 5.8.2 Near Wall Interpolation from LDA Data in CC-75 at Ta_i = 147.96: Azimuthal (a) and Axial Velocities (b) at the Rotating Inner Wall and Azimuthal (c) and Axial Velocities (d) at the Stationary Outer Wall

5.12 Shear Stress Profiles from LDA Data

The velocity flowmaps shown above are a representative sample taken from a larger set of LDA measurements on flows covering a wide range of Ta_i in both CC-25 and CC-75. The flowmaps are based on a matrix of measured mean velocities in the defined flow domain. Equation (5.19), and is then applied based on the velocities and the spatial resolution within the domain. The result of equation (5.19) is used in equation (5.24) to evaluate the pseudo-shear rate for particles in the domain. The shear stress is then readily evaluated in the domain by incorporation of the pseudo shear rate into

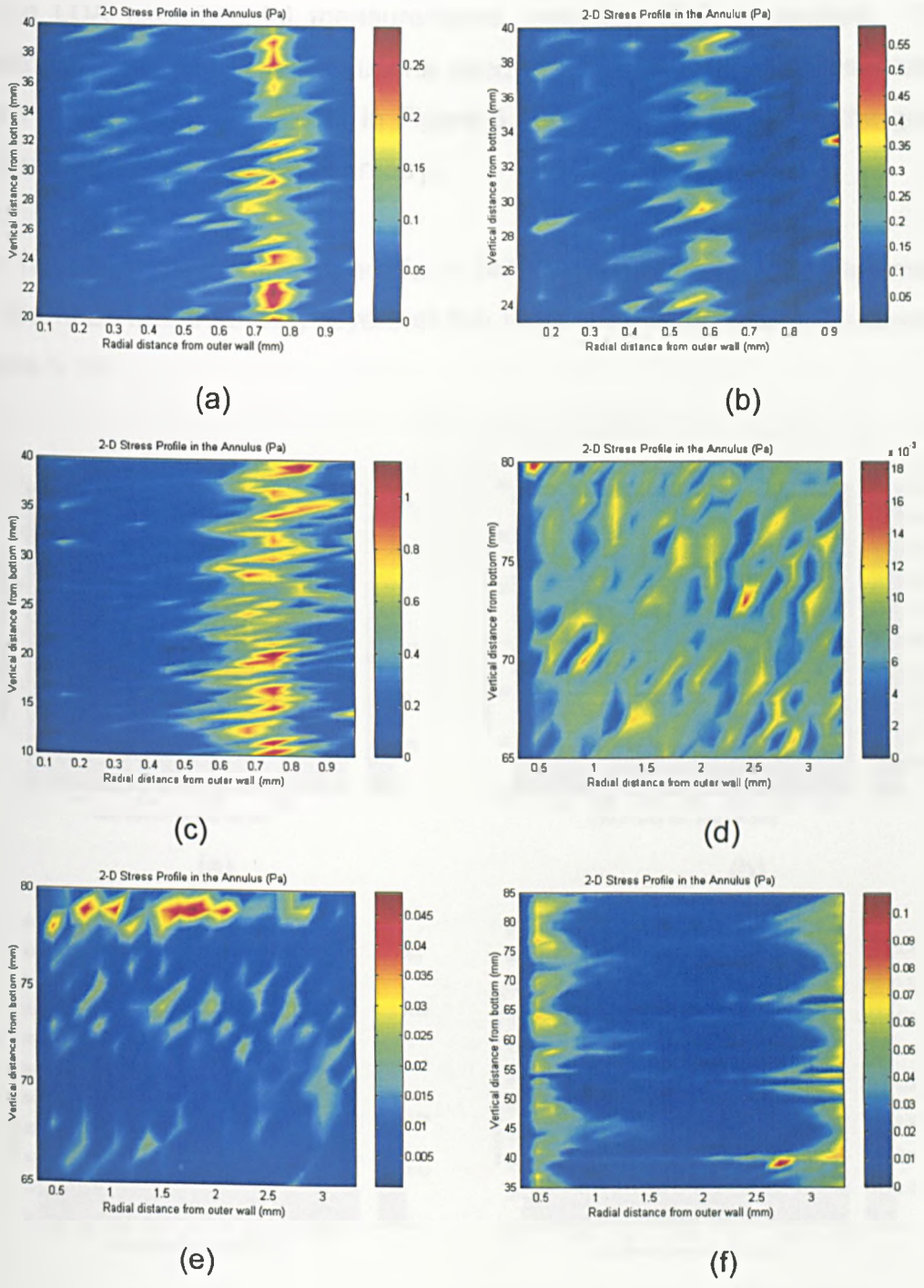

Figure 5.9 **Shear stress in the Core Region of the Annulus: (a) CC-25 at Ta_i = 35.07, (b) CC-25 at Ta_i = 45.06, (c) CC-25 at Ta_i = 141.92, (d) CC-75 at Ta_i = 38.83, (e) CC-75 at Ta_i = 45.25, (f) CC-75 at Ta_i = 147.96**

the constitutive equation for the fluid rheology. For the Newtonian fluids used in the LDA experimental measurements, equation (5.5) is applied. The Newtonian viscosity of the solutions used is 0.00989 Pas. Representative shear stress maps are shown in Figure 5.9 for the core region at the given Taylor number and system geometry.

For Ta_i = 141.924 in CC-25 and Ta_i = 147.963 in CC-75 shear stress maps for the near wall boundary layers of the inner and outer wall are shown in Figure 5.10.

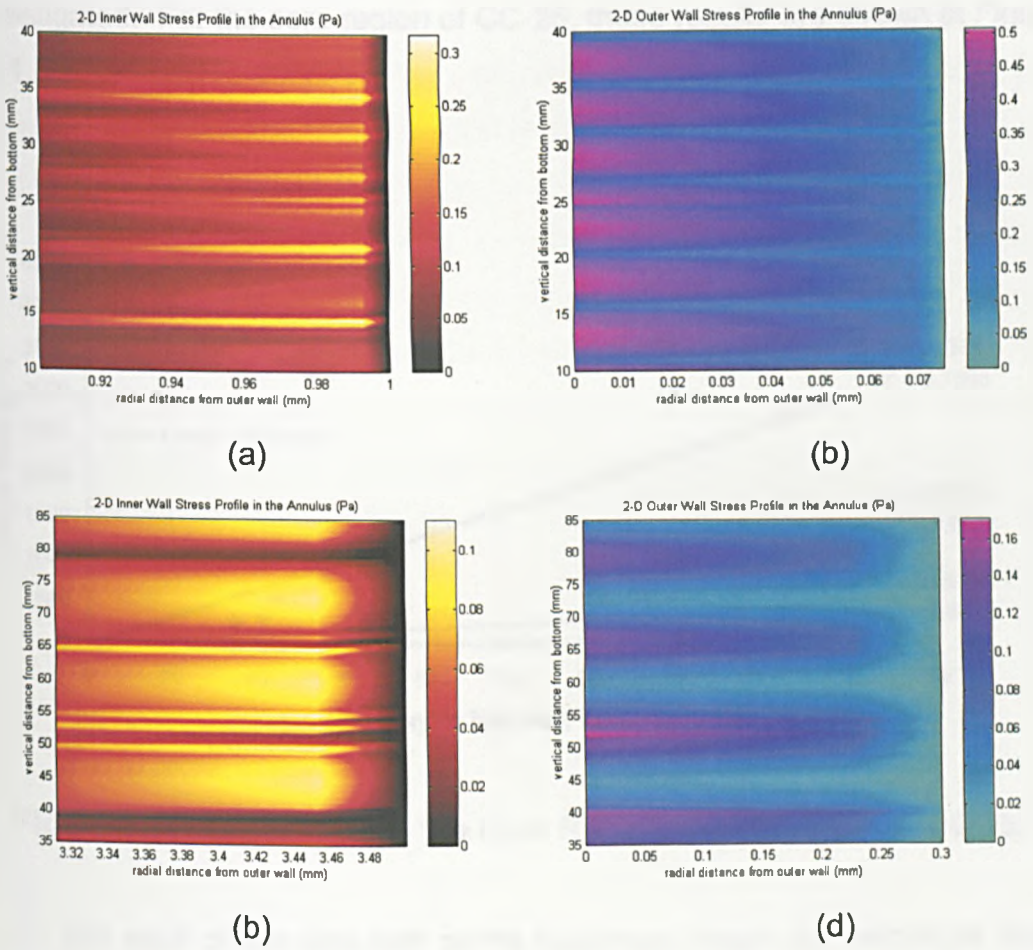

Figure 5.10 Shear Stress in the near Wall Regions: (a) Inner Rotating and (b) Outer Stationary Wall of CC-25 at Ta_i = 141.92, (c) Inner Rotating (d) and Outer Stationary Wall of CC-75 at Ta_i = 147.96

5.12.1 Shear Rates in CC-25

Evaluation of the shear rates in the annulus is initially of more value if alternative different constitutive equations are to be used to quantify the shear stress. The core region, inner wall boundary layer and outer wall boundary layer are treated separately, since these in effect are three distinctly different regions of the annular flow. For each of these regions of the flow, a matrix of shear rates is obtained for different points in the flow domain. Using these, the maximum and minimum observed shear rates are determined, along with the mean shear rate, for each of the Taylor numbers investigated. For the core region of CC-25, these results are shown in Figure 5.11.

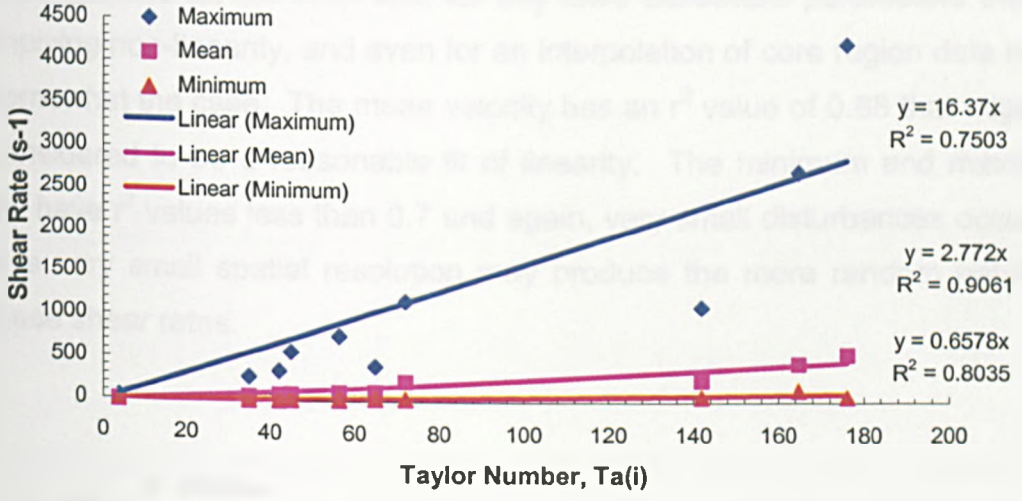

Figure 5.11 Shear Rate in the Core Region for Varying Ta_i (CC-25)

For each of the data sets of the maximum, mean and minimum shear rate with variation of Ta_i the best fit to the data is a linear relationship. The correlations are reported in Figure 5.11. It is observed firstly that the goodness of fit is reasonable for the mean shear rate with an r^2 value of 0.91. The goodness of fit is less good for the minimum shear rate (r^2 = 0.80) and is not very good for the maximum shear rate (r^2 = 0.75). For the small spatial resolution used in the calculation, it is not surprising to find that a very good

correlation cannot be obtained to describe the maximum and minimum shear rates since these are likely to arise out of tiny (micro) spatial disturbances measured in the flow and therefore may not be representative of the macroscale flow condition. It is not unreasonable to suggest that a linear relationship does exist even for the maximum and minimum shears that are generated in the flow on the basis of these findings. Although the correlation is not particularly good, it can be used as a guideline to estimate maximum and minimum shears the particles may experience for varying Taylor number.

Shear rates for the inner wall boundary layer for varying Taylor number are shown in Figure 5.12 and this is for the moving wall. The best correlations to fit the maximum, mean and minimum shear rates observed in the boundary layer on the inner wall with varying Ta_i are linear and it is generally observed that the goodness of fit is less than that observed for the core region. From LDA measurements it was observed that the data rate was spurious on the inner wall for any fixed Burstware parameters thereby implying non-linearity, and even for an interpolation of core region data this is somewhat the case. The mean velocity has an r^2 value of 0.88 that might be considered to be a reasonable fit of linearity. The minimum and maximum fits have r^2 values less than 0.7 and again, very small disturbances occurring in a very small spatial resolution may produce the more random nature of these shear rates.

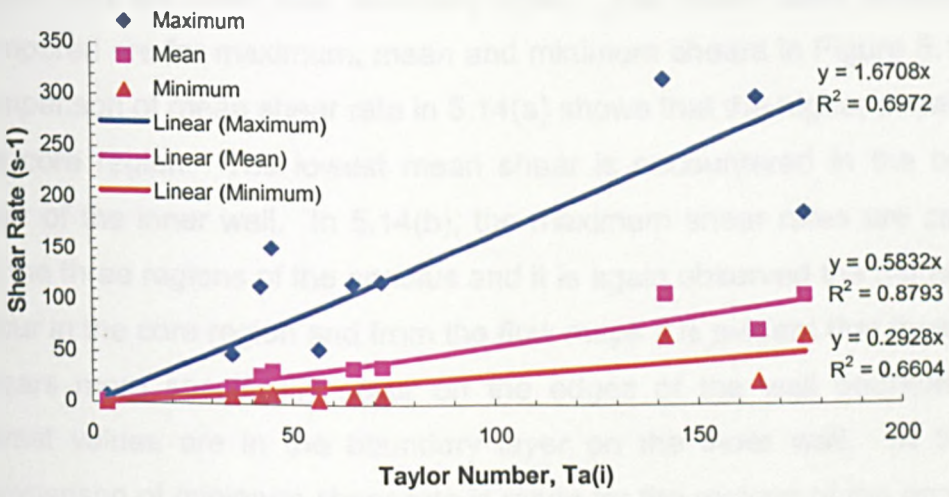

Figure 5.12 Shear Rate at the Inner Wall for Varying Ta_i (CC-25)

Shear rates for the inner wall boundary layer for varying Taylor number are shown in Figure 5.13 and this is for the stationary wall. A laminar boundary layer is predicted on the outer wall and it is therefore expected that a good correlation for shear rate will be found. This is observed to be the case with very good linear fits for the maximum, mean and minimum shear rates with $r^2 > 0.95$ in all cases.

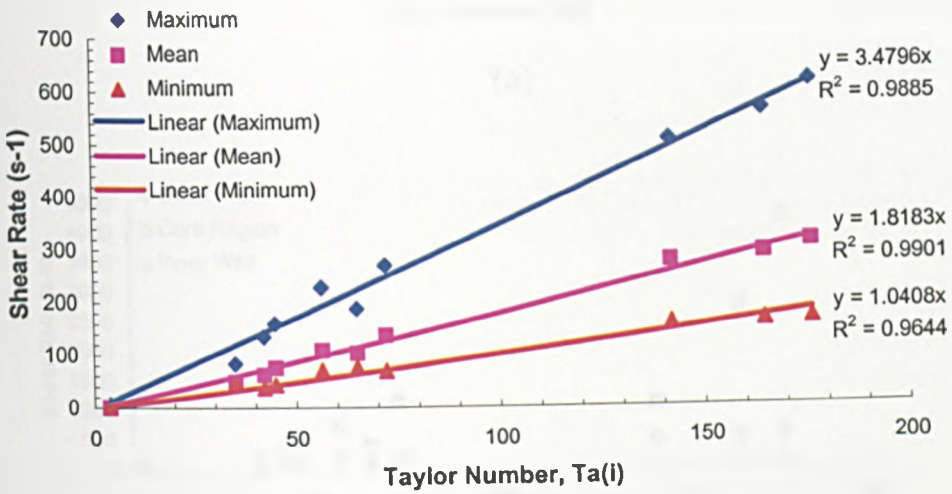

Figure 5.13 Shear Rate at the Outer Wall for Varying Ta_i (CC-25)

A comparison is made of the shear rates observed for the three regions of the annulus in CC-25; the outer wall boundary layer, the core region and the inner wall boundary layer. The shear rates independently compared are for maximum, mean and minimum shears in Figure 5.14. The comparison of mean shear rate in 5.14(a) shows that the higher shears are in the core region. The lowest mean shear is encountered in the boundary layer of the inner wall. In 5.14(b), the maximum shear rates are compared for the three regions of the annulus and it is again observed the higher values occur in the core region and from the flow maps it is evident that these higher shears more specifically occur on the edges of the wall boundary. The lowest values are in the boundary layer on the inner wall. In 5.14(c) a comparison of minimum shear rate is made for the regions of the annulus. In this case, the highest shears are encountered on the outer wall and the

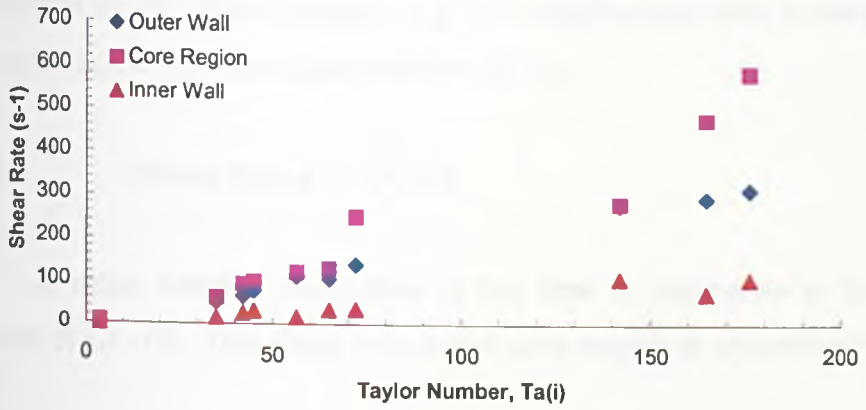

(a)

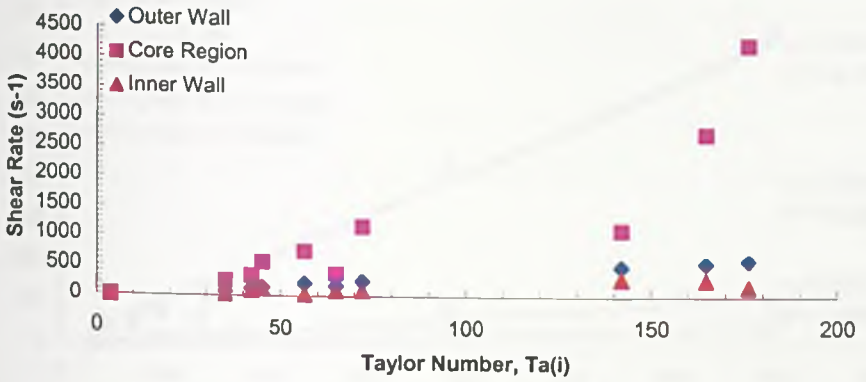

(b)

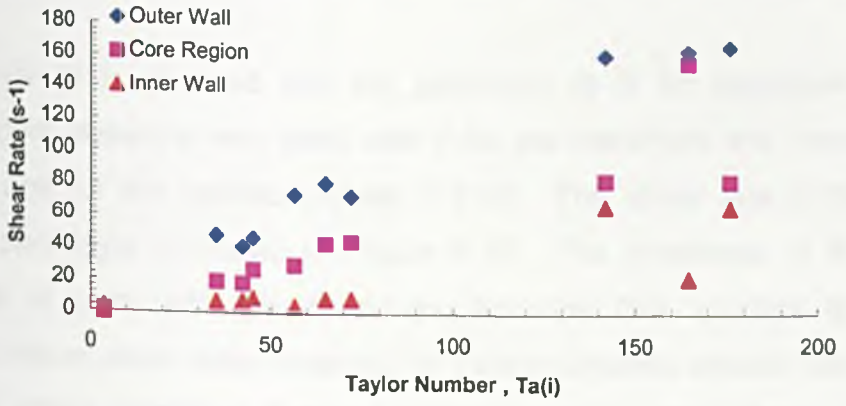

(c)

Figure 5.14 Comparison of shear rates in the annulus (CC-25) for mean (a), maximum (b) and minimum (c)

lowest on the inner wall. It is noted that in Figure 5.14 the observations are consistent for all Taylor number, e.g. the mean shear rate is *always* higher in the core region than the outer wall for all Ta_i.

5.12.2 Shear Rates in CC-75

A more detailed resolution of the flow is attainable in the scaled-up system of CC-75. The shear rate in the core region is shown in Figure 5.15.

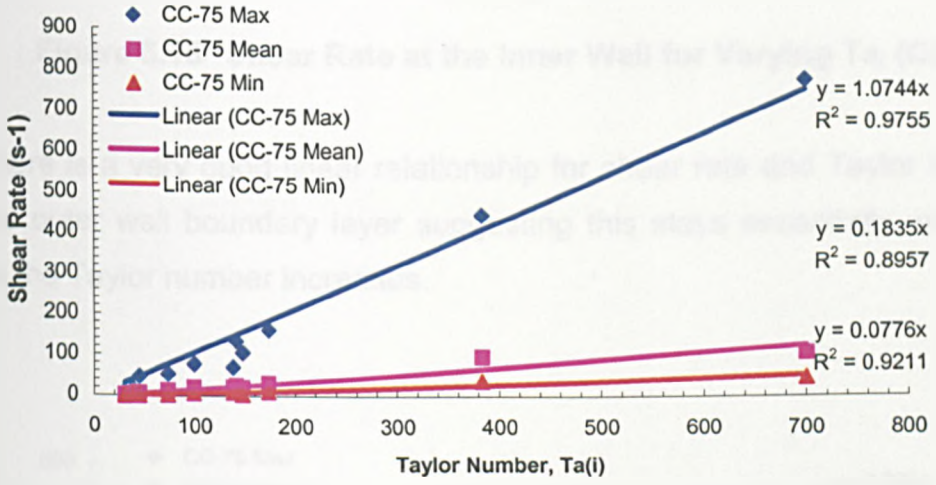

Figure 5.15 Shear Rate in the Core Region for Varying Ta_i (CC-75)

A linear fit is obtained and the goodness of fit for maximum, mean and minimum shears is very good with r^2 for the maximum and mean shear of > 0.98 and for the minimum shear > 0.93. The shear rate in the inner wall boundary layer is shown in Figure 5.16. The goodness of fit for a linear model is poor with low r^2 values, however this appears to be due to randomised shear rates obtained for Taylor numbers around 150 which is the point where transition is made to stable wavy vortex flow. Beyond this, linearity appears to resume, and it may be due to the initial formation of the wavy structure that small scale shears become non-linear in a small region of Ta_i. The shear rate in the outer wall boundary layer is shown in Figure 5.17.

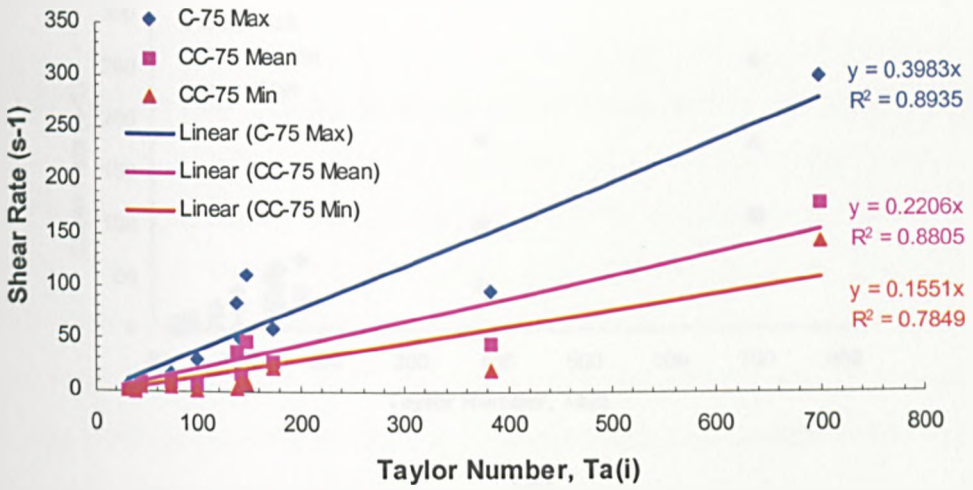

Figure 5.16 Shear Rate at the Inner Wall for Varying Ta_i (CC-75)

There is a very good linear relationship for shear rate and Taylor number in the outer wall boundary layer suggesting this stays essentially undisturbed as the Taylor number increases.

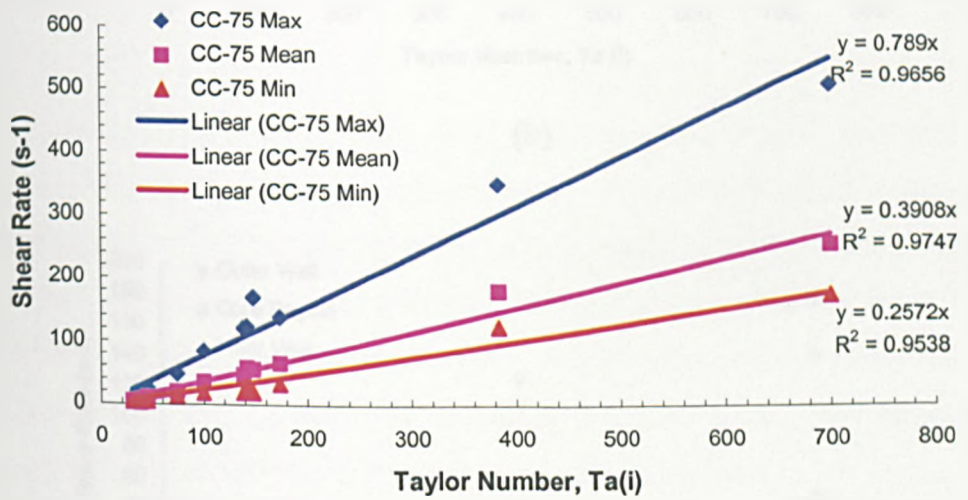

Figure 5.17 Shear Rate at the Outer Wall for Varying Ta_i (CC-75)

A comparison is made of the shear rates observed in the three regions of the annulus in terms of the mean (a), maximum (b) and minimum (c) shears in Figure 5.18 for system CC-75.

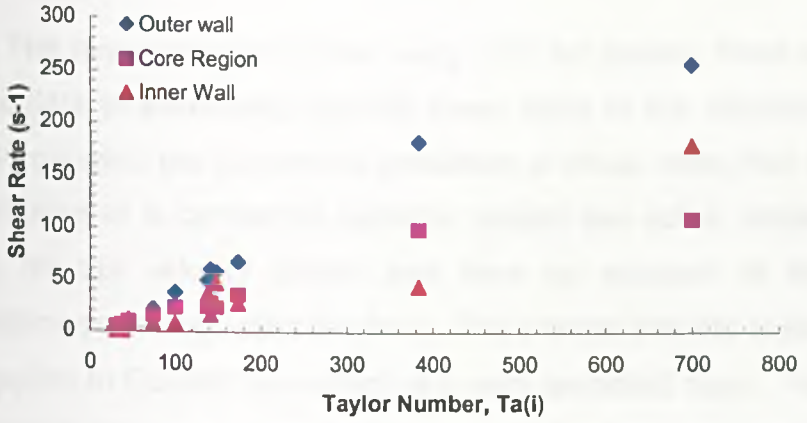

(a)

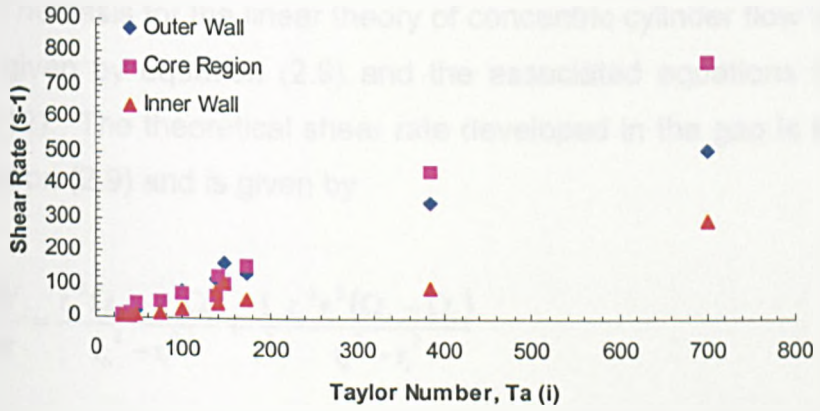

(b)

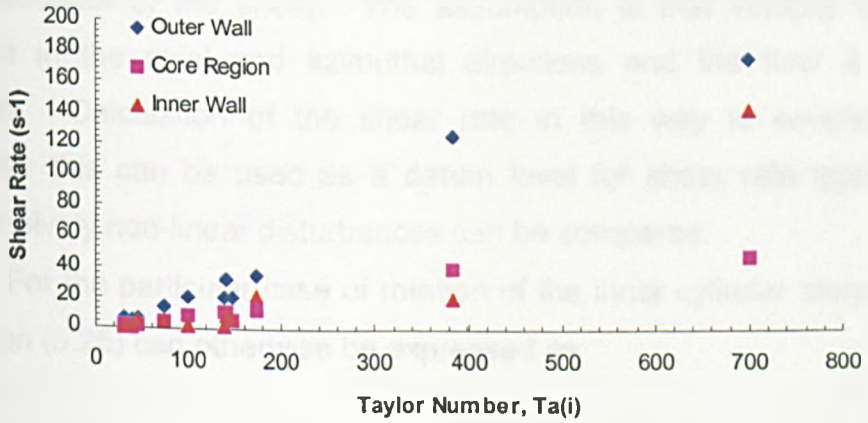

(c)

Figure 5.18 Comparison of Shear Rates in the Annulus (CC-75) for mean (a), maximum (b) and minimum (c) shears

5.13 Comparison of Experimental and Theoretical Shear Rates

The measurements made using LDA for particle flows in the annulus provide data to essentially quantify shear rates at the microscale within the gap. In general, the theoretical prediction of shear rates that occur within a fluid rotating in a concentric cylinder system are solely based on a linear theory for the velocity profile and take no account of the non linear fluctuations occurring within the fluid. This means that the linear theory really only applies to Couette flow which is a very restricted case. For operation of a concentric cylinder system as a bioreactor it is important to assess how the non-linear perturbation, that grows with increasing Taylor number, will affect the resulting shear stress that is imparted on cells in the flow.

The basis for the linear theory of concentric cylinder flow is the velocity profile given by equation (2.9) and the associated equations (2.10), (2.11) and (2.12). The theoretical shear rate developed in the gap is the derivative of equation (2.9) and is given by

$$\frac{dV}{dr} = \frac{r_o^2\Omega_o - r_i^2\Omega_i}{r_o^2 - r_i^2} + \frac{1}{r^2}\frac{r_o^2 r_i^2(\Omega_o - \Omega_i)}{r_o^2 - r_i^2} \qquad (5.25)$$

It is self evident from this equation that the shear rate is based solely on velocity changes occurring in the radial direction and is therefore a 1-D linear representation of the shear. The assumption is that velocity is spatially uniform in the axial and azimuthal directions and the flow is therefore Couette. Calculation of the shear rate in this way is severely limited. However this can be used as a datum level for shear rate against which progressively non-linear disturbances can be compared.

For the particular case of rotation of the inner cylinder alone ($\Omega_o = 0$), equation (5.25) can otherwise be expressed as

$$\frac{dV}{dr} = \frac{r_i^2\Omega_i}{r_o^2 - r_i^2} + \frac{1}{r^2}\frac{r_o^2 r_i^2\Omega_i}{r_o^2 - r_i^2} \qquad (5.26)$$

The particular cases which are of interest for comparative purposes to the LDA data are for

- inner wall shear rate ($r = r_i$)

$$\left|\frac{dV}{dr}\right|_{r=r_i} = \frac{\Omega_i\left(r_i^2 + r_o^2\right)}{r_o^2 - r_i^2} \tag{5.27}$$

- outer wall shear rate ($r = r_o$)

$$\left|\frac{dV}{dr}\right|_{r=r_o} = \frac{2r_i^2\Omega_i}{r_o^2 - r_i^2} \tag{5.28}$$

- mid-gap shear rate ($r = (r_o - r_i)/2$)

$$\left|\frac{dV}{dr}\right|_{r=(r_o-r_i)/2} = \frac{r_i^2\Omega_i}{r_o^2 - r_i^2} + \frac{4}{(r_o - r_i)^2}\left[\frac{r_o^2 r_i^2\Omega_i}{r_o^2 - r_i^2}\right] \tag{5.29}$$

The geometry of the two systems is given in Table 5.4 and on this basis and on the angular velocity of the inner cylinder for a given Taylor number the theoretical shear rates at the three regions of the annulus can be evaluated using equations (5.26) through (5.29). The comparison of these theoretical shears to those obtained from experiments using LDA are shown in Figure 5.16 for the outer wall boundary layer (a), the core region (b) and the inner wall boundary layer (c) in the system CC-25 and in Figure 5.20 for CC-75.

Radius (m)	CC-25	CC-75
Inner Cylinder	0.0125	0.037
Outer Cylinder	0.0135	0.0405

Table 5.4 Cylinder Radii for CC-25 and CC-75

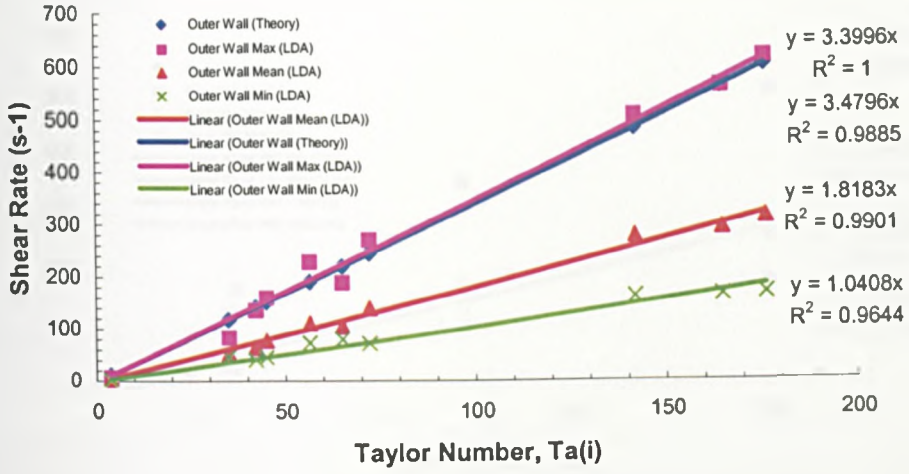

(a)

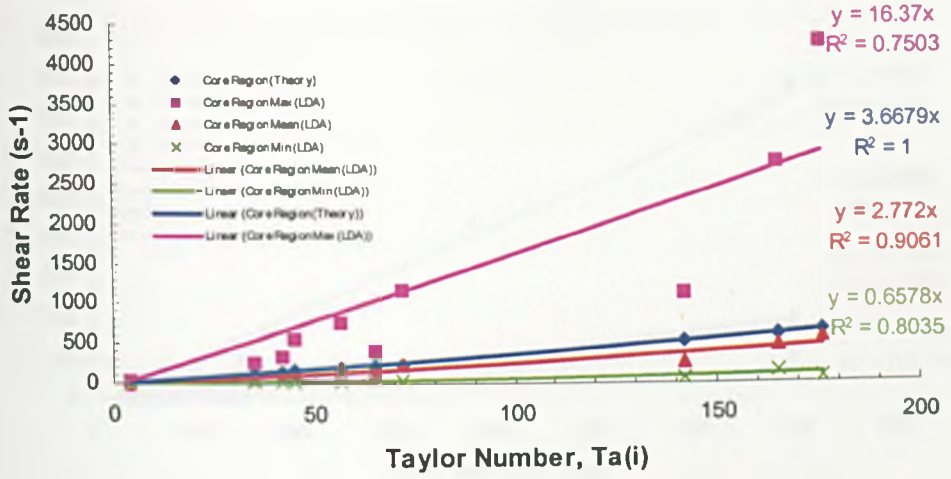

(b)

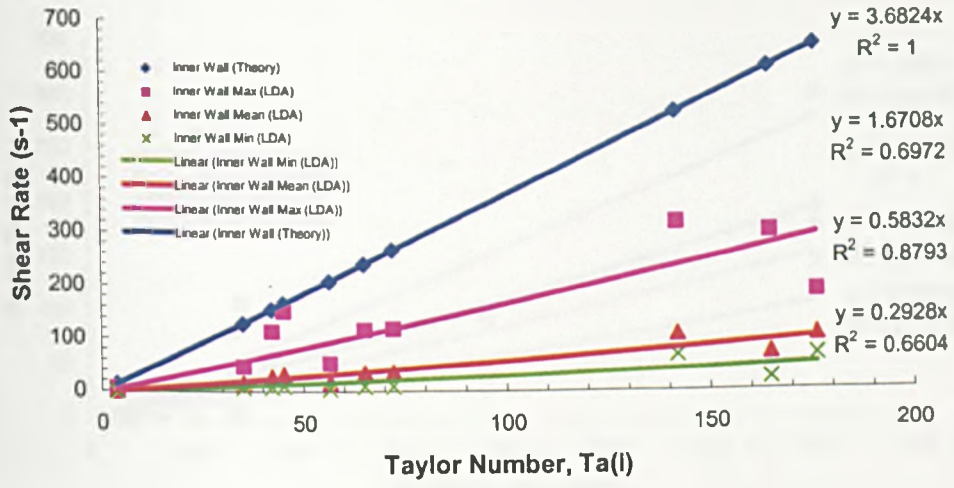

(c)

Figure 5.19 Comparison of shear rates for theory and LDA data in CC-25

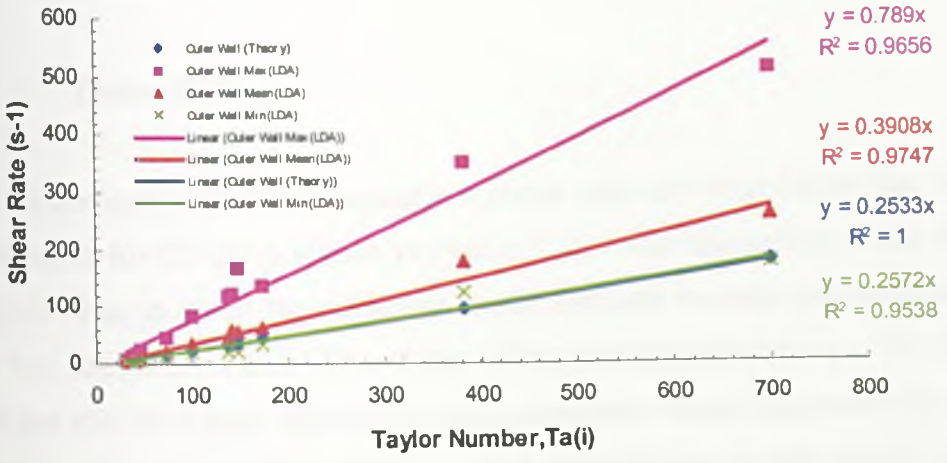

(a)

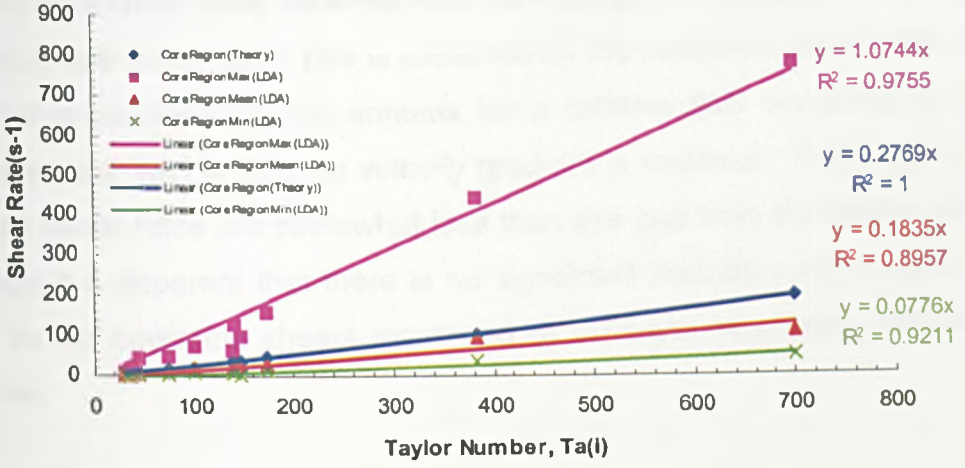

(b)

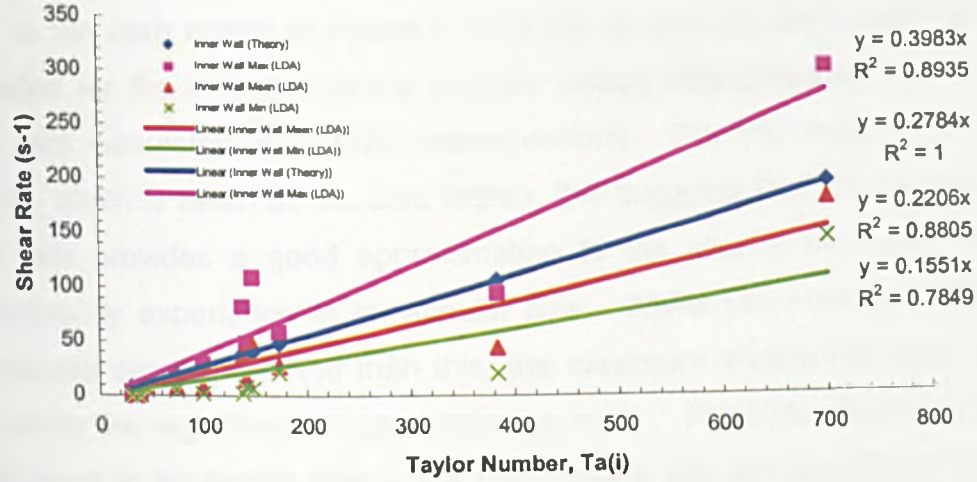

Figure 5.20 Comparison of shear rates for theory and LDA data in CC-75

5.13.1 CC-25

5.13.1.1 Outer Wall

The comparison of the theoretical shear rate and that based on LDA measurements for CC-25 is shown in Figure 5.19. The theoretical shear rate in Figure 5.19(a) is given for cells that would actually contact the outer wall when $r = r_o$ (equation 5.28). The shear rates calculated from the LDA data apply to the thin fluid layer (boundary layer) adjacent to and approaching the outer wall, and it is therefore clear that the magnitudes of the shear rates when compared should differ in some respect. It is observed from the data that maximum shear rates obtained from the LDA data very closely match the theoretical wall shear rate. This is expected as the maximum shear rate that would be encountered in the annulus for a rotating fluid would be at the stationary outer wall where the velocity gradient is maximal. The mean and minimum shear rates are somewhat less than this and from the shear stress flowmaps it is apparent that there is no significant boundary layer effect on shear, so the maximum shears measured by LDA are most likely very near wall ones.

5.13.1.2 Core Region

In the core region of Figure 5.19(b) the theoretical shear rate that is calculated for the midpoint of the annulus closely approximates the mean shear rate calculated from LDA measurements. For the majority of the annulus, which is taken as the core region, this suggests that the theoretical shear rate provides a good approximation to the shears the cells might predominantly experience in an annular flow. Whilst the minimum shears experienced are slightly less than this, the maximum shears the cells may experience are significantly higher than the mean. From the flowmaps this would seem to be largely due to the high shears that are developed at the edge of the inner wall boundary layer and the core region. Outside of this, the shears tend to be much lower and almost uniform for the remainder of the core region.

5.13.1.3 Inner Wall

It is clearly observed in Figure 5.19(c) that the theoretical shear rate calculated for the inner wall is significantly higher than the shear rates predicted by LDA measurements. As for the outer wall, it must be remembered that the theoretical shear rate is calculated for cells that would actually be in contact with the wall and this is likely to be higher than shears in the boundary layer adjacent to and approaching the wall that are calculated from the LDA measurements. Even the maximum shear rate from LDA data at the inner wall is much lower than the theoretical shear rate whereas at the outer wall the maximum and theoretical shears nearly coincide. This may be a consequence of the scale of the vessel; namely that at smaller scales geometrical imperfections may present themselves as artefacts and provide discrepancy between the observed maximum shear from LDA data and the theoretical shear.

5.13.2 CC-75

It is self-evident that in the larger scale system for similar Taylor number (when the same flow regime prevails) the spatial magnitudes of the three regions of the annular flow will be proportionally larger than for the small scale system. In a bioreactor environment of course, the cellular entities will remain fixed in size and this is significant in terms of the shear effects on these as the vessel scale changes.

5.13.2.1 Outer Wall

It is observed clearly that in the larger system the theoretical shear very closely approximates to the minimum shear rate calculated from LDA data, in contrast to observations in CC-25. These data suggest that in the outer wall boundary layer, flow disturbances therein produce higher stresses on particles than would be produced at the wall alone. This implies that very steep velocity gradients are present in the outer wall boundary layer,

particularly as the Taylor number increases. The mean shear encountered in the outer wall boundary layer approximates the theoretical shear only up to about $Ta_i = 200$ but then becomes higher with increasing Taylor number. It is observed that the maximum shears encountered are often significantly higher than the theoretical shear and this again is likely to be due to the relative sizes of the particle and the shear gradients encountered within the boundary layer.

5.13.2.2 Core Region

The shear trends observed in the core region for CC-75 as shown in Figure 5.20(b) are very similar to those observed in Figure 5.19(b) for CC-25. Essentially, this indicates that the flow patterns in the core regions for the two systems are the same for a prescribed Taylor number. This quantitatively verifies the qualitative data from flow visualisation that the dimensional analysis approach to scale-up using the Taylor number is successful. Of course the magnitude of the shear rate is different between the two systems and this is of course due to the relative sizes of the velocity gradient intervals and the particle size in the two systems. As for CC-25 then, the theoretical shear is slightly larger than the observed mean shear from LDA data, with the maximum shear being significantly higher than the theoretical shear, this being due to the high shears generated at the edge of the boundary layer on the core region/inner wall interface.

5.13.2.3 Inner Wall

Comparison of Figures 5.19(c) and 5.20(c) for inner wall shear rates again highlights discrepancy between the two systems. In CC-75 the theoretical shear approximates the mean observed shear from LDA data from the linear trend but on closer inspection, the theoretical shear data more closely follows the maximum shear from LDA data up to about $Ta_i = 200$. It is evident that in the very near wall regions, the relative size of the boundary layers, spatial resolution of the LDA velocity measurements and how the

particle size relates to these has a significant bearing on the resultant shear calculation.

5.13.3 Calculated Shears at Comparable Taylor Number

It is noted that the range of Taylor numbers used in the two systems is different. In the CC-25 system studies were made up to a Taylor number of 176.11 whereas in CC-75 studies were made to Taylor number 700.07. Whilst the trends of Figures 5.19 and 5.20 can be compared to provide general conclusions of the influence of scale-up on shear rate, some quantitative comparisons between the two systems at comparable Taylor numbers is useful, and how far these actually deviate from the theoretical prediction. Rudman (1992) made a study of this kind using computational fluid dynamics in a virtual system using the physical properties of water with r_i = 0.1m and d = 0.005m. It was observed in that work that the lowest shears were located in the centre of the core region and that the highest shears were generated on the edge of the boundary layers near the walls. It was further observed that the distribution of shear rates became more uneven as Ta_i increased and that a significant portion of particles in the flow (up to 74%) experienced shears greater than the mean. The findings generally agreed with the calculations in this work however the CFD approach is idealised and consequently artefacts are removed from the system.

In Table 5.4, shear rate data is presented for four different comparable Taylor numbers in the systems CC-25 and CC-75. The theoretical shear rates are calculated based on the linear theory and given by equations (5.26) through (5.28) for the three annular regions, outer wall, core region, inner wall. The absolute percentage difference (%d) from these theoretical values based on the obtained LDA data is quoted for maximum, mean and minimum shears for the three regions of the flow and for both scales of vessel. It is evident that the deviation from the linear theory can be very large, and this is particularly so for maximum shears and in the smaller scale system.

Whilst it is common to use a fixed geometrical ratio when scaling up bioreactors, it is an interesting exercise to investigate if scale-up can be

based on shear rates in the vessel. Given the large amount of data and the wide variation of Taylor number in the current study it is possible to do this.

	Ta	theory	max	%d	mean	%d	min	%d
25-out	35.07	119.24	86.38	27.56	53.60	55.05	48.67	59.18
25-core	35.07	128.65	286.11	122.39	64.78	49.65	20.36	84.18
25-in	35.07	129.16	48.96	62.09	16.91	86.91	8.10	93.73
75-out	38.83	9.84	15.24	54.85	8.64	12.19	5.20	47.15
75-core	38.83	10.76	18.47	71.75	6.97	35.25	2.97	72.36
75-in	38.83	10.81	5.27	51.27	1.84	83.00	0.76	93.02
25-out	45.06	153.18	162.67	6.20	80.10	47.71	47.02	69.31
25-core	45.06	165.27	588.35	256.00	103.52	37.36	27.89	83.12
25-in	45.06	165.92	153.77	7.32	33.41	79.86	10.36	93.76
75-out	45.25	11.47	26.83	134.00	12.16	6.08	6.79	40.75
75-core	45.25	12.53	48.84	289.66	10.60	15.45	2.87	77.14
75-in	45.25	12.60	10.45	17.07	9.05	28.16	5.30	57.96
25-out	72.12	245.16	272.56	11.18	141.24	42.39	73.38	70.07
25-core	72.12	264.51	1194.93	351.75	159.98	4.60	45.33	82.86
25-in	72.12	265.56	120.54	54.61	38.12	85.65	9.87	96.28
75-out	74.14	18.79	49.77	164.90	23.03	22.57	14.53	22.65
75-core	74.14	20.54	55.59	170.66	16.79	18.26	5.09	75.20
75-in	74.14	20.65	18.03	12.70	9.05	56.16	5.30	74.34
25-out	141.92	482.48	506.87	5.06	278.34	42.31	161.58	66.51
25-core	141.92	520.56	1134.98	118.03	282.49	45.73	83.82	83.90
25-in	141.92	522.62	317.27	39.29	109.17	79.11	67.99	86.99
75-out	141.54	35.87	125.64	250.26	61.07	70.25	32.32	9.90
75-core	141.54	39.21	136.12	247.15	29.05	25.91	12.23	68.82
75-in	141.54	39.43	50.31	27.61	16.83	57.32	8.91	77.40

Table 5.5 Quantitative Comparison of Shear Rate for Comparable Ta_i in Systems CC-25 & CC-75

In Table 5.5, the ratio of shear rates calculated for each of the systems CC-25 and CC-75 is presented for each of the three flow regions and for theoretical, maximum, mean and minimum cases for four comparable Ta_i..It is evident from the linear theory that the ratio varies very little both with location in the annulus and Ta_i and generally falls between 12 and 13. The minimum is 11.94 and the maximum is 13.85 with a mean of 12.82. This is for a scale-up factor of 3. Theoretically then it is predicted that for a scale-up factor (φ_1/φ_2) the resulting shear rate ratio (γ_2/γ_1) can be expressed as

$$\left(\frac{\varphi_1}{\varphi_2}\right)^{\alpha} = \left(\frac{\gamma_2}{\gamma_1}\right) \tag{5.30}$$

Ta=35-38	theory	max	mean	min
outer	12.12	5.67	6.20	9.36
core	11.96	15.49	9.30	6.85
inner	11.94	9.29	9.19	10.73

Ta=45	theory	max	mean	min
outer	13.36	6.06	6.59	6.92
core	13.19	12.05	9.77	9.73
inner	13.17	14.71	3.69	1.95

Ta=72-74	theory	max	mean	min
outer	13.05	5.48	6.13	5.05
core	12.88	21.50	9.53	8.90
inner	12.86	6.69	4.21	1.86

Ta=141	theory	max	mean	min
outer	13.45	4.03	4.56	4.99
core	13.28	8.34	9.72	6.86
inner	13.26	6.31	6.49	7.63

Table 5.6 Ratio of Shear Rates for CC-25 & CC-75 for Comparable Ta_i

Based on an average value of 12.82 for the theoretical case of Table 5.6 and a scale-up factor 3, α is calculated to be 2.32 in equation (5.30). For the data based on LDA measurements, there is much more variation than in the linear case both with position and Ta_i. Of most interest in the practical case is determining an approximate correlation for the core region where the particles have the largest residence time in the reactor. With particular reference to the mean ratio of Table 5.6, which is again of most general use in bioreactor design purposes, it is observed that the ratio of shear rates varies little, with a minimum value of 9.30 and a maximum value of 9.76 again for a wide range of Ta_i. Importantly this range would cover the majority used in a functional bioreactor. The mean is 9.58 and on this basis, α is

2.06. It would appear that no simple correlation can be applied to the data for maximum and minimum shears, particularly at the inner and outer walls.

5.14 Particle Behaviour in the Systems

In Sections 4.4.7.1 and 4.4.7.3 a number of theoretical predictions were presented on how the particles might behave in the annular flow systems in terms of drag forces, sedimentation behaviour and flocculation. Based on the particles and fluid environments employed some of these predictions are computed here.

5.14.1 Particle Reynolds Number (Re_p)

The particle Reynolds number is calculated for the two types of particles used in the system, Timiron flakes and glass spheres, in both CC-25 and CC-75 at the range of Taylor numbers explored. The results are shown in Figure 5.21.

The particle Reynolds number here is defined as

$$\mathrm{Re} = \frac{\mathrm{ud}\rho}{\mu} \qquad (5.31)$$

where u is the particle velocity in the fluid (assumed to be the fluid velocity for neutrally buoyant particles), d is the particle diameter (assuming spherical particles), and μ and ρ are the fluid viscosity and density respectively.

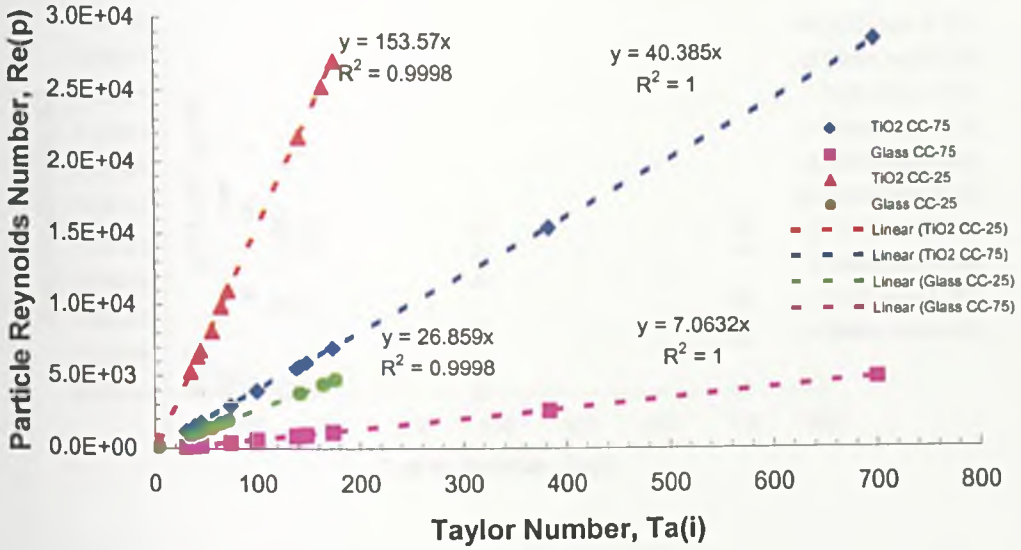

Figure 5.21 Variation of Particle Reynolds Number Re_p with Ta(i)

5.14.2 Drag Force on Particles

Drag on the particles is best described by the drag coefficent, C_D that can be evaluated by the alternative correlations given by equations (4.30) through (4.35) in Chapter 4. These are based on the particle Reynolds number Re_p and are compared for the two particle types in the two systems, CC-75 (a) and CC-25 (b) in Figure 5.22. It is evident from Figure 5.22 that the drag force on particles is increased due to buoyancy forces over particles in creeping flow (Stokes Law) governed by equation (4.30). It is further observed that the drag force is greater for the glass particles than TiO_2 particles and that this becomes independent of Ta(i) as Ta(i) increases beyond around 150 in both systems. At this Ta(i) the regular wavy-vortex structure begins to become disturbed. Equation (4.31) is not used in the calculation of C_D as this has applicability only for $Re_p < 2$ and was found to express values of C_D far in excess of those shown in Figure 5.19. For the high Re_p encountered in these systems (Figure 5.18), equations (4.34) and (4.35) are best recommended to evaluate C_D. Based on Figure 5.22, this suggests that the drag coefficient in both systems approximates to around 0.5 for a broad range of Ta(i).

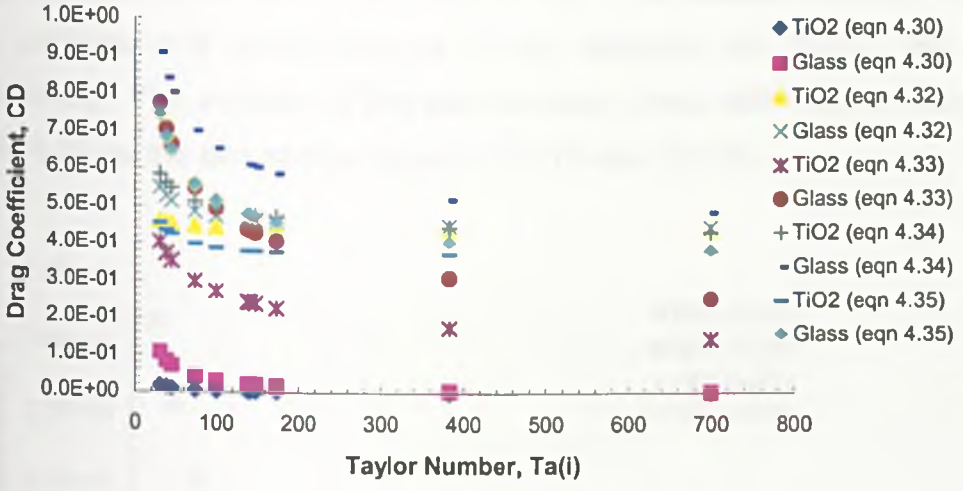

(a)

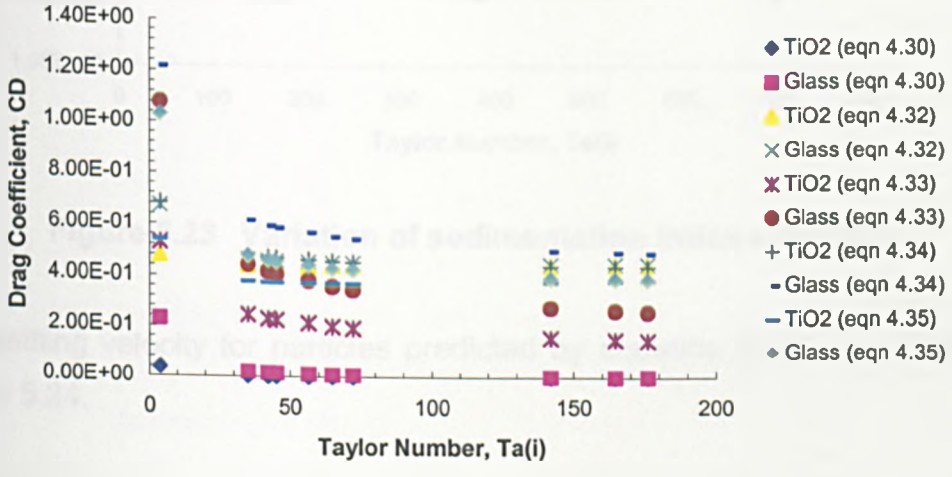

(b)

Figure 5.22 Comparison of drag coefficient C_D for particles in CC-75 (a) and CC-25 (b) with Ta(i) using selected correlations

5.14.3 Settling Velocity of Particles

In the annular flows investigated in this study, hydrodynamic disturbances are non-linear and the particles experience forces that are not simply in the orthogonal planes of the gravitational field and the centrifugal field. The only occurrence of this situation is for the linear hydrodynamic motion of laminar Couette flow. The settling velocity can be approximated

using equation (4.44) with (4.43) and (4.45). The Galileo number, Ga for TiO_2 particles and glass spheres in the systems are 62907 and 246 respectively. The variation of the sedimentation index with Ta(i) is shown in Figure 5.23 for the two particle types in CC-75 and CC-25.

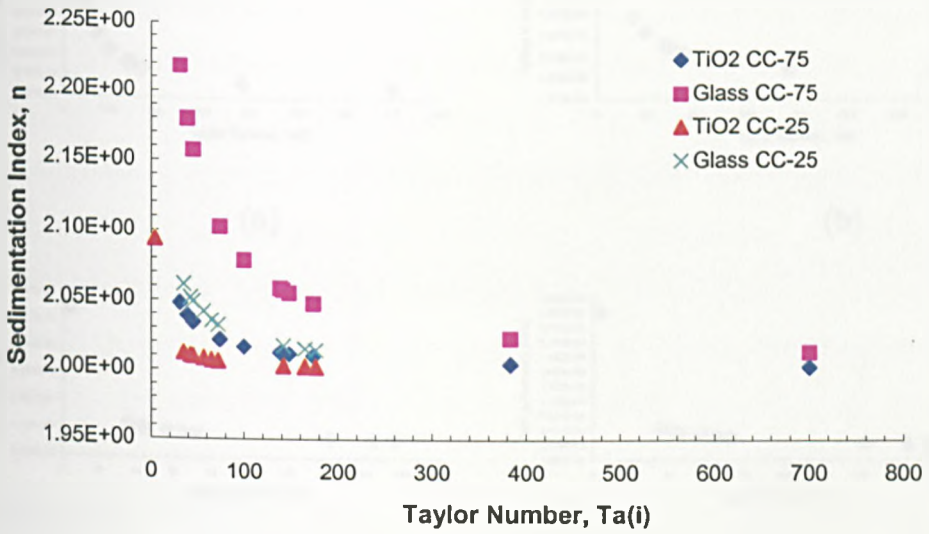

Figure 5.23 Variation of sedimentation index with Ta(i)

The settling velocity for particles predicted by equation (4.44) are shown in Figure 5.24.

The axial velocity flowmaps provide qualitative information on the particle falling velocities that are measured experimentally. These can be compared against those predicted by equation (4.44). A summary of comparison is given in Table 5.7 for CC-25 and CC-75 at comparable Taylor numbers. The change in the settling velocity predicted by equation (4.44) is negligible to 3 significant figures over the range of Tai investigated. This is expected as the theory is based on a linear pertubation (Couette flow). It would therefore be expected that for $Ta_i < 42$, which indicates laminar Couette flow, there should be good comparison between the predicted settling velocity and the experimental value obtained from LDA. No rigid value exists from the LDA data so a mean is taken. For system CC-25, the correlation of equation (4.44) overpredicts the settling velocity but the order

of magnitude is good. For CC-75 however there is excellent agreement between the LDA data and the predicted value.

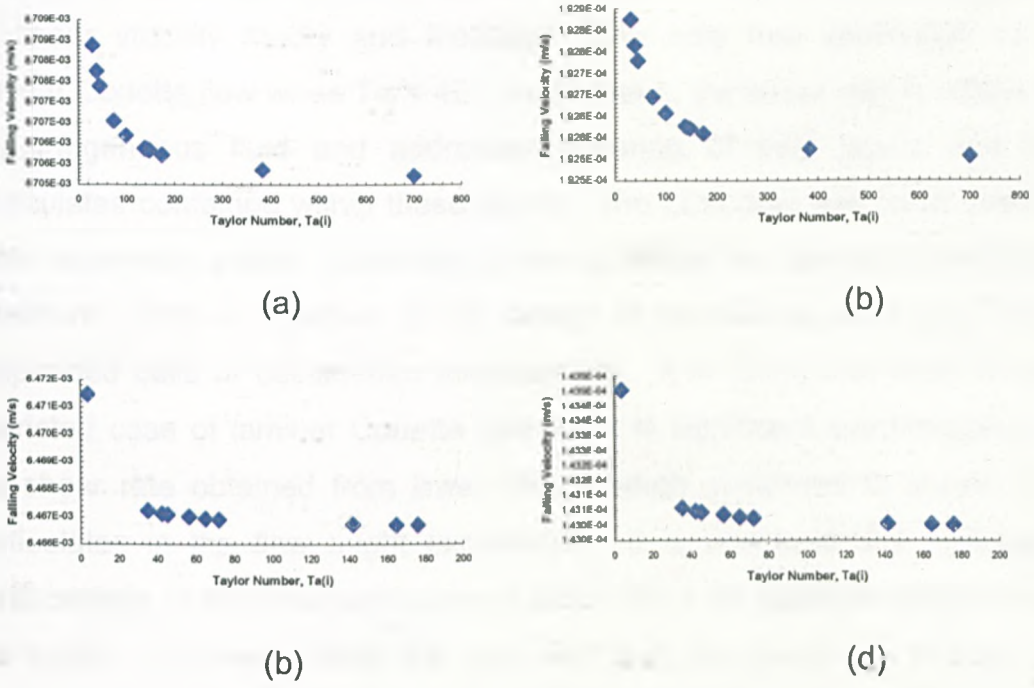

Figure 5.24 Estimated particle falling velocities with varying Ta(i) for TiO_2 in CC-75 (a), Glass in CC-75 (b), TiO_2 in CC-25 (c) and Glass in CC-25 (d)

CC-25			CC-75		
Ta_i	eqn (4.44)	LDA	Ta_i	eqn (4.44)	LDA
35.07	-0.006	-0.001	38.83	-0.009	-0.009
45.06	-0.006	0	45.25	-0.009	-0.006
72.12	-0.006	±0.004	74.14	-0.009	±0.002
141.92	-0.006	±0.04	141.54	-0.009	±0.007

Table 5.7 Comparison of settling velocities (ms^{-1}) from LDA data and from equation (4.44) for comparable Ta(i) in CC-25 & CC-75

5.15 Concluding Remarks

The shear rate experienced by a fluid in an annular flow can theoretically be predicted using equations (5.26) through (5.29) but is based on linear stability theory and therefore really only has application for a laminar Couette flow when $Ta_i < 42$. Furthermore, the shear rate is related to a homogeneous fluid and addresses shearing of fluid layers and not particulates contained within these layers. The LDA data has been used to more accurately predict particulate shearing where the spatial resolution is important. This is important for the design of bioreactors employing freely suspended cells or cell-seeded microcarriers. It is found that even for the restricted case of laminar Couette flow there is significant overprediction of the shear rate obtained from linear theory when compared to shears that particulates in the flow might experience. It is observed that non-linear perturbations in the flow which prevail when $Ta_i > 42$ generate a non-linear distribution of shear across the gap and that the maximum shears are encountered on the edge of the boundary layer of the moving inner wall for a system where only the inner wall rotates. In general, the maximum shear occurs in a small spatial domain relative to the whole of the annular flow domain and the magnitude of the maximum shear is significantly higher than that seen elsewhere. For cells/cell-constructs in such a flow domain it means that in general they will experience low shears for the majority of the time and for very small time periods will intermittently experience these higher shear stresses. Whilst as a general guideline 0.6 Pa is taken as a critical shear stress (Hua, 1993; Ludwig, 1992; Kunas, 1990), it is seen that for the range of Ta_i investigated in this study using a fluid which has similar viscometric properties of cell culture media, the shear stress is in general much lower than this value. Much higher stresses are generated in the smaller scale system CC-25 for the same Ta_i than in CC-75 and it is suggested from the data shown that an upper limit for operation is at around $Ta_i = 141$. At this point the thin region of high stresses approximates in the region 0.6 to 0.9 Pa whilst the majority of the domain is of the order 0.2 Pa. With only a small increase in Taylor number at this scale the stresses increase to between 0.5 and 1.0 Pa in the major flow domain and between 2.0 and 3.5 Pa in the high

shear region. This would be considered super-critical for long-term cell culture. By contrast in CC-75, for the same media conditions and Ta_i = 141, the maximum stresses encountered are only around 0.12 Pa and the predominant stresses are only between 0.02 and 0.04 Pa. Only with Ta_i as high as 700 do the maximum shear stresses begin to become critical. Clearly, the scale of the vessel has implications on the resultant shear stresses that will be generated in cell seeded bioreactors and this is important not only in terms of cellular viability but also for mechanotransduction and biomechanical signalling pathways.

References

Ashwin P, King GP, A Study of Particle Paths in Non-Axisymmetric Taylor-Couette Flow. *J.Fluid Mech.* **338** 341-362 (1997)

Chien S, Usami S, Taylor HM, Lundberg JL, Gregersen MI, Effects of Hermatocrit and Plasma Proteins on Human Blood Rheology at Low Shear Rates. *J. Appl. Physiol.* **21** (1) 81-87 (1966)

Chong MS, Perry AE, Cantwell B, A General Classification of Three Dimensional Flow Fields. *Phys. Fluids A* **2** 765-777 (1990)

Dintenfass L, Molecular Rheology of Human Blood: Its Role in Health and Disease (Today and Tomorrow?). *Proc. 8th Int. Congr. on Rheology* **3** 467-480 (1980)

Ditzel J, Kampmann J, Whole Blood Viscosity, Hermatocrit and Plasma Protein in Normal Subjects at Different Ages. *Acta Physiol. Scand.* **81** 264-268 (1977)

Hanselman D, Littlefield B, Mastering Matlab, Matlab Curriculum Series, Prentice Hall, New Jersey, 133 (1996)

Howes T, Rudman M, Flow and Axial Dispersion Simulation for Travelling Axisymmetric Taylor Vortices. *AIChE Journal* **44** (2) 255-262 (1998)

Jones CA, On Flow Between Counter-Rotating Cylinders. *J. Fluid Mech.* **120** 433-450 (1982)

Kay JM, Nedderman RM, Fluid Mechanics and Transfer Processes. Cambridge University Press. (1985)

King GP, Rowlands G, Rudman M, Yannacoupoulos AN, Predicting Chaotic Dispersion with Eulerian Symmetry Measures: Wavy-Taylor Vortex Flow. *Phys. Fluids* **13** (9) 2522-2528 (2001)

Kunas KT, Papoutsakis ET, Damage Mechanisms of Suspended Animal Cells in Agitated Bioreactors with and without Bubble Entrainment. *Biotech. Bioeng.* **36** 476-483 (1990)

Ludwig A, Kretzmer G, Schugerl K, Determination of a "Critical Shear Stress Level" Applied to Adherent Mammalian Cells. *Enz.Microb.Technol.* **14** 209-213 (1992)

Majumdar AK, Spalding DB, Numerical Computation of Taylor Vortices. *J. Fluid Mech.* **81** 295-304 (1977)

Marcus PS, Simulation of Taylor-Vortex Flow. Part 2. Numerical Results for Wavy-Vortex Flow with One Travelling Wave. *J. Fluid Mech.* **146** 65-113 (1984)

Meyer KA, Time-Dependent Study of Taylor-Vortex Flow. *Phys. Fluids* **10** 1874-1879 (1967)

Moser RD, Moin P, Leonard A, A Spectral Numerical Method for the Navier-Stokes Equations with Applications to Taylor-Couette Flow. *J. Comp. Phys.* **52** 524-544 (1983)

Ninomiya M, Fujii M, Niwa M, Sakamoto K, Kanai H, Physical Properties of Flowing Blood. *Biorheology* **25** 319-328 (1988)

Rudman M, Mixing and Particle Dispersion in the Wavy-Vortex Regime of Taylor-Couette Flow. *AIChE Journal* **44** (5) 1015-1026 (1998)

Rudman M, Thompson MC, Hourigan K, Particle Shear Rate History in a Taylor-Couette Column. *ASME FED Liquid-Solid Flows* **189** 23-30 (1994)

Rudolph M, Shinbrot T, Lueptow, RM, A Model of Mixing and Transport in Wavy Taylor-Vortex Flow. *Physica D* **121** 163-174 (1998)

Ryrie S, Mixing by Chaotic Advection in a Class of Spatially Periodic Flows. *J. Fluid Mech.* **236** 1-19 (1992)

Thurston GB, Rheological Parameters for the Viscosity, Viscoelasticity and Thixotropy of Blood. *Biorheology* **16** 149-162 (1979)

Weiss JB, Knobloch E, Mass Transport and Mixing by Modulated Waves. *Phys. Rev. A* **40** 2579-2583 (1989)
Wells RE, Denton R, Merrill EW, Measurement of Viscosity of Biologic Fluids by Cone Plate Viscometer. *J. Lab. & Clin. Med.* **57** (4) 646-656 (1961)

Wereley ST, Lueptow RM, Azimuthal Velocity in Supercritical Circular Couette Flow. *Expt. Fluids* **18** 1-9 (1994)

Wereley ST, Lueptow RM, Spatio-Temporal Character of Non-Wavy and Wavy Taylor-Couette Flow. *J. Fluid Mech.* **364** 59-80 (1998)

Wereley ST, Lueptow RM, Inertial Particle Motion in a Taylor-Couette Rotating Filter. *Phys. Fluids* **11** (2) 325-333 (1999a)

Wereley ST, Lueptow RM, Velocity Field for Taylor-Vortex Flow with an Axial Flow. *Phys. Fluids* **11** (12) 3637-3649 (1999b)

Chapter 6

Relationships and Techniques for Mass Transport Studies

6.1 Mass transport: General Considerations

Mass transport is the term used to denote the transference of a component in a mixture from a region in which its concentration is high to a region where the concentration is lower. It can result from random velocity fluctuations of molecules (molecular diffusion) or from the circulating or eddy motions present in a moving fluid (eddy diffusion). The diffusion can occur in single or multiphase systems. The rate of diffusion is governed by Fick's Law, first proposed by A. Fick in 1855. It expresses the mass transfer rate as a linear function of the molar concentration gradient. For the case of a mixture of two ideal gases **A** and **B**, Ficks Law for steady state diffusion is written as:

$$N_A = -D_{AB}\frac{dC_A}{dy} \qquad (6.1)$$

An exactly similar equation exists for **B**:

$$N_B = -D_{BA}\frac{dC_B}{dy} \tag{6.2}$$

For a constant pressure ideal gas mixture, ($C_A + C_B$) is constant, and

$$\frac{dC_A}{dy} = -\frac{dC_B}{dy} \tag{6.3}$$

For the pressure (or molar concentration) to remain constant in such a system there should be no net transference of numbers of molecules and the process is referred to as *equimolar counterdiffusion*. This relation is satisfied only if $D_{AB} = D_{BA}$ so the suffixes can be dropped:

$$N_A = -D\frac{dC_A}{dy} \tag{6.4}$$

This describes the mass transfer rate arising purely from the random movement of the molecules and is only applicable to a stationary medium or a fluid in streamline (laminar) flow. When circulating currents or eddies are superimposed on the flow then the mechanism for molecular transport will be reinforced and the total transfer rate can be generally expressed as:

$$N'_A = -(D + E_D)\frac{dC_A}{dy} \tag{6.5}$$

D is a physical property of the system and is dependent only on composition, pressure and temperature. E_D, the *eddy diffusivity*, is dependent on the prevailing flow pattern in the system and is dependent on position in the system. The molecular diffusivity, D, can be expressed in terms of the molecular velocity u_m and the mean free path of the molecules, λ. When the kinetic theory of gases is applicable, the molecular diffusivity is proportional to $u_m\lambda$. Equation (6.5) can otherwise be described as:

$$N'_A = N_A + u_F C_A \tag{6.6}$$

where N'_A is the total transfer (moles/area time), N_A is the diffusional transfer by Fick's Law, and $u_F C_A$ is the transfer by bulk flow. The bulk flow velocity, u_F, is (total moles transferred/area time)/total molar concentration:

$$u_F = \frac{N'_A + N'_B}{C_T} \tag{6.7}$$

In reality mass transfer processes are not instantaneous; unsteady state conditions prevail and the process becomes time dependent. For equimolecular counter-diffusion,

$$\frac{\partial c_A}{\partial t} = D\frac{\partial^2 c_A}{\partial y^2} \tag{6.8}$$

This is referred to as Fick's Second Law. It can be solved for a number of boundary conditions, and becomes important in free surface mass transfer.

Bioreactor operation normally requires the mass transport of both solutes (ions, biomolecules) and gases (oxygen, carbon dioxide), through a liquid medium. The diffusion in a liquid is governed by the same equations as for gas phase diffusion described above, but the diffusion coefficient, D, is about two orders of magnitude lower for a liquid than for a gas. The diffusion coefficient additionally becomes a more complex function of the molecular properties of the diffusing species and the surrounding media. Whilst for an ideal gas (and approximately for real gases and vapours) the total molar concentration remains constant, this is very often not the case for liquids. For this reason the diffusion equations are normally expressed in terms of a mass flux, J_A, (mass/unit area, unit time) and the concentration gradients in terms of mass concentrations, c_A. The conversion from molar flux to mass flux is made simply, making use of the molecular mass of the diffusing component. Equation (6.4) can be converted in this way:

$$J_A = -D\frac{dc_A}{dy} = -D\rho\frac{d\omega_A}{dy} = -DM_A\frac{dC_A}{dy} \tag{6.9}$$

where ρ is mass density (taken as a constant), and ω_A is the mass fraction of **A** in the liquid. The diffusional process in a liquid gives rise to a situation of equal transferral *mass* rates for components in the system, the mass flux equivalent of equimolar counter diffusion. Liquid phase diffusivities are strongly dependent on the concentration of the diffusing species in contrast to gas phase diffusivities that are essentially independent of concentration. Liquid phase diffusivities that are often quoted in the literature refer to very dilute concentrations of the species relative to the bulk liquid, and for the purposes of most studies, this condition is normally met experimentally. The diffusivities of some components pertinent to this study are shown in Table 6.1 (Perry, 1984).

Solute	Solvent	D ($m^2/s \times 10^9$)
O_2	Water	1.80
CO_2	Water	1.50
NH_3	Water	1.76
N_2	Water	1.64
Glucose	Water	0.60
Sucrose	Water	0.45
Sodium Chloride	Water	1.35
Ethanol	Water	1.00
CO_2	Ethanol	3.4

Table 6.1: Diffusivities for various solutes at 293K

Liquid phase diffusivities can be calculated empirically for dilute solutions from:

$$D = \frac{7.7 \times 10^{-16} T}{\mu \left(V^{1/3} - V_o^{1/3} \right)} \qquad (6.10)$$

where D is the diffusivity in m^2/s, T is the temperature in K, μ the viscosity in Ns/m^2, V_o is 0.008 for water or 0.0149 for ethanol in $m^3/kmol$ and V is the molecular volume. The molecular volume is the volume in m^3 of 1 kmol of the material in liquid form at its boiling point, and is a measure of the volume occupied by the molecules themselves. This may not be known but can be approximated using Kopp's law of additive volumes. Kopp assigned a value

for the equivalent atomic volume of each element. The equivalent atomic volume is estimated by adding the volumes of the constituent atoms of the unknown molecule. Some atomic volumes are given in Table 6.2.

Component	Atomic Volume (m^3/kmol)
Air	0.0299
Carbon	0.0148
Hydrogen	0.0037
Oxygen, double bonded	0.0074

Table 6.2: Atomic Volumes of molecules for use in Kopp's law

6.2 Mass transport: Bioreactor Considerations

The importance of the relative scales and magnitudes pertinent to cellular proliferation in terms of solute and oxygen utilisation has been previously discussed. In the working bioreactor, the scales of distance become extremely large relative to the size of the cell. The probability that the overall rate of solute and oxygen utilisation by cells is limited by a physical transport process, than it is by the rate of metabolism of the cells, increases considerably as the ratio of the reactor volume to the cell volume increases. Weisz (1973) suggests that cells operate at their maximum possible metabolic rate in the absence of any serious diffusional limitations. The mass transport of the solutes and the gases has to be treated independently because of diffusional differences. For correct cellular respiration to proceed, sufficient nutrient and oxygen concentrations need to be established at the surface of the cell and the presence of aerobic or anaerobic activity is entirely dependent on the local bulk oxygen concentration and the diffusion of oxygen through the media to the metabolic site. The general nature of the mass transport problem in a cellular bioreactor has been represented schematically by Bailey (1985) and is illustrated in Figure 6.1:

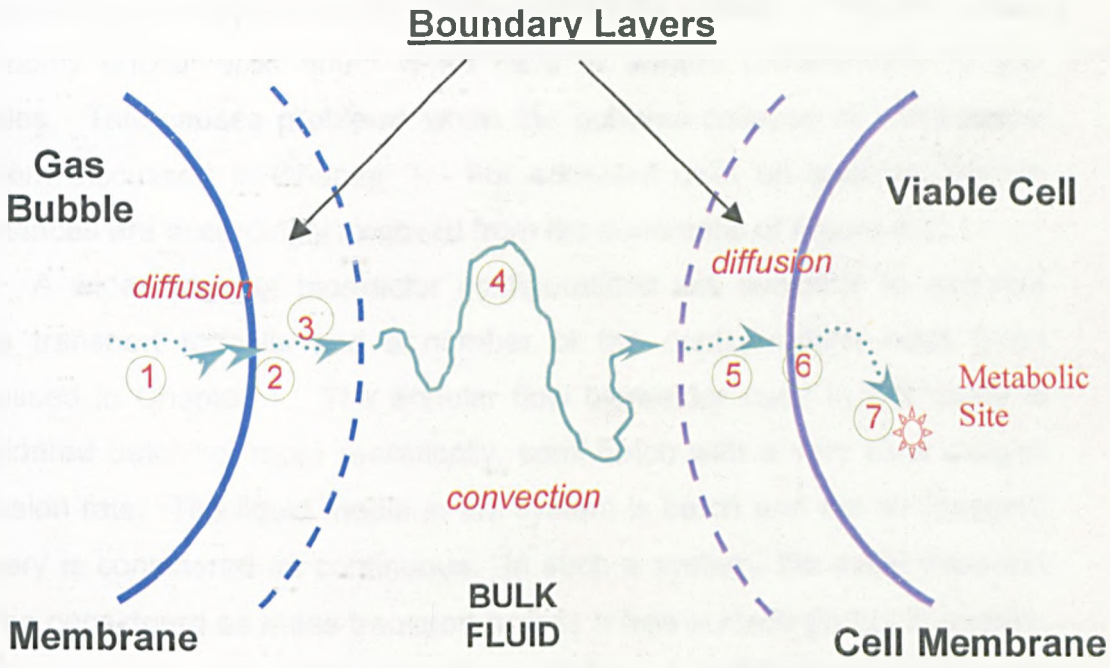

Figure 6.1 Schematic of the oxygen transport process from an air bubble to a viable cell

This schematic represents transfer of gaseous oxygen from a bubble of oxygen in the system, through the surrounding media and across the cell membrane and into the cell to be respired. There are a number of transport resistances through which the oxygen must pass before reaching the cell and these are:

1. Diffusion from the bulk gas to the gas-liquid interface
2. Movement through the gas-liquid interface
3. Diffusion of the solute through the relatively unmixed liquid region adjacent to the bubble and into the well mixed bulk liquid
4. Transport of the solute through the bulk liquid to a second relatively unmixed liquid region surrounding the cells
5. Transport through the second unmixed liquid region associated with the cells
6. Diffusive transport to the cellular floc
7. Transport across the cell envelope and to intracellular metabolic site

For individual cells, the sixth resistance is absent. The use of bubbles for oxygenation is considered to be detrimental to the viability of the cell, and a commonly encountered effect is for cells to adhere preferentially to gas bubbles. This causes problems when the bubbles collapse or coalesce, a problem discussed in Chapter 1. For adherent cells on bubbles, certain resistances are accordingly removed from the schematic of Figure 6.1.

A wide range of bioreactor configurations are available to optimise mass transport to cells and a number of the configurations have been discussed in Chapter 1. The annular flow bioreactor used in this study is considered batch, or more realistically, semi-batch with a very slow oxygen perfusion rate. The liquid media in the system is batch and the air (oxygen) delivery is considered as continuous. In such a system, the initial transport can be considered as mass transport across a free surface phase boundary, much as for the gas bubble of Figure 6.1, but a 2-D flat surface. In quantifying the overall transport in the bioreactor, it is first important to outline the theory of transport across the free surface phase boundary.

6.3 Mass transport across a phase boundary

The theory presented in section 6.1 has addressed mass transfer within a single phase where no discontinuities exist and for the limited condition of a stationary system or one in laminar flow. Before addressing the more complex problem of a system with a flow imposed that is not laminar, it is important to address the problem of transport across a phase boundary. This scenario is commonly encountered in a wide variety of industrial applications as well as in bioreactor design. Common examples are distillation, gas absorption and liquid-liquid extraction processes. The unifying concept is that there is transference of material across an interface. The transfer rate between two fluid phases (the gas phase considered as a fluid phase) depends on the physical properties of the two phases, the concentration difference of the transferring species in the two phases, the interfacial area available for transport and of course, any fluid motion in the phases. Mass transport facilities are designed to optimise all these effects, and the bioreactor can be considered as such a facility. Ideally then, a large

concentration gradient should be maintained to facilitate transport, the interfacial area should be maximal, and normally, the hydrodynamics of the bioreactor should be tailored to improve the transport.

A number of mechanisms have been proposed to represent conditions in the region of a phase boundary where the concentrations of a diffusing species is different either side of the boundary. The more common mechanisms are described below.

6.3.1 Two-Film theory

The theory was first proposed by Whitman in 1923 and was the first attempt to mathematically describe the conditions when material is transferred from one fluid stream to another. Whilst not accurately reproducing the conditions commonly encountered in practice, expressions are derived which can be applied to generally available experimental data and in that sense the theory provides useful guideline data. The theory assumes that a laminar layer exists at the interface in the two fluids. Fluid motions outside this laminar layer reinforce the random molecular motion and the resistance to transfer becomes progressively smaller. The concept is illustrated in Figure 6.2. For equimolecular counter-diffusion the concentration gradient is linear close to the interface and becomes less at greater distances from it, indicated by lines ABC and DEF in Figure 6.2. The theory assumes that two layers or films exist either side of the interface in which transport takes place by molecular diffusion alone.

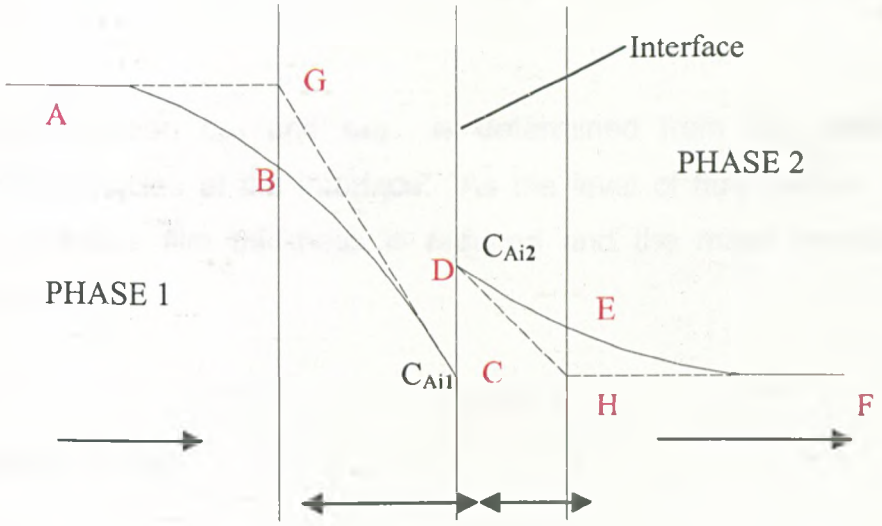

Figure 6.2 Two-Film Theory of Mass Transport

The concentration gradient is hypothetically considered linear inside these layers and zero outside, indicated by lines AGC and DHF in Figure 6.2. L_1 and L_2 are the film thicknesses. Equilibrium is assumed at the interface and the relative positions of C and D is determined from the equilibrium relationship between the phases. For the steady state assumption for mass transfer to be valid, the time for concentration gradients to be established must be small relative to the time of transfer or alternatively, the capacity of the films must be negligible. The mass transfer rate for equimolecular counter-diffusion for phase 1 can be expressed using equation (6.8) as:

$$J_A = \frac{D_1}{L_1}(c_{Ao1} - c_{Ai1}) = k_1(c_{Ao1} - c_{Ai1}) \qquad (6.11)$$

and similarly for the second phase,

$$J_A = \frac{D_2}{L_2}(c_{Ai2} - c_{Ao2}) = k_2(c_{Ai2} - c_{Ao2}) \qquad (6.12)$$

Material does not accumulate at the interface and so,

$$\frac{k_1}{k_2} = \frac{c_{Ai2} - c_{Ao2}}{c_{Ao1} - c_{Ai1}} \qquad (6.13)$$

The relationship between c_{Ai1} and c_{Ai2} is determined from the phase equilibrium for the species at the interface. As the level of fluid motion is increased, the effective film thickness is reduced and the mass transfer coefficients increase.

6.3.2 Penetration Theory

The *penetration theory* for mass transfer was developed by Higbie in 1935 in a study to investigate transfer resistance at the interface of a pure gas absorbed in a liquid in a 3mm diameter glass tube. In his experiments a bubble of carbon dioxide rose through a column of water. Liquid ran back over the bubble as a thin film. The assumption was that elements of liquid were exposed to the gas for a certain time period as the gas bubble passed. This time was estimated based on the bubble size and its velocity and in the Higbie experiments varied between 0.01 and 0.1s. The liquid was considered to have infinite depth since the exposure time was so short. Absorption is considered to take place due to unsteady state molecular diffusion into the liquid. Typical data for concentration profiles is illustrated in Figure 6.3. Immediately at the surface, the saturation goes from 0 to 100. For longer exposure times, the concentration profile develops further down into the liquid with increased exposure time, so that for any given percentage saturation, a time-distance relationship can be established. The penetration theory is particularly applicable for gaseous transfer into a liquid phase through a free surface. The fluid motion brings an element of fluid to the surface that is exposed to the gas for a definite time period before being transferred back into the bulk liquid. Equilibrium at the phase interface is assumed and that unsteady state transfer occurs for the fixed time period before the fluid element returns to the bulk liquid.

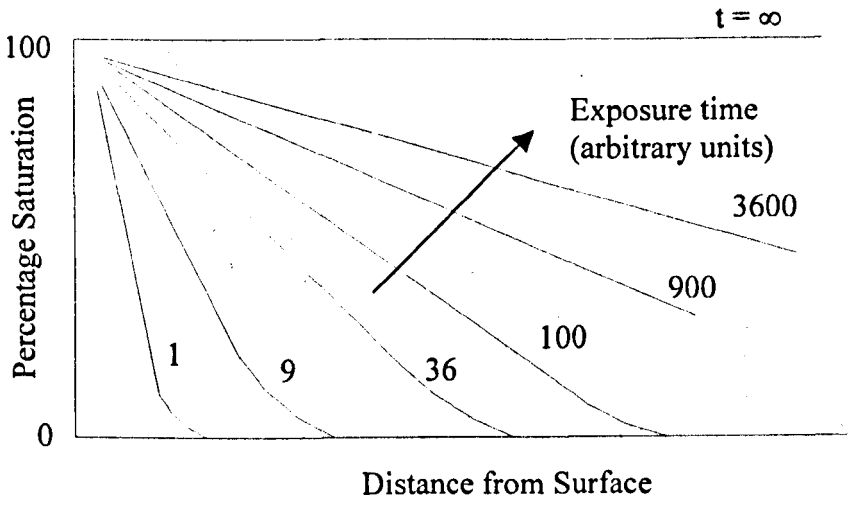

Figure 6.3 Penetration of Solute into a Solvent Based on Higbie Theory

In considering a vertical body of liquid into which gas diffuses from the free surface, the diffusion of species **A** from the gas through the interface and into the liquid in a vertical direction, z, is described by equation (6.8):

$$\frac{\partial c_A}{\partial t} = D\frac{\partial^2 c_A}{\partial z^2} \qquad (6.14)$$

assuming equimolecular counter-diffusion, for a low concentration of diffusing species the following boundary conditions apply:

$$\begin{array}{llll} t=0 & 0<z<\infty & c_A = c_{Ao} \\ t>0 & z=0 & c_A = c_{Ai} \\ t>0 & z=\infty & c_A = c_{Ao} \end{array} \qquad (6.15)$$

Equation (6.14) is first order in t and second order in z, and with the given boundary conditions can be solved analytically. The result is:

$$\frac{\partial c_A}{\partial z} = -(c_{Ai} - c_{Ao})\frac{1}{\sqrt{\pi Dt}}e^{-z^2/4Dt} \qquad (6.16)$$

The mass transfer rate at any position, z, at time t is given by:

$$J_A = -D\frac{\partial c_A}{\partial z} = (c_{Ai} - c_{Ao})\sqrt{\frac{D}{\pi t}}e^{-z^2/4Dt} \qquad (6.17)$$

The mass transfer rate at the surface is then given by:

$$(J_A)_{z=0} = -D\left(\frac{\partial c_A}{\partial y}\right)_{z=0} = (c_{Ai} - c_{Ao})\sqrt{\frac{D}{\pi t}} \qquad (6.18)$$

The point value of the mass transfer coefficient is $\sqrt{\frac{D}{\pi t}}$.

6.3.3 Surface Renewal Theory

It is evident from the penetration theory that the mass transfer rate decreases progressively as the exposure period increases, theoretically from infinity at t = 0 to zero at t = ∞. Ideally, the average mass transfer rate over a time, t_e, for which a fluid element is exposed to the interface, is required. This can be determined by integrating the total mass transferred in time t_e and dividing by the time. Using the Higbie assumption that all the surface elements are exposed to the interface for the same time period,

$$(J_A)_{av} = (c_{Ai} - c_{Ao})\sqrt{\frac{D}{\pi}}\frac{1}{t_e}\int_0^{t_e}\frac{dt}{\sqrt{t}}$$

$$= 2(c_{A_i} - c_{Ao})\sqrt{\frac{D}{\pi t_e}} \qquad (6.19)$$

It is evident from equation (6.19) that the shorter the exposure time, t_e, then the higher the average mass transfer rate will be. In practice it is almost impossible to accurately assign a value for t_e, but in general, one can say that as the liquid is increasingly agitated the value of t_e will decrease and so the transfer rate will increase. Again assuming that fluid elements all contact the

interface for time t_e, equation (6.19) is the overall mean rate of transfer and is linearly proportional to the concentration difference, and proportional to the diffusivity raised to the power 0.5, which can be compared to the two film theory where the diffusivity is raised to the power 1.0.

6.3.4 Random surface renewal theory

The random surface renewal theory proposed by Danckwerts (1951) is an extension of the surface renewal theory where it is assumed that elements of fluid would not be exposed to the interface for a fixed time, t_e, but a random distribution of ages would exist. A further assumption made is that the probability of any element of surface being disrupted and remixed with the bulk fluid is independent of the age of the element. The rate of production of fresh surface per unit total surface area is given by φ. φ is independent of the age of the element. The area of surface of age between t and t + dt will be a function of t, i.e. f(t)dt. The age distribution of the surface takes an exponential form:

$$f(t) = \varphi e^{-\varphi t} \tag{6.20}$$

The mass transfer rate from the penetration theory is given by equation (6.18), so the overall transfer rate per unit area for random surface renewal is:

$$\begin{aligned} J_A &= (c_{Ai} - c_{Ao}) \int_{t=0}^{t=\infty} \sqrt{\frac{D}{\pi t}} \varphi e^{-\varphi t} dt \\ &= (c_{Ai} - c_{Ao}) \varphi \sqrt{\frac{D}{\pi}} \int_0^{\infty} t^{-1/2} e^{-\varphi t} dt \end{aligned} \tag{6.21}$$

Equation (6.21) is solved analytically using the substitution $\varphi t = \beta^2$ and then $\varphi dt = 2\beta d\beta$. Then,

$$J_A = (c_{Ai} - c_{Ao})\varphi\sqrt{\frac{D}{\pi}}\frac{2}{\varphi^{1/2}}\int_0^{\infty} e^{-\beta^2} d\beta \qquad (6.22)$$

The value of the integral in equation (6.22) is $\sqrt{\pi}/2$ and so,

$$J_A = (c_{Ai} - c_{Ao})\sqrt{D\varphi} \qquad (6.23)$$

Whilst equation (6.23) might be considered to underestimate the mass transfer rate as there will be a finite upper age to the surface elements, the number of these older elements will be small in proportion to the total number of elements, so the overall mass transfer rate will be largely unaffected. The mass transfer rate is seen to be proportional to the concentration difference at the interface and the square of the diffusivity. φ is difficult to quantify, but in general terms its value will increase as the agitation of the liquid phase increases.

6.3.5 Film penetration theory

Toor and Marchello (1958) proposed a theory that incorporates aspects of both the two film theory and the penetration theory. Transfer is assumed to take place in a thin laminar film at the interface but as an unsteady state process. Fresh surface is generated by the liquid motion, mass transfer occurs as described by the penetration theory but resistance occurs in a thin film and the transferring species is immediately mixed with the bulk fluid after traversing the film. For short t_e, the process follows the penetration theory. For long t_e, when concentration gradients are allowed to develop the process is described by the two film theory. The transfer process is described by equation (6.14) but the third boundary condition is applied for z = L, the film thickness, and not z = ∞. The solution is found analytically as in Section 6.3.2 using Laplace transforms with the result,

$$\frac{1}{c_{Ai}-c_{Ao}}\frac{\partial c_A}{\partial z}=\sum_{n=0}^{n=\infty}-\frac{2}{\sqrt{\pi}}\frac{1}{2\sqrt{Dt}}e^{-(2nL+z)^2/(4Dt)}-\sum_{n=0}^{n=\infty}\frac{2}{\sqrt{\pi}}\frac{1}{2\sqrt{Dt}}e^{-[2(n+1)L-z]^2/4(Dt)} \tag{6.24}$$

At the free surface, z = 0,

$$\frac{1}{c_{Ai}-c_{Ao}}\left(\frac{\partial c_A}{\partial z}\right)_{z=0}=-\frac{1}{\sqrt{\pi Dt}}\left(1+2\sum_{n=1}^{n=\infty}e^{-(n^2L^2)/(Dt)}\right) \tag{6.25}$$

The mass transfer rate across the interface per unit area, is given by a form of equation (6.9):

$$J_A=-D\left(\frac{\partial c_A}{\partial y}\right)_{y=0}=(c_{Ai}-c_{Ao})\sqrt{\frac{D}{\pi t}}\left(1+2\sum_{n=1}^{n=\infty}e^{-(n^2L^2)/(Dt)}\right) \tag{6.26}$$

It can be shown that with an error not exceeding 9%, the convergence solution for equation (6.26) is:

$$0<\frac{L^2}{Dt}\le\pi \quad J_A=(c_{Ai}-c_{Ao})\frac{D}{L} \qquad \text{(a)}$$

$$\pi\le\frac{L^2}{Dt}<\infty \quad J_A=(c_{Ai}-c_{Ao})\sqrt{\frac{D}{\pi t}} \qquad \text{(b)} \tag{6.27}$$

Either the two-film theory (equation (6.27a)) or the penetration theory (equation (6.27b) can be used to describe the mass transfer process. Equation (6.27a) more commonly applies for applications where there is a well-defined interface, as in free surface aeration, whereas equation (6.27b) is more applicable when the phase interface is less well defined, for example when one of the phases is dispersed as droplets in the other phase or for bubbled aeration through a liquid media.

6.4 Phase Equilibrium

The transfer of species from one phase to another depends on the system properties of temperature and pressure, and the compositions of the phases either side of the phase interface.

6.4.1 Ideal Behaviour

When an assumption is made that all the molecules in the phases are of equal size and the forces between the molecules are equal the phase is considered to be an *ideal phase*. For an ideal gas phase, the Ideal Gas Law is often used to describe the thermodynamic properties of the system where the molar volumes of the pure species, V_i^{ig} are all equal to RT/P. When two or more ideal gases are mixed there is no volume change on mixing since the molar volume of the mixture is the sum of the component species:

$$V^{ig} = \sum y_i V_i^{ig} \tag{6.28}$$

Analogously, the ideal solution is formed from pure species at actual molar volumes V_i, and the volume change on mixing is zero provided the pure species and mixture are at the same temperature and pressure:

$$V^{id} = \sum x_i V_i \tag{6.29}$$

Mass transfer between phases occurs due to the chemical potential, μ, of the species contained therein, and this is related to an energy required to facilitate the transfer, the Gibbs free energy of the species. The chemical potential is therefore related to the Gibbs free energy and the temperature of the system for both ideal gases and solutions as:

$$\mu_i^{ig} = G_i^{ig} + RT \ln y_i \quad \text{(a)}$$

$$\mu_i^{id} = G_i + RT \ln x_i \quad \text{(b)} \tag{6.30}$$

If ideal gas and ideal solution models are assumed for the transfer of oxygen into a bioreactor media, the vapour/liquid equilibrium criterion produces two simple and useful equations. When the mass fraction of species *i* is high, the following relationship often referred to as Raoults Law holds:

$$y_i P = x_i P_i^{sat} \tag{6.31}$$

The left hand side of equation (6.31) is the partial pressure of species ι in the vapour phase that is equal to the product of the liquid phase mole fraction at its vapour pressure at temperature T. For free surface aeration at atmospheric pressure, only the vapour pressure at the operating temperature of the liquid phase is required to establish the equilibrium condition assuming ideal behaviour. In most cases however, the mass fraction x_i is small, and a proportionality factor called Henry's constant, H, is used instead of the vapour pressure of the species:

$$P = Hx_i \tag{6.32}$$

6.4.2 Non-ideal behaviour

It is beyond the scope of this work to make rigorous thermodynamic measurements on the vapour/liquid equilibrium (VLE) state at the gas/liquid interface for oxygen transfer studies. It is deemed sufficient to use Raoults Law to quantify the transfer across the phase boundary at the surface, since the influence of the fluid motion at the surface for redistribution of oxygen into the bulk fluid is considered more important than the thermodynamics of the transport process. It should be noted though that in any *real* system, the thermodynamic state will deviate from the *ideal* behaviour which Raoults Law describes. Raoults Law is often sufficient to describe VLE for simple systems such as oxygen absorption into water and deviates as the molecular complexity of either or both phases increases. It is clear that in these studies, the liquid phase comprising media and cells is a complex one, but this will be overlooked for simplicity. Deviations from ideal behaviour are

normally expressed through the introduction of two auxiliary thermodynamic properties related to the Gibbs energy, fugacity coefficient and activity coefficient. The definitions of these coefficients extend from the concept of fugacity, which provides an alternative to the chemical potential as a criterion for phase equilibrium.

6.5 Measurement of mass transfer coefficients

In general, equation (6.23) or other mass transfer equations of this form are often expressed as:

$$J_A = k_\ell (c_{Ai} - c_{Ao}) \qquad (6.33)$$

where k_l is the mass transfer coefficient. The calculation of this coefficient is dependent on the choice of theory applied to the transfer process. In the two-film theory, k_l is directly proportional to the film thickness. From the penetration theory it is proportional to the square root of the diffusivity for surface elements all exposed for an equal time and inversely proportional to the square root of the exposure time. Assuming random surface renewal, it is proportional to the square root of the rate of renewal and for the film penetration theory the mass transfer coefficient is complex function of diffusivity, film thickness and either exposure time or surface renewal rate. Whilst a number of factors in these calculations cannot be accurately determined, in most of the analogies it is observed that

$$k_\ell \propto D^{1/2} \qquad (6.34)$$

In situations where circulating eddies prevail at the surface, the mass transfer is enhanced due to more rapid surface renewal. Danckwerts (1970) has suggested that the surface renewal time, t_e can be estimated from the circulating eddy velocity, u_{ed} and the depth (or diameter) of the eddy, d_{ed} as

$$t_e \approx \frac{d_{ed}}{u_{ed}} \tag{6.35}$$

O'Connor and Dobbins (1966) made measurements on the re-aeration of oxygen deficient lakes and streams and concluded that the renewal time is better approximated using d_{ed}^3 instead of d_{ed}. A correlation described by Broecker (1974) uses the Higbie penetration theory and a root mean square eddy velocity to predict

$$k_\ell = 1.46\left(\frac{Du_{rms}}{d_{ed}}\right)^{1/2} \tag{6.36}$$

Whilst the mass transfer coefficient can be theoretically predicted for a simplified system using the theories above, to determine the mass transport coefficient of oxygen in a bioreactor system where a complex flow prevails, it is firstly necessary to have an accurate method to measure the oxygen concentration at a well defined location in the bioreactor, and to have a sufficient transient response of the oxygen measuring probe.

6.5.1 Traditional measuring methods for oxygen transfer rate

The preceding discussion has addressed only the transfer of oxygen across the gas-liquid phase interface when oxygen is introduced to the bioreactor via the free surface of the liquid. Transport throughout the liquid to the metabolic site at the cells is then governed by the mixing and hydrodynamics in the vessel, and generalised correlations to predict the transport can be established based on forced convection transport which is discussed in section 6.6. To verify such correlations, direct measurements of the changes in the oxygen concentration in the bioreactor are required and techniques to achieve this are described here.

A review on the more common methods to measure oxygen concentration in model dynamic systems has been made by Van't Riet (1979). These are broadly summarised as:

- Dynamic gassing-out method
- Oxygen transfer rate (OTR) measurement
- Sulfite method
- CO_2 absorption
- Contact area measurements
- Dynamic pressure method

In all cases, it must be emphasised that some of the important characteristics that dictate the oxygen transfer process in the *real* bioreactor may not be represented in a model system and these include the fluid rheology, gas-liquid resistances and oxygen diffusivities and solubilities. Not withstanding this, the oxygen absorption rate is needed. This is often expressed on a per unit reactor volume basis and can be related to the mass flux of equation (6.33):

$$Q_{O_2} = k_\ell (c_{Ai} - c_{Ao}) \frac{A}{V} = k_\ell a' (c_{Ai} - c_{Ao}) \qquad (6.37)$$

As a consequence, lumped measurements of $k_\ell a'$ are evaluated where a' is the gas-liquid interfacial area per unit volume of reactor. Q_{O2} is then the local volumetric oxygen uptake of oxygen at some point in the reactor, with the overall uptake in the reactor liquid volume being:

$$\overline{Q_{O_2}} = \frac{1}{V} \int_0^V Q_{O_2} dV \qquad (6.38)$$

The overall value from (6.38) would equal the local value only if the hydrodynamic conditions, interfacial area/volume and oxygen concentrations are uniform throughout the vessel.

The dynamic gassing-out method involves deoxygenating the liquid media by passing nitrogen through it, and then allowing oxygen to pass into the liquid by the chosen oxygen delivery method and measuring the oxygen

concentration profile over an appropriate time period. On the assumption that oxygen is sparingly soluble in the media, the phase equilibria is taken as a linear partition law relationship such as Henry's law, with the Henry partition coefficient, H and is often also incorporated into equation (6.37) to provide a generalised equation that incorporates phase interface transfer:

$$Q_{O_2} = k_\ell a' \left(\frac{c_{Ai}}{H} - c_{Ao} \right) \tag{6.39}$$

A mass balance on oxygen between two measurement periods t_1 and t_2 can be used in the evaluation of $k_\ell a'$:

$$\frac{dc_{Ao}(t)}{dt} = k_\ell a' \left(\frac{c_{Ai}}{H} - c_{Ao}(t) \right)$$

$$k_\ell a' = \frac{\ln \left[\dfrac{c_{Ai}/H - c_{Ao}(t_2)}{c_{Ai}/H - c_{Ao}(t_1)} \right]}{t_2 - t_1} \tag{6.40}$$

There are restrictions on the applicability of this technique, and these are largely due to limitations of the measurement probe which is typically a polargraphic electrode but this is discussed in section 6.5.2. In accounting for the limitations of an oxygen measuring electrode, the following expression can be used to provide a guideline value for $k_\ell a'$:

$$k_\ell a = \frac{1}{t_{0.63}} \tag{6.41}$$

where $t_{0.63}$ is the time required to reach 63% of air saturation in the liquid media starting from 0% (Zhang, 1992).

The OTR measurement technique strictly requires measurement of oxygen concentration in the gas phase whilst simultaneously making measurements in the reactor liquid phase. It is then possible to directly

measure the value of k_la' directly by rearrangement of equation (6.39). This technique has effectively been employed in the current study, however the oxygen concentration in air above the liquid free surface of the reactor has been assumed to be constant.

The sulfite method is based on the chemical oxidation reaction of Na_2SO_3 with oxygen. Copper or cobalt ions can be used as a supporting catalyst. A concentration range exists where the reaction rate is very rapid and the effective oxygen concentration in the liquid is zero. This provides easy evaluation of k_la' however in practice problems are encountered through an inexact knowledge of the kinetics and influences from the particle size of the supporting catalyst and reacting substrate.

CO_2 absorption operates on the similar principles as the sulfite method, and when combined with the gassing-out method has been proported to be more accurate than the sulfite method (Robinson and Wilke, 1973) but the experimental approach has been questioned (Prasher, 1975). In general the same problems of kinetics and substrate size with particular regard to a' become important.

The inherent problems presented by an inaccurate knowledge of a' using a model system have led experimentalists to more accurately control the value of a' by using substrate and catalyst particles whose surface areas are better well-defined and quantified using photography and microscopy techniques. Once a' is defined better, control over the chemical reaction type methods is possible. A review on further methods in the evaluation of a' and k_la' has been provided by Joshi (1982) for measurements in impeller stirred tanks.

Linek (1987) has described the dynamic pressure method, where a small change in the total system pressure is introduced, generating a concentration change in the dispersed gas. The oxygen concentration is changed simulataneously in all bubbles dispersed in the liquid phase irrespective of gas phase mixing. Upward pressure changes should be used

for measurement as downward pressure changes are often accompanied by bubble nucleation and increased k_la values. The method is typically used in impeller driven bioreactors where continuous delivery of oxygen is provided by a feed stream. Pressurisation is achieved by throttling the gas stream.

Whilst model systems provide some guideline criteria for k_la', real bioreactor values often differ, and this is apparent even when taking into account the physico-chemical differences between a working bioreactor and a model system (Gauthier, 1991). A comparison of the various chemical methods for k_la measurements has been provided by Gogate (1999) using correlations from the literature and the dynamic pressure method as the basis for comparison. The difference in the measured values between the techniques is very large in some cases and it is suggested that these methods are not well suited to practical mass transfer measurements in bioreactors.

6.5.2 Oxygen measuring electrodes

The principal types of dissolved oxygen electrodes are galvanic (potentiometric) or polarographic (amperometric or Clark) types. Polarographic electrodes, used for the biomedical measurement of oxygen concentrations, have been developed since the 1950's (Clark, 1953) and the major biomedical use is for measuring oxygen concentrations in whole blood. Numerous improvements and designs have been made on the basic Clark-type electrode (Schuler, 1967; Hahn, 1974; Westenskow, 1977; Albery, 1978), but a significant drawback of these types of electrodes for work with cell culture populations is their bulky size and slow response time. More recently efforts have been successful in producing smaller microelectrodes for measurements in tissue (O'Hare, 1991) and to study mass transport effects in biofilms in the bioremediation industry (Larsen, 1994; De Beer, 1996; Rasmussen, 1998). These microelectrodes can be produced with sensing tips of only micron scale diameters, however the principle of oxygen concentration measurement is still always susceptible to a lag time which may be significant if the oxygen transfer and utilisation rates are high. In

aerobic bioreactor systems, the solubility of oxygen is low due to ionic salts and nutrients present in the media. The general design comprises an oxygen permeable membrane that separates the probe internals from the medium fluid. Reduction of oxygen occurs at a platinum cathode surface:

$$\tfrac{1}{2}O_2 + H_2O + 2e^- \xrightarrow{Pt} 2OH^-$$

$$2KCl + 2OH^- \rightarrow 2KOH + 2Cl^-$$

A constant voltage is applied across the cathode and the silver anode in a polarographic electrode so at the anode:

$$Ag + Cl^- \xrightarrow{Ag} AgCl + e^-$$

The current that is generated, and which depends only on the oxygen flux to the cathode, is measured. Transport of oxygen across the permeable membrane followed by reaction at the electrode contributes to typical characteristic response times of 10 to 100s and that may be significant. In addition, accumulation of ions generated in the redox reactions, or fouling of the membrane may increase the response time further, or introduce drift errors on the measurements taken. The vulnerability and reliabilty of electrode based oxygen probes in pipe flow conditions has been demonstrated by Berger (1977) and in biofilm applications by Rasmussen (1998).

6.5.3 Oxygen measurement by optical sensing

Alternatives to electrode based oxygen probes have been continually sought to overcome initially the problem of probe dimensions, but more recently slow response time. One approach has been to analyse oxygen binding to myoglobin (Honig, 1984) in real time, and although successful, myoglobin is only present in muscle tissue. Subczynski (1984) monitored changes in the electron spin resonance of spin-labelled cells. Again, whilst

successful, this is an expensive and demanding procedure to perform, for repeated experiments. Of the most promising techniques are the optical techniques of chemiluminescence and fluorescent/phosphorescent quenching (Vanderooki, 1987; Klimant, 1995). Chemiluminescence is less advantageous than the dynamic quenching techniques since the luminescence is limited due to the low sensitivity to oxygen. Furthermore, intensity rather than lifetime is usually measured (Sasso, 1986) and changes in turbidity or absorption interfere with the measurement.

The principle of dynamic luminescence quenching by molecular oxygen is shown schematically in Figure 6.4. The luminophore particles are normally water soluble derivatives of porphyrins, typically containing Pt(II) or Pd(II) as the central atom. Other alternatives for the oxygen probes are water based derivatives of fluorescein (Vanderooki, 1987), polycyclic aromatic hydrocarbons, or transition metal complexes of Ru(II), Os(II) and Rh(II) (Sasso, 1986; Klimant, 1995). The collision of oxygen with a luminophore particle in its excited state results in radiationless deactivation and is referred to as dynamic quenching. After collision, energy transfer takes place from the excited indicator molecule to oxygen that is transferred from its ground (triplet) state to its excited (singlet) state. As a consequence of this, the indicator molecule does not emit luminescence and the measurable luminescence signal decreases. The dynamic quenching by oxygen is diffusion limited and can be described by the Stern-Volmer relationship, modified for phosphorescence lifetime and is also related to the oxygen concentration in the sample and the luminescence intensity:

$$\frac{I_o}{I} = \frac{\tau_o}{\tau} = 1 + \tau_o k_q [O_2] \qquad (6.42)$$

τ_o is the luminescence lifetime in the absence of oxygen, τ is the luminescence lifetime in the presence of oxygen, I and I_o are similarly the luminescence intensities and $[O_2]$ is the oxygen concentration. The term $\tau_o k_q$ is the Stern-Volmer constant representing the quenching efficiency and therefore the sensitivity of the sensor. The quenching rate constant is k_q and

for a diffusion-limited reaction can be described by the Smoluchowski equation:

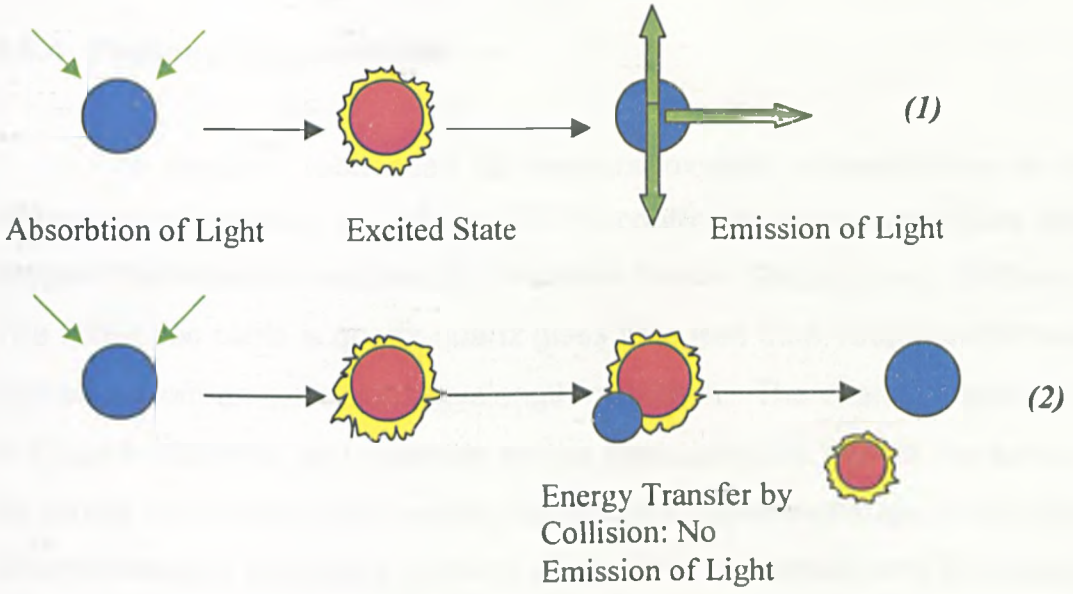

Figure 6.4 Principle of Dynamic Quenching of Luminescence by Molecular Oxygen: (1) Luminescence process in the absence of Oxygen; (2) Deactivation of the luminescent indicator molecule by molecular Oxygen

$$k_q = 4\pi Np(D_D + D_A) \times 10^3 \qquad (6.43)$$

D_D and D_A are the diffusion coefficients of the donor (probe) and acceptor (oxygen) respectively, N is Avogadro's constant and *p* is a factor related to the probability of each collision causing quenching and to the radius of interaction between the probe and oxygen. Gijzemann (1973) suggests a value of p=1/9.

The advantages of optical oxygen sensors can be summarised as:

- No oxygen is consumed during the measurement
- The signal is independent of changes in flow velocity
- Unaffected by electrical/magnetic fields
- Near instantaneous response time

6.5.4 PreSens Oxygen Probe

The oxygen probe used to measure oxygen concentrations in the bioreactor in this study is a Microx TX PC-controlled one channel fibre optic oxygen micro-optode supplied by PreSens GmbH (Regensburg, Germany). The fibre-optic cable is quartz-quartz glass fibre less than 150μm in diameter operating from an excitation wavelength of 505nm. The chemical sensor tip is 40μm in diameter and operates on the basic principle that as the sensing tip comes into contact with oxygen, its optical properties change, in this case its luminescence properties, in terms of the lifetime, intensity and polarisation of the luminescence. Light acts as the carrier of the information. The major components of the system are:

- A light source to illuminate the sensor tip comprising a laser, light emitting diodes and a lamp
- An optical fibre as a signal transducer
- A photodetector comprising a photodiode, photomultiplier tube and CCD-array
- An optical sensing tip comprising a chemical indicator immobilised in a solid matrix

6.5.4.1 Probe luminescence decay time

The luminescence decay time is an intrinsically referenced parameter, and its measurement has the following advantages over conventional intensity measurements:

- The decay time is independent of the sensitivity of the detector and fluctuations in the intensity of the light source
- The decay time is independent of signal losses due to fibre bending or geometry distortions in the sensing tip
- The decay time is independent of the chemical indicator concentration in the sensing tip, so photobleaching and leaching of the indicator dye has no influence on the measuring signal

The measurement of the luminescence decay time of the immobilised indicator is the oxygen dependent parameter, so

$$\tau = f([O_2]) \tag{6.44}$$

Phase modulation is used to determine the decay time. The sensor is stimulated with a sinusoidally varying intensity of modulated light and the decay time causes a time delay in the emitted light signal that is transmitted down the fibre-optic cable. This delay is the phase angle difference between the exciting signal and the emitted signal and the phase angle is shifted as a function of the oxygen concentration. The decay time and phase angle are related as

$$\tau = \frac{\tan \Phi}{2\pi f_{mod}} \quad \text{(a)}$$

$$\tau \equiv \tan \Phi \equiv \Phi \equiv f([O_2]) \quad \text{(b)} \tag{6.45}$$

6.5.4.2 Determination of Oxygen Concentration

This is based on the Stern-Volmer relationship of equation (6.42),

$$\frac{\tan \Phi_o}{\tan \Phi} = \frac{\tau_o}{\tau} = 1 + K_{sv}[O_2] \tag{6.46}$$

where K_{sv} is the Stern-Volmer constant, Φ_o is the phase angle of oxygen free water, Φ is the measured phase angle and $[O_2]$ is the oxygen concentration. This relationship has been shown to be non-linear for the Microx TX optode and this is common for a number of other sensors of this type (Klimant, 1999). The non-linear phase behaviour for the optode is described by

$$\frac{\tan\Phi_o}{\tan\Phi} = \left(\frac{0.804}{1+K_{sv}[O_2]} + \frac{0.196}{1+\frac{1}{22.9}K_{sv}[O_2]} \right)^{-1} \qquad (6.47)$$

6.5.4.3 Temperature dependence on oxygen measurements

The oxygen content can be measured in a number of different units using the PreSens probe, and these include %-air saturation (which is used in this study), partial pressure of oxygen in milli-bar or in Torr, or concentration expressed as mg/L, ppm or μmol/L. In all cases, the value obtained in the chosen unit is dependent on temperature. Water vapour pressure is strongly affected by temperature variations and this influences the partial pressure of oxygen in air saturated water and water vapour saturated air. The oxygen partial pressure in such circumstances varies as

$$p(O_2) = 0.2095(p_{atm} - p_w(T)) \qquad (6.48)$$

Variation of water vapour pressure with temperature, $p_w(T)$ is given in Table 6.3

θ[°C]	0	5	10	15	20	25	30	35	40	45
T[K]	273	278	283	288	293	298	303	308	313	323
$P_w(T)$ [mbar]	6.1	8.7	12.3	17.1	23.3	31.7	42.4	56.3	73.7	123.3

Table 6.3: Variation of water vapour pressure $P_w(T)$ with temperature

and is described by the non-linear equation

$$p_w(T) = \exp\left(52.57 - \frac{6690.9}{T} - 4.681 \ln T\right) \quad (6.49)$$

The solubility of oxygen in water is temperature dependent and decreases as the temperature rises. It is determined from the oxygen partial pressure $p(O_2)$ and the Bunsen absorption coefficient $\alpha(\theta)$,

$$c_s(p,\theta) = \frac{p(O_2)}{p_{atm}} \alpha(\theta) \quad (6.50)$$

where $c_s(p,O_2)$ is the temperature dependent solubility of oxygen in water. The variation of the Bunsen absorption coefficient with temperature is given in Table 4.4:

θ[°C]	0	5	10	15	20	25	30	35	40	50
$\alpha[T].10^3$	49.01	42.94	38.11	34.17	31.01	28.43	26.30	24.63	23.16	20.85

Table 6.4: Variation of Bunsen absorption coefficient α(T) with temperature

This data is described by:

$$\ln(1000\alpha) = \frac{8553}{T} + 23.78 \ln T - 160.8 \quad (6.51)$$

With a knowledge of the Bunsen absorption coefficient and the water vapour pressure at a given temperature, the solubility of oxygen in air saturated water can be calculated from

$$c_s(p_{atm},\theta) = 0.0295\alpha(\theta)\left[\frac{p_{atm} - p_w(\theta)}{p_N}\right]\frac{M_{O_2}}{V_M} \quad (6.52)$$

One further factor that influences the oxygen solubility is the salt concentration of the liquid phase. There is a decreased oxygen solubility with increased salt concentration and is generally known as the *salting-out effect*. It is noted that this effect has not been accounted for in experimental measurements made in this study.

6.6 Dimensional analysis for mass transfer

Mass transfer, enhanced by fluid motion is known as forced convection mass transfer. The fluid motion is induced by mechanical means; a pump, impeller, or some other solid moving part. In free convection, the fluid motion is induced by the density differences resulting from the mass transport process itself.

6.6.1 Dimensional analysis for forced convection mass transfer

The use of dimensionless ratios in the analysis of experimental data has been a longstanding feature of fluid mechanics and fluid mechanical related phenomena. The practice is closely linked with the principle of similitude proposed by Lord Rayleigh. In any equation which expresses a fundamental relationship between a number of different physical quantities, each term in the equation must have the same dimensions. This is the principle of dimensional homogeneity. All physical quantities can be expressed in terms of a limited number of fundamental dimensions. For the interrelated problem of fluid mechanics and mass transport, only three fundamental variables are required in order to describe all the physical qualities associated with the problem and these are mass, length and time. For the associated problem of heat transfer, thermodynamic temperature is a fourth required variable, and in mass transport studies where molar quantities are addressed rather than mass concentrations, the amount of substance, or mole, is required as a fundamental variable. The present study is restricted to mass concentrations so the first three fundamental variables suffice. SI

units are used throughout in the analyses. Dimensional analysis is then based on Buckinghams Pi theorem (Kay, 1985).

Initially in the dimensional analysis, consideration is made for mass transport in a circular pipe. The local molar flux is N, the pipe diameter is d, the mean velocity of flowing fluid is u_m and the fluid has density ρ and viscosity μ, the diffusivity is D and the concentration difference is ΔC. Therefore,

$$N = f(\Delta C, D, u_m, \rho, \mu, d) \qquad (6.53)$$

There are seven quantities and four fundamental variables, mass [m], length [l], time [t] and for now, assume moles [n]. From Buckingham Pi Theorem, if there are j quantities and k fundamental variables then the number of independent dimensionless groups, Π, that can be formed is:

$$\Pi = j - k \qquad (6.54)$$

For forced convection mass transport there are 3 independent dimensionless groups. Only two of the parameters, N and ΔC, contain the dimension [n] having dimensions $[nl^{-2}t^{-1}]$ and $[nl^{-3}]$ respectively and can therefore only appear as the ratio $N/\Delta C$ which is the mass transfer coefficient k_l. An alternative to equation (6.53) is

$$k_l = f(u_m, \rho, \mu, d, D) \qquad (6.55)$$

In this case j = 6 and k = 3 which again reduces to Π = 3. The three dimensionless groups are the Reynolds number (Re), the Sherwood number (Sh) and the Schmidt number (Sc) and these are defined, for this system, as

$$Re = \frac{\rho u_m d}{\mu} \quad (a)$$

$$Sh = \frac{k_l d}{D} \quad (b) \qquad (6.56)$$

$$Sc = \frac{\mu}{\rho D} \quad (c)$$

The dimensionless Reynolds number has been introduced in Chapter 2 for the fluid mechanical analysis of concentric cylinder flow. The definition is different in that case, but this is only to accommodate geometric differences between a concentric cylinder system and the example case of pipe flow described above. In general, the Reynolds number is the ratio of the inertial to viscous forces in any system so any appropriate definition can be used. The Sherwood number can be modified accordingly for the concentric cylinder system since only the geometric quantity is different. The Schmidt number will remain unchanged as no geometric related quantities are expressed. Other dimensionless numbers can be derived from these three numbers and are often used in reviews of forced convection mass transport. Two of these are the modified Stanton number,

$$St' = \frac{Sh}{Re\,Sc} = \frac{k_l}{u_m} \qquad (6.57)$$

and the modified Peclet number,

$$Pe' = Re\,Sc = u_m \frac{d}{D} \qquad (6.58)$$

The physical significance of the dimensionless numbers is important. As stated already, the Reynolds number is the ratio of inertial to viscous forces. The Sherwood number is interpreted as the ratio of the actual mass transfer coefficient to the purely diffusive value. The modified Stanton number is an alternative mass transfer coefficient and gives a measure of the ratio of the

flux of mass along the streamlines to that of convection along the streamlines. The Schmidt number is simply the ratio of the kinematic viscosity to the molecular diffusivity and therefore gives a measure of the relative efficiency of the fluid as a conductor of momentum and solute. When these numbers are equal to 1.0, the velocity and concentration profiles are geometrically similar and the degree of similarity decreases as departure is made from 1.0. Mass transport coefficients are often correlated by equations employing these dimensionless numbers. Correlation by this method better serves to scale-up (or down) the mass transport process. Some of the functional forms of the correlations are,

$$Sh = f(Re, Sc) \quad (a)$$

$$St' = f(Re, Sc) \quad (b) \qquad (6.59)$$

$$Sh = f(Pe', Re) \quad (c)$$

The correlations are often expressed in the generalised form (using equation 6.59a as an example):

$$Sh = \alpha \, Re^{\beta} \, Sc^{\gamma} \qquad (6.60)$$

where α, β and γ are constants which are determined from experimental measurements.

6.6.2 Dimensional analysis for free convection

In free convection the motion of the fluid is induced by density differences resulting from the mass transfer process itself and these have no effect except in a gravitational field. In systems with a gravitational field, free and forced convection are expected to occur simultaneously and in the dimensional analysis the gravity, g, becomes a fundamental variable. Dimensional analysis leads to the generation of an additional dimensionless group called the Grashof number, Gr:

$$Gr = \frac{\rho \Delta \rho g d^3}{\mu^2} \tag{6.61}$$

Correlations for free convection normally take the general form,

$$Sh = \alpha Gr^{\beta} Sc^{\gamma} \tag{6.62}$$

where α, β, γ are again constants. In gravitational systems where free surface transport is also occurring, one further dimensionless group, the Froude number, Fr, may be considered and is the ratio of the free surface dynamics effects to the mechanical mixing effects in the transport process:

$$Fr = \frac{u_m^{\ 2}}{gd} \tag{6.63}$$

References

Albery WJ, Brooks WN, Gibson SP, Hahn CEW, An Electrode for P_{NO2} and P_{O2} Analysis in Blood and Gas. *J. Appl. Physiol.* **45** 637-643 (1978)

Bailey JE, Ollis DF, Biochemical Engineering Fundamantals. 2nd Edition. McGraw-Hill Inc. New York. (1986)

Berger FP, Hau KFFL, Mass Transfer in Turbulent Pipe Flow Measured by the Electrochemical Method. *J. Heat Mass Transfer* **20** 1185-1194 (1977)

Broecker WS, Peng TH, Gas Exchange Rate Between Air and Sea. *Tellus* **26** 21-35 (1974)

Clark LC, Wolf R, Granger D, Taylor Z, Continuous Recording of Blood Oxygen Tensions by Polarography. *J. Appl. Physiol.* **6** 189-193 (1953)

Danckwerts PV, Gas Liquid Reactions. McGraw Hill Inc. New York. (1970)

Danckwerts PV, Significance of Liquid Film Coefficients in Gas Absorbtion. *Ind. Eng. Chem.* 1460-1468 (1951)

DeBeer D, Stoodley P, Lewandowski Z, liquid Flow and Mass Transport in Heterogeneous Biofilms. *Wat. Res.* **30** (11) 2761-2765 (1996)

Fick A, Ueber Diffusion. *Ann. Phys.* **94** 59 (1855)

Gauthier L, Thibault J, LeDuy A, Measuring $k_l a'$ with Randomly Pulsed Dynamic Method. *Biotech. Bioeng.* **37** 889-893 (1991)

Gijzeman OLJ, Kaufman F, Poter G, Statistical Approach to the Quenching Efficiency of Phosphorescence. *J. Chem. Soc. Faraday Trans.* **2** 708-720 (1973)

Gogate PR, Pandit AB, Survey of Measurement Techniques for Gas-Liquid Mass Transfer Coefficient in Bioreactors. *Biochem. Eng. J.* **4** 7-15 (1999)

Hahn CEW, An Ag-Pb Galavanic Cell P_{O2} Electrode for Blood gas Analysis. *J. Appl. Physiol.* **36** 439-442 (1974)

Higbie R, The Rate of Absorbtion of Pure Gas Into a Still Liquid During Short Periods of Exposure. *Trans. Am. Inst. Chem. Eng.* **31** 365-373 (1935)

Honig CR, Gayesk TEJ, Federspiedl W, Clark A, Clark P, Muscle O2 Gradients from Hemoglobin to Cytochrome: New Concepts New Complexities. *Adv. Exp. Med. Biol.* **169** 23-38 (1984)

Joshi JB, Pandit AB, Sharma MM, Mechanically Agitated Gas-Liquid Reactors. Review Article #7. *Chem. Eng. Sci.* **37** (6) 813-844 (1982)

Kay JM, Nedderman RN, Fluid Mechanics and Transfer Processes. Cambridge University Press. (1985)

Klimant I, Wolfbeis OS, Oxygen Sensitive Luminescent Materials Based on Silicone Soluble Ruthenium Diimine Complexes. *Ann. Chem.* **67** 3160-3166 (1995)

Klimant I, Ruckruh F, Liebsch G,Stangelmayer A, Wolfbeis OS, Fast Response Micro-Optodes Based on Novel Soluble Ormosil Glasses. *Mikrochim. Acta.* **131** 35-46 (1999)

Larsen TA, Harremoes P, Combined Reactor and Microelectrode Measurements in Laboratory Grown Microfilms. *Wat. Res.* **28** (6) 1435-1441 (1994)

Linek V, Vacek V, Benes PA, A Critical Review and Experimental Verification of Correct Use of Dynamic Method for the Determination of Oxygen Transfer in Aerated Agitated Vessels to Water, Electrolyte Solutions and Viscous Liquids. *Chem. Eng. J.* **34** 11-34 (1987)

O'Connor DJ, Dobbins W, The Mechanism of Reaeration in Natural Streams. *J. Sanit. Eng. Div., Proc. ASCE,* **82** SA6 (1966)

O'Hare D, Winlove CP, Parker KH, Electrochemical Method for Direct Measurement of Oxygen Concentration and Diffusivity in the Intervertebral Disc: Electrochemical Characterization and Tissue Sensor Interactions. *J. Biomed. Eng.* **13** 304-312 (1991)

Perry RH, Green D, Perry's Chemical Engineers Handbook. 6th Edition. McGraw-Hill Inc. New York. (1990)

Prasher BD, Observations on the Absorbtion of Carbon Dioxide by a Stirred Liquid. *AIChE J.* **21** 407-411 (1975)

Rasmussen K, Lewandowski Z, The Accuracy of Oxygen Flux Measurements Using Microelectrodes. *Wat. Res.* **32** (12) 3747-3755 (1998)

Robinson CW, Wilke CR, Carbon-Dioxide Absorbtion in Thin Liquid Films. *Biotech. Bioeng.* **15** 755-761 (1973)

Sasso MG, Quina FH, Bechara EGH, Ruthenium(II) Tris(Bipyridyl) Ion as a Luminescent Probe for Oxygen Uptake. *Anal. Biochem.* **156** 239-243 (1986)

Schuler R, Kreuzer F, Rapid Polarographic In Vivo Oxygen Catheter Electrodes. *Respiration Physiol.* **3** 90-110 (1967)

Subczynski WK, Hyde JS, Diffusion of Oxygen in Water and Hydrocarbons Using an Electrospin Resonance Spin Label Technique. *Biophys. J.* **45** 743-748 (1984)

Toor HL, Marchello JM, Film Penetration Model for Mass and Heat Transfer. *AIChE J.* **4** 97-103 (1958)

Vanderkooi JM, Maniara G, Green TJ, Wilson DF, An Optical Method for Measurement of Dioxygen Concentration Based Upon Quenching of Phosphorescence. *J. Biol. Chem.* **262** (12) 5476-5482 (1987)

Van't Riet K, Review of Measuring Methods and Results in Non-Viscous Gas-Liquid Mass Transfer in Stirred Vessels. *Ind. Eng. Chem. Proc. Des. Dev.* **18** (3) 357-363 (1979)

Weisz P, Diffusion and Chemical Transformation: An Interdisciplinary Excursion. *Science* **179** 433 (1973)

Westenskow DR, Johnson CC, Jordan WS, Gehmlich DK, Instrumentation for Measuring Continuous Oxygen Consumption of Surgical Patients. *IEEE Trans. Biomed. Eng.* **24** 331-337 (1977)

Whitman WG, The Two-Film Theory of Absorbtion. *Chem. and Met. Eng.* **29** 147-154 (1923)

Zhang S, Hand-Corrigan A, Spier RE, A Comparison of Oxygenation Methods for High Density Perfusion Cultures of Animal Cells. *Biotech. Bioeng.* **41** 685-692 (1993)

Chapter 7

Mass Transport in Concentric Cylinder Flows

7.1 Transport Mechanism in Taylor-Vortex Flows

A concentric cylinder apparatus in which the inner cylinder rotates produces a diverse number of stable steady flow states and these have been described in Chapter 2. With the rotational speed of the inner cylinder slowly increasing, the distinguishable flow states observed are progressively, laminar Couette flow (LCF), laminar Taylor-vortex flow (LTVF), wavy vortex flow (WVF), modulated wavy vortex flow (MWVF) and turbulent vortex flow (TVF). Coles (1965) has suggested that these flow states are evident only if the radius ratio of the cylinders $\eta > 0.714$. For $\eta < 0.714$ the transition from LTVF to TVF is immediate with none of the other intervening states being clearly observed from flow visualisation studies. Taylor vortex reactors have been employed for a number of varied chemical and biochemical applications where they can be operated as batch, closed systems, but are typically operated in a continuous mode. In this mode, continuous operation might be achieved by feeding into one end of the vessel and removing at the other end thereby generating an axial flow superimposed on the Taylor vortex flow.

Reactors of this type are referred to as Taylor-Poiseuille flow reactors. These have been studied extensively (Inamura et al. 1993; Kataoka et al. 1975, 1977, 1995; Ogihara et al. 1995). Alternatively, the reactants can be fed into the top and bottom of the vessel at equal rates so that there is no axially imposed flow. Reactors operating in this way have been studied by Campero and Vigil (1997), Tam and Swinney (1987), and Vastano and Swinney (1990). This type of Taylor-vortex reactor approximates to a one-dimensional reaction-diffusion device.

Mass transport in concentric cylinder systems occurs by inter-vortex exchange and intra-vortex mixing. In laminar Couette flows the fluid experiences a solid body rotation and no transport is assumed to occur in the radial or axial directions since motion is confined to the azimuthal direction only. In the case of LTVF, the unitary vortex cell consists of two counter-rotating vortices. This unitary cell comprises two inflow boundaries that direct fluid radially into the rotating wall. These are located at the centre of the cell and both move together in parallel. At either end of the vortex cell an outflow boundary exists. This directs fluid away from the rotating inner wall and out towards the stationary outer wall. Ohmura (1997) has shown that the inflow boundaries act as a barrier to inter-vortex mixing and that the outflow boundaries promote inter-vortex mixing. The average vortex height was found to be important and was non-dimensionalised as h_v/d. When $h_v/d = 1$, the vortex motion is stable with no waves on either inflow or outflow boundaries. When $h_v/d < 1$ small amplitude wave motion is evident at both inflow and outflow boundaries and for $h_v/d > 1$, the wave motion is evident only at the inflow boundaries. The acceleration to the equilibrium speed for the rotating inner cylinder is very influential in the value of h_v/d. Intra-vortex mixing consists of a tangential (circumferential) dispersion accompanied by axial and radial mixing. In LTVF the tangential dispersion is weak (Kataoka (1981), Legrand and Coueret (1986)) and numerical models of Howes and Rudman (1990) indicate weak radial and axial mixing in the vortex core for LTVF. In contrast, layers of fluid near to vortex boundaries are readily mixed. Inflowing boundaries produce excellent micromixing in a thin layer as the inflowing boundaries from each counter rotating part of the vortex come into contact (Liu (1999)). Effective mixing is also achieved at the outflowing

boundaries, but at these boundaries, unitary vortex cells meet, and the mixing here is essentially an exchange of material from one unitary vortex cell to the next. It is at these out flow boundaries that inter-vortex exchange takes place. Carefully controlled dye tracer experiments performed by Desmet et al (1996) have shown that dye injected into the centre of a vortex is slowly transported to the outflowing boundaries but concentrated at the inflowing boundaries. Injection near to the outflowing boundaries shows very efficient transfer from one vortex to the next.

As the speed of the inner cylinder is increased, WVF is initiated for $\eta > 0.714$, and the wavy motion forces fluid from the vortex boundaries, directing it into the core. The waviness produces regions of upward and downward vortex deformation corresponding to regions of upward and downward axial flow. Axial (and intra-vortex) mixing is therefore increased. Of course, superimposed on this is the azimuthal (circumferential) motion. Radial mixing is therefore also promoted. Broomhead and Ryrie (1988) showed that with even very small deviations from LTVF to WVF, fluid trajectories became chaotic even in the absence of molecular diffusivity resulting in an enhanced effective diffusivity or axial dispersion. From numerical simulations of the flow field (which agree with experimental observations), Rudolph (1998) have shown that up to 50% of the volume of a vortex can be transported into and out of a vortex in one azimuthal wave period. They verify the findings of Broomhead in terms of chaotic particle paths and suggest that axial scalar transport is substantially increased over molecular diffusion. They propose from their numerical model that optimum fluid transport between vortices takes place at Ta = 253 and that mixing and transfer decrease at both higher and lower Ta than this for WVF. Whilst the axial dispersion coefficient can be up to three times higher in TVF, this will be intrinsic to the turbulence rather than to axial transport between vortices.

7.2 Ideal Behaviour of the Vortex Cell

The vortex cell (vortex pair) in laminar Taylor-vortex flow behaves as an ideal batch reactor described in Chapter 1. Evidence of this behaviour has been demonstrated by Kataoka (1975) using a salt tracer technique. In

this study, $6.5x10^{-3}$M aqueous sodium chloride solution was added as tracer to a working viscous fluid of 40wt.% glycerine and conductivity measurements were made. A small amount of green dye that did not influence these measurements allowed for visualisation of the transport. A more refined series of experiments to investigate inter-vortex mixing in WVF and TVF using a similar technique was performed by Ohmura et al. (1997). They concluded that inter-vortex mixing is dependent on the vortex height, h_v, and the wave motion in WVF and turbulence character in TVF and that intra-vortex mixing increases monotomically with increasing Reynolds number. Inamura et al. (1993) produced near monodispersed sized polystyrene latex particles in a continuous Couette-Taylor-vortex flow. Sodium Lauryl sulphate, potassium persulphate and chemical grade styrene were mixed in the system producing non-coagulated monodisperse beads. A similar series of experiments by Kataoka (1995) produced a similar result. Ogihara et al. (1995) produced monodisperse silica particles in this flow regime and accounted this to the ideal batch reactor behaviour of the vortex cells.

7.3 Visualisation of the Transport Process: Present Study

The behaviour of the transport process in concentric cylinder flow has been visualised qualitatively using dye tracer injection in the system CC-75. Images were captured using the Canon Power Shot Pro70 digital image camera used for the flow visualisation studies of Chapter 3. Dye tracer injection studies were not performed in the system CC-25. It was not possible to obtain sufficiently good images of the dispersion at this small scale without using more advanced imaging and lighting equipment, and also having more sophisticated equipment to accurately deliver a much smaller volume of dye tracer in a controlled way. With the flow visualisation images of Chapter 3 and LDA data from Chapter 5, sufficient information is available to make reasonable qualitative assessment of transport behaviour in the smaller system CC-25 from observations made in CC-75. The concentric cylinder configuration for CC-75 was the same as that used for LDA measurements but with some small modifications. A different viewbox was fixed to the outer cylinder and this was filled with water. The flat edges of the

view box improved visualisation of injected dye into the vortex flows by removing light glare from the camera. The system is shown in Plate 3.7. A number of injection ports were added to add and remove fluid from the viewbox (1). Ports inserted on the top of the vessel allowed for dye injection into the top of the annular space (2) or into the top of the vessel at the centre of the axis of inner cylinder rotation (3). This could be used to qualitatively observe dispersion from entrance effects in the vessel. A number of ports were added in the outer wall of the vessel down the vessel axis (4). This allowed for study of the transport mechanism observing any gravitational effects. Alternatively, ports (1) or (2) could be used to impose an axial flow through the vessel by incorporating a recirculating pump to provide a flow loop. In general, when this approach was used, the lower port on the axis (4) was used in conjunction with ports (1) or (2) to form the loop. A peristaltic pump (Watson-Marlow, Falmouth UK, model MHRE200) was used in the flow loop. The pump direction is reversible so that the imposed axial flow in the vessel could be bottom-to-top or top-to-bottom.

The dye used in tracer experiments was a 40vol.% Quink permanent writing ink in distilled water. In order to provide neutral buoyancy with the dye, a 39.38wt.% aqueous sodium chloride solution was used as the annular fluid in experiments. When operating the vessel in closed batch mode, a 1ml. syringe was filled with 0.2ml. of 40wt.% dye and inserted into a pre-selected injection port for the experimental run. The annular space was filled with sodium chloride solution and the inner cylinder rotated to a prescribed speed to generate a desired steady state flow condition. This is done on the basis of observations from Chapter 3. Whilst it has been observed that the steady flow condition is achieved rapidly, the system was still left for 2 minutes as an insurance of an equilibrated flow state. The dye was injected by hand as a rapid but controlled injection from the syringe, and given the relatively small volume of injection relative to the vessel fluid volume, this was considered as a δ-function pulse injection. A stopwatch was used to record the time of injection. Subsequently digital images of the flow were recorded using the camera. A time stamp on the images captured in the camera allowed for the transport of dye in the vessel to be followed transiently. A selection of these sequences for different experimental flow

conditions are shown. In Plate 7.1, laminar Couette flow prevails at Ta_i = 24.01 and the path of injected dye is shown with progressing time. It is assumed that the ink is non-homogeneous and is heavily laden with concentrated micro-particulates, and it is for this reason and the volume of injection, that the initial broadening of the dye streak is assumed to occur. This broadening occurs in a relatively small time scale (~19s) and is stable by 57s. Once stable, there is essentially no subsequent disturbance to the flow and the dye moves azimuthally with no axial (and although not visualised but assume) no radial dispersion.

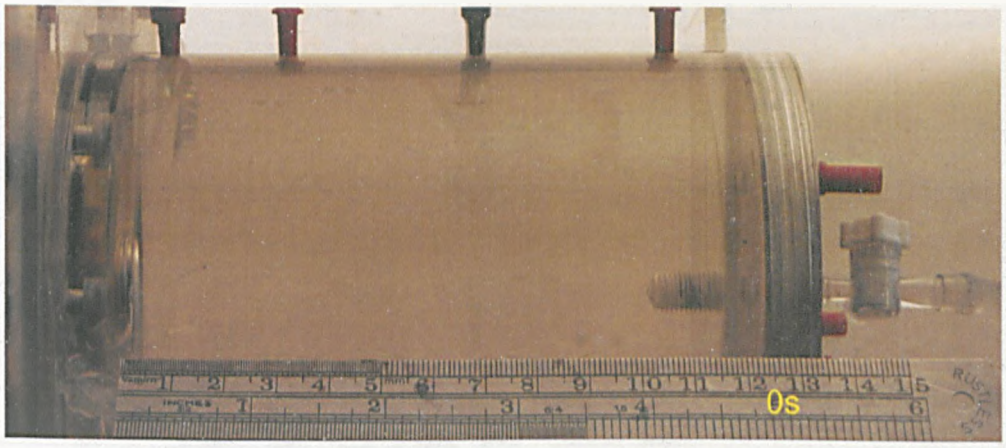

(a)

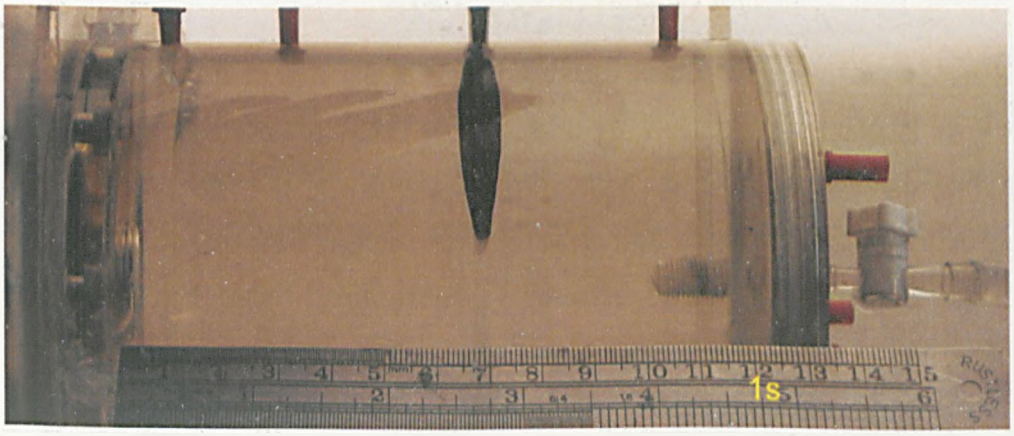

(b)

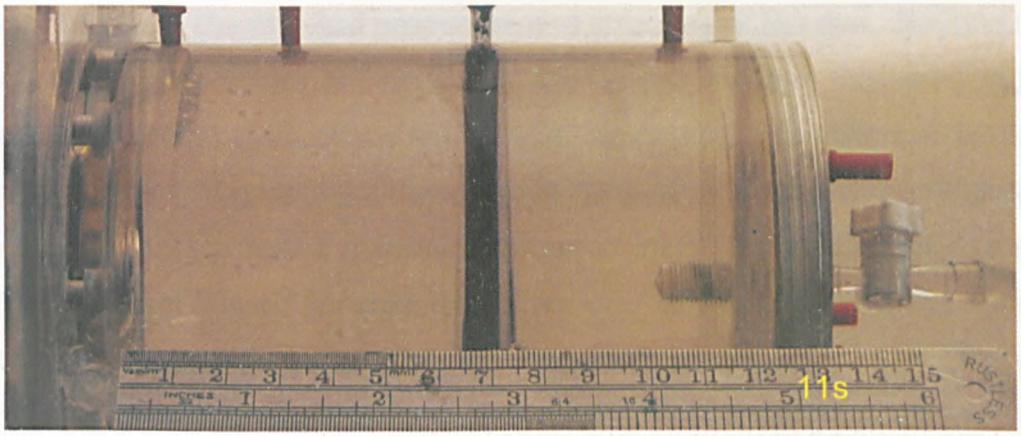

(c)

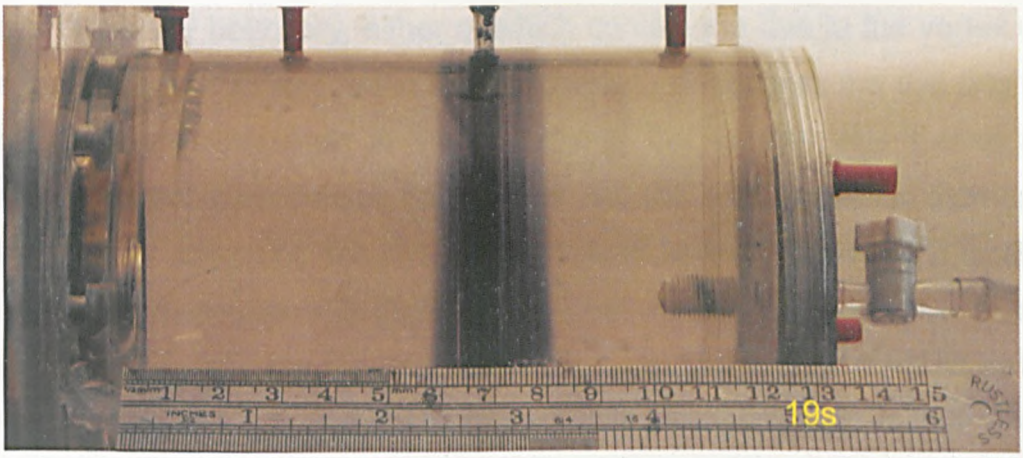

(d)

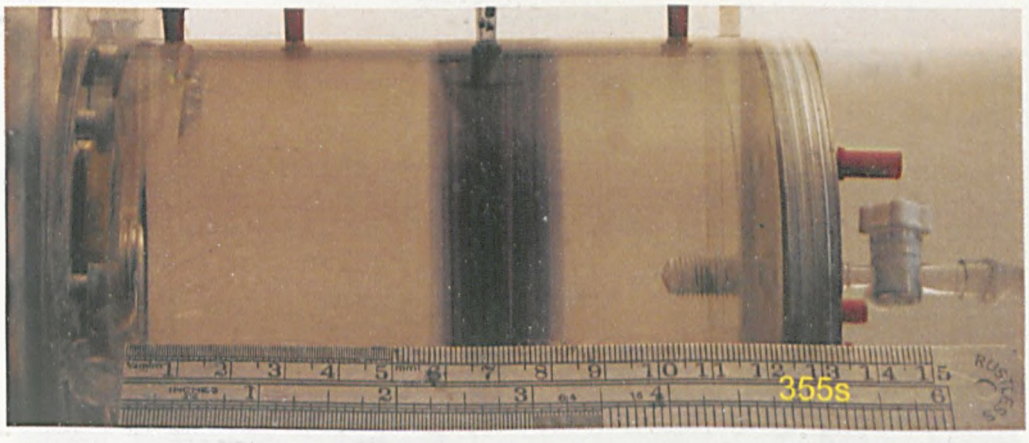

(e)

Plate 7.1 Laminar Couette Flow at Ta_i =24.01

In Plate 7.2, laminar Taylor-vortex flow is generated at Ta_i = 44.95. The initial dispersion at 9s is similar to the Couette flow dispersion at 11s and this

is attributable to the physical properties and structure of the dye. Beyond this point, the dye becomes entrained into the Taylor vortices that exist in the flow, and as time progresses the dye is distributed into different vortices along the axis of the vessel. The concentration of dye is weaker as the axial location increases from the initial injection point. The transfer of dye into axially adjacent Taylor vortices is entirely due to the action of the outflow boundaries for each vortex cell as described in Section 7.1. The dye concentration will accordingly decrease as the axial location increases from the injection point as only a small proportion of the dye moves into the outflow boundary. A larger proportion is contained at the vortex centre or enters the inflow boundary, either of which contain the dye to the vortex cell at a fixed axial location. The inflow boundaries concentrate the dye into the bands that are visualised in Plate 7.2 and the weaker dye bands are observed on adjacent outflow boundaries. As the axially position increases from the injection point, the dye concentration between inflow and outflow boundaries progressively becomes more uniform. As time progresses and equilibrium is approached, it is observed that the dye is concentrated on the vortex boundaries and that there is very little dye contained in the vortex centres. The mass transport of the injected dye is enhanced in LTVF than LCF.

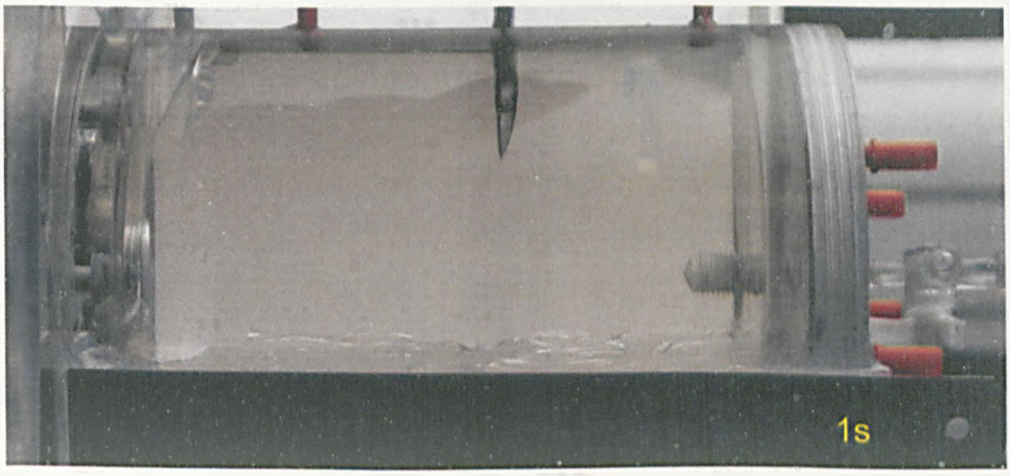

(a)

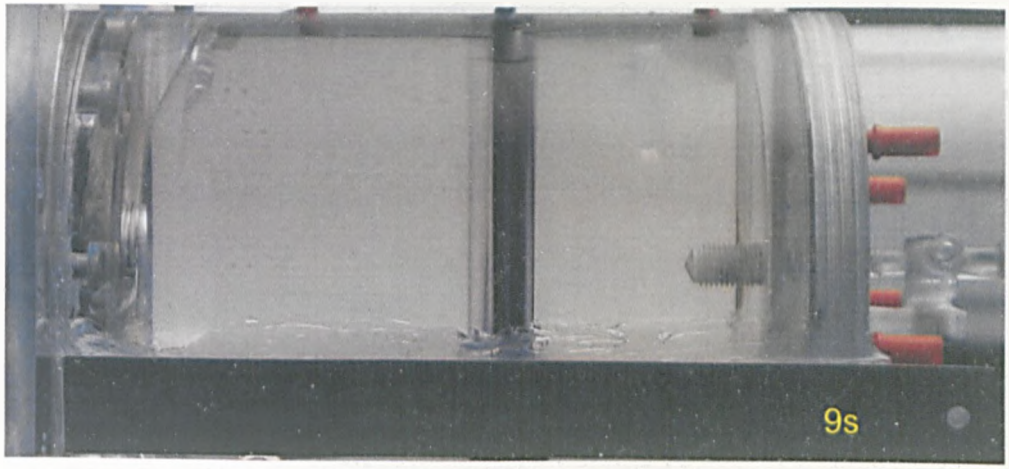

(b)

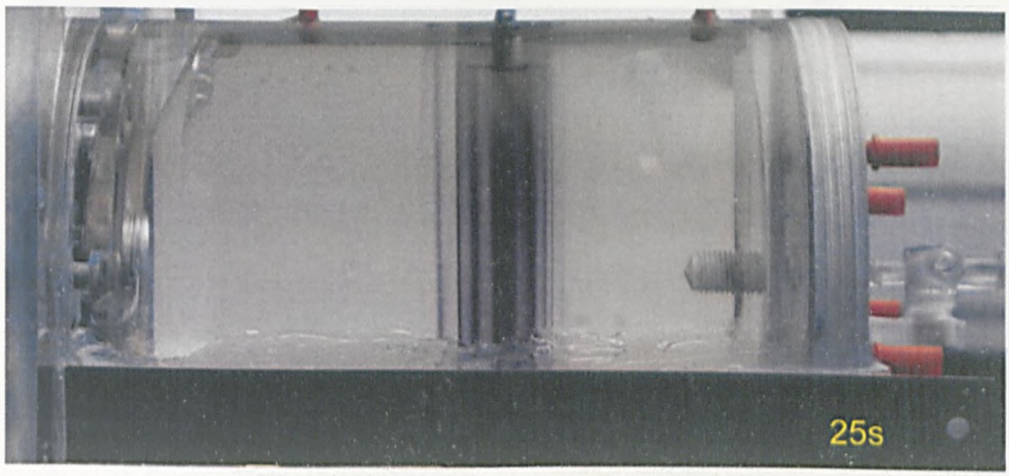

(c)

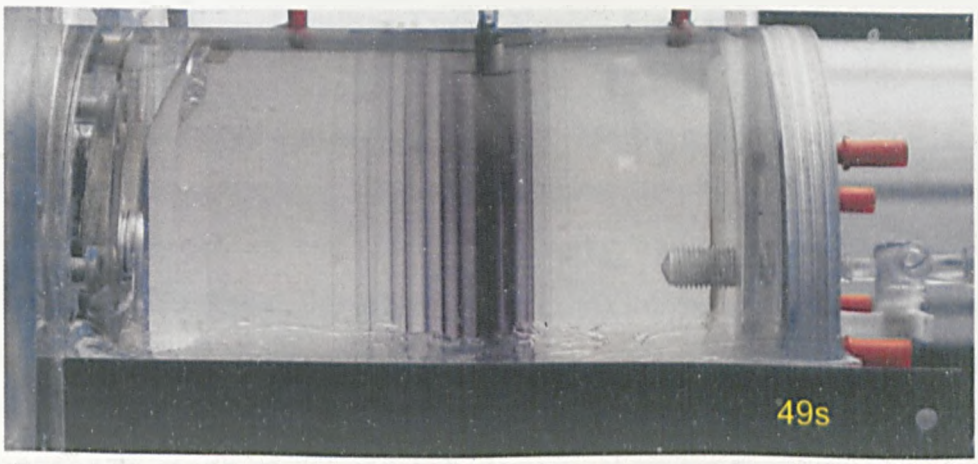

(d)

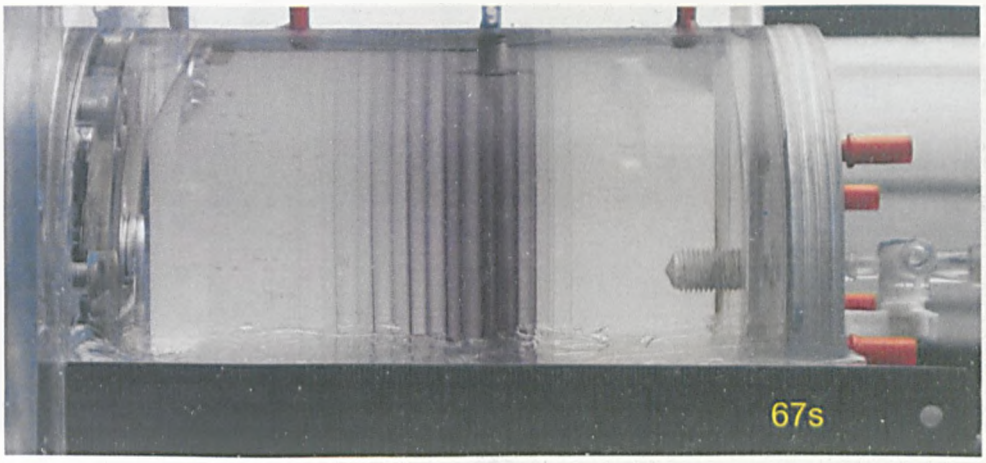

(e)

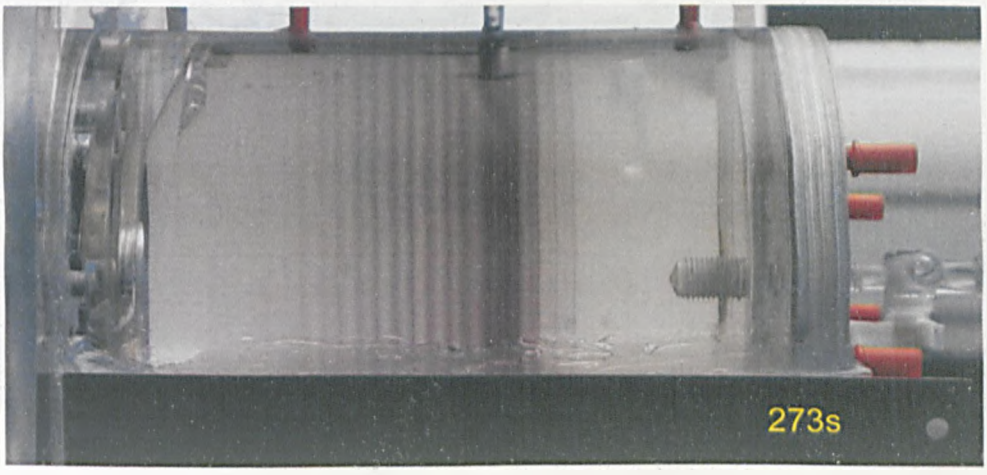

(f)

Plate 7.2 Laminar Taylor-Vortex Flow at Ta_i = 44.95

Dye injection for wavy vortex flow at Ta_i = 154.87 is illustrated in Plate 7.3. Both intra-vortex mixing and inter-vortex mixing are immediately evident upon injection of the dye at 1s. At 7s, the wavy nature of the Taylor vortex boundaries is clear and the transferral of dye between adjacent vortices is self-evident. As a consequence of this, the axial dispersion is significantly increased relative to LTVF and the degree of mixing is therefore faster. A comparison is made of the axial dispersion at given time stamps between Plates C1, C2 and C3. In LCF a 2.5mm axial dispersion occurs in 57s compared against 3.5mm in 49s for LTVF and in excess of 7mm in 37s for WVF. This is comparable with the observations of Rudolph (1998) noted in Section 7.1 and in general verifies the dye tracer studies of Desmet (1996).

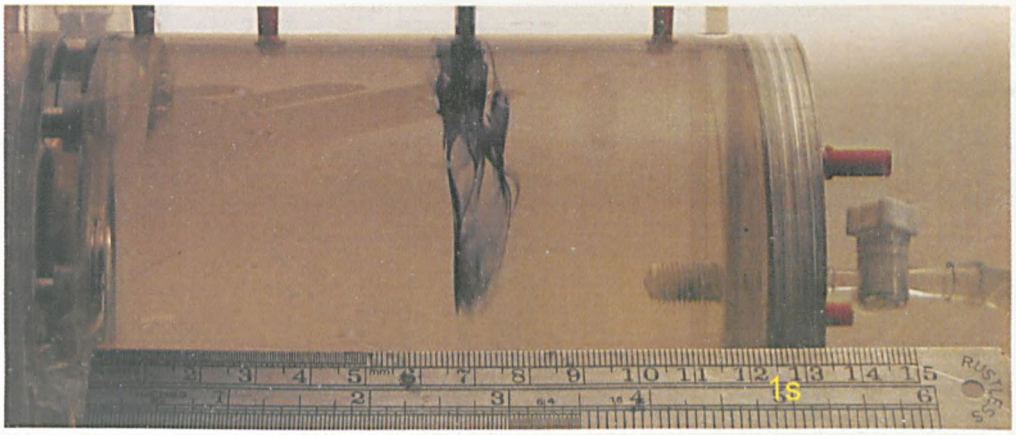

(a)

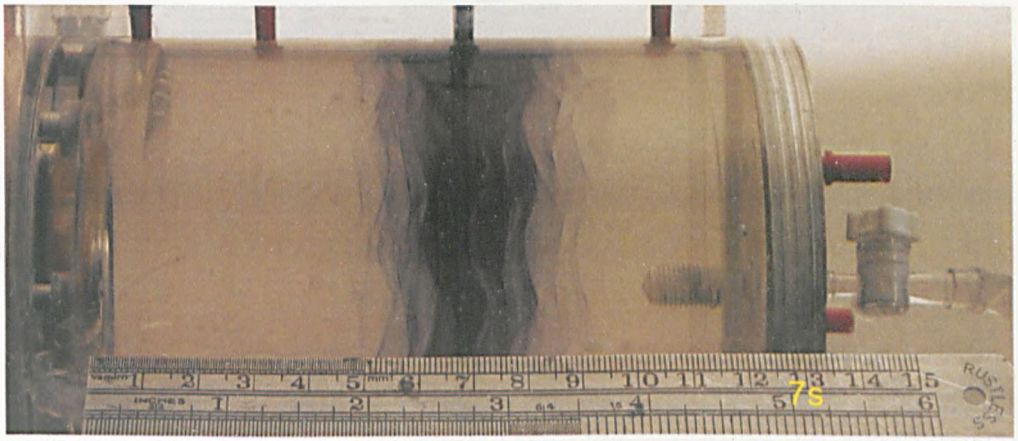

(b)

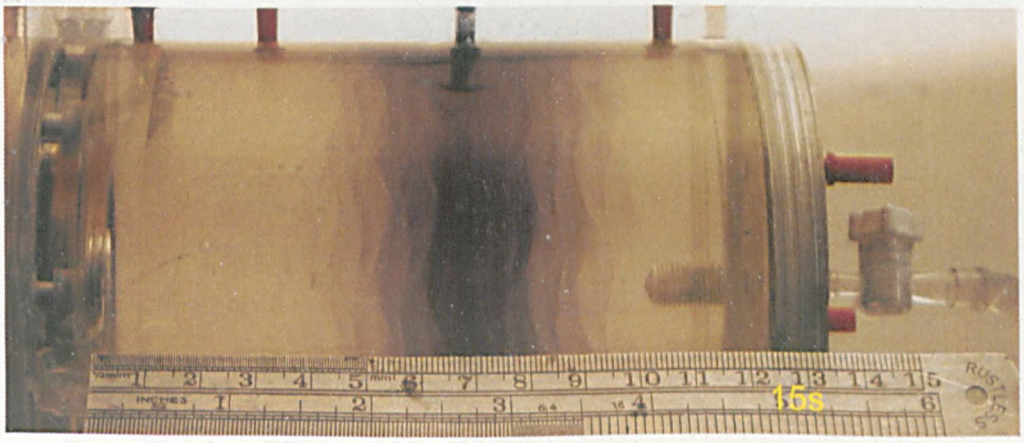

(c)

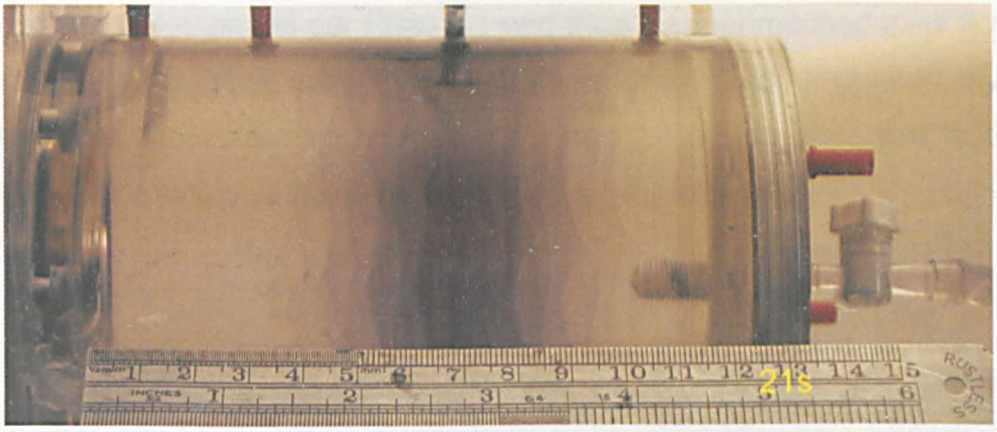

(d)

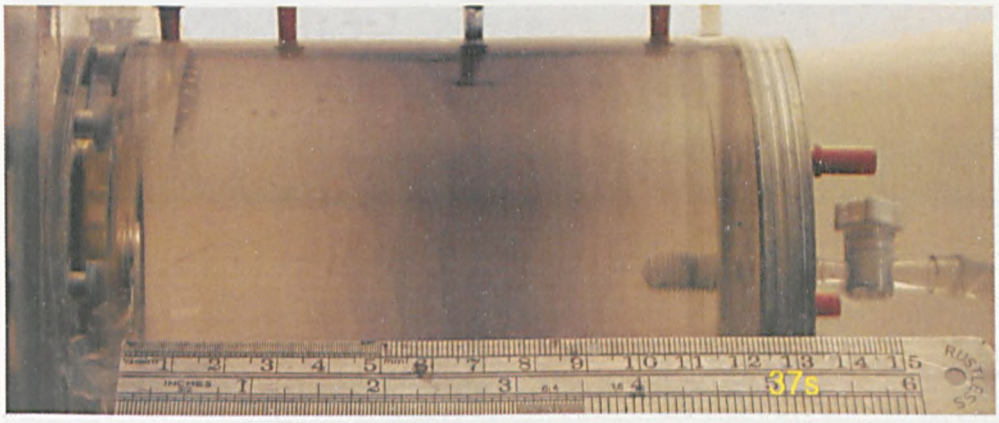

(e)

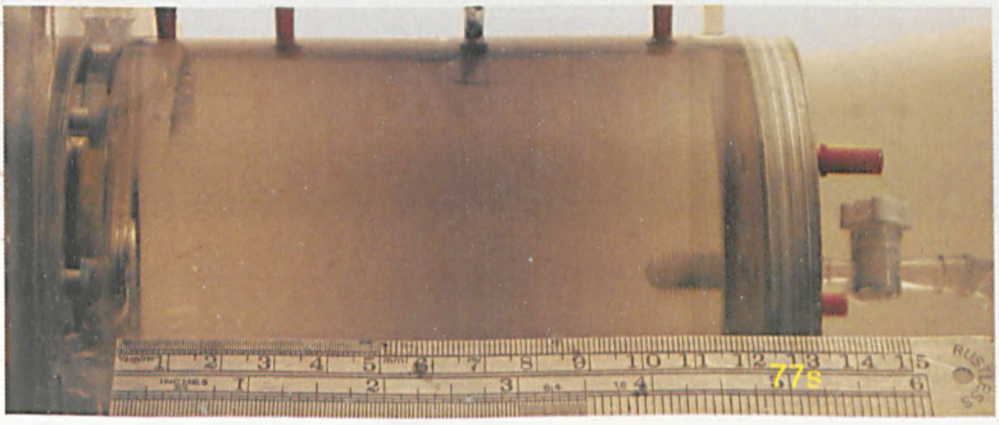

(f)

Plate 7.3 Wavy-vortex flow at Ta_i = 154.87

In qualitative experiments using a superimposed perfusion on the rotating flow (Poiseuille-Taylor flow), the rate and direction of axial dispersion can be controlled. As a comparison, a rotational flow using Ta_i = 24.01 was

applied to the system as per Plate 7.1 and then a superimposed axial flow of 60ml/min was applied using the peristaltic pump. The dispersion of dye under these circumstances is shown in Plate 7.4 and is observed to differ from the preceding dispersion regimes.

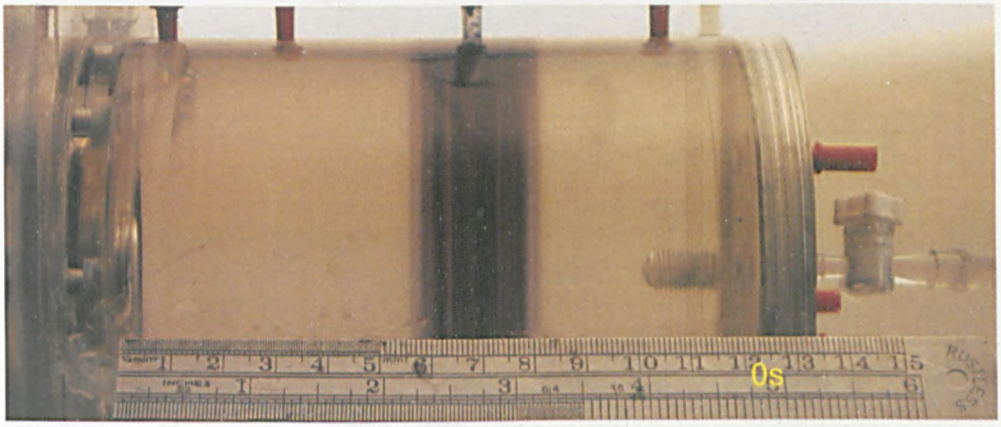

(a)

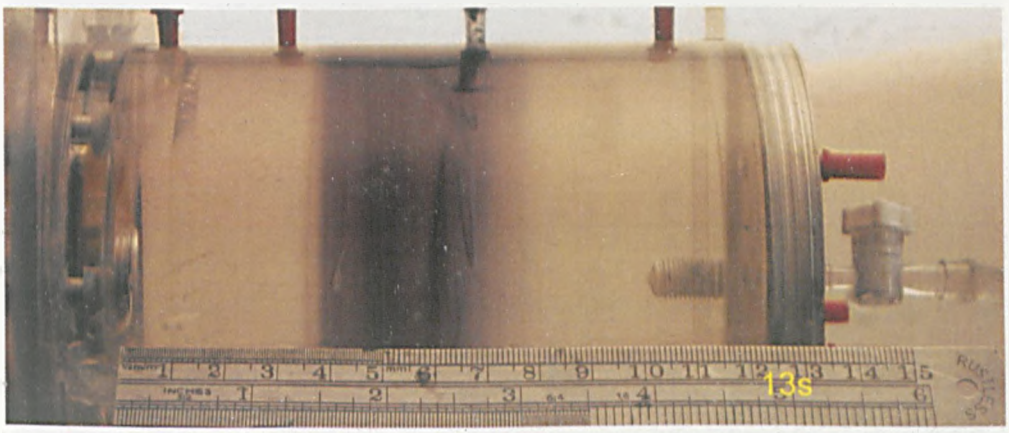

(b)

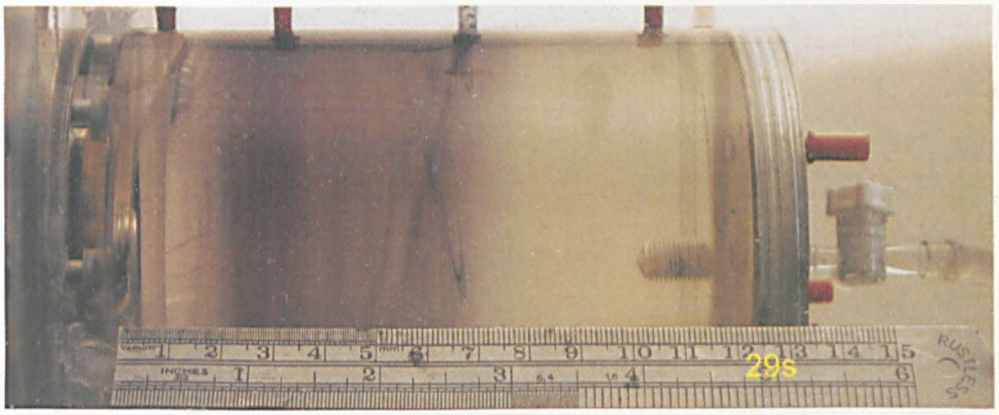

(c)

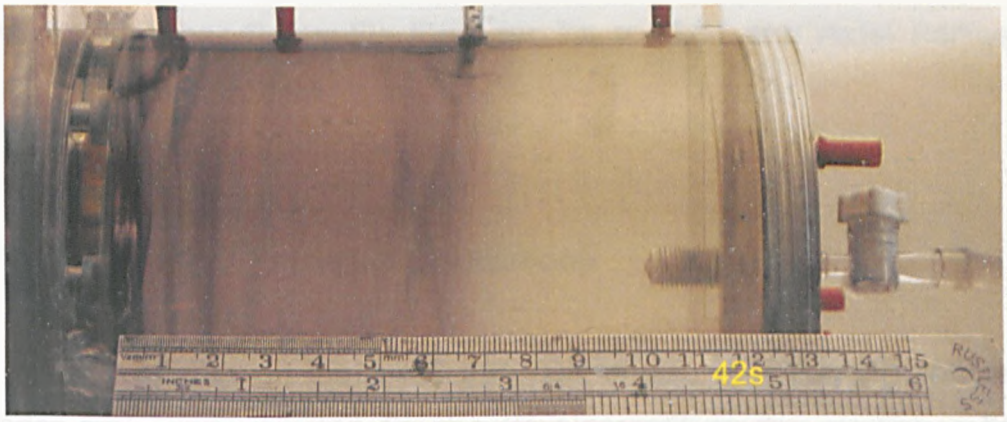

(d)

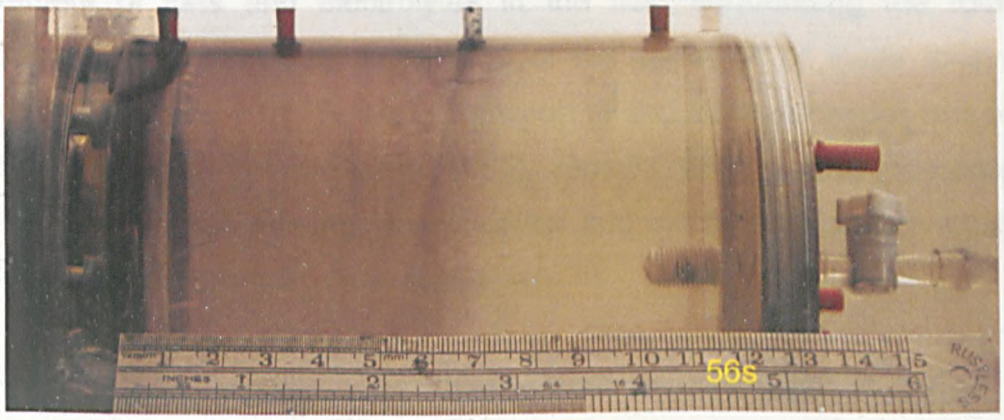

(e)

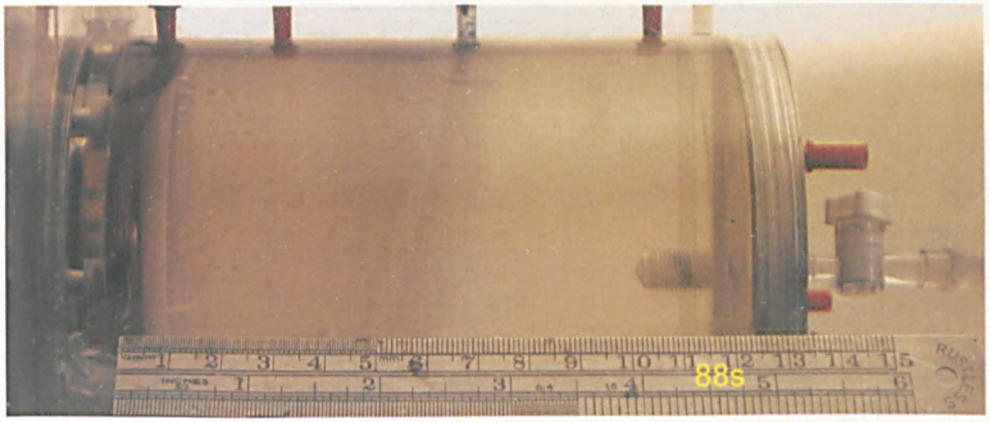

(f)

Plate 7.4 Laminar Poiseuille Flow for Ta_i = 24.01 and Axial Perfusion Rate 60ml/min

7.4 Global Mass Transport Correlations

Early studies on the mass transport effects in a rotating concentric cylinder flow were initiated for the development of the rotating cylinder electrode (Gabe (1983)). These electrodes operated on the principle of the movement of ions and electrolytes in the fluid surrounding the rotating electrode and an in depth knowledge of the transport of these ions was needed (Mizushina (1971)). Mass transport to and from electrodes has been studied extensively by Eisenberg (1955). Grifoll (1986) studied the transport near the wall of the rotating inner cylinder and a modified form of equation (6.60) was experimentally determined

$$Sh = 0.5 C_f \, Re \, Sc^{0.356} \qquad (7.1)$$

where C_f is a friction factor incorporating the shear stress on the inner wall, τ_i. The dimensionless number definitions here are given by the following relationships:

$$Sh = \frac{2k_l r_i}{D} \quad (a)$$

$$Sc = \frac{\nu}{D} \quad (b) \qquad (7.2)$$

$$Re = \frac{2r_i^2 \Omega_i}{\nu} \quad (c)$$

$$C_f = \frac{2\tau_i}{\rho(r_i\Omega_i)^2} \quad (d)$$

The mass transport of ferricyanide ions in an electrochemical concentric cylinder reactor with only the inner wall rotating for both smooth and rough inner wall surfaces was investigated. The redox reaction chosen is between a solution of potassium ferrocyanide and potassium ferricyanide as the tracer on a sodium hydroxide electrolyte solution and has been described by Berger and Hau (1977). The supporting electrolyte ensures negligible contribution of ionic migration to mass transfer. All solutions were prepared from distilled water and the redox reaction is,

$$Fe(CN)_6^{3-} + e^- \rightarrow Fe(CN)_6^{4-}$$

This reaction is measured on the cathode, and the limiting current technique is applied. The potential on the electrode is increased gradually and the current also increases until a stable value is reached. This value is the limiting current and corresponds to the condition when the concentration of the reacting species of ions on the surface of the electrode equals zero. The ion transfer rate under these conditions is determined by molecular and convective diffusion through the boundary layer surrounding the electrode and the mass transfer coefficient can be determined from,

$$k_l = \frac{I_{lim}}{n_e F A c_b} \qquad (7.3)$$

For the range 770 < Sc < 8000 and 20000 < Re < 900000, Grifoll observed the following correlation to hold for smooth cylinders,

$$Sh = 0.0987\,Re^{0.70}\,Sc^{0.33} \tag{7.4}$$

Pang and Ritchie (1981) described a similar correlation for Re > 10000 and Sc > 650,

$$Sh = 0.0138\,Re^{0.866}\,Sc^{0.33} \tag{7.5}$$

Smith and Grief (1975) studied mass conservation in circular Couette flow and proposed the following correlation,

$$Sh = 0.827 Sc^{\frac{1}{3}} (C_f/2)^{\frac{1}{2}} \left\{ Re\, Sc^{\frac{1}{3}} [1 + 40/(C_f\, Re)]^{\frac{2}{3}} \right\} \tag{7.6}$$

Experiments performed by Holman and Ashar (1970) looked at the mass transport from a cast benmzoic acid rotating inner cylinder into three types of annular fluid; water, 9.5M glycerol and 0.46M sodium hydroxide. This corresponded to a non-reacting and in the latter case, reacting system. The forced convection transfer correlations used were

$$Sh = 9.30\, Sc^{\frac{1}{3}}\, Re^{0.425} \tag{7.7}$$

For the non-reacting system and

$$Sh = 88.2\, Sc^{\frac{1}{3}}\, Re^{0.492} \tag{7.8}$$

for the reacting system. In this paper they quote other potentially useful correlations of this type most notably those of Marangozis (1960),

$$Sh = 0.635\, Sc^{\frac{1}{3}}\, Re^{0.70} \tag{7.9}$$

that is quoted as being good for the range 100 < Re < 100000 with a maximum mean deviation of 16.7% and two more general forms for use with experimental data in the range 1000 < Re < 100000

$$Sh = \beta\, Sc^{\frac{1}{3}}\, Re\left(\frac{C_f}{2}\right)^{\frac{1}{2}} \tag{7.10}$$

$$Sh = \phi\, Sc^{0.356}\, Re^{0.70} \tag{7.11}$$

where β and φ are constants. An analysis of experimental literature data yeielded a good fit for the following correlation according to Sherwood and Ryan (1958)

$$Sh = 1.97\, Sc^{\frac{1}{3}}\, Re^{0.73} \tag{7.12}$$

Finally, Eisenberg (1954) correlated experimental data with a Chilton-Colburn j-factor analogy

$$j'_D = \frac{k_l}{v} Sc^{0.644} = 0.0791\, Re^{-0.30} \tag{7.13}$$

7.5 Local Mass Transport from Global Data

Gu and Fahidy (1985) made mass transport measurements in a concentric cylinder system using simultaneous chemical and electrochemical measurements. The chemical approach relied on monitoring pH changes in a solution of sodium chloride in deionised water (5 < pH < 6) when a small aliquot of alkaline solution (pH=12) was added. In the electrochemical approach, the outer cylinder is fitted with wire electrodes to polarize the cylinders as anode and cathode. Depletion of hydronium ions at the cathode was then used as the basis of measurement. Flow visualisation using dye tracer injection confirmed the prevailing flow condition. Sophisticated

mathematical techniques were used to determine local mass transport coefficients varying with time, position and hydrodynamics from global mass transport data obtained from more general mass transport correlations. The initial basis for calculation relied on a modified Taylor number, Ta_m for the hydrodynamics instead of Reynolds number. The regular Taylor number was defined by equation (2.21h) and Ta_m then defined as

$$Ta_m = \frac{Ta}{\Theta} \qquad (a)$$

$$\Theta = \frac{\pi^2}{41.3}\vartheta \qquad (b) \qquad (7.14)$$

$$\vartheta = \frac{2}{(2-\lambda)\left[A\left(1-B\frac{\lambda}{2-\lambda}\right)+C\left(1-B\frac{\lambda}{2-\lambda}\right)-1\right]^{0.5}} \qquad (c)$$

where A = 0.0571, B = 1.304 and C = 0.00056 in equation (7.14c). These constants were taken from Holman and Ashar (1970). λ is a modifying factor to account for the annular gap effect on the transport and is determined from

$$\lambda = \frac{2(r_o - r_i)}{r_o + r_i} \qquad (7.15)$$

The constant 41.3 in equation (7.14b) is based on Taylor's classical theory and may be adjusted accordingly for the given constant for the transition from laminar Couette to Taylor-vortex flow obtained experimentally. Kataoka (1977) showed a sinusoidal variation in the local mass transport coefficient in Taylor-vortex flow with axial position, based on microelectrode measurements for ferricyanide transport experiments described above. This oscillatory behaviour has been described by Gu and Fahidy in terms of a simple physical model due to the Taylor vortex motion. Inflowing portions of the vortex to the inner wall promote ion transport to the electrode and enhance the mass transport coefficient whereas outflowing portions from the inner wall will have the reverse effect. The principle is illustrated in Figure

7.1. The global mass transport correlation is determined from a form of equation (6.60) or employing a Taylor number for hydrodynamics. In this case, the correlation used is

$$Sh = 0.74 Ta_m^{\frac{1}{2}} Sc^{\frac{1}{3}} \qquad (7.16)$$

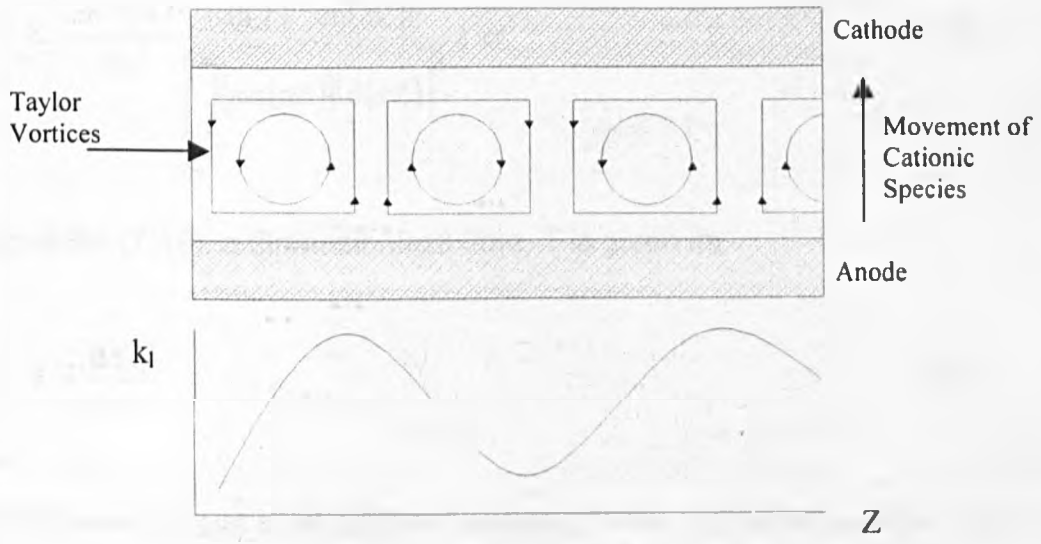

Figure 7.1 Conceptualisation of the periodic nature of mass transfer coefficients in Taylor-vortex flows

A time and space averaged value of the mass transfer coefficient is then calculated from

$$\overline{K} = \frac{0.74D}{2\nu} Ta_m^{\frac{1}{2}} Sc^{\frac{1}{3}} \qquad (7.17)$$

With a knowledge of the wavenumber, α, predetermined from flow visualisation studies, the amplitude of the of the velocity gradient at the rotating surface, ξ, is calculated from

$$\overline{K} = \frac{0.3798}{Sc^{\frac{1}{3}}} \xi^{\frac{1}{2}} \alpha^{\frac{1}{2}} \qquad (7.18)$$

The local mass transfer coefficient, K is dependent on the time and location in the system. Hence to obtain a value of the local mass transfer coefficient, either the time is fixed and a series of values are expressed for positions along the cylinder axis, or the location on the axis is fixed and the variation of the mass transfer coefficient is expressed with increasing time.

$$K = \frac{0.5383}{Sc^{\frac{1}{3}}} \frac{(\sin T)^{\frac{1}{3}}[\sin(\alpha Z)]^{\frac{1}{2}}}{\left[\int_0^{\alpha Z}[\sin(\alpha Z)]^{\frac{1}{2}} d(\alpha Z)\right]^{\frac{1}{2}}} \xi^{\frac{1}{3}} \alpha^{\frac{1}{3}} \qquad (7.19)$$

In equation (7.19), a dimensionless time, T is given by

$$T = \frac{t\Omega_i r_i}{r_o - r_i} \qquad (7.20)$$

and a dimensionless axial position is related to the real axial position, z by

$$Z = \frac{z}{r_o - r_i} \qquad (7.21)$$

The solution of equation (7.19) is only achieved numerically since no analytical solution exists for the integral term in the denominator. In addition, and as mentioned above, T must be fixed for a range of Z, or vice-versa. Dimensional values are calculated from the dimensionless values using

$$k_l = \frac{\nu}{r_o - r_i} K \qquad (7.22)$$

This is also true for the global values of $\overline{K}$.

7.6 Tanks-in-Series Mass Transport

This concept of vortex cells themselves behaving as ideal mixing units has led to the transport process being analogous to the tanks-in-series model described by Levenspiel (1972). Legrand and Coeuret (1986) have studied mass transport in Taylor-vortex flows using the ferricyanide electrochemical technique and the tanks-in-series concept for mass transport.

The axial length of a vortex pair, Δ is approximately twice the annular gap size (Kataoka (1975)) in the range $41.3 < Ta < 300$ and has been shown to have little variation beyond this point. Koschmeider (1979) showed that

$$\Delta = 2.4(r_o - r_i) \qquad \text{for } 320 < Ta < 8200 \qquad (7.23)$$

The toroidal vortex cell is considered as a tubular batch reactor of length L,

$$L = \pi(r_o + r_i) \qquad (7.24)$$

with complete recirculation. The flow can be modelled as that in a tube of infinite length in which longitudinal dispersion occurs. The dispersion is characterised by the dimensionless Bodenstein number, Bo,

$$Bo = \frac{u_t L}{D_d} \qquad (7.25)$$

and this is related to the number of perfect mixing elements, or vortex cells, N, of equal size

$$Bo = 2N \qquad (7.26)$$

The circumferential dispersion coefficient is then calculated from

$$D_d = \frac{u_t L}{2N} \tag{7.27}$$

u_t is the mean circumferential velocity of the vortex cell. Legrand (1986) found the dispersion coefficent related to the Taylor number according to

$$\frac{D_d}{\nu}\left[\frac{r_i d^3}{L^4}\right]^{\frac{1}{2}} = 0.000239 Ta \tag{7.28}$$

From experimental measurements, it is possible to plot the term on the left hand side of equation (7.28) against Taylor number to evaluate the constant for the given experimental configuration provided the number of vortices and the mean velocity of the vortex is known. For intermixing the vortex region, the dispersion coefficient calculated by this method can be replaced in the forced convection correlations of the form Sh=f(Re, Sc) to evaluate the mass transfer coefficient in the intervortex mixing region.

7.7 One-Dimensional Axial Mixing Model

A similar but alternative approach to the tanks-in-series model is the one-dimensional axial mixing model. The method has been described by Tam and Swinney (1987) who used an optical absorption technique to quantify concentration changes in an injected solute. Dye was injected into a fluid experiencing a turbulent Taylor-vortex flow and concentration of the dye was monitored at three axial locations using a He-Ar laser source as illumination and photodiodes. Ohmura (1997) performed similar experiments in laminar Taylor vortex flow using a glycerol solution and phenolphthalein as the injected tracer. Conductivity measurements using Nickel electrodes were made at two different axial locations in the Taylor-vortex column to provide transport data. In both cases, an effective mass diffusion coefficient, D_z is calculated. This is equivalent to the dispersion coefficient determined from the tanks-in-series model. The transport of tracer with a concentration c(z,t) in a tubular reactor with 1-D axial dispersion is given by

$$\frac{\partial c(z,t)}{\partial t} + u_z \frac{\partial c(z,t)}{\partial z} = D_z \frac{\partial^2 c(z,t)}{\partial z^2} \tag{7.29}$$

u_z is the fluid velocity in the axial direction and only becomes important for Taylor-Poiseuille flow. In batch Taylor vortex flow with no axially imposed flow rate $u_z=0$. For the model to be valid, the following conditions must be satisfied:

The tracer is well mixed in the radial and azimuthal directions on a time scale that is short compared to the time scale for the transport in the axial direction The length scale of the annular section is large compared to the size of the vortices

For batch Taylor-vortex flow equation (7.29) reduces to,

$$\frac{\partial c(z,t)}{\partial t} = D_z \frac{\partial^2 c(z,t)}{\partial z^2} \tag{7.30}$$

For a pulse injection of tracer described by a δ-function into an infinitely long annulus the analytical solution to equation (7.30) is given by

$$c(z,t) = \frac{1}{2\sqrt{\pi D_z t}} e^{-z^2/4D_z t} \tag{7.31}$$

The tracer concentration at two different axial locations are related to the effective diffusion coefficient from the solution of equation (5.25) as

$$\ln\left(\frac{c(z_1,t)}{c(z_2,t)}\right) = -\frac{\left(z_1^2 - z_2^2\right)}{4D_z t} \tag{7.32}$$

the effective diffusion coefficient is then readily determined from the slope of $\ln[c(z_1,t)/c(z_2,t)]$ versus $1/t$.

This technique is particularly attractive for qualitatively measuring solute transport in annular flows from a pulse injection of solute. The basis of this theory is proposed for future mass transport studies described in Chapter 10.

References

Berger FP, Hau KFFL. Mass Transfer in Turbulent Pipe Flow Measured by the Electrochemical Method. *Int. J. Heat Mass Transfer* **20** 1185-1194 (1977)

Campero RJ, Vigil RD. Axial Dispersion During Low-Reynolds Number Taylor-Couette Flow: Intra-Vortex Mixing Effects. *Chem. Eng. Sci.* **52** 3303-3310 (1997)

Desmet G, Verelst H, Baron GV. Local and Global Dispersion Effects in Couette-Taylor Flow [I]: Decription and Modelling of the Dispersion Effects. *Chem. Eng. Sci.* **51** (8) 1287-1298 (1996)

Desmet G, Verelst H, Baron GV. Local and Global Dispersion Effects in Couette-Taylor Flow [II]: Quantitative Measurements and Discussion of the Reactor Performance. *Chem. Eng. Sci.* **51** (8) 1299-1309 (1996)

Legrand J, Coeuret F. Circumferential Mixing in One-Phase and Two-Phase Taylor Vortex Flows. *Chem. Eng. Sci.* **41** (1) 47-53 (1986)

Gabe DR, Walsh FC. The Rotating Cylinder Electrode: A Review of the Development. *J. Appl. Electrochem.* **13** 3-22 (1983).

Grifoll J, Farriol X, Giralt F. Mass transfer at Smooth and Rough Surfaces in a Circular Couette Flow. *Int. J. Heat Mass Transfer* **29** (12) 1911-1918 (1986)

Gu ZH, Fahidy, TZ. Mass Transport in the Taylor-Vortex Regime of Rotating Flow. *Chem. Eng. Sci.* **40** (7) 1145-1153 (1985)

Holman KL, Ashar ST. Mass Transfer in Rotating Cylinders with Surface Chemical Reaction in the Presence of Taylor Vortices. *Chem. Eng. Sci.* **26** 1817-1831 (1971)

Howes T, Rudman M. Flow and Axial Dispersion Simulation for Traveling Axisymmetric Taylor Vortices. *A.I.ChE. J.* **44** (2) 255-262 (1998)

Inamura T, Saito K, Ishikura S. A New Approach to Continuous Emulsion Polymerization. *Polym. Int.* **30** 203-206 (1993)

Kataoka K, Doi H, Hongo, T, Futagawa M. Ideal Plug Flow Properties of Taylor Vortex Flow. *J. Chem. Engng. Japan* **8** 472-476 (1975)

Kataoka K, Doi H, Komai T. Heat and Mass Transfer in Taylor Vortex Flow with Constant Axial Flowrates. *Int. J. Heat Mass Transfer* **20** 57-63 (1977)

Kataoka K, Takigawa T. Intermixing Over Cell Boundary Between Taylor Vortices. *A.I.Ch.E. J.* **27** 504-508 (1981)

Kataoka K, Ohmura N, Kouzu M, Simamura Y, Okubu M. Emulsion Polymerization of Styrene in a Continuous Taylor Vortex Flow Reactor. *Chem. Eng. Sci.* **50** (9) 1409-1416 (1995)

Koschmeider EL. Turbulent Taylor-Vortex Flow. *J. Fluid Mech.* **93** 515-527 (1979)

Levenspiel O. Chemical Reaction Engineering. 2nd Edition. Wiley Publications, New York. 253-314 (1972)

Liu CI, Lee DJ. Micromixing Effects in a Couette Flow Reactor. *Chem. Eng. Sci.* **54** 2883-2888 (1999)

Marangozis J. Ph.D. Thesis. University of Toronto, Toronto, Canada. (1960)

Mizushina T. The Electrochemical Method in Transport Phenomena. *Adv. Heat Transfer* **7** 87-161 (1971)

Ogihara T, Matsuda G, Yanagawa T, Ogata N, Fujita K, Nomura M. Continuous Synthesis of Monodispersed Silica Particles using Couette-Taylor Vortex Flow. *J. Soc. Ceram. Jpn. Int. Ed.* **103** 151-154 (1995)

Ohmura N, Kataoka K, Shibata Y, Makino T. Effective Mass Diffusion Over Cell Boundaries in a Taylor-Couette Flow System. *Chem. Eng. Sci.* **52** (11) 1757-1765 (1997)

Pang J, Ritchie IM. Mass Transfer at the Surface of a Rotating Cylinder. *Electrochim. Acta* **26** 1345-1350 (1981)

Rudolph M, Shinbrot T, Lueptow RM. A Model of Mixing and Transport in Wavy Taylor-Couette Flow. *Physica D* **121** 163-174 (1998)

Sherwood TK, Ryan JM. Mass Transfer in Rotating Liquid Flows. *Chem. Eng. Sci.* **11** 81-90 (1958)

Smith RN, Grief R. Turbulent Transport to a Rotating Cylinder for Large Prandtl or Schmidt Numbers. *J. Heat Transfer* **97** 594-597 (1975)

Tam WY, Swinney HL. Mass Transport in Turbulent Couette-Taylor Flow. *Phys. Rev. A* **36** 1374-1381 (1987)

Vastano JA, Russo T, Swinney HL. Bifurcation to Spatially Induced Chaos in a Reaction-Diffusion System. *Physica D* **46** 23-42 (1990)

Chapter 8

Experimental Studies of Oxygen Transport

8.1 Introduction

The transport of oxygen to the metabolic site of proliferating cells is a key area in the design of bioreactors and plays a major role in determining their long-term success. Oxygen transport in bioreactors is influenced by a number of factors and these include:

- type and concentration of cells
- method of culture (free suspension, microcarrier, scaffold)
- delivery and measurement of oxygen
- physico-chemical environment
- internal hydrodynamics
- scale of vessel

In order to successfully study the transport of oxygen quantitatively it is important to establish which of the variables will be manipulated and which will be controlled or kept constant. The objectives of this work are to understand how the hydrodynamic environment of annular flows influences

the transport mechanism and thereby develop a correlation to relate the fluid hydrodynamics to the oxygen transfer capability. Based on this correlation it may then be possible to predict oxygen transport in scaled-up annular flow bioreactors given that the scale-up of the hydrodynamic environment has been well characterised in Chapter 5. Studies have been made in a bioreactor using the geometry of the CC-25 system described previously. This is based on a commercially available rheometer (Rheologica Stresstech) within the Department of Clinical Engineering at the University of Liverpool. The design and operation of this bioreactor, from here on referred to as CC-25R, is described in this chapter along with details of the cell and media preparations and the results of the oxygen transport measurements.

8.2 CC-25R Bioreactor

The CC-25R bioreactor and its associated components are shown in Plate 8.1.

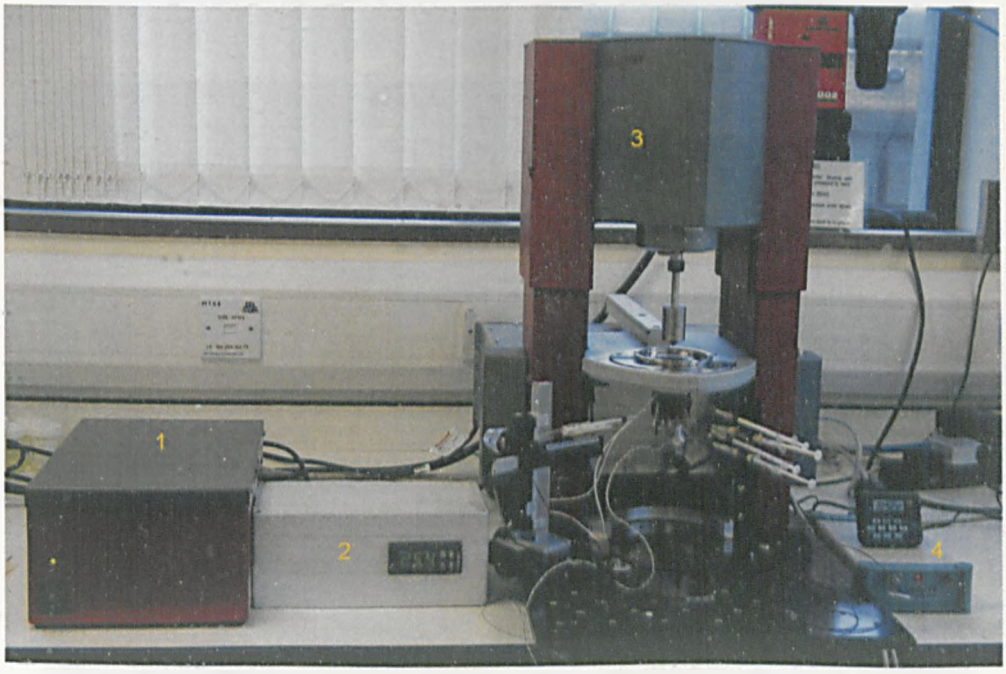

Plate 8.1 CC-25R Bioreactor and associated components

The ancillary components listed in Plate 8.1 are the power supply (1), a PID temperature control unit (2), and electronic motor to raise and lower the inner cylinder of CC25-R powered by (1) and the PreSens Microx TX oxygen measurement control box (4). The CC25-R reactor is shown in Plate 8.2 in more detail.

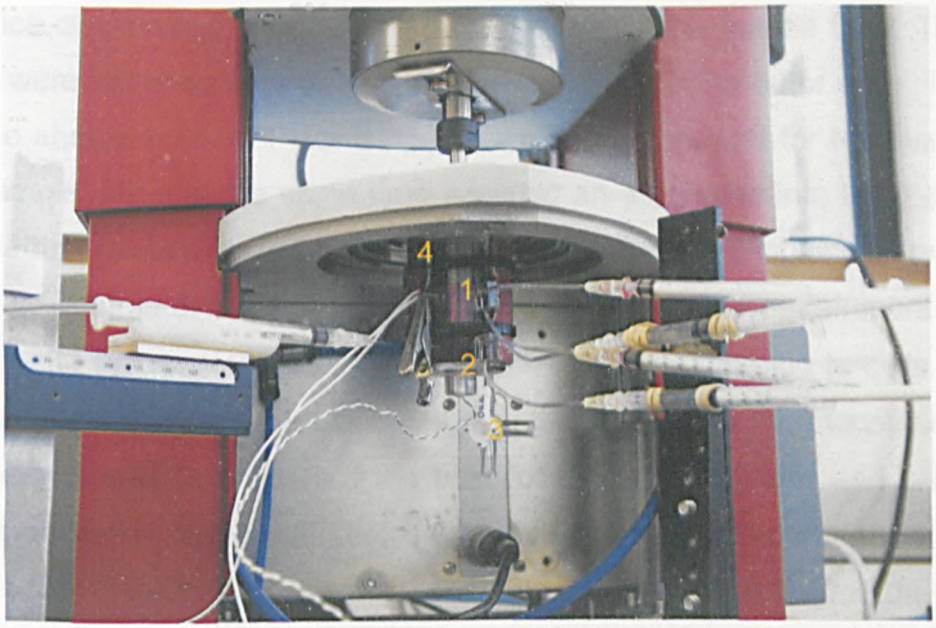

(a)

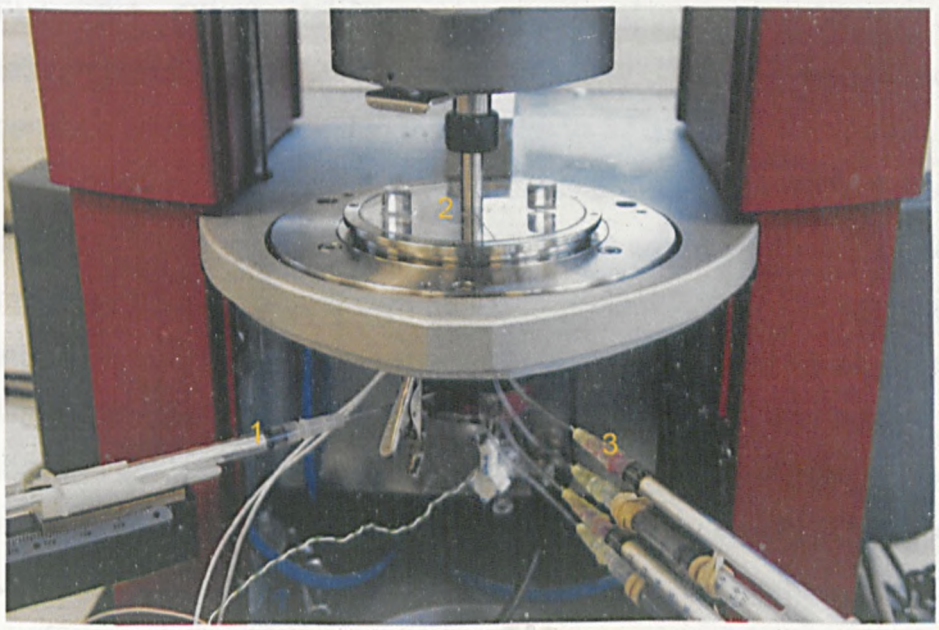

(b)

Plate 8.2 **CC25-R Bioreactor viewed from below (a) and from above(b)**

The CC-25R has a stationary outer cylinder of PMMA construction and a stainless steel inner cylinder that can be caused to rotate at a prescribed speed. In Plate 8.2(a) the stainless steel inner cylinder along with a portion of cell containing media can be seen at (1). A series of ports were made in the outer wall to allow for sampling of fluid and for insertion of the Microx TX oxygen-monitoring probe described in Section 6.5.4. The ports consisted of a T-piece of stainless steel tube to accommodate 20G needle tips. The T-pieces were set in a piece of PMMA that was fixed to the outer wall. These are also shown at (1) in Plate 8.2(a). The T-piece allowed for removal of a fluid sample whilst at the same time injecting an air bubble into the T-piece. This method caused the air bubble to travel into the sampling line to provide a discrete volume of sampling fluid and also prevented the entrainment of air bubbles into the reactor media that are known to be damaging to cells. The fluid samples were collected in 1.0ml syringes. A J-type thermocouple (RS Components UK) was inserted the base of the outer cylinder and set in a silicone adhesive (2). A drain valve was also set into the bottom of the outer cylinder (3). A silicone-heating mat (Farnell, UK) was fitted around the outer cylinder and both the thermocouple and the heating mat were fed to a control box (Plate 8.1 (2)) containing a proportional-integral-derivative (PID) temperature control card (IR32V2L000, Carel, Italy). This allowed for control of temperature of the media within the reactor to 37 ± 0.3°C.

The PreSens Microx TX oxygen-monitoring probe is a fibre-optic detector with a 50μm tip. This is housed inside a syringe and a 20G needle as a protective housing and shown as (1) in Plate 8.2 (b). The syringe was fitted onto a microscope traverse mounting to provide accurate alignment of the optic tip with the port on the outer wall. Once aligned, the needle tip of the probe was sealed with silicone adhesive. It was then possible to insert or remove the fibre-optic to or from the media for measurement. The oxygen probe was connected to the Microx TX control unit that was subsequently connected to a PC where real-time oxygen concentration profiles were generated using Microx TX software. The PC also controlled the speed of rotation of the inner cylinder and the raising/lowering mechanism of the inner cylinder using Stresstech Rheologica software.

Oxygenation of the media was controlled by only allowing transfer through the upper free surface of the fluid in the annular space. This was further restricted by fitting a cap at the top of the reactor whereby air could only pass through a 150μm ring between the cap and the rotating shaft shown in Plate 8.2 (b) as (2).

8.3 Cells and Media Preparation

An immortal cell line of L929 murine fibroblasts (ECAC, Salisbury UK) was used exclusively in this study. These were initially cultured for 7 days in 75cm^3 culture flasks in an incubator maintained at 37°C and 5% carbon dioxide concentration. The media used throughout was Gibco Minimum Essential Medium containing Earles salts, L-glutamine, 10% fetal calf serum and antibiotics. After 7 days of culture the cells were removed from the culture flasks by trypsinisation in a laminar flow cabinet, centrifuged at 1250 rpm for 5 minutes and resuspended in fresh media to a volume of 16ml at a concentration of 2.5x10^5 cells/ml. This volume was then allowed to warm to 37°C in an incubator and added to CC25-R to provide a free suspension of cells. Before addition of the cell containing media, the bioreactor is flushed with 70% ethanol and then several flushes of distilled water. Prior to initialising rotation of the inner cylinder, the fluid contents were allowed to equilibrate to 37°C and a 200μl sample was withdrawn. This was used to confirm the cell concentration using a haemocytometer and the viability of the cells by flow cytometry (Chapter 9).

8.4 Reactor Operation and Oxygen Measurement

The tip of the oxygen probe was moved in through the wall of CC25-R prior to the addition of the cell containing media. The relative locations of the probe and sampling ports are shown in Figure 8.1. The tip of the oxygen sensor was located at a radial distance equivalent to the mid-point of the gap (0.5mm from the outer wall) and 1mm below the base of the annular region. One sampling port was located in the same plane but 180° from the oxygen probe, and two other ports were situated at the axial mid-point of the annulus,

again in the same plane at 180° to each other. After addition of the cell containing media the inner cylinder was gently caused to rotate by hand and then mechanically lowered into the outer cylinder using the PC software. This gentle rotation was found to prevent the formation of air bubbles on the inner cylinder as it passed into the media. The cap shown in Plate 8.2(b) was then fitted to the top of the reactor and the oxygen probe initialised to collect concentration data at a rate of 10 samples per minute that was logged by the PC. Once the oxygen concentration had equilibrated (which occurred very quickly) rotation of the inner cylinder was initiated to a prescribed speed.

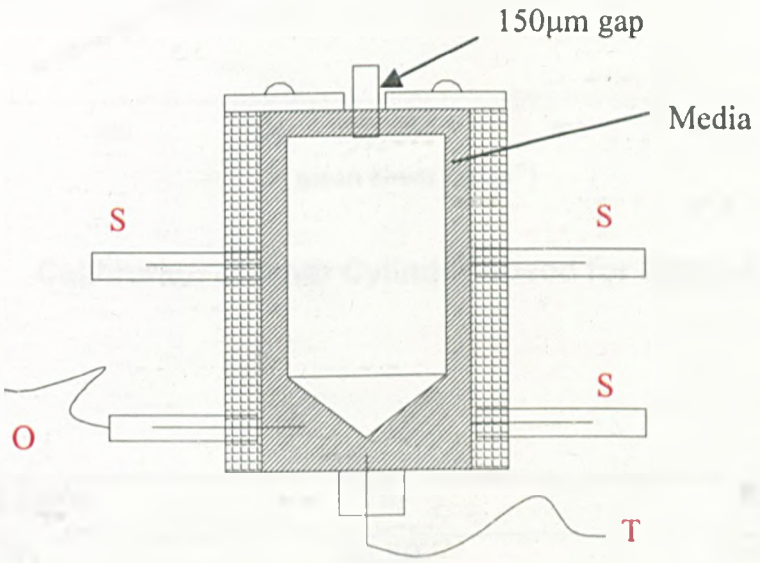

Figure 8.1 Schematic of CC-25R Bioreactor: (S) fluid sampling port; (O) oxygen measuring probe; (T) thermocouple

Rotation of the inner cylinder using the Rheologica software was based on selection of a mean shear rate in the gap that assumes linear theory. This had to be calibrated to a rotational speed which, when coupled with a knowledge of the reactor geometry and fluid kinematic viscosity, could be

converted to a Taylor number, Ta_i. The speed calibration was performed using the digital microprocessor tachometer as in Chapter 2. The calibration data is shown in Figure 8.2 and the hydrodynamic operating values used in oxygen transfer studies are shown in Table 8.1.

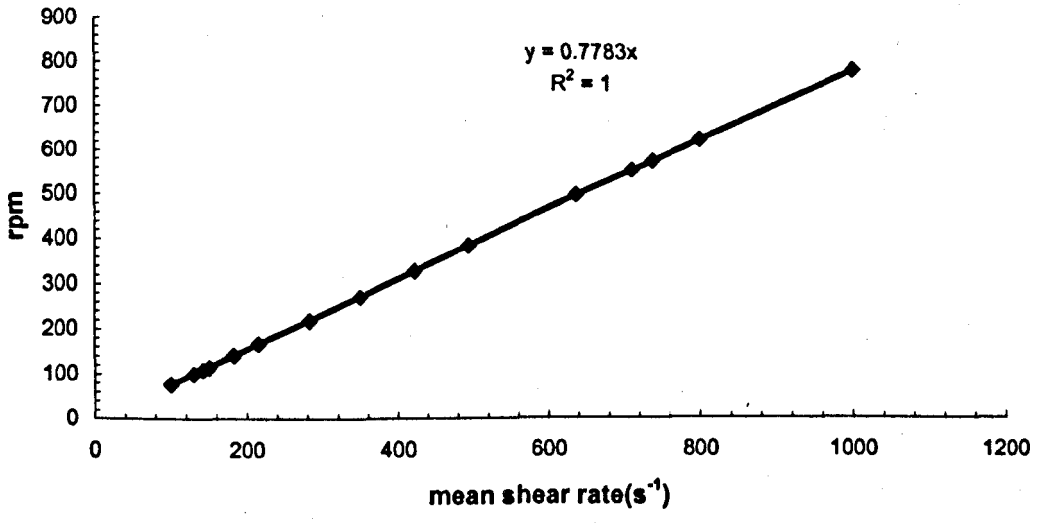

Figure 8.2 Calibration of Inner Cylinder Speed for Control of CC25-R

Speed (rpm)	Ta_i	Ro_i
77.81	28.80	101.83
100.96	37.37	132.13
116.81	43.25	152.92
155.64	57.65	203.84
311.30	115.25	407.45
389.13	144.08	509.38
466.96	172.88	611.23
778.28	288.11	1018.63

Table 8.1 Hydrodynamic Operating Parameters for CC25-R for Oxygen Transport Studies

8.5 Oxygen Concentration Profiles

Measurements of oxygen concentration in CC25-R were made over a 24h time period. As a comparison of data for the varying hydrodynamic condition presentation is made for a 16h time period. Beyond this time, in laminar Couette flow, the oxygen concentration levels were too low to make a direct comparison with other flow conditions. The initial levels of oxygen concentration in the media varied between experiments, and this would be due to the external environment, small variations in ambient temperature and atmospheric pressure, but more critically slight variations in the physico-chemical condition of the media. For this reason, to obtain meaningful comparisons between experiments, dimensionless absolute relative percentage oxygen was taken using the following formula:

$$\text{abs.rel.\% } O_2 = \frac{O_2(i) - O_2(t)}{O_2(i) - O_2(f)} \text{ x } 100 \qquad (8.1)$$

where $O_2(i)$ is the initial concentration of oxygen in the media at time zero, $O_2(t)$ is the oxygen concentration at time t, and $O_2(f)$ is the oxygen concentration measured at the end of the experiment. Oxygen concentration profiles for a range of steady Taylor number are shown in Figure 8.3. Whilst experiments were carried out over a 24h period, the data is presented for time periods of 15.75h. It is observed in laminar Couette flow that the oxygen level reaches zero at this point, so for comparative purposes only data to this time point was used for all other flows.

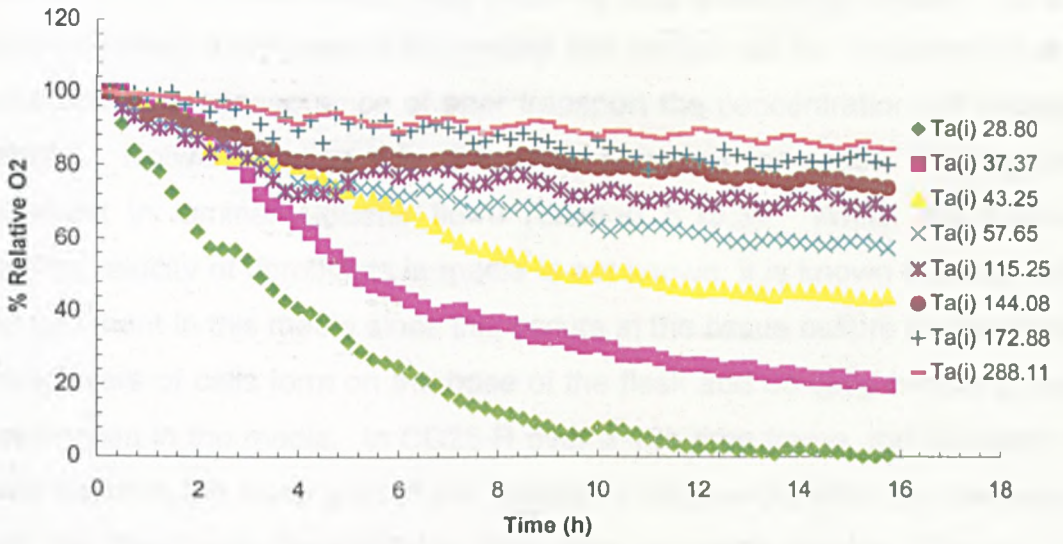

Figure 8.3 Oxygen Concentration Profiles for Freely Suspended L929 Fibroblasts at 2.50×10^6 Cells/ml Concentration

From the data of Figure 8.3 a number of facts are clearly evident. As the Taylor number increases, the oxygen concentration at the base of the reactor more closely approaches that at the free surface of the reactor (100% absolute). This implies that the enhanced hydrodynamic environment of Taylor-vortex and wavy-vortex flow better transports oxygen from the free surface at the top of the reactor down into the bulk fluid.

- *Laminar Couette Flow*

At Ta_i = 28.80, laminar Couette flow prevails. In this regime there is no axial component of velocity, only radial and azimuthal components. Oxygen transport in the radial and azimuthal directions is very good as there is significant forced convection transfer and it is assumed that near to the free surface the absolute relative % O_2 will be close to 100% for the length of the experiment. Axial transport in this flow regime is significantly limited since transport in the absence of an axial velocity component in the flow will be due to molecular diffusion and free convection only. Initially, the cells in free-suspension are assumed to be randomly distributed throughout the fluid volume and are moving in a solid body rotation in an azimuthal direction. If

viable, these cells are aerobically respiring and consuming oxygen. In the probe location at the base of the vessel, the oxygen will be consumed by the cells and as a consequence of poor transport the concentration will deplete rapidly. Notwithstanding this, the cells have an increased tendency to sediment in laminar Couette flows (Section 5.15.3). Whilst the precise settling velocity of fibroblasts in media is not known, it is known that the cells will sediment in this media since this occurs in the tissue culture flasks where monolayers of cells form on the base of the flask and no cells remain in free suspension in the media. In CC25-R over a 16h time frame, the numbers of cells found in the lower part of the reactor in laminar Couette flow increases and this has been demonstrated from flow cytometry studies (Chapter 9). Increased cell numbers in this region will further reduce the $\%O_2$.

- *Laminar Taylor-vortex flow*

From Taylor's theory, Ta_{crit} occurs at 41.8 and there is sudden transition from laminar Couette flow to Taylor-vortex flow. From the LDA data for the system CC-25 the results indicate that this is true for our system, although the transition is not as drastic; there is some gradual disturbance on approach to Ta_{crit}. Although this disturbance is very small it might well be significant in terms of gaseous transport effects. In oxygen transport studies hydrodynamic conditions just sub critical (Ta_i = 37.37) and just supercritical (Ta_i = 43.25) have been made. In the former case, there is clearly a marked improvement in the transport of oxygen over the condition for Ta_i = 28.80. This is likely due to a combination of two things. A slightly reduced effect on cellular sedimentation is likely as it observed from the LDA data for CC-25 and Ta_i = 35.07 that there is a very small upward axial velocity to counteract sedimentary effects. Secondly this slightly increased axial motion will have an improved effect on the transfer of oxygen from the free surface into the bulk of the fluid.

Transport is further enhanced in laminar Taylor-vortex flow at Ta_i = 43.25. The steady laminar Taylor vortices will significantly reduce sedimentation of cells to the base of the vessel and this will reduce consumption of oxygen in this region. The vortices do not intermix in this

flow regime so although there will be transferral of oxygen from the free surface into the bulk fluid the overall rate of transference to the base of the vessel will be still quite slow and in general, there will a depletion of the oxygen concentration over time at the measurement point.

- *Wavy-vortex flow*

Wavy-vortex flow is developed by Ta_i = 57.65 and beyond this, the amplitude and frequency of the waviness will increase. Beyond laminar Taylor-vortex flow, the problem of sedimentation of cells contributing to increased depletion of oxygen at the measuring probe is removed and oxygen consumption is entirely due to the transport of oxygen from the free surface as a function of the hydrodynamics. It is observed in general that as the Taylor number continues to increase the absolute % O_2 continues to increase over the 16h experimental time period, however it is apparent that degree of change becomes less and that there is approach to asymptotic behaviour. It is known from the LDA data that beyond about Ta_i =150 for CC-25, the shear stress exerted on cells in the fluid becomes supercritical. This means that beyond this point the viability of the cells will rapidly decrease. Once this occurs, the consumption of oxygen by cells will decrease and this will influence the oxygen concentration data; a converse situation to the cell sedimentation problem is set up. In the sedimentation problem excessive consumption of oxygen occurs due to an uneven distribution of cells in the reactor and this places bias on the transport profile. For non-viable cells there is reduced consumption. It can be concluded from this that the higher oxygen concentrations shown beyond Ta_i = 144.08 will be due to reduced cell viability and not improvement in the transfer process. Conceptually, the optimum transport should occur at around Ta_i =141 from the LDA data, when regular wavy vortex flow prevails. At this point there is both intra and inter vortex mixing to facilitate the transport process. This is the point where the asymptote for transfer is expected. The asymptote is a consequence of the limitation of transfer due to the physico-chemical arrangement imposed on the reactor at the free surface.

8.6 Free Surface Mass Transport

The transfer of oxygen in CC25-R for the arrangement shown in Figure 8.2 originates at the free surface of the fluid at the top of the reactor. Oxygen is allowed to pass through a 150μm gap around the rotating shaft. In order to quantify the transport process for the varying flow regimes, the oxygen transport across this phase boundary is the appropriate starting point.

8.6.1 Phase Equilibrium for Oxygen and Media

The phase equilibrium for the transfer of oxygen across the phase boundary is governed by the partial pressure of oxygen in the atmosphere and the Henry constant by equation (6.32). Schematically, one can think of the phase boundary at the free surface as analogous to the boundary layer shown in Figure 8.1 for the gas bubble. The Henry constant varies with temperature as shown in Figure 8.4.

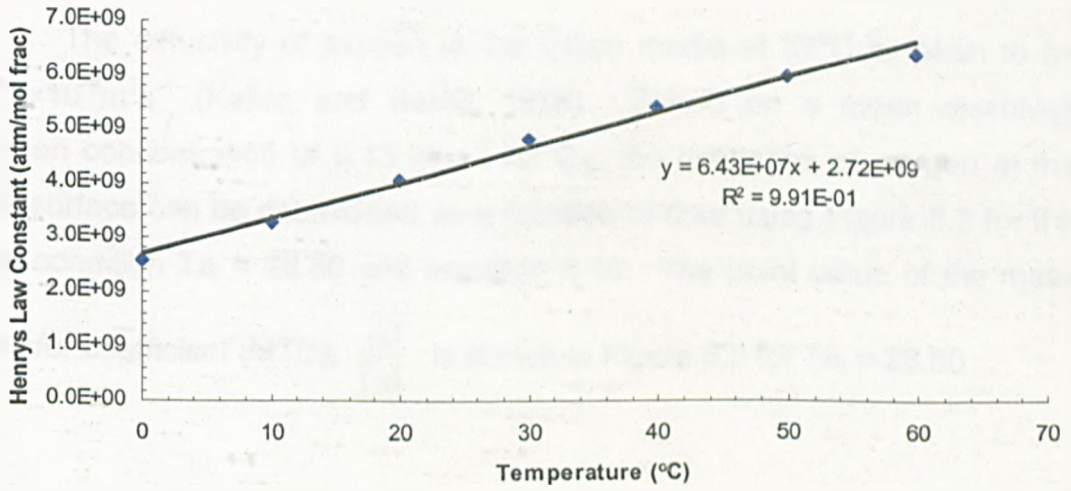

Figure 8.4 Variation of Henry Constant with Temperature for Oxygen

The media in CC25-R varied between 36.6 and 37.4°C and a mean value for H was taken as 5.06×10^9 Pa molfrac^{-1}. The partial pressure of oxygen in air is 0.2095 atm or 2.12×10^4 Pa. The density of Gibco media is 985 kgm^{-3} which results in a mean dissolved oxygen concentration of 0.13 mg per litre across the phase boundary.

8.6.2 Laminar Couette Flow

Since the fluid has a solid body rotation in Couette flow, only the upper layer of fluid is exposed to the free surface for oxygen transfer. Fluid below this layer is not directly exposed to the phase boundary and transfer into this region is only by molecular diffusion and free convection. In Section 6.3 a number of theories were presented to describe the mass transport across a phase boundary. The two-film theory is a simplistic approach and probably only has applicability for transfer to a stagnant fluid. In laminar Couette flow where a constant layer of fluid is exposed to the free surface and there is no axial disturbance, the penetration theory of Section 6.3.2 best describes the transfer process.

The diffusivity of oxygen in the Gibco media at 37°C is taken to be 1.70×10^{-9}m^{2}s^{-1} (Kallos and Behie, 1998). Based on a mean dissolved oxygen concentration of 0.13 kgm^{-3} for C_{Ai}, the mass flux of oxygen at the free surface can be determined as a function of time using Figure 8.3 for the flow condition Ta_i = 28.80 and equation 6.18. The point value of the mass transfer coefficient (MTC), $\sqrt{\frac{D}{\pi t}}$, is shown in Figure 8.5 for Ta_i = 28.80

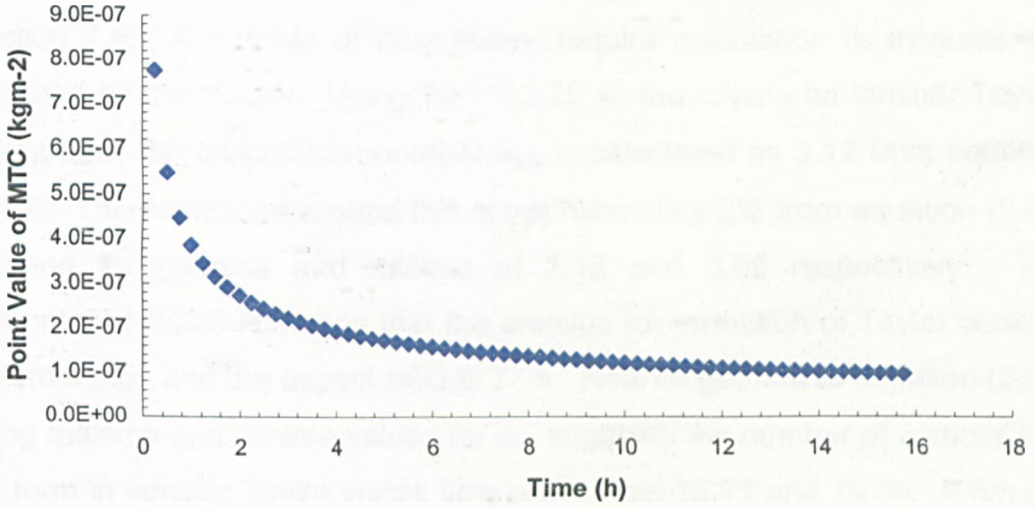

Figure 8.5 Point Value of the Mass Transfer Coefficient at Ta_i = 28.80

The mass flux over time is shown in Figure 8.6, for Ta_i = 28.80

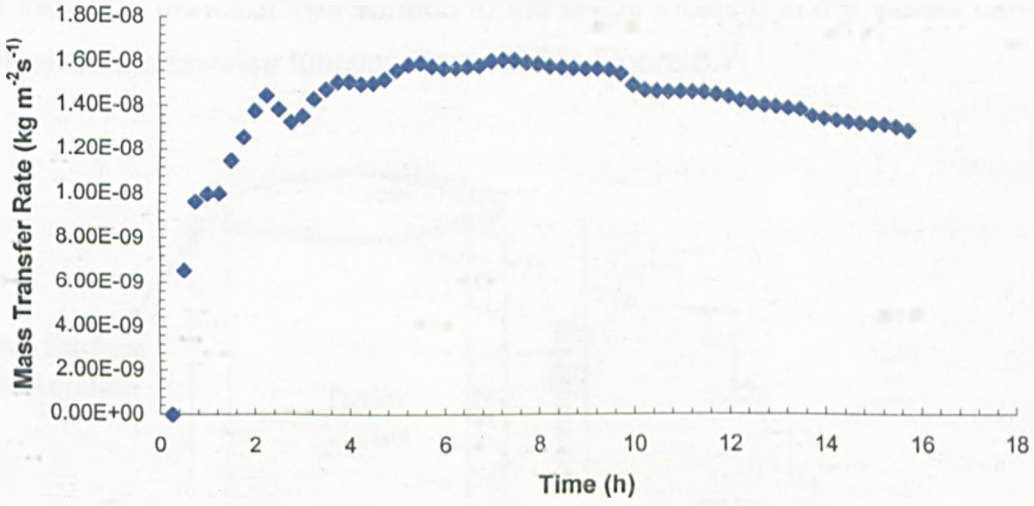

Figure 8.6 Mass Transfer Rate at Ta_i = 28.80

8.6.3 Laminar Taylor-Vortex Flow

In pure laminar Taylor vortex flow, only the top vortex is exposed to the free surface. It is known that there is poor intra-vortex mixing in this flow regime so transport only occurs by inter-vortex exchange and this is known to occur on the vortex flow boundaries (Section 7.1). Under this flow regime,

the transport can be considered as a tanks-in-series model described in Section 7.4. A number of parameters require calculation to evaluate the transport by this theory. Using Ta_i = 43.25 as the criteria for laminar Taylor-vortex flow, the critical wavenumber α_{crit} is calculated as 3.12 from equation (2.29). The fluctuation around this is approximately 2% from equation (2.49) allowing for maxima and minima of 3.18 and 3.06 respectively. The geometry of CC25-R means that the annulus for formation of Taylor vortices is 25mm high and the aspect ratio is 37.5. Rearrangement of equation (2.48) using maxima and minima values for α_{av} suggests the number of vortices that will form in laminar Taylor vortex flow is between 15.71 and 16.35. From the quantization condition that only a whole number can form it is expected that this will normally be 16 but might reach 17. This is verified in the flow visualisation images of Chapter 3. Working on the basis of 16 vortices forming, the Bodenstein number, Bo is 32 from equation (7.26). Because transport occurs on the vortex boundaries and all the vortices are identical, the transport from the free surface to the probe location in the vessel can be conceived a step-wise function illustrated in Figure 8.7.

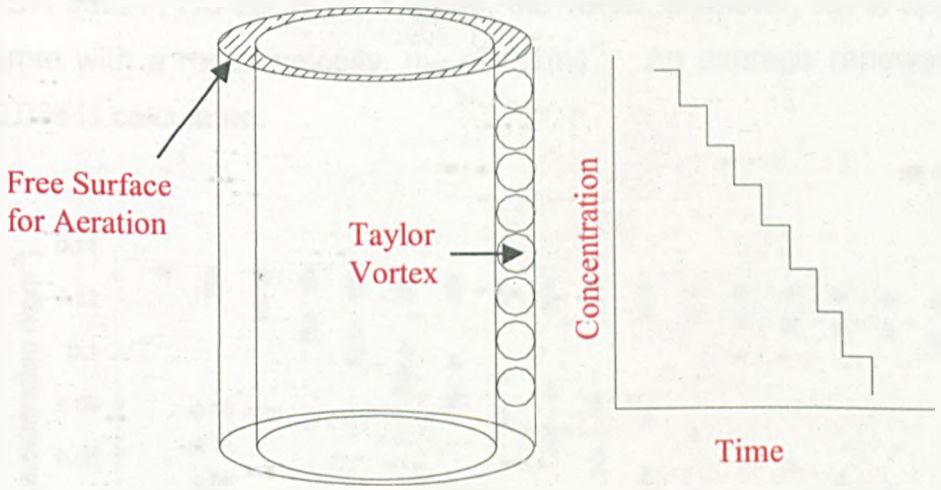

Figure 8.7 Conceptualisation of Tanks-in-Series Transport in Laminar Taylor Vortex Flow

At the free surface, elements of fluid in the upper Taylor-vortex are readily exposed to the surface due to the rotational motion of the vortex.

Free surface transport here is best described by the surface renewal theory of Section 6.3.3. Using the step-wise concept of Figure 8.7, and knowing the oxygen concentration at the free surface and at the probe (base of the vessel), the concentration at the intermediate step can be approximated at any time interval for measurement using 16 steps (Taylor-vortices) as the basis of calculation. Data are shown in Figure 8.8 for time periods of 30 min, 1h, 5h, 10h and 15h for Ta_i = 43.25. The circumferential dispersion coefficient is calculated from equation (7.27) using a vortex velocity, u_t. The value of u_t is best approximated by the azimuthal component of velocity as the magnitude of this far exceeds any of the other components. From the LDA data, the mean azimuthal velocity is taken as $0.1ms^{-1}$ for CC-25 at Ta_i = 45.058. This best approximates the laminar Taylor vortex flow for oxygen measurements in CC-25R. The dispersion coefficient, D_d is then calculated as $2.55x10^{-4}$ m^2s^{-1}. It is observed that this is approximately three orders of magnitude higher than the diffusivity of oxygen in the media. In order to evaluate the mass transfer flux using the surface renewal theory, the time of exposure of fluid elements in the top vortex requires calculation. This is probably best done as a guideline using equation (6.35). Again using the LDA data in CC-25 at Ta_i = 45.06, the vortex diameter, d_{ed} is approximately 3mm with a mean velocity, u_{ed} of $0.1ms^{-1}$. An average renewal time, t_e of 0.03s is calculated.

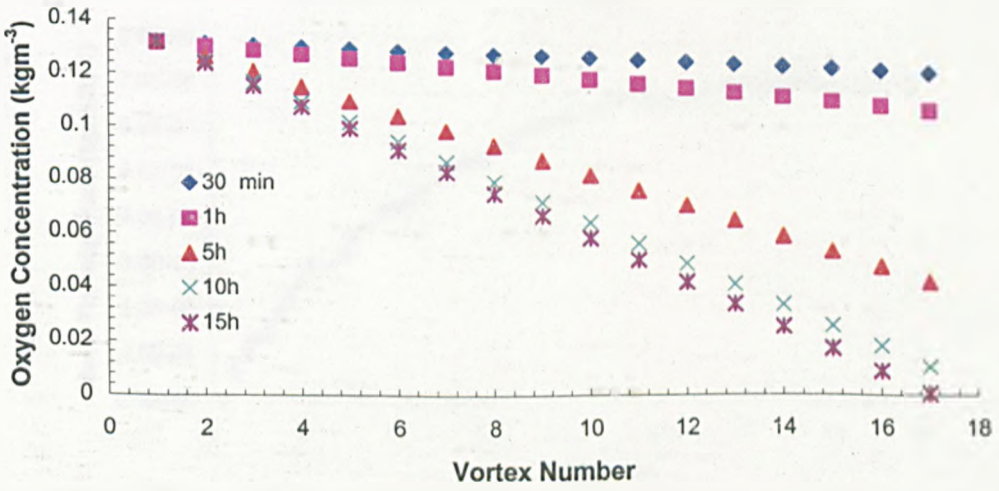

Figure 8.8 Oxygen concentration at Taylor-vortex boundaries for five different experimental times at Ta_i = 43.25

The average mass flux predicted by equation (6.19) only accounts for the diffusivity of oxygen in the media, and takes no account of further dispersion by the fluid motion. This motion will further enhance the flux, so modification of equation (6.19) should be made to account for this and is given by equation (8.2) here.

$$(J_A)_{av} = 2(c_{Ai} - c_{Ao})\sqrt{\frac{D + D_d}{\pi t_e}} \qquad (8.2)$$

The calculation suggests that for a fixed flow regime there will be a constant flux from the free surface for a given bulk concentration of oxygen, c_{Ao}. Flux calculations are shown in Figure 8.9 accounting for diffusivity only (D) and for diffusivity and dispersion ($D + D_d$).

It is observed from comparison of Figure 8.9 to Figure 8.6 that the magnitude of the transfer rate is significantly increased by virtue of the hydrodynamics in laminar Taylor-vortex flow to laminar Couette flow. When taking account of diffusivity alone, the Taylor-vortex flow provides a transfer rate that is three orders of magnitude higher 8.9(a) and when dispersion effects are additionally considered this grows to around six orders of magnitude higher.

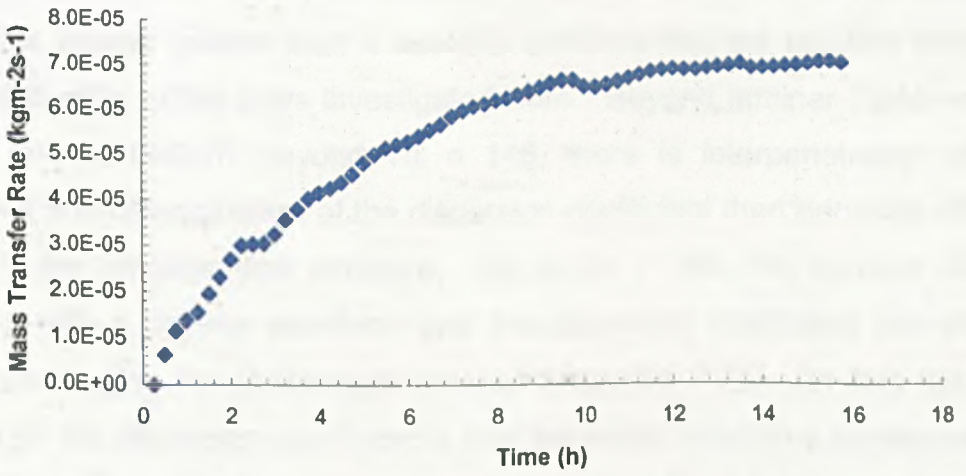

(a)

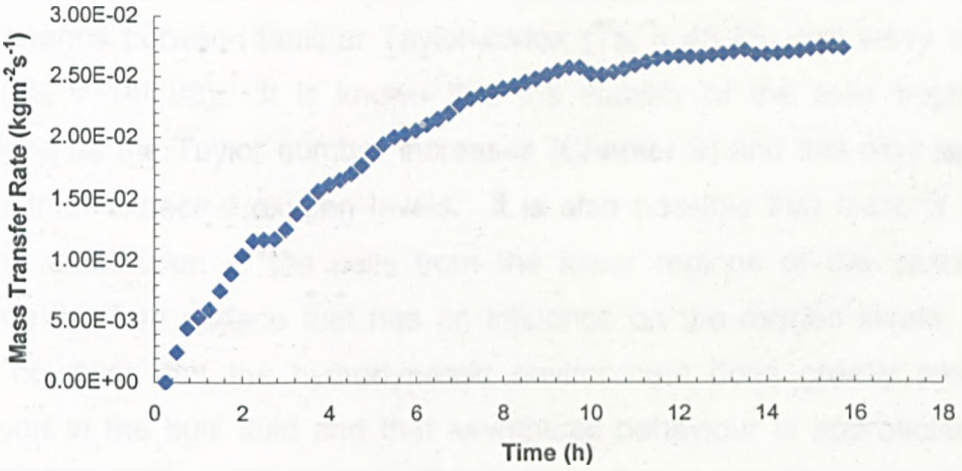

(b)

Figure 8.9 Mass Flux of Oxygen in Laminar Taylor-vortex Flow with Diffusivity (a) and Diffusivity and Dispersion (b)

8.6.4 Wavy Vortex Flow

Whilst the random surface renewal theory of section 6.3.4 might better describe the free surface transport in wavy-vortex flow conceptually, there is little difference in the mathematical theory to provide anything further quantitatively than the regular surface renewal theory. It is noted that from the film penetration theory of section 6.3.5, the value of L^2/Dt in equation (6.27) is always greater than π and this confirms that the two-film theory is not applicable to the flows investigated here. Beyond laminar Taylor-vortex flow, and particularly beyond Ta_i = 145, there is interpenetration of the vortices and determination of the dispersion coefficient then becomes difficult due to the irregular flow structure. Up to Ta_i = 145, the vortices remain unique with a definite waveform and the dispersion coefficient can still be evaluated using the Bodenstein number (equation 7.25). In fact the only effect on the dispersion coefficient is that the vortex velocity u_t increases with increasing Ta_i. Similar calculations to those for Ta_i have shown that the transfer rate for oxygen increases but at a progressively slower rate for supercritical Ta_i. This is not really in keeping with the observations of Figure

8.3, where there is still a significant difference in the levels of oxygen maintenance between laminar Taylor-vortex (Ta_i = 43.25) and wavy vortex flow (Ta_i = 144.08). It is known that the viability of the cells begins to decrease as the Taylor number increases (Chapter 9) and this may lead to higher than expected oxygen levels. It is also possible that there is more uniform distribution of the cells from the lower regions of the vessel up towards the free surface that has an influence on the oxygen levels. It is clear however that the hydrodynamic environment does greatly promote transport in the bulk fluid and that asymptotic behaviour is approached for optimal transport. What is clear in this study is that over time, the oxygen concentration is falling, suggesting that consumption by cells in general exceeds supply. However. the system has been designed to reduce the supply and maximise the consumption as a baseline to see how this can be influenced by the hydrodynamics, so this is not surprising. The dispersion coefficient, D_d for varying Ta_i is shown in Figure 8.10. This is based on equation (7.27) and the LDA for u_t.

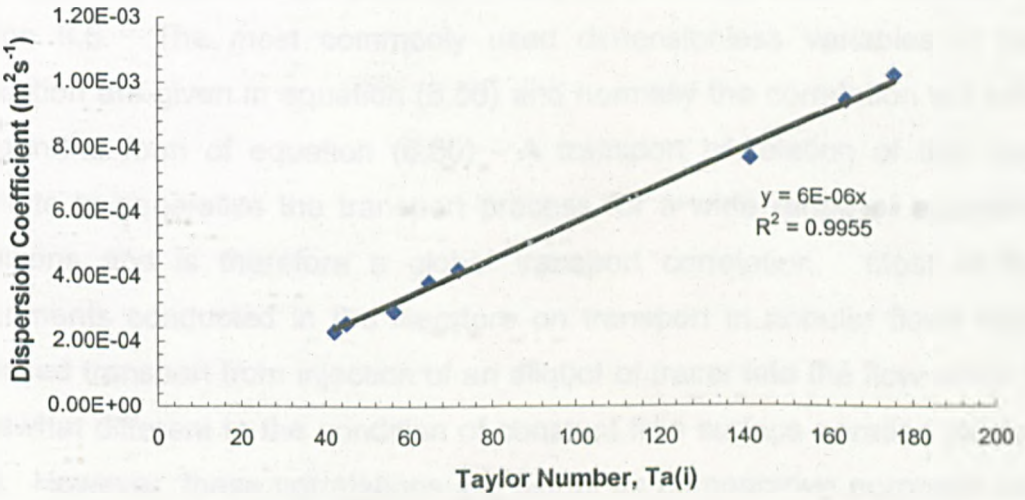

Figure 8.10 Variation of dispersion coefficient D_d with Ta_i in CC25-R

Whilst equation (7.28) allows for varying geometry and fluid physical properties it is concluded from this study that a linear relationship does exist between D_d and Ta_i.

The limitations on using D_d are that the vortices are not unique beyond about Ta_i = 145. In such circumstances mass transfer coefficient based on the local nature of the flow is more appropriate. The general approach to the problem has been outlined in section 7.3 and the appropriate form of the equation to use is (7.17). This requires a suitable general mass transfer correlation for the flow of a form like equation (7.16). This type of correlation is dependent on the type of system used and is best determined from experimental data.

8.7 General Mass Transfer Correlation

The mass transport of gases and solutes in bioreactors is driven by the processes of molecular diffusivity, free convection transfer and (where a fluid flow prevails) forced convection transfer. The latter of these is often several orders of magnitude greater than the former two, and the transport process can essentially be evaluated on the basis of a forced convective transfer correlation alone for this reason. This correlation is based on dimensionless variables to allow for scale-up and has been discussed in section 6.6. The most commonly used dimensionless variables in the correlation are given in equation (6.56) and normally the correlation will take the general form of equation (6.60). A transport correlation of this type attempts to generalise the transport process for a wide range of operating conditions and is therefore a global transport correlation. Most of the experiments conducted in the literature on transport in annular flows have assessed transport from injection of an aliquot of tracer into the flow which is somewhat different to the condition of constant free surface aeration studied here. However, these correlations are useful as comparative purposes and can serve as guidelines for future solute transport studies. A number of such correlations were presented in section 7.4.

It is clear that the definition of the dimensionless variables is important and in general these operate from the basis of a selected geometry of the reactor. This basis must be maintained for all the dimensionless variables. In this study, the Reynolds number, Re_i has been defined by equation (2.22)

where $\Omega_o = 0$. The equivalent Taylor number, Ta_i is determined using Figure 3.6. On this geometric basis, the Sherwood number is defined as

$$Sh = \frac{(r_o - r_i)k_l}{D} \tag{8.3}$$

The Schmidt number, Sc, has no geometric components and is defined by equation (7.2b). In the transport correlation, Re_i and Sc can be readily determined for the given flow regime. In order to evaluate Sh, the mass transfer coefficient needs to be known for the given flow. Once this is established for a range of flows, the transport correlation can be developed.

8.7.1 Global Mass Transfer Coefficient

To this point, the mass transfer coefficient (k_g) has been calculated on the basis of the free surface oxygen transport and this has been assumed to be equally valid in the bulk fluid. This is really only true for a stagnant fluid but can be applied in the case of laminar Couette flow where axial transport is due to diffusion and free convection alone. Beyond laminar flow, it is necessary to establish a mean mass transfer coefficient in the bulk fluid (k_l) which accounts for forced convective transport due to the hydrodynamics that can be used to calculate experimental Sherwood numbers and subsequently formulate a mass transport correlation for the process. In establishing mean liquid phase mass transfer coefficients for given regimes of flow, a number of assumptions must be firstly made:

- Laminar Couette flow provides a datum level with respect to axial mass transport as a consequence of the hydrodynamic environment. In this regime it is assumed there is no forced convective transport axially.
- It is assumed that consumption of oxygen by cells throughout the bulk fluid is constant.
- At time 15.75h in laminar Couette flow the absolute oxygen concentration has reached zero (Figure 8.3). For other more agitated

regimes of flow at this time point, the oxygen concentration is higher. This is assumed to be due to enhanced mass transport by forced convection alone.

- The relative increase in the concentration of oxygen at time 15.75h relative to Couette flow is assumed to be directly proportional to the relative increase in the liquid phase mass transfer coefficient, k_l.

Using these assumptions, a mean mass transport coefficient in the liquid phase, k_l can be assigned for any of the flow regimes of Figure 8.3 once a mean transfer coefficient has been assigned to the laminar Couette flow condition. In Figure 8.3, the oxygen profile for this condition closely approximates an exponential decay and for this reason an average overall transfer coefficient, k_la' is calculated using equation (6.41). The average overall transfer coefficient is evaluated as $5.96 \times 10^{-5} m^2 s^{-1}$. The interfacial area available for oxygen transport in CC-25R per unit volume of fluid at the free surface, a' is $0.212 m^{-1}$. An average mass transfer coefficient in laminar Couette flow is then $2.81 \times 10^{-4} ms^{-1}$.

Re	101.68	132.24	152.62	203.56	407.32	509.19	611.07	1018.59
Ta	28.76	37.40	43.17	57.57	115.21	144.02	172.83	288.10
$\%O_2$ (15.75h)	31.9	53.2	73.1	74.2	75.6	80.2	91.4	93.2
$\frac{\%O_{2(Re)}}{\%O_{2(Re=101.68)}}$	1	1.67	2.29	2.33	2.37	2.51	2.87	2.92
k_l (E-04)	2.81	4.69	6.45	6.55	6.67	7.07	8.06	8.22

Table 8.2 Average mass Transfer Coefficients (ms^{-1}) for Varying Regimes of Flow in CC-25R

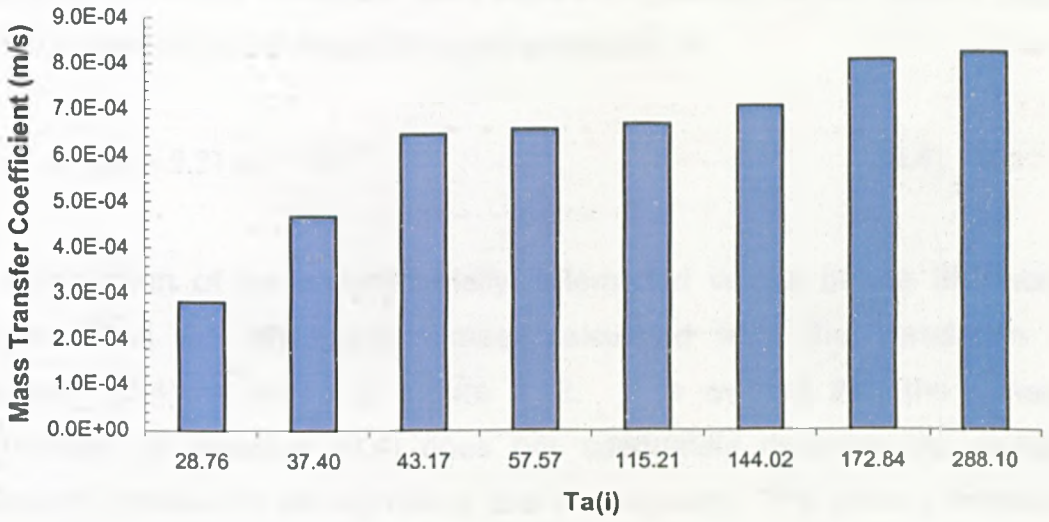

Figure 8.11 Variation of Average Mass Transfer Coefficient with Ta_i in CC-25R

As a guideline, Bailey (1986) suggests mass transfer coefficients for large and small bubbles are $4.0x10^{-4}$ and $1.0x10^{-4}ms^{-1}$ respectively. The experimental data of this study for free surface aeration and varying flow regime in Figure 8.11 has coefficients of the same order of magnitude. Using the data of Figure 8.11, the dimensionless parameters used to formulate the transport correlation are shown in Table 8.3.

Sh	Sc	Re_i
165.47	588.24	101.68
276.01	588.24	132.24
379.58	588.24	152.62
385.35	588.24	203.56
392.40	588.24	407.32
416.40	588.24	509.19
474.39	588.24	611.07
483.63	588.24	1018.59

Table 8.3 Dimensionless Transport Parameters for CC-25R

Applying a multiple non-linear least squares regression to the data of Table 8.3, the general global mass transport correlation is:

$$Sh = 9.21\,Re^{0.28}\,Sc^{0.33} \qquad (8.4)$$

A comparison of the experimentally determined values of the Sherwood number and the Sherwood number calculated from the correlation of equation (8.4) is shown in Figure 8.12. It is evident that the general correlation of equation (8.4) does not adequately describe the oxygen transport process for all regimes of flow investigated. The primary transition from laminar Couette flow to laminar Taylor-vortex flow occurs at approximately Re_i = 150. When this transition is applied to Figure 8.12 it is apparent that separate correlations might better represent the transport process; (1) for laminar Couette flow and (2) beyond the onset of vortex flow. These are shown in Figure 8.13 and are given by

$$Sh = 0.36\,Re^{0.50}\,Sc^{0.63} \qquad \textit{laminar Couette flow} \qquad (8.5)$$

$$Sh = 15.22\,Re^{0.16}\,Sc^{0.37} \qquad \textit{vortex flow} \qquad (8.6)$$

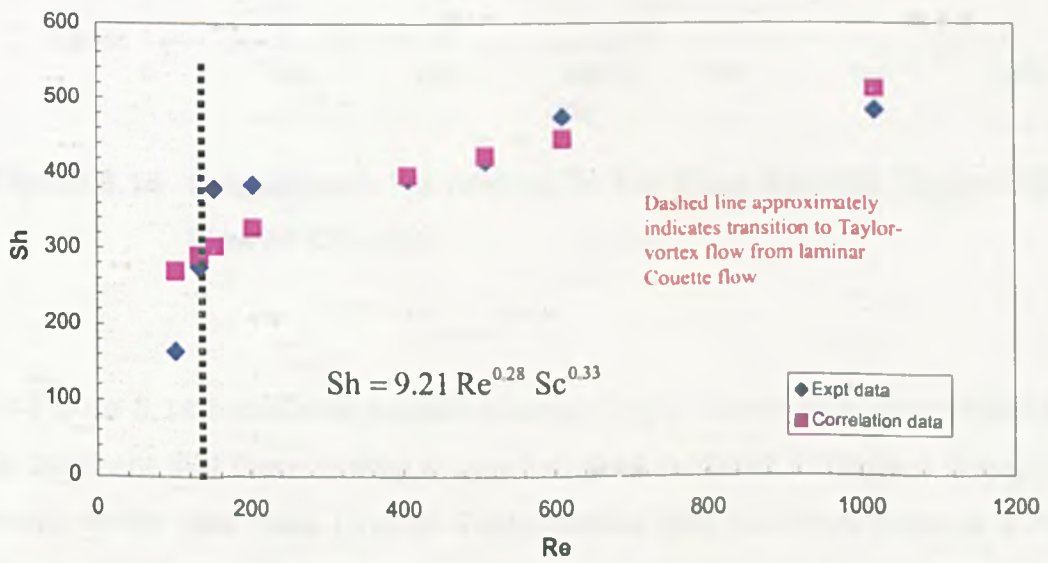

Figure 8.12 Comparison of Experimental Sherwood Number and that obtained from equation (8.4) in CC-25R

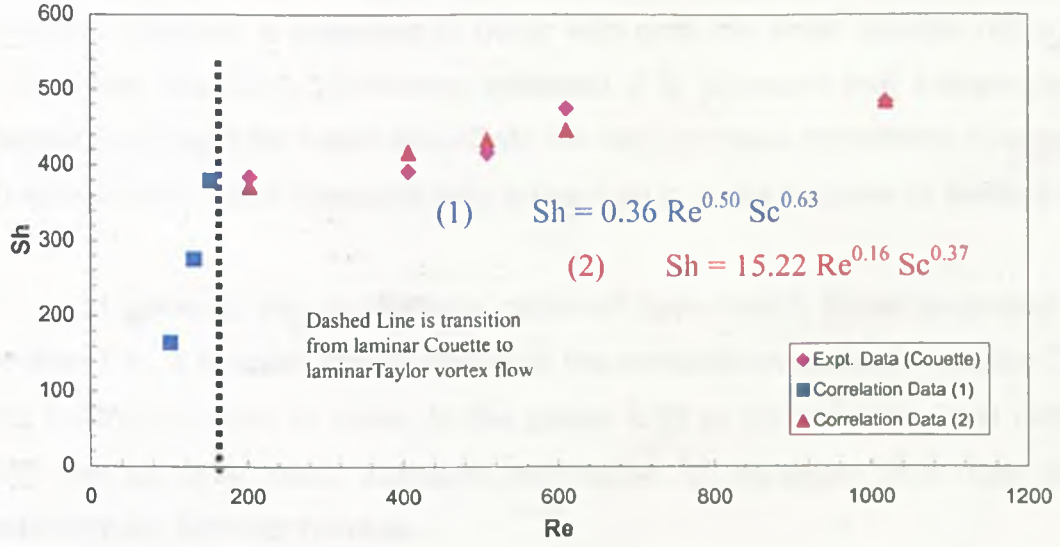

Figure 8.13 Independent Transport Correlations for Couette and Vortex Flow Regimes in CC-25R

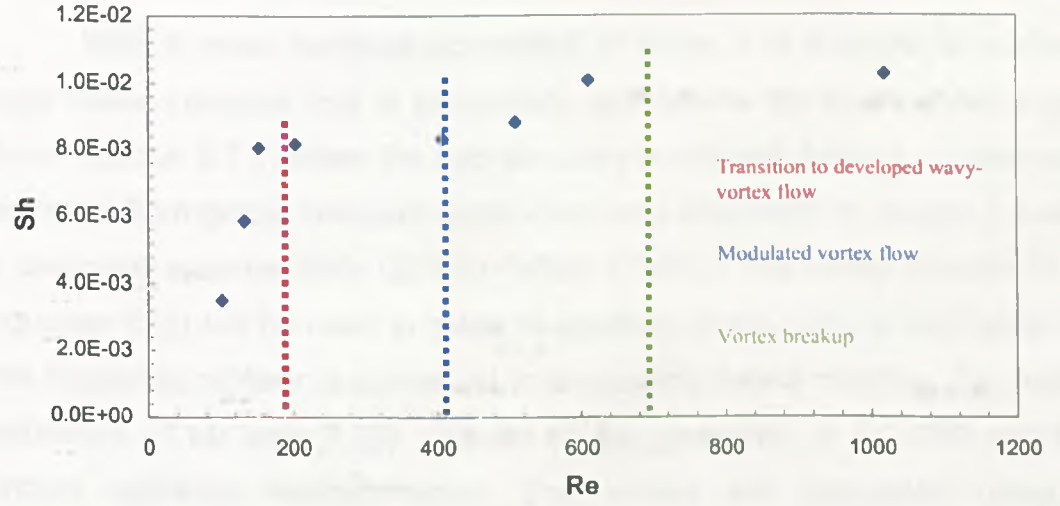

Figure 8.14 Subsequent Transitions in the Flow Beyond Taylor-Vortex Flow in CC-25R

In Figure 8.14 transitions beyond laminar Taylor vortex flow are indicated. It is apparent that there is only a very marginal increase in oxygen transport in wavy-vortex flow from laminar Taylor-vortex flow however there is a more discernible increase in transport when modulated wavy-vortex flow ensues. In this condition secondary vortices form and interpenetrate the primary vortex structure so an increase in the axial transport process would be

expected. Beyond vortex break-up, turbulent vortex flow ensues where maximal transport is expected to occur with only the inner cylinder rotating. With these transition boundaries indicated it is apparent that independent correlations might be better developed for each of these transitions, however to achieve this, more transport data is required in these regimes to verify this.

In general, the correlations obtained here match those proposed in section 7.4. It is noted that in almost all the correlations quoted in section 7.4 the Schmidt number is raised to the power 0.33 or thereabouts. It is noted that the general mass transport correlation of equation (8.4) has this exponent for Schmidt number.

8.7.2 Local Mass Transfer Coefficient

With a mass transport correlation in place, it is possible to address local mass transport that is particularly appropriate for supercritical vortex flows (section 8.7.4) when the fluid structure is not well defined. Local mass transport from global transport correlations was discussed in section 7.3 with a particular example from Gu and Fahidy (1984). The vortex correlation of equation (8.6) will be used in place of equation (7.16). In the first instance, the Reynolds number is converted to a modified Taylor number, Ta_m using equations (7.14) and (7.15). Based on the geometry of CC-25R and the known operating hydrodynamics Ta_m values are calculated using a calculated value of $\Theta = 1.063$. Ta_m and Ta_i are compared against Re_i in Figure 8.15. The transport correlation of equation (8.6) is then,

$$Sh = 26.64\ Ta_m^{0.14} Sc^{0.33} \qquad \textit{(Vortex)} \qquad (8.7)$$

A time averaged and space averaged local mass transfer coefficient in the vortex regime is best expressed as

$$\overline{K} = \frac{26.64\,\nu}{(r_o - r_i)}\,Ta_m^{0.14}\,Sc^{0.33} \qquad \textit{(Vortex)} \qquad (8.8)$$

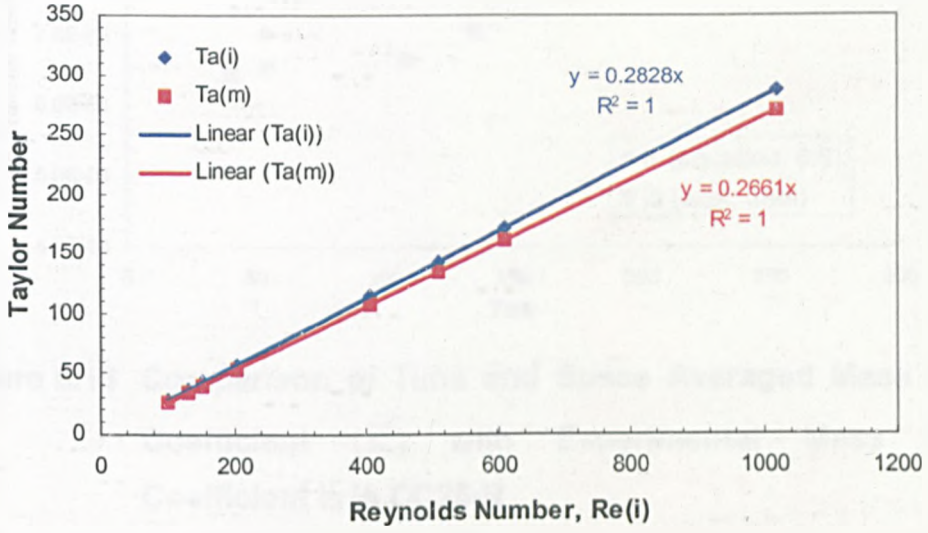

Figure 8.15 Comparison of Ta_i and Ta_m with Re_i for CC25-R

Calculated values of $\overline{K}$ are shown in Figure 8.16 in comparison to the experimentally determined mean values of the mass transfer coefficient k_l for the vortex flow regime. It is apparent that a space and time averaged mass transfer coefficient obtained using equation (8.8) reasonably approximates the measured mass transfer coefficients, but that independent correlations for the changing flow regime as suggested by Figure 8.13 will provide greater accuracy.

Equation (6.36) provides an alternative and simpler approach to estimating a time and space averaged mass transfer coefficient accounting for a simplified vortex flow structure. Values for the root mean square velocity, u_{rms} and the eddy diameter can be estimated using a combination of the LDA data and flow visualisation images for CC-25. These values are summarised in Table 8.4:

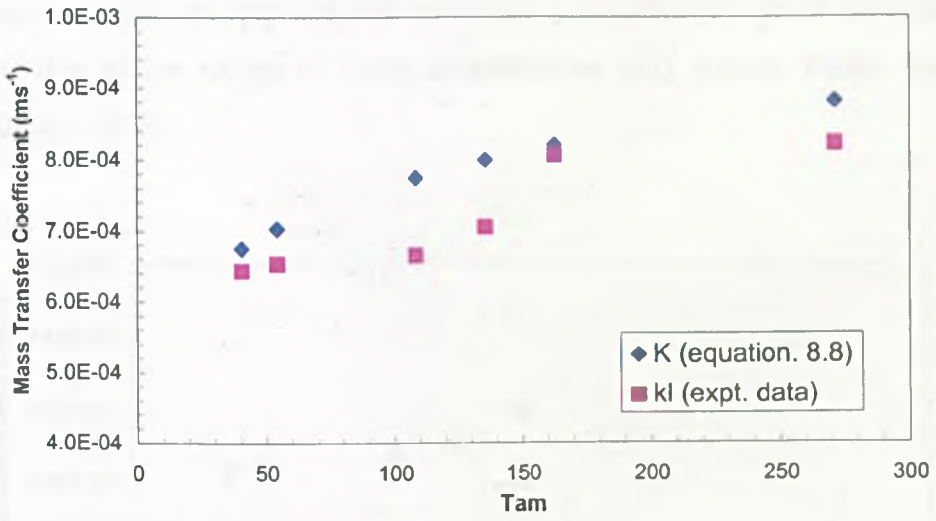

Figure 8.16 Comparison of Time and Space Averaged Mass Transfer Coefficient ($\overline{K}$) with Experimental Mass Transfer Coefficient k_l in CC25-R

Re	u_{rms} (ms^{-1})	d_{ed} (m)
101.68	0.07	0.003
132.24	0.1	0.0015
152.62	0.15	0.0015
203.56	0.16	0.0015
407.32	0.2	0.0015
509.19	0.28	0.002
611.07	0.43	0.0025
1018.59	0.7	0.0025

Table 8.4 Estimated values for u_{rms} and d_{ed} for Equation (6.36) using experimental data from flow visualisation and LDA studies

Using the data of Table 8.4 in equation (6.36) a time and space averaged mass transfer coefficient can be calculated. This is compared to the experimentally determined values of the mass transfer coefficient for varying

flow regime in Figure 8.17. Using approximated values for u_{rms} and d_{ed} it is observed that equation (6.36) provides a reasonably good estimation of k_l over the whole range of flows investigated and seems better suited than equation (8.8).

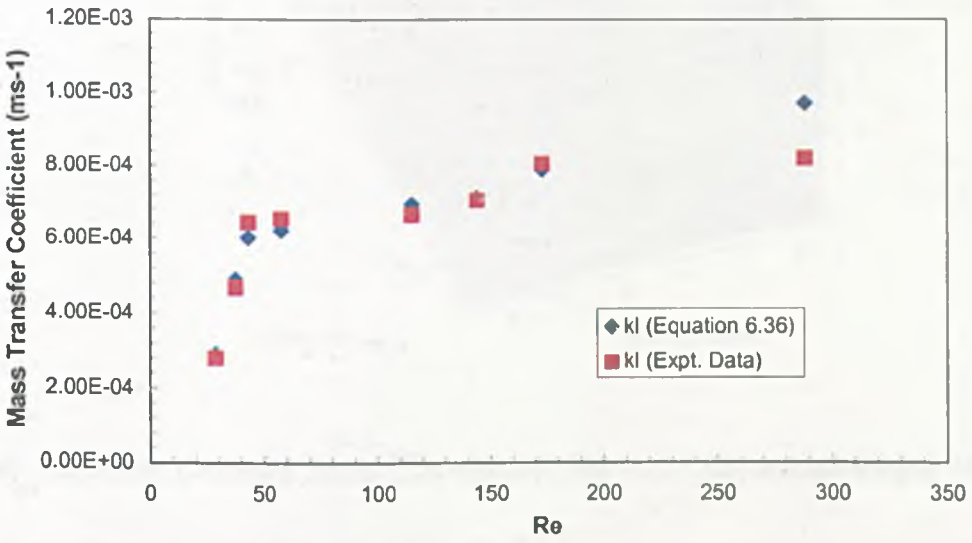

Figure 8.17 Comparison of Experimentally Determined Mass Transfer Coefficients and those Calculated by Equation (6.36)

Whilst a space and time averaged mass transfer coefficient is useful from a practical viewpoint it is known that the mass transfer coefficient will vary in time and space. In the simplest case, this can be evaluated assuming that Ficks second law (equation 6.14) holds, and that the boundary conditions are constant 100 abs.% at the free surface and follow the oxygen concentrations of Figure 8.3 at the oxygen probe boundary. Equation (6.14) has been solved numerically using these boundary conditions assuming that consumption of oxygen is constant for all regimes of flow and is accounted for in the lower boundary conditions. The results of the numerical simulations are shown in Figure 8.18.

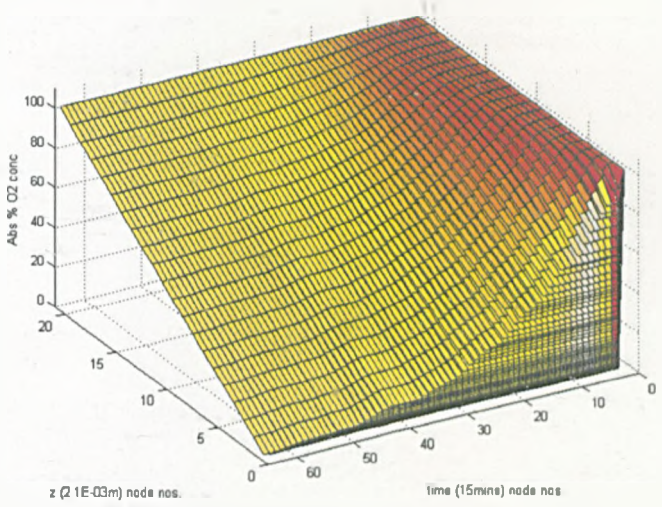

(a) Laminar Couette Flow (Ta_i =28.80; Re =101.68; mean shear 100s^{-1})

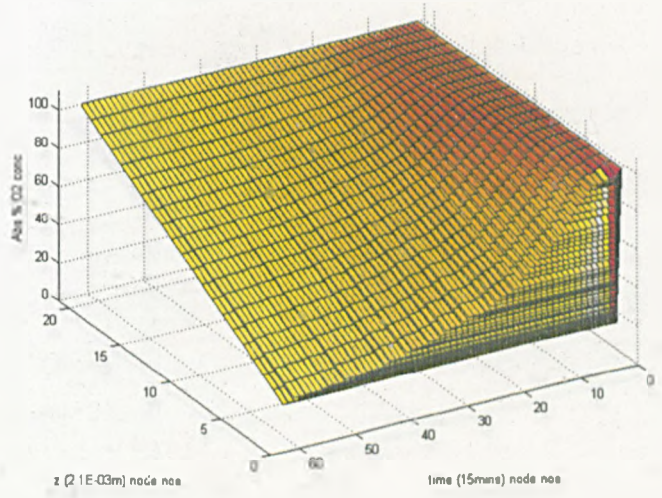

(b) Just approaching LTVF (Ta_i =37.40; Re = 132.24; mean shear 130s^{-1})

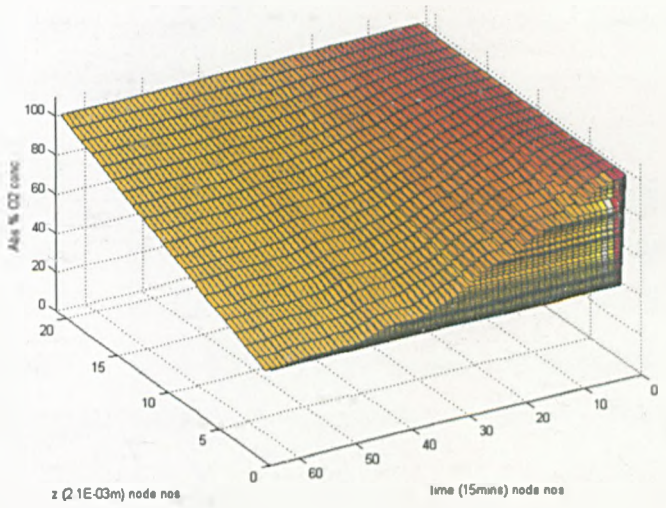

(c) Laminar Taylor Vortex Flow (Ta_l =43.17; Re =152.62; mean shear 150s^{-1})

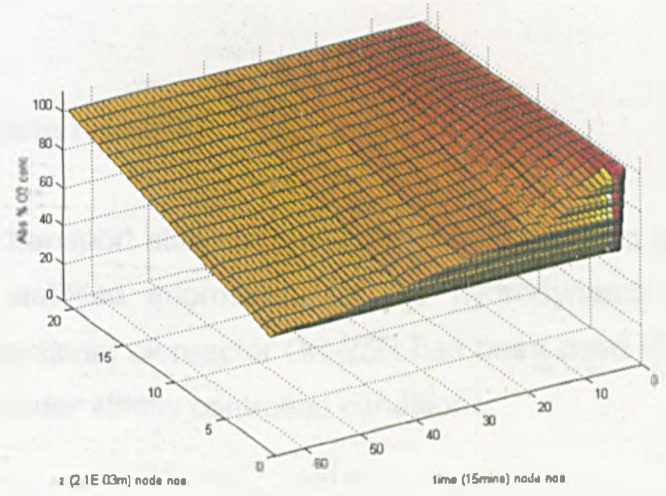

(d) Mild Wavy-Vortex Flow (Ta_l = 57.57; Re = 203.56; mean shear 200s^{-1})

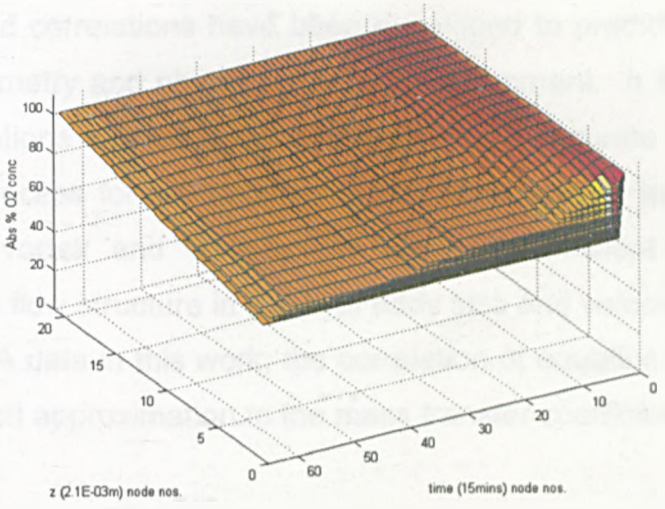

(e) Wavy-Vortex Flow (Ta_i = 144.02; Re = 509.20; mean shear 500s^{-1})

Figure 8.18 Numerical simulation of oxygen transfer process based on Ficks second law (equation 6.14)

8.8 Concluding Remarks

Oxygen transport studies have been conducted in a system based on CC-25 where detailed information on the hydrodynamic environment is known. The functional bioreactor CC-25R has been used to provide oxygen transport data under strictly controlled conditions:

- Temperature 36.7°C → 37.3°C
- Free surface aeration through a 150μm
- Cell concentration 2.5x10^5 cells/ml
- Media conditions
- Hydrodynamic regime

The data obtained has clearly shown that the hydrodynamic environment can be used to influence the transport of oxygen in the bulk fluid of the reactor. The transport process improves with an enhanced hydrodynamic environment and correlations have been developed to predict this based on the system geometry and physico-chemical environment. It is apparent that different correlations can be used to provide more accurate information on the transport process for the regimes of flow investigated, laminar Couette, laminar Taylor-vortex and wavy-vortex flow. If sufficient information is available on the flow structure in terms of eddy size and velocity, such as that provided by LDA data in this work, the correlation of equation (6.36) appears to provide a good approximation to the mass transfer coefficient.

Chapter 9

Flow Cytometry

9.1 Introduction

An immortal cell line of L929 murine fibroblasts were exposed to well defined hydrodynamic conditions in the CC-25R bioreactor described in Chapter 8. The media composition, temperature and oxygenation were carefully controlled and the initial concentration of cells was maintained at $2.5x10^5$ cells/ml in a 15.9ml fluid volume in the bioreactor. With a well defined hydrodynamic and mass transport environment it remained to investigate how the viability of the freely suspended cell culture would be influenced by the changing flow regime and the time of exposure to this flow regime. This has been determined using the technique of flow cytometry.

9.2 Flow Cytometry

Flow Cytometry is a technology developed in the 1970's that allows the simultaneous measurement of multiple physical characteristics of a single cell. Cells contained in a fluid media are hydrodynamically focussed such that they pass through a laser measurement section in single file at a high speed (500 to 4000 cells per second). A focussed laser beam is directed at

the cells and on the basis of scattered light from the cells (or emitted fluorescence) it is possible to establish some important parameters

- Relative size (forward scattered light, FSC)
- Relative granularity or internal complexity (side scattered light, SSC)
- Relative fluorescence intensity (FL1, FL2 or FL3)

Forward scattered light is diffracted at low angles between 1 and 10 degrees and is generally proportional to the cell size. It is directed along the axis of incident light in the forward direction (Figure 9.1). Side scattered light is reflected at high angles and is proportional to the cell granularity and is detected at 90° to the incident light axis.

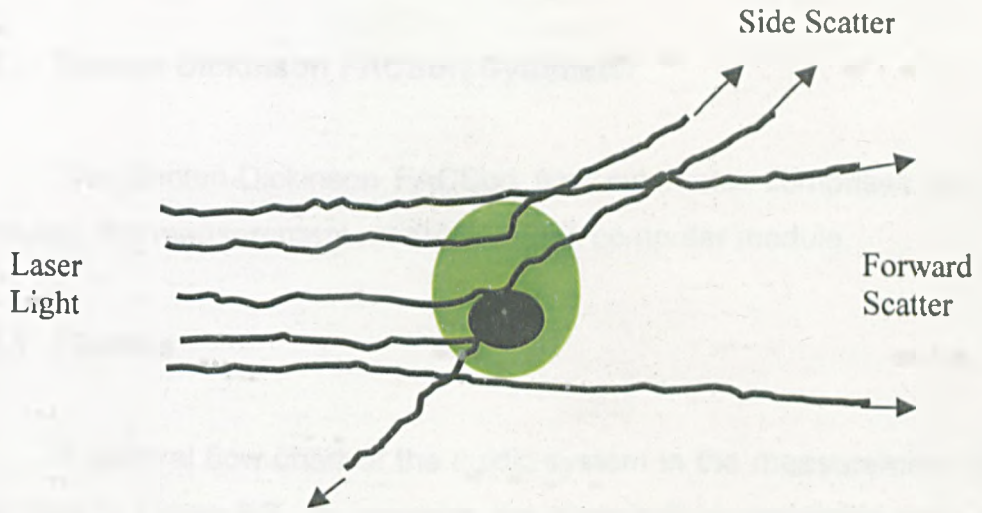

Figure 9.1 Forward and Side Scatter from Cells in Flow Cytometry

To function correctly the flow cytometer needs a combined system of fluidics to introduce and restrict the cells for analysis, optics to provide an excitation source and collection of scattered light, and electronics to convert the optical signals to digital information for quantitative assessment. The system used in this study is a Becton Dickinson FACSort flow cytometer.

The flow cytometer often takes the acronym FACS for fluorescence activated cell sorter, and modern flow cytometers have a historical development from the primitive form of blood cell counter developed by Coulter (1956). Kamentsky (1965) developed a spectrophotometer that measured and recorded the scatter and absorbtion of UV light from cells flowing at a rate of 500 per second.
Dittrich and Gohde (1969) described a flow chamber where fluorescence intensity histograms could be generated based on ethidium bromide fluorescence of fixed cells. Van Dilla (1969) reported the development of the first fluorescence detection cytometer the used hydrodynamic focussing with the flow, illumination and detection all orthogonal to each other. With an Argon laser source, this formed the basis of the modern flow cytometers. Herzenberg (1976) used a similar cytometer to detect fluorescent staining of the DNA of Chinese Hamster Ovary (CHO) cells and their system was in essence the first Becton-Dickinson FACSort instrument.

9.3 Becton Dickinson FACSort Cytometer

The Becton-Dickinson FACSort flow cytometer comprises two basic modules, the measurement module and the computer module.

9.3.1 Fluidics

A general flow chart of the fluidic system in the measurement module is shown in Figure 9.2. In essence, the sample fluid containing cells is held in the sample FACS test tube (1) and is allowed to flow into the measurement assembly (2) at a controlled flow rate.

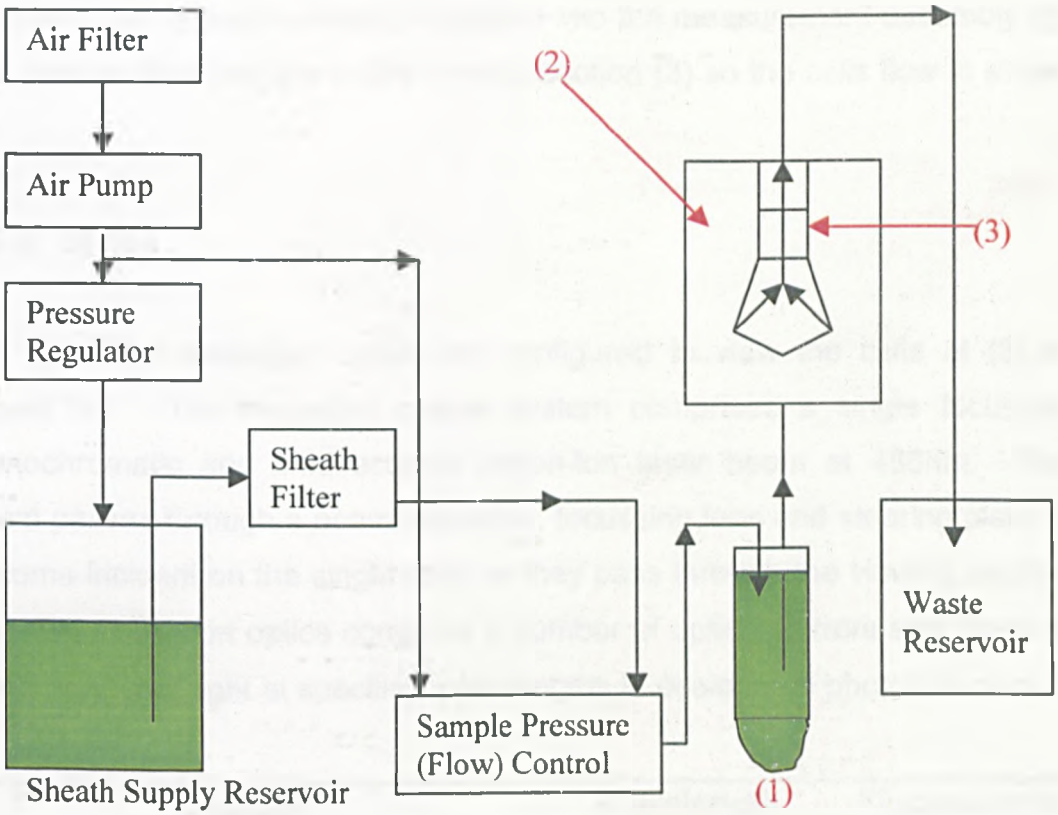

Figure 9.2 FACSort Fluidic System

The flow of sample fluid is initiated by an air pump and the flow is controlled by pressure regulation. The sheath fluid is isotonic saline and is pressurised at 4.5 psig. The sheath fluid is held in reservoir and acts as a supporting vehicle for directing particles through the measurement system. The sheath fluid is filtered top remove extraneous particles and then directed to the measurement assembly (2). The sample fluid containing the cells for investigation is held in a small FACS plastic tube. The tube fits into a tight seal around an O-ring on a manifold (1). A narrow tube runs from the manifold down to the base of the tube and a pressurised air delivery pushes the cell containing fluid out of the tube and into the measurement section (2). For low-pressure flows of the sample, the flow rate is 12µl per min at 4.6 psig air delivery pressure. For medium pressure it is 35µl per min and 4.8 psig and for high pressure it is 60µl per min at 5.0 psig. High-pressure flow is used exclusively in this work. The differential pressure between the sheath fluid and the sample fluid, coupled with a converging pipe section, allows the

sample to be hydrodynamically focussed into the measurement assembly (2) and laminar flow prevails in the viewing section (3) so the cells flow in single file.

9.3.2 Optics

The excitation optics are configured to view the cells at (3) in Figure 9.2. The excitation optical system comprises a single focussed monochromatic and unidirectional Argon-ion laser beam at 488nm. The beam passes through a beam expander, focussing lens and steering plate to become incident on the single cells as they pass through the viewing section (3). The collection optics comprise a number of optical mirrors and filters to direct scattered light at specified wavelengths to designated photodetectors.

Detector	Wavelength Band (nm)	Fluorescence Channel
Fluorescein-Isothiocyanate (520nm) (FITC) *green*	$515 < \lambda < 545$	FL1
Phycoerytherin (585nm) (PE) *orange*	$564 < \lambda < 606$	FL2
Peridinin Chlorophyll α Protein (677nm) (Per_CP) *red*	$650 < \lambda$	FL3

Table 9.1 Wavelength Filter Bands for 90° Scattered Fluorescence

The collection system is configured to detect forward scattered light (FSC), side scattered light (SSC) and three channels of fluorescence intensity, FL1, FL2 and FL3. The detectors of fluorescence have three wavelength band filters to remove background light and these are given in Table 9.1.

The fluorescence from cells is initiated by the incident laser beam if fluorochrome markers have attached to specific binding sites on the cells. A number of fluorochrome markers are available as indicators of particular

cellular activity or function. In this study, specific markers have been used to detect the viability of cells described in section 9.4.

9.3.3 Electronics

The electronic system is used to convert the incident light pulses received by the photodetectors to numerical data that can be stored on a computer interface operating from a MAC platform. The FACSort measurement module schematically represented in Figure 9.2 is interfaced with a computer holding the FACSort software, LYSIS II. The optical signals incident on the photodetectors are converted to proportional voltage pulses. Analysis of the height of the voltage pulses is made and an analogue to digital conversion is made. The digital information is used in the LYSIS II software to provide numerical and graphical interpretation of the data received.

9.4 Fluorochromes for Cell Viability

The viability of cells passing through the measurement section of the flow cytometer has been established using a commercially available assay, LIVE/DEAD Viability/Cytotoxicity Kit (L-3224) (Molecular Probes Europe BV, Leiden, Netherlands). This is a two colour fluorescence cell viability assay that can simultaneous measure live and dead cells in a sample. Calcein AM is used as the fluorochrome for live cells. Live cells are distinguished by the presence of intracellular esterase activity and this is determined by the enzymatic conversion of non-fluorescent Calcein AM to intensely fluorescent Calcein. The polyanionic Calcein is well retained within live cells producing an intense uniform green fluorescence in live cells. The green fluorescence is detected as FL1 in the flow cytometer. Ethidium homodimer (EthD-1) is used as the fluorochrome for dead cells. EthD-1 enters cells with damaged membranes and undergoes a 40-fold enhancement of fluorescence upon binding to nucleic acids within the cell thereby producing a bright red fluorescence in dead cells. EthD-1 is excluded by the intact plasma

membrane of live cells. Cell viability in a given sample is determined from these physical and biochemical properties of cells.

9.5 Experimental Measurements on Cell Viability in CC-25R

A series of experiments have been conducted to assess the viability of freely suspended L929 murine fibroblasts under prescribed flow regimes for prescribed time periods in the bioreactor CC-25R. The cells and media conditions are the same as those described in section 8.3. Data has been obtained for four distinct hydrodynamic regimes of flow given in Table 9.2.

Mean Shear (s^{-1})[+]	Ta_I	Re_I	Regime
100	28.80	101.83	Laminar Couette
150	43.25	152.92	Laminar Taylor-Vortex
400	115.25	407.95	Wavy-Vortex
1000	288.11	1018.63	Turbulent Wavy-Vortex

Table 9.2 Hydrodynamic Regimes Used for Viability Studies

9.5.1 Preparation of the Fluorochrome Markers

The L-3224 LIVE/DEAD assay is supplied as a kit containing 2 vials of Calcein AM, 40μl each at a concentration of 4mM in anhydrous DMSO, and 2 vials of Ethidium homodimer-1, 150μl each at a concentration of of 2mM in DMSO/H_2O 1:4 (v/v). The signal of the markers obtained in the flow cytometer as FL1 for Calcein and FL2 for Ethidium is dependent on their concentration and the cell type used. This requires calibration using populations of cells which are known to be dead or alive. Cells were killed by covering them with 70% ethanol for 30 minutes. Optimum calibration of the fluorochrome markers was established following the protocol given on the

[+] Mean shear from linear theory used as the basis for control with Rheologica Stresstech rheometer

product information sheet for the L-3224 kit from Molecular Probes (1996). In essence this protocol requires establishing a concentration for which a bright red signal is obtained for a dead population of the given cell for study. Then establish a concentration of Calcein AM which produces no signal in dead cells but produces a bright green signal in live cells. The optimum concentrations were found to be 1μM for Calcein AM and 10μM for Ethidium homodimer-1. Dilution of the original stock solutions was made using Dulbeccos Phosphate Buffered Saline solution (PBS).

9.5.2 Cell Sampling and Analysis

Samples of 200μl of cell containing media were withdrawn from CC-25R at hourly intervals over a period of 8h and a further sample was withdrawn after 22h. The samples were withdrawn at two locations whilst the fluid was in a given flow regime. In Figure 8.1, the sample location points are indicated. On the right side of this figure two sample ports are identified and these have been the ones used. The upper sample port removes cells from the 'vortex' region of flow, that is to say the annular space where Taylor vortices can form. The lower port removes cells from the 'base' region of the vessel that is below the annular space and where vortices generally do not form. The fluid samples withdrawn were placed in FACS test tubes (Becton-Dickinson) to which 100μl each of Calcein AM at 1μM and Ethidium homodimer-1 at 10μM were added. The tubes were briefly agitated in a tube shaker (Whirlimixer, UK) and left in a hot room maintained at 37°C for 15 minutes prior to analysis in the flow cytometer.

In addition to optimising the fluorochrome concentrations, the signal-to-noise ratio was optimised for the photodetectors in the flow cytometer using parameters in the LYSIS II software. This was again achieved using a population known to be either live cells or dead cells. The FL3 photodetector was not used in this study so the parameter setting for this was adjusted to effectively provide a zero reading for all conditions. The optimum parameter settings used are given in Table 9.3.

Photodetector	LYSIS II Parameter Setting
FSC	358
SSC	210
FL1	550
FL2	489
FL3	291

Table 9.3 Photodetector Settings In LYSIS II Software

Representative data obtained from flow cytometry measurements is shown in Figure 9.3. As mentioned, the light signals received by the photodetectors are converted to voltage pulses. These can be processed directly or passed through a logarithmic amplifier. This amplifies weak signals and compresses large signals so both weak and strong signals can be displayed on the same scale. The FACSort uses a logarithmic amplifier. The output of voltage pulses after A/D conversion is a stream of numbers that require meaningful interpretation. The LYSIS II software does this. The side scatter and forward scatter is best represented as a dual-parameter correlated plot (or dot plot) for individual cell events measured and these can be displayed separately for live and dead cells or on the same graph. In the graphs shown here, the red regions indicate live cells and the green regions indicate dead cells; the colours are arbitrary and can be adjusted in the software. The shape of the cells can be inferred from dot plots of SSC-FSC, but there is always some degree of interpretation. Cells clumped at 10^2 on each axis suggests uniformly (elliptical) shaped cells. Dead cells usually show decreased FSC and slightly increased SSC. The scale on these axes is not a true measurement of size but a relative degree of scattered light. It is evident that a wealth of information can be obtained about the state of the cells from flow cytometry but from a viability perspective, the important information here is the population cell count and relative proportions of live and dead cells in this population. Statistical data is established by setting boundary markers (eg M1, R1, R2 etc.) to gate the numerical data. The relative degree of spreading of the dot plot of SSC-FSC is generally indicative of the degree of

physical damage incurred by the cells as a consequence of exposure to a given flow regime and in general, increased spreading is accompanied by a decrease in the FL1 signal and an increase in the FL2 signal. Whilst the FL1 and FL2 signals clearly identify live or dead cells, there is some overlap or intermediate situation, evident from the statistical analysis. In the sample data of Figure 9.3 statistically it suggests 91.11% of the population is live and 7.59% is dead which leaves a small population (1.30%) which on face value is neither live nor dead. It equally occurs in the data that sometimes the statistics indicate a combined percentage in excess of 100%, suggesting populations of cells are exhibiting fluorescence in both fluorochromes. This is possible for a distribution and variable concentration of fluorochrome marker on one cell. In fact, in situations where a population is exhibiting either expression of both markers or of no marker, the suggestion is that the cell is in a state of apoptosis. It is known that cells have an in-built programme which, when triggered, causes the death of the cell. The program by which programmed cell death is executed is called apoptosis. Apoptosis is involved in many normal biological processes and is a huge area of biological research and can be induced by a number of cytotoxic processes. In fact flow cytometry lends itself very well to the study of apoptosis in cells. In general, cells that produce neither definite live or dead expression are likely to be in an apoptotic state.

9.5.2.1 LIVE Cells

Data is presented for the percentage of live cells of the whole 200μl population obtained in samples taken from the vortex and base regions of CC-25R for given Taylor numbers at varying sample time in Figure 9.4. In Figure 9.6 data is presented showing the number of cells that remain in free suspension in the annular region. This is important as it indicates how the flow regime can provide adequate mixing and resuspension of cells over quantified time periods. Cells which 'fallout' of the annular region are then exposed to different shear stresses and oxygenation conditions which have a

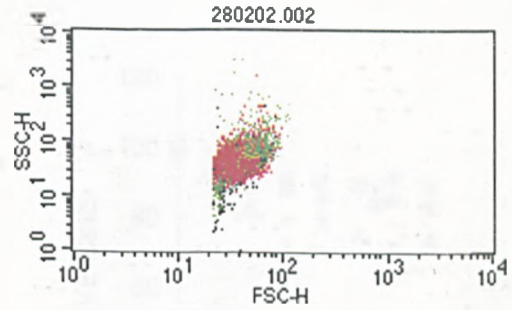

28/02/02
Fibroblast L929
Sample Time: 1h
Shear: 130s^{-1} (Ta_i = 37.37)
Region: Vortex
Stain: CAL-EthD1

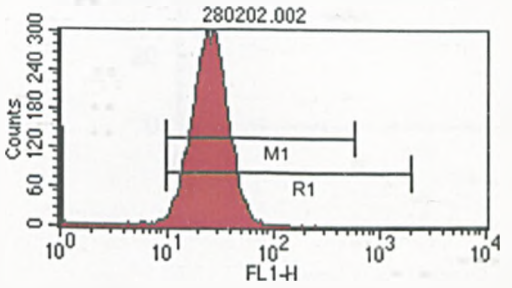

File: 280202.002 Acquisition Date: 28-Feb-2
Total Events: 30000

Marker	Left, Right	Events	% Total
All	1, 9910	30000	100.00
M1	10, 594	27333	91.11

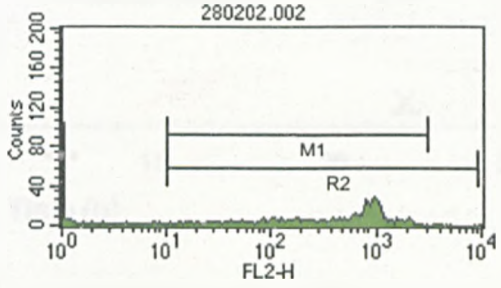

File: 280202.002 Acquisition Date: 28-Feb-2
Total Events: 30000

Marker	Left, Right	Events	% Total
All	1, 9910	30000	100.00
M1	10, 3134	2278	7.59

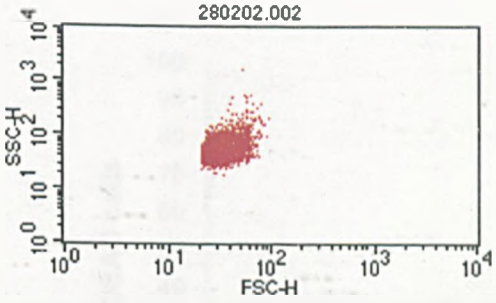

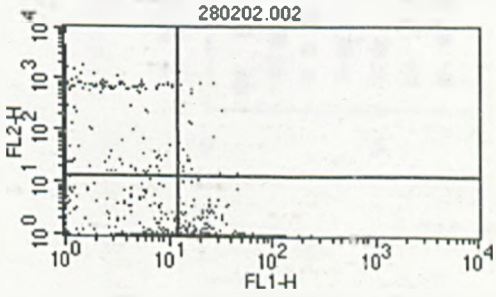

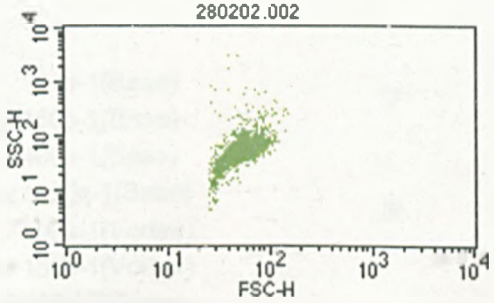

File: 280202.002 Acquisition Date: 28-Feb-2
Total Events: 30000 Y Parameter: FL2-H (Log)
Quad Location: 12, 12

Quad	Events	% Total	Y Mean	Y Geo Mean
UL	2260	7.53	638.27	367.33
UR	20	0.07	241.18	85.67
LL	1071	3.57	1.57	1.21
LR	26649	88.83	1.00	1.00

Figure 9.3 **Representative Data Obtained from Flow Cytometry Measurements: L929 Fibroblasts at Ta_i = 37.37 Sampled from the Vortex Region of Flow**

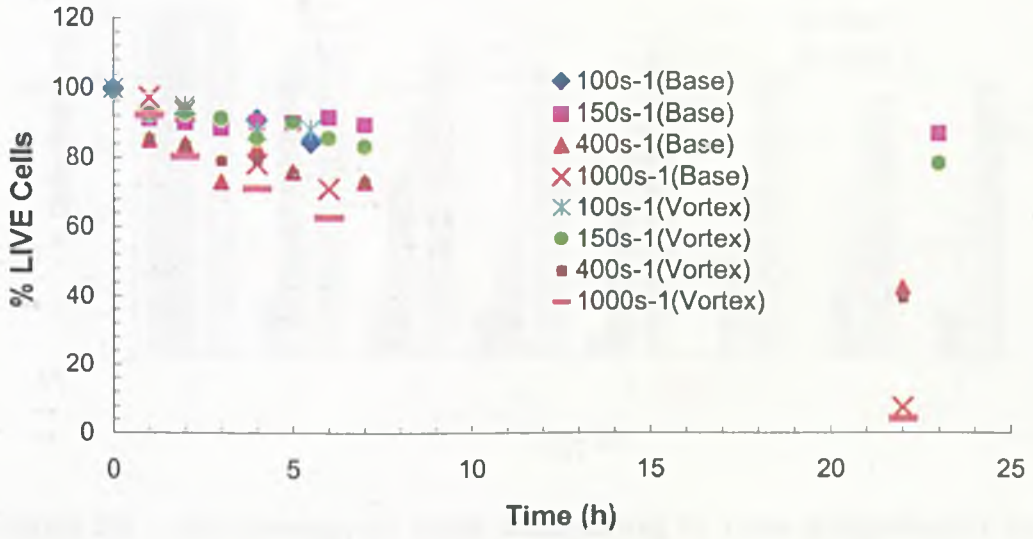

Figure 9.4 Percentage of LIVE Cells from Sample Population for Varying Flow Condition and Exposure Time

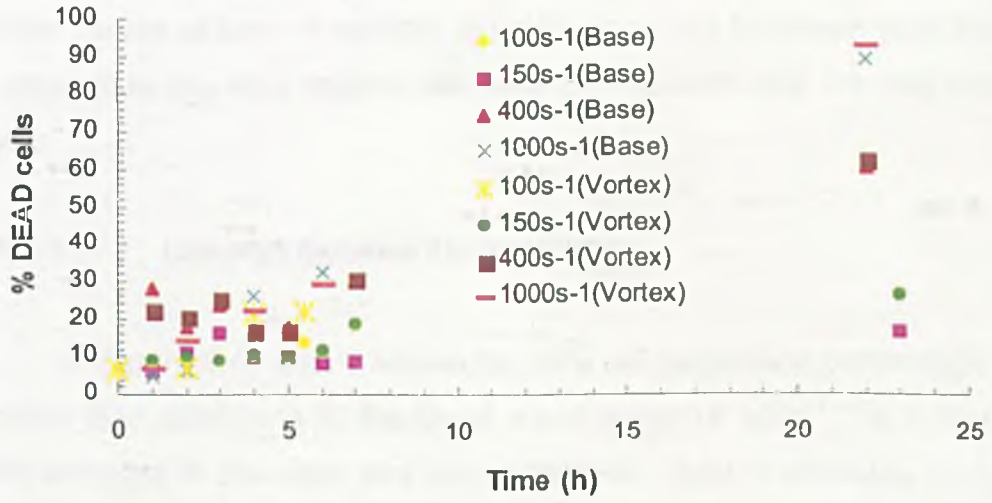

Figure 9.5 Percentage of DEAD Cells from Sample Population for Varying Flow Condition and Exposure Time

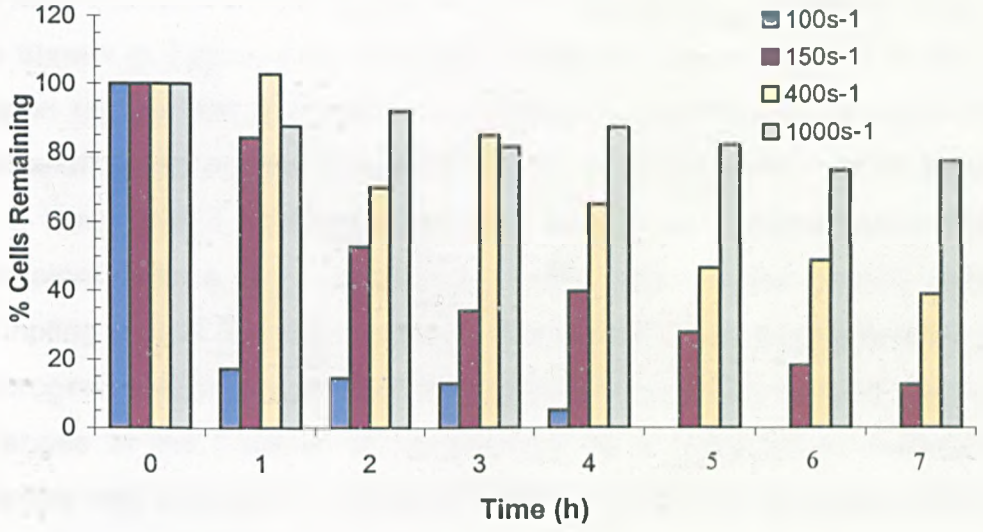

Figure 9.6 Percentage of Cells Remaining in Free Suspension in the Annular Region of CC-25R for Varying Flow Regime

bearing on their viability. Although not quantified from LDA measurements, it is observed from flow visualisation in CC-25 (Appendix A) that in the 'base' region the flow is noticeably more laminar (for lower Ta_i) and it is assumed that the cellular shear stresses in this region are lower than those in the 'vortex' region of flow. A number of conclusions can be drawn from this data in respect to the flow regime, the time of exposure and the cell sampling point.

9.5.2.1.1 Laminar Couette Flow ($100s^{-1}$)

In Figure 9.4, data is shown for LIVE cell population percentage under laminar flow conditions at the linear mean shear of $100s^{-1}$ (Ta_i = 28.80) for cells sampled in the base and vortex regions. Data is available up to a 6h sampling period and shows that the viability of the cells in both regions is good up to that time period (>80% cells LIVE). This suggests that up to this point the shear stresses the cells experience are not excessive and the decrease in viability is possibly due to oxygen transport limitations or changes in the chemical environment of the media (pH etc.). The maximum and mean shear stresses attained under this regime are 0.0991 Pa and 0.0518 Pa respectively from LDA measurements. Data is not presented

beyond this time period as the fallout of cells under the laminar flow is high as shown in Figure 9.6. The percentage of cells remaining in the vortex region rapidly falls and this is likely due to a combination of sedimentation, flocculation and maybe adherence of cells to the stationary wall of the vessel. It is likely that if flocculation of cells occurs and sedimentation becomes prevalent then a large population of the cells will be located below the sampling port in the base region of the vessel. This suggests strongly that microgravity rotating systems might alleviate the gravity settling problem and changes in the material of construction to a hydrophobic material might prevent wall attachment ultimately leading to reduced cell concentration and mass transport gradients.

9.5.2.1.2 Laminar Taylor Vortex Flow ($150s^{-1}$)

The LIVE cell population expressed in laminar Taylor-vortex flow ($150s^{-1}$; $Ta_i = 43.25$) is reasonably high (>80%) over a 23h sampling period in CC-25R from Figure 9.4. It is observed that the increased shear stress that cells might experience in the vortex region relative to the base region contributes to a slightly reduced viability with increasing time of exposure though in general, this difference is not large. It seems apparent that the percentage of LIVE cells in this flow regime is in fact slightly higher than in laminar Couette flow ($100s^{-1}$). It has been established that the shear stresses experienced by the cells are higher in this regime of flow (maximum 0.15 Pa; mean 0.078 Pa), however, the mass transport effects are much improved. It is suggested that the enhanced mass transport capabilities of this flow regime supersede the shear stress effects. It is emphasised that it is not known at this stage whether the increased shear might facilitate the cell viability from a biomechanical signalling mechanism and remains as a point for future study. From the perspective of cell fallout in the annular region in Figure 9.6 it is observed that the vortex flow significantly improves resuspension of cells in the vortex region compared with the Couette flow. In Couette flow there is a very rapid (exponential-like) fallout however in the laminar Taylor-vortex flow although fallout is evident it appears more linear.

It is suggested that this might be due to cell adhesion to the stationary wall and suggests modification of this for future studies.

9.5.2.1.3 Wavy-Vortex Flow ($400s^{-1}$)

The percentage of LIVE cells in wavy-vortex flow ($150s^{-1}$; Ta_i = 115.25) decreases more rapidly over a 22h time period than laminar vortex flow from observations of Figure 9.4. The percentage of LIVE cells is around 40% after this time period. The enhanced agitation of wavy flow does further promote resuspension of cells maintaining a higher percentage of cells in the vortex region from Figure 9.6 and it is known that mass transport in this regime is significantly enhanced. The reduced viability of the cells can then be attributed to shear stresses proving to be supercritical over this time period. The maximum and mean stresses in this case are 0.40 Pa and 0.21 Pa. It is evident that reduction of the Taylor number to provide a more gentle wavy motion will reduce this shear stress whilst also improving the mass transport and resuspension of cells. It is possible that somewhere slightly beyond laminar Taylor-vortex flow might be a good region for hydrodynamic operation.

9.5.2.1.4 Turbulent-Vortex Flow ($1000s^{-1}$)

Turbulent vortex flow significantly maintains resuspension of cells into the vortex region of the bioreactor from Figure 9.6. It is inferred from oxygen transport studies that this regime will provide very good mass transport and essentially remove oxygen/nutrient and cell concentration gradients. However, the fluid shear stresses generated by this type of flow are excessive and cause a significant reduction in the viability of the cells. After a 22h period of exposure to this regime the viability of the cells is less than 15%. The maximum and mean stresses occurring in this regime (Ta_i = 288.11) are 0.99 Pa and 0.52 Pa respectively.

It is observed in general that the percentage of LIVE cells in the base region is slightly higher than in the vortex for all time periods and regimes of

flow. This in itself suggests that the reduced stresses in the base region that are assumed to prevail are the major contributory factor to this, however it is only in laminar Couette flow that there is severe mass transport limitations from top-to-bottom of the vessel.

9.5.2.2 DEAD Cells

With a decrease in the percentage of LIVE cells with increasing Taylor number and exposure time one would expect a corresponding increase in the percentage of DEAD or apoptotic cells with increasingly agitated flow regime and exposure time. Apoptotic cells can be described as cells, which although still respiring, are in cycle of programmed cell death and thus will ultimately die irrespective of changes in their surrounding physico-chemical environment. In theory, the sum of the percentage of LIVE cells and DEAD cells at any given Ta_i and sample time should be 100% and general observations from Figures 9.4 and 9.5 suggest this to be the case. Small discrepancies which account for a value of 100% not being met are here considered to be small populations of apoptotic cells. Specific markers for apoptosis can be used to confirm this in flow cytometry studies. For the bioreactor system used, flow regimes, exposure times, oxygen delivery and media composition, the cells appear to have negligible populations experiencing apoptotic behaviour and in general there is clear evidence of either LIVE or DEAD populations.

9.6 Concluding Remarks

Flow cytometry has been used to establish how the viability of a controlled population of L929 murine fibroblasts is influenced by the hydrodynamic environment in an annular flow bioreactor. It is established that the hydrodynamics play a significant role. On the one hand, the hydrodynamics are influential in the resuspension of cells and progressively agitated regimes of flow appear to provide a more uniform distribution of cells throughout the fluid volume. In addition to resuspension, enhanced agitation provides better mass transport and for the primary transition from laminar

Couette to laminar Taylor-vortex flow it would appear that this is more important with respect to cell viability than the influence of shear stress is. Beyond this point, the shear stress appears to be the primary influencing factor on the cell viability, and it is suggested from the observations made here that mean stresses less than 0.2 Pa provide increased viability over longer time scales. A flow regime close to laminar Taylor-vortex but just beyond, into wavy vortex flow, might be well suited to longer-term viability, given the benefits of enhanced mass transport in a wavy regime. This regime of flow is achieved for a Taylor number between 50 and 60. There are limitations in the system used here, but on the basis of the results obtained, these limitations can be improved to see how significant they are on the long-term viability of cells.

References

Coulter WH, High Speed Automatic Blood Cell Counter and Size Analyzer. *Proc. Natl. Electronics Conf.* **12** 1034-1040 (1956)

Kamentsky LA, Melamed MR, Derman H, Spectrophotometer: New Instrument for Ultrarapid Cell Analysis. *Science* **150** 630-631 (1965)

Dittrich W, Gohde W, Impulsfluorometrie dei einzelzellen in suspensionen. *Z. Naturforsch.* **24b** 360-361 (1969)

Van Dilla MA, Trujillo TT, Mullaney PF, Coulter JR, Cell Microfluorimetry: A Method for Rapid Fluorescence Measurement. *Science* **163** 1213-1214 (1969)

Herzenberg LA, Sweet RG, Fluorescence Activated Cell Sorting. *Sci. Am.* **234** 108-115 (1976)

Chapter 10

Conclusions

Tissue engineering is a relatively new area of research and encompasses a very broad range of scientific disciplines. A great deal of knowledge and experience has yet to be achieved before the long-term goals of tissue engineering are met. The behaviour of cells in a dynamic flow environment is one area of tissue engineering that has large gaps in knowledge, in particular the relationship that exists between the flow condition, the shear forces the cells experience as a consequence of this flow condition and the delivery of oxygen and nutrients that the cells will see, again as a consequence of the flow condition. In this study, some basic relationships have been established that attempt to bring these phenomena together.

The shear stress effects on cells are dependent on the cell type and culture condition and it is emphasised that this work is based on a freely suspended culture of L929 fibroblasts, which in some senses is an unrealistic tissue engineering environment. The shortcomings of this work are discussed in the next chapter and suggestions for improvement are made. This work does however provide qualitative and quantitative data that provide grounds to suggest that an annular flow bioreactor might be an optimum choice for the initial mass proliferation of cells. In general terms, shear stresses in the range 0 to 1 Pa (0 to 10 dyn/cm^2) appear to be the optimum for long term cell culture. On the basis of LDA data measured in this study, it is apparent that freely suspended cells experience a non-uniform shear stress distribution in annular flows. The maximum shear stresses are encountered on the edge of

the boundary layer for the moving inner wall for all flow regimes beyond laminar Couette flow. It is observed that the stresses in this region are significantly higher than in other regions of the annulus. The radial thickness of this 'high shear' layer is approximately 1/10 of the radial gap size. This suggests that the time period for which cells are periodically exposed to high shear is small and this may be of significance. A significant finding of the shear stress calculations is that the shear stresses experienced by cells will be significantly lower in CC-75 for the same flow regime than in CC-25. As an example, the range of shear stress observed in CC-25 at Ta_i = 141.9 is between approximately 0.7 and 1 Pa. For Ta_i = 138.3 in CC-75 this range is 0.01 to 0.7 Pa. It is observed that the shear rate experienced by cells in all regions of the annulus follows an approximately linear relationship with Ta_i. For a larger range of shear data in the two scales of system it has been possible to provide a correlation that relates the scale-up ratio of the vessel to the corresponding mean shear ratio that will be encountered and this has been given as equation (5.30). On the basis of shear stress data, it seems apparent that larger scale reactors can be operated in more agitated regimes of flow whilst maintaining subcritical levels of shear stress and this has interesting implications for commercialising bioreactor systems. Fluid rheology is an important relationship used in the evaluation of the shear stress level in the fluid. Comparisons of the rheology of cell culture medium containing cells at 37°C and of 0.1wt% Timiron particles that were used for LDA modelling (Figure 3.7) show that the viscosity of the media is higher particularly beyond laminar Couette flow. This means that prediction of cellular shear stress from LDA data is slightly underestimated.

The mechanism of transport as a consequence of the bioreactor fluid dynamics has been well established from the dye tracer studies. Measurements of oxygenation have relied on using surface aeration, fixed initial cell populations and known fluid dynamics as a control to developing appropriate transport correlations. Whilst the actual concentration of oxygen in the atmosphere and the surrounding pressures might vary, the use of absolute changes in concentration has effectively removed this problem. It is understood that consumption of oxygen occurs by respiring viable cells and

this has not been specifically incorporated into any transport correlation (*viz.* equation 8.4). It is felt that the use of a fixed initial population and repeated studies controlling all other factors means that this effect can potentially be incorporated into the exponents of the transport correlation. Further studies to generate more data points for smaller changes in the flow regime (smaller Ta_i increments) might serve to elucidate this point better. The findings of this work show that oxygen is better transported through the system with enhanced agitation, however the increased shear stresses will reduce viability of cells and thereby cause a reduced consumption.

In assuming that oxygen and solute transport is due to forced convection mass transport alone, the viability of the cells can be directly related to the hydrodynamics. This will have the detrimental effect of increased shear stress but the benefits of better oxygenation and resuspension of cells. On this basis the experimental findings suggest that an optimum regime of flow in the annular flow bioreactor CC-25 is at a Ta_i of around 60. This is just slightly beyond the transition in flow from laminar Taylor-vortex to wavy-vortex flow. At this Taylor number, the mean shear rate is around $215s^{-1}$ and cell viability is maintained at around 80% in the annulus after 24h. The absolute oxygen concentration levels appear to be maintained at around 75% of the atmospheric condition. For lower Ta_i than this optimum condition oxygen transport becomes significantly reduced and problems of sedimentation of cells occurs. For cell-seeded microcarriers, these problems will likely be worsened. For higher Ta_i there are progressively smaller improvements in oxygen transport and cell suspension but this is at a cost of significantly higher levels of shear stresses on the cells. These higher stresses although not critical in the short term experiments conducted here are anticipated to be critical in the longer term. Further experiments will be required to confirm the hypothesis that the reduced shear stresses observed in CC-75 can be used to increase the Taylor number beyond the optimum of around 60 in CC-25 and provide better mass transport. Proposals to achieve this are discussed in the next chapter.

Chapter 11

Recommendations for Future Work

The findings from this study have highlighted a number of areas to improve the bioreactor design that it is hoped will elucidate further the relationship between the dynamic environment and the behaviour of cells in the system.

Experiments in this study have been short term; the maximum duration time for measurements made in the working bioreactor CC-25R has been 24h and this falls very far short of a culture time for tissue engineering bioreactor which would be of the order of weeks. The short-term experiments have been necessitated arising from difficulties to maintain a sterile environment within CC-25R. This problem is immediately being addressed. A new design for the manifold of the working bioreactor will remove the need for using the Rheologica Stresstech rheometer and will allow for a scaleable working bioreactor to verify the claims of this study that a more agitated regime of flow will maintain cell viability in a larger system. The manifold of the new system is shown in Plate 11.1. The purchase of a CO_2 controller (Portomatic 3063, Thermo Forma, USA) and a sterilisation chamber in which to house the

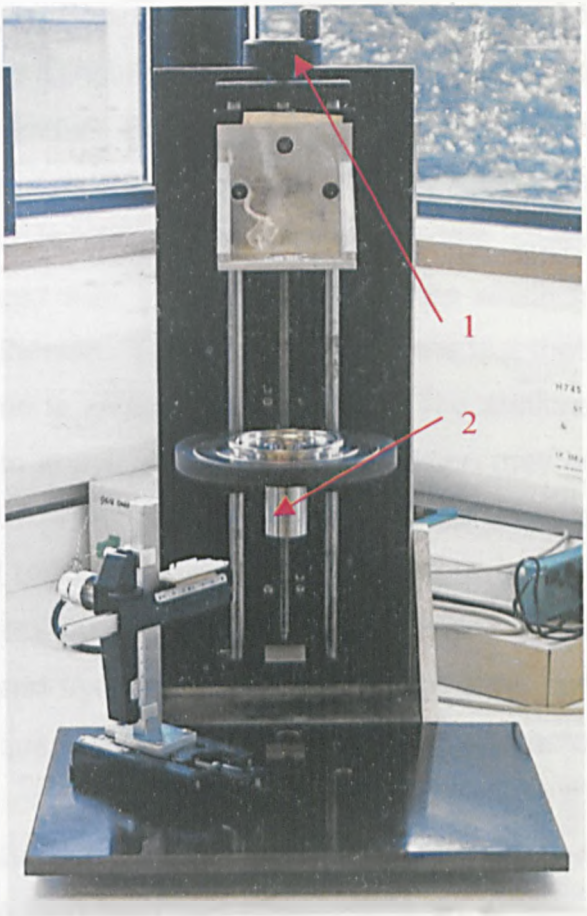

Plate 11.1 Manifold system for CC-25R as replacement to Rheologica Stresstech rheometer; (1) Manual mechanism to raise and lower the inner cylinder, (2) Outer cylinder of reactor

reactor manifold (Cellgenix GmbH) will allow the complete reactor system incorporating the cell sampling and oxygen probe (Chapter 8) to be housed in a hot room maintained at 37°C and operate under sterile conditions for much longer time periods.

The number of cells remaining in the (ideal) Taylor-vortex region within the bioreactor is an important question that is not completely answered from the current study. Sampling from the vortex region and from the base region below the annulus in some part gives an indication of the sedimentation of cells under a prescribed regime of flow but the adherence of cells to the stationary outer wall or to the rotating inner wall in the current reactor operation protocol is not known. This information is required for optimising

the hydrodynamics. Preliminary studies, not described in this work, have used a polyethylene (Tecoflex) membrane, 100μm thick, dip coated onto the wall of the inner cylinder. Scanning Electron Microscopy (SEM) from various regions of this membrane have showed that no cells appear to adhere to it under all the flow conditions investigated in this study, even when the membrane is treated with 10% foetal calf serum which is known to initiate preferential cell adhesion. This may be due to the fact that the wall is moving and insufficient time is allowed for adhesion. The stationary outer wall is of PMMA construction in this study and cell adhesion may occur there but due to the geometry it has not been possible to make repeated SEM studies of this wall to see if cell adhesion is occurring there. It is proposed that the outer wall will be replicated in polytetrafluoroethylene (PTFE) that is known to be non-cytotoxic and hydrophobic so should not allow cell adherence. This should clarify the question of wall adhesion in the bioreactor from this study.

The purpose of the current work has been to understand the relationship between the hydrodynamics and mass transport effects on the viability of cells in an annular reactor and the use of freely suspended cells has been sufficient to address this. In general, for tissue engineering applications, the cells are required to be seeded onto an appropriate supporting scaffold. This opens up a wider area for study when using this type of bioreactor. In the first instance freely suspended scaffolds (microcarriers), which have been employed for a number of years, are promising replacements for the freely suspended cells. It is intended to use these in the upgraded annular flow bioreactor system as: (1) a copopulation with freely suspended cells to see if a particular flow regime enhances the cell attachment to the microcarriers and (2) as a homogeneous population of well seeded carriers in a range of flows to investigate if a particular flow regime might enhance the shear and mass transport capabilities to overcome necrotic cores in the microcarriers, a commonly encountered problem.

Within the Department of Clinical Engineering at the University of Liverpool a number of other research collaborators are looking to develop new approaches to manufacturing well-characterised porous and non-porous

scaffolds from a range of polymeric materials, most notably Tecoflex, poly-L-lactic acid (PLLA) and polycaprolactone (PCL). It is anticipated to incorporate these scaffold materials into the bioreactor system on the rotating inner wall once they have been seeded with an appropriate cell type and then investigate how the hydrodynamic and mass transport environment facilitates proliferation and ingress of cells onto and into the scaffold material. The techniques of SEM, confocal microscopy and real time PCR are available to facilitate these investigations.

It has been mentioned above that the vertical orientation of the system CC-25R is not conducive to allowing cells to seed onto a material on the rotating inner wall. A separate annular flow system has been devised where the outer wall and the inner wall co-rotate at the same speed. The scaffold material is attached to the inner wall and a free cell-media suspension exists in the annular space. The outer wall is of PTFE construction to prevent cell attachment on that wall and the system rotates laterally on a roller table in a pseudo-microgravity hydrodynamic environment. The inner cylinder comes directly from the CC-25R reactor. It is modified such that the supporting shaft is hollow and has orifices to allow perfusion of oxygen into the cells and media in the annulus. This bioreactor has been designated as CC-25T for future work and is shown in Plate 11.2. Preliminary SEM studies have shown that cells will readily attach to a Tecoflex membrane using the CC-25T reactor. It is proposed to transfer the inner cylinder from CC-25T when the scaffold is seeded with cells into CC-25R and then experience it to the range of flow conditions described in this work to investigate the effects on the cells using analysis techniques described above.

These series of studies that have been described above are in essence 'proof of principle' experiments to establish operating criteria for an annular flow bioreactor under various configurations and regimes of flow. In parallel, designs are in place to develop a universal rotating bioreactor that encompasses all of the features that the work so far has shown to be of importance:

- Independent rotation of the walls
- scaleable geometries
- versatile internal (e.g. an inner cylinder can be replaced with an impeller)
- long-term sterile operation
- choice of batch or perfusion regime
- vertical or lateral operation

Designs for the manifold to support this universal bioreactor are in place and fabrication has now begun.

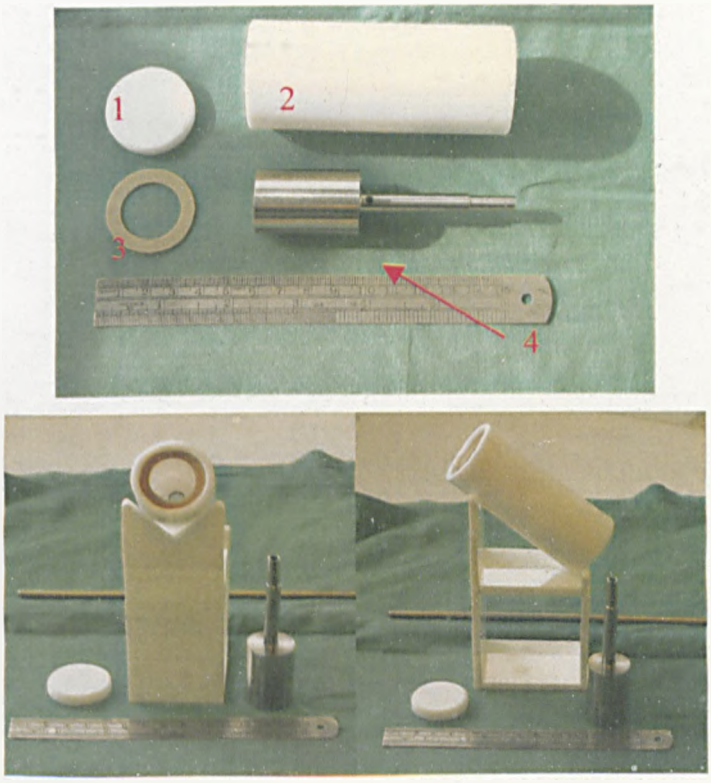

Plate 11.2 **CC-25T bioreactor for lateral rotation and cell seeding of scaffolds; (1) End cap in PTFE, (2) Outer cylinder in PTFE, (3) Silicone O-ring for end cap, (4) Orifice in inner cylinder shaft for oxygenation. Lower plates show support for CC-25T to facilitate introduction of cells and media into the annulus.**